VIETNAM NATIONAL UNIVERSITY
UNIVERSITY OF ENGINEERING AND TECHNOLOGY

TRẦN NHƯ CHÍ

DEVELOPMENT OF A PROTEIN DETECTION SYSTEM FOR POINT-OF-CARE TESTING (POCT) IN BIOMEDICAL DIAGNOSTICS

(Nghiên cứu phát triển hệ thống phát hiện proteins cho các ứng dụng chẩn đoán tại chỗ (Point-of-care) trong xét nghiệm y sinh)

PhD DISSERTATION IN ELECTRONIC ENGINEERING

HANOI - 2025

VIETNAM NATIONAL UNIVERSITY
UNIVERSITY OF ENGINEERING AND TECHNOLOGY

TRẦN NHƯ CHÍ

DEVELOPMENT OF A PROTEIN DETECTION SYSTEM FOR POINT-OF-CARE TESTING (POCT) IN BIOMEDICAL DIAGNOSTICS

(Nghiên cứu phát triển hệ thống phát hiện proteins cho các ứng dụng chẩn đoán tại chỗ (Point-of-care) trong xét nghiệm y sinh)

PhD DISSERTATION IN ELECTRONIC ENGINEERING

MAJOR : ELECTRONIC ENGINEERING

MAJOR CODE : 9510302.01

SUPERVISOR : Assoc. Prof. Dr. BUI THANH TUNG

HANOI - 2025

Declaration of Authorship - Lời cam đoan

I hereby declare that this dissertation is solely my own work. The data in this dissertation are the results of my personal research and have not been used in other publications by anyone else.
Tôi xin cam đoan đây là công trình nghiên cứu của riêng tôi. Các số liệu, kết quả nêu trong luận án là trung thực và chưa được công bố bởi ai khác.

Hanoi, February 01 2025
PhD Student

Trần Như Chí

Acknowledgment

I would like to begin by expressing my heartfelt gratitude to my advisor, Assoc. Prof. Dr. Bui Thanh Tung, for his unwavering support throughout my Ph.D. journey. His patience, motivation, and extensive knowledge have been invaluable, and this work would not have been possible without his guidance and encouragement. I am equally grateful to Prof. Chu Duc Trinh and Dr. Do Quang Loc, who were always available to provide insights and answer my questions about my research and writing. Their advice and openness were invaluable, as they allowed me the freedom to develop my own ideas while ensuring I stayed on the right path.

I would also like to extend my sincere thanks to Dr. Nguyen Dang Phu and Dr. Vu Quoc Tuan, who provided me with meaningful opportunities both in my studies and in my personal development. My deep appreciation goes to Prof. Chun-Ping Jen and my friends in the Department of Mechanical Engineering and Automation for their support during my internship at National Chung Cheng University. Additionally, I am thankful to my colleagues in the Faculty of Electronics and Telecommunications for their camaraderie, support, and for creating a warm and collaborative environment. Finally, I owe my deepest gratitude to my family for their unwavering encouragement and spiritual support, which has sustained me throughout my life and academic journey.

This dissertation was funded by the Vietnam Ministry of Science and Technology under Grant NĐT.101.TW/21. Chi Tran Nhu was funded by the Master, PhD Scholarship Programme of Vingroup Innovation Foundation (VINIF), code VINIF.2022.TS015 and VINIF.2023.TS.016.

Contents

List of Abbreviations

anti-BSA anti-albumin antibody

anti-NSE anti-neuron-specific enolase

APCI Atmospheric pressure chemical ionizatio

BSA-FITC Bovine serum albumin - fluorescein isothiocyanate conjugate

CE Capillary electrophoresis

CPL Concentration polarization layer

CRP C-reactive protein

CV Cyclic voltammetry

DFT Discrete Fourier transform

DI Deionized water

DL Diffuse layer

DNA Deoxyribonucleic acid

EDC N-(3-Dimethylaminopropyl)-N-ethylcarbodiimide hydrochloride

EDL Electric double layer

EIS Electrochemical impedance spectroscopy

ELISA Enzyme-linked immunosorbent assay

EOF Electroosmotic flow force

EPF Electrophoresis force

ESI Electrospray ionization

FAS Field amplification stacking

GUI Graphical user interface

hGH Human growth hormone

HPLC High-performance liquid chromatograph

I2C Inter-integrated circuit

IAC Immunoaffinity chromatograph

IC Integrated circuit

ICP Ion concentration polarization

IEF Isoelectric focusing

IHC Immunohistochemistry

IHP Inner Helmholtz plane

IPA Isopropyl alcohol

ITP Isotachophoresis

JFET Junction Field Effect Transistor

KCl Potassium chloride

LE Leading electrolyte

LOC Lab-on-a-Chip

LOD The limit of detection

MEKC Micellar electrokinetic chromatography

MEMS Micro-electromechanical systems

MS Mass spectrometry

NHS N-Hydroxysuccinimide

NSE Neuron-specific enolase

OCT Point-of-care testing

OHP Outer Helmholtz plane

OLC Over-limiting current

PANI Polyaniline

PBS 1X 1X Phosphate-Buffered Saline

PCB Printed circuit board

PCC Phantom Camera Control

PCR Polymerase chain reaction

PF Preconcentration factor

pI Isoelectric point

PDMS poly-dimethylsiloxane

PEO Poly(ethylene oxide)

PSA Prostate-specific antigen

SAM Self-Assembled Monolayer

SDS Sodium dodecyl sulfate

SCL Space charge layer

SPI Serial peripheral interface

TE Terminating electrolyte

UART Universal Asynchronous Receiver/Transmitter

List of Figures

List of Tables

Dissertation introduction

Background and context of the research

Proteins, composed of amino acid chains linked by peptide bonds, play pivotal roles in the human body. Beyond serving as structural components of cells, they participate in nearly all biological processes, from catalyzing metabolic reactions to regulating the immune response. For instance, proteins help form immune serum (antibodies), which defends the body against infections and pathogens. Due to these critical functions, protein testing has become an essential tool in diagnosing and treating various diseases, particularly cancers.

Currently, several immunoassay-based techniques, such as immunohistochemistry (IHC), enzyme-linked immunosorbent assay (ELISA), and flow cytometry, are used to detect and quantify proteins in clinical settings. These methods, relying on optical measurement, provide high accuracy and specificity and are widely implemented in clinical and research laboratories. However, traditional techniques face challenges such as detection sensitivity limits, extended processing times, and the need for skilled operators, limiting their feasibility for point-of-care testing (POCT) applications. Consequently, researchers are increasingly focusing on the development of more adaptable and automated solutions.

Emerging microfluidic and biosensing technologies offer potential solutions to these challenges, with several advantages such as enhanced sensitivity, reduced sample volume, and streamlined workflows. Microfluidic channels, in particular, allow precise sample manipulation and can isolate, concentrate, and analyze biological markers in small volumes, providing an ideal foundation for POCT systems. By integrating biosen-

sors with microfluidic platforms, these systems could effectively replace conventional, lab-bound techniques.

In this study, an automated POCT system that combines biosensors with a microfluidic chip was developed to detect and quantify protein concentration the the solution, offering preliminary diagnostic insights. This system minimizes user intervention while offering rapid, reliable, and accessible diagnostic results, representing a significant advancement in early disease detection and monitoring.

Objective and significance of the research

This dissertation focuses on developing a protein enrichment and detection system, designed to integrate with a microfluidic platform for efficient preconcentration and detection of proteins using minimal volumes and short experiment times. The research objective is to investigate, design, and conduct experiments on the proposed system, utilizing a microfluidic chip based on electrochemical immunosensor principles. The chip detects target proteins in solution by monitoring changes in fluorescence and electrical signals. These output signals are recorded, processed, and displayed, offering a streamlined approach to protein detection and analysis.

Scientific and practical significance

This research sits at the intersection of multiple fields, including electronics, control systems, microfluidics, physics, biology, and microfabrication. The proposed system aims to detect the presence of specific proteins and quantify their concentrations in solutions. Successfully implementing this system would provide a cost-effective alternative to high-end commercial equipment, enabling rapid protein detection without the need for extensive laboratory infrastructure. Additionally, the system offers on-site detection and quantification, requiring only a short processing time, minimal sample volume, and a straightforward operational process.

Methods and scope of the study

To achieve the specific objectives, this dissertation encompasses several key research components: a comprehensive literature review, system modeling, structural analysis, fabrication processes, and experimental measurements to evaluate system performance. Specifically, the work involves designing a microfluidic structure integrated with preconcentration units and sensing electrodes, as well as modeling and analyzing the system's operation. Additionally, the study focuses on control circuit design, protein preconcentration within the microchannel, and signal processing circuits to accurately detect protein presence in the sensor region.

Overview of the dissertation structure

The dissertation consists of 5 main chapters. In Chapter 1, an overview of protein and the role of protein in the human is presented. Then, a review of protein immunoassay methods is provided. Finally, protein preconcentration principles and methods and the theory of ion polarization in nanofluidic channels are given.

Chapter 2 details the development of a microfluidic chip for protein preconcentration using a dual-gate structure and ion-selective nanomembrane. First, a preconcentrator is designed and modeled to analyze the operation of the structure. Then, the chip fabrication process is outlined, employing photolithography and soft lithography techniques. Finally, experiments are conducted to evaluate the functionality and performance of the proposed chip.

Chapter 3 describes the development of immunosensors through the electrode surface functionalization process, applied to both gold and carbon electrodes. Fluorescence and electrical measurements are then conducted to detect protein captured on the electrode surface. Additionally, a performance comparison between sensors based on two-electrode and three-electrode configurations is presented, highlighting the strengths and limitations of each configuration in terms of sensitivity and detection accuracy.

Chapter 4 presents the development of a pre-concentration control system and an

electrochemical measurement circuit. First, the system's design and block diagram are introduced to outline its functional components and workflow. Following this, the embedded algorithms and graphical user interface (GUI) are described, detailing their roles in system operation and user interaction. Finally, experimental tests are conducted to evaluate the system's performance, verifying its effectiveness in pre-concentration control and electrochemical measurement.

Chapter 5 presents the development of an integrated microfluidic chip for protein concentration and detection. First, the chip design is introduced, providing an overview of its operation and functional layout. Following this, the fabrication processes for the electrode and microchannel structures are presented. Finally, a series of experiments are conducted to evaluate and verify the chip's performance, assessing its efficiency in protein concentration and detection.

Finally, the author concludes the research and suggests directions for future studies.

Chapter 1

Overview

1.1 Introduction of protein and the role of protein in the body

1.1.1 Protein

Protein, also known as polypeptides, is a vital biological molecule composed of multiple amino acids linked by covalent peptide bonds. Proteins play essential roles in cellular processes, including participation in metabolic reactions, DNA replication, response to stimuli, and the transport of molecules from one location to another [107, 3, 116]. Proteins are found throughout the body, from large structures like muscles, skin, and bones to microscopic components such as tissues and cells. Their functions in the human body are incredibly diverse, with at least 10,000 different types of proteins contributing to human structure and sustaining bodily functions. This diversity primarily arises from the sequence of amino acids, which is directed by the nucleotide sequence of corresponding genes, and from the way protein molecules fold into specific three-dimensional structures that enable specialized functions.

Proteins are large biological molecules composed of amino acid chains. Amino acids are linked by peptide bonds to form polypeptide chains, which, in turn, self-assemble into complete proteins. Each protein possesses a unique amino acid sequence, consistent across all molecules of that protein. To date, thousands of distinct proteins have been

identified, each defined by its specific sequence of amino acids. The core structure of the polypeptide chain, known as the polypeptide backbone, comprises a repetitive sequence of atoms. Attached to this backbone are the side chains of the amino acids, which do not participate in peptide bonding.

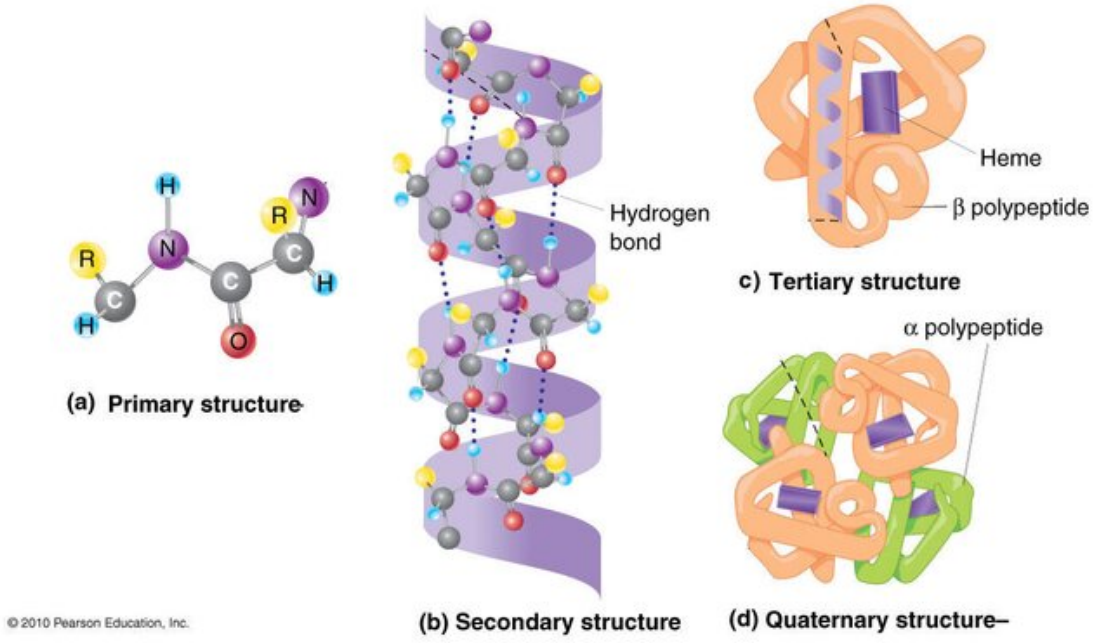

Figure 1.1: Four levels of protein structure [114]

These side chains, of which there are 20 distinct types, confer unique properties to each amino acid [3]. The amino acid sequence determines the unique three-dimensional structure and specific function of each protein. Figure 1.1 illustrates the four levels of protein structure in space. The primary structure is the simplest level, where amino acids are connected by peptide bonds, forming a polypeptide chain. The primary structure dictates interactions within the polypeptide chain, which ultimately shapes the protein's structure and properties [116, 64].

The secondary structure of proteins involves the regular spatial arrangement of polypeptide chains. Polypeptide chains often coil into α-helices or form β-sheets, structures stabilized by hydrogen bonds between amino acids. This structure influences the protein's shape; for example, fibrous proteins like keratin and collagen commonly contain abundant α-helices, while globular proteins tend to have more β-sheets.

The tertiary structure is the folding of α-helix and β-sheets into unique three-dimensional configurations specific to each protein type. This spatial structure determines the protein's activity and function, governed by the properties of the R groups in the polypeptide chains. The quaternary structure consists of multiple polypeptide chains interacting to form the protein's final structure. The quaternary structure of these polypeptide chains is stabilized by weak interactions, such as hydrogen bonds.

The diversity of protein structures enables them to participate in a wide range of biological processes, from cellular architecture to metabolism and signal transduction. Studies of protein structure and function are crucial for understanding these biological processes and provide a foundation for research and therapeutic strategies in disease treatment. Amino acids are organic compounds containing an amino group ($-NH_2$) and a carboxylic acid group (–COOH) attached to the same carbon atom. Each amino acid has a unique R group, contributing to the diversity of amino acids. In nature, approximately 20 types of amino acids are found in proteins and other biological molecules. These amino acids are classified into two main groups: basic amino acids and acidic amino acids. Basic amino acids have R groups with alkaline properties, while acidic amino acids have R groups with acidic properties. Amino acids are further categorized based on the nature of their R groups, which may include alkyl, aromatic, hydroxyl, or sulfur-containing groups.

Amino acids are the building blocks of polypeptide chains, connected through peptide bonds to form proteins. This diversity allows for the formation of numerous proteins with various properties and functions, forming the basis for the diversity of biological processes. A peptide bond is a chemical link between two amino acid molecules, where the carboxyl group (–COOH) of one amino acid joins with another amino group ($-NH_2$), creating a peptide linkage (–CO–NH–) and releasing a molecule of water. When amino acids are connected through peptide bonds, their R groups extend outward, forming the "wings" of the new polypeptide chain. These chains can then fold together to form more complex protein structures. Peptide bonds are essential to protein structure as they link amino acids into polypeptide chains, forming the foundation of protein architecture. The variety of amino acids and peptide bonds enables the formation of proteins

with diverse properties and functions. Figure 1.2 The formation of protein structures [21] illustrates the structure of amino acids linking to form proteins via peptide bonds.

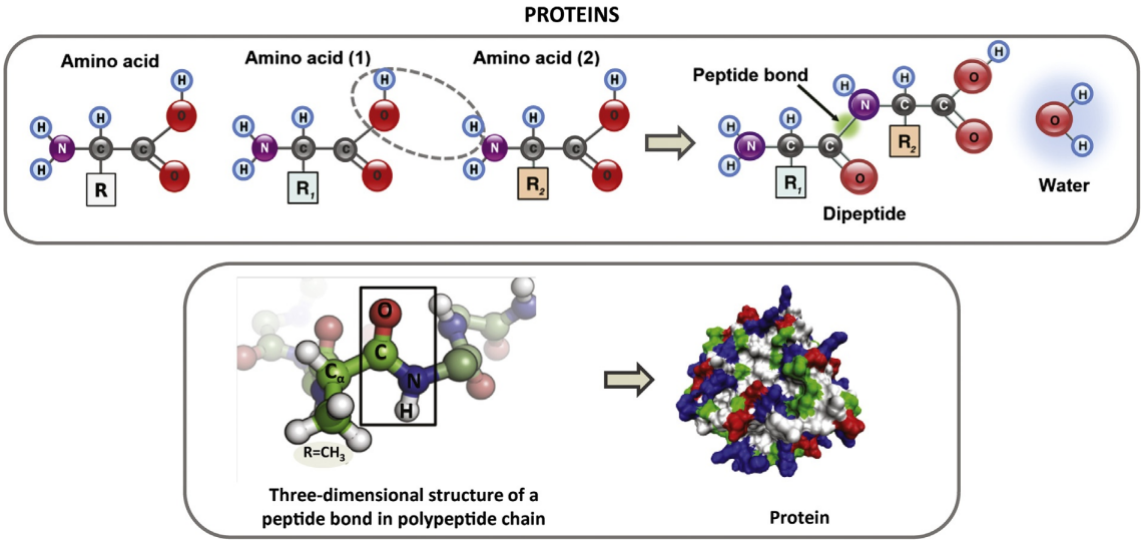

Figure 1.2: The formation of protein structures [21]

1.1.2 The role of protein in the body

Proteins play an indispensable role in sustaining life and human bodily functions, directly impacting numerous aspects of normal physiology. Accounting for up to 50% of the cell's total dry mass, proteins serve not only as crucial structural components but also actively participate in the maintenance, repair, and growth of the body. Protein deficiency can lead to various health issues, including malnutrition, weakened immunity, stunted growth, and a frail physical condition [60].

In the body, proteins perform a multitude of essential functions. They form the structural components of the cellular framework, participating in all cellular processes and helping to maintain cell shape and function. Certain fibrous proteins provide rigidity to tissues and cells. Keratin, for example, is a structural protein found in the skin, hair, and nails, while collagen, the most abundant protein in the human body, is a key structural component of bones, tendons, ligaments, and skin. Proteins also support body growth through muscle formation, cell renewal, and division. Additionally, proteins are vital for the transport of oxygen and nutrients throughout the body. Most

nutrients are transported from the site of absorption in digestion to the bloodstream, then delivered to tissues and cells by proteins. Hemoglobin, a transport protein, carries oxygen from the lungs to other cells, ensuring cellular function [38].

Proteins also play a crucial role in protecting the body. White blood cells, largely composed of proteins, defend against harmful agents entering the body. The immune system produces various proteins, such as interferons, to combat viruses and other pathogens. This protective role becomes evident when the body's ability to synthesize and absorb protein decreases, leading to a weakened immune system and increased susceptibility to illness. Additionally, proteins act as signaling units. Some proteins function as hormones, serving as messengers that facilitate communication between cells, tissues, and muscles. Common examples of protein hormones include insulin, glucagon, and human growth hormone (hGH).

Additionally, proteins provide a substantial amount of energy for the body, accounting for approximately 10–15% of the basic diet and supporting cellular function and vitality. Proteins also play a role in pH balance, helping maintain circulatory stability and regulate water levels in the body. In summary, the role of proteins in human health is indispensable, making a crucial contribution to life and normal bodily function. Consequently, protein levels in the body can reflect overall health status and are often indicative of abnormalities related to liver, kidney, and joint diseases. Early detection of abnormal protein levels through testing can guide physicians toward accurate diagnoses and timely interventions.

1.1.3 Protein is a biomarker for disease detection

In medicine and biological research, proteins are regarded as essential biomarkers, aiding in the identification and diagnosis of various diseases as well as in monitoring their progression. Biomarkers are biological indicators used to detect or track a biological process, disease state, or body response to treatment. A biomarker can be a molecule, cell, gene, enzyme, or hormone. They provide critical information about an individual's health status and support disease diagnosis, staging, and evaluation of treatment effectiveness. Figure 1.3 shows some types of biomarkers for cancer detection.

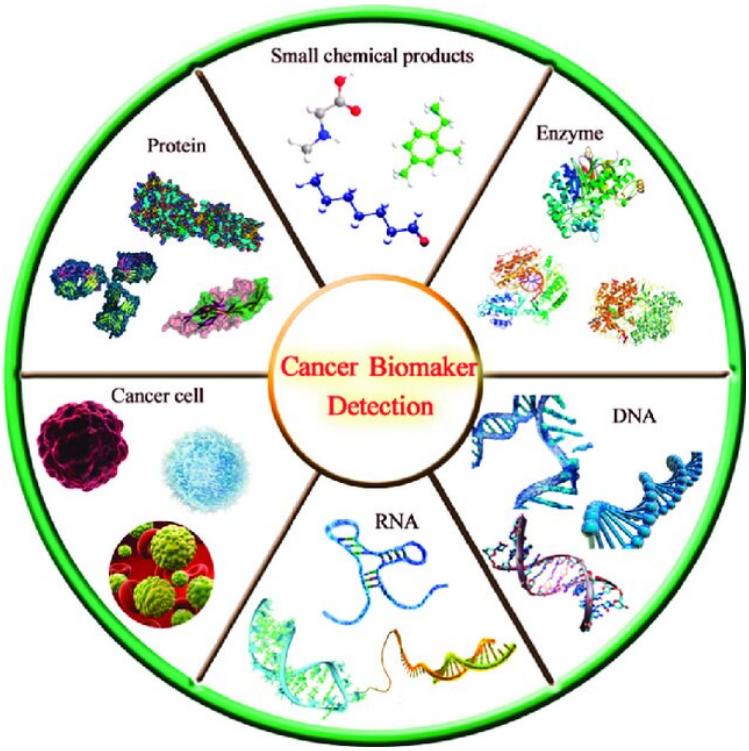

Figure 1.3: Schematic illustration of various cancer biomarkers [140]

Proteins are widely used as biomarkers due to several advantages. Firstly, they exhibit high specificity in detecting diseases. Certain proteins are only present in specific tissues or cells, allowing for precise information about disease conditions. For example, Prostate-Specific Antigen (PSA) serves as a biomarker for prostate cancer [125]. Secondly, proteins can be easily detected through various technologies. Modern technology enables the sensitive detection and quantification of proteins. Techniques such as Enzyme-Linked Immunosorbent Assay, western blotting, and mass spectrometry allow for the identification and measurement of specific proteins in biological samples [132]. Thirdly, many proteins are directly linked to pathological processes, such as enzymes involved in cancer progression or inflammatory proteins associated with autoimmune diseases [31]. Fourth, proteins can be used to monitor treatment progress. Changes in the concentration of certain proteins in blood or other tissues can reflect treatment effectiveness. For instance, levels of C-reactive protein (CRP) may decrease when patients respond well to anti-inflammatory therapy [95].

Notably, proteins aid in the early detection of various cancers. For instance, elevated

levels of the protein CA-125 may indicate ovarian cancer [9]. Some proteins can help determine the stage and severity of cancer. For example, HER2/neu protein levels can assist in staging and treatment selection for breast cancer [111]. By tracking changes in protein levels during treatment, doctors can assess treatment effectiveness and adjust treatment plans if necessary [22].

1.2 Protein immunoassay methods

Protein testing primarily relies on immunoassays with various techniques, including immunohistochemistry (IHC) [144, 133], ELISA [133, 117], and flow cytometry [28], as illustrated in Figure 1.4. The techniques listed above are widely used in biological testing and disease diagnostics at medical centers, describing commonly used methods as well as those currently under development for protein analysis.

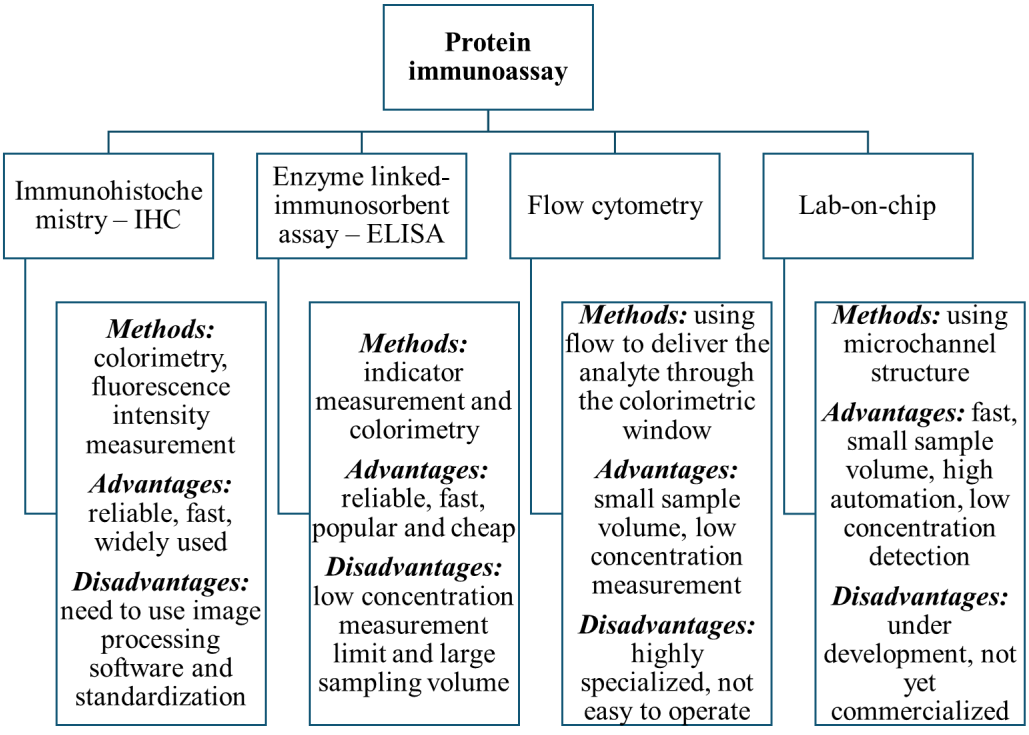

Figure 1.4: Protein assay methods based on immunoassay methods

Protein biomarkers are valuable indicators for monitoring tumor progression and serve as markers in disease detection assays. ELISA is considered a standardized

method for quantifying proteins in solution, where target proteins are captured on a surface and labeled with enzymes that produce a color change, allowing detection. However, this method requires a high concentration of the target protein. At low concentrations, colorimetric detection and optical systems are inadequate. In such cases, protein biomarkers need to be concentrated to increase their levels above the detection limits of sensors. Moreover, sensors must exhibit high sensitivity and reliability. In hospitals and medical facilities, tumor markers are identified using traditional analytical methods such as ELISA, polymerase chain reaction (PCR), and fluorescence-labeled immunoassays. These methods provide accurate and selective results but require lengthy analysis times, expensive reagents, single-marker analysis, and specialized equipment [113].

1.2.1 Immunohistochemistry

Immunohistochemistry is a technique that utilizes antibodies to detect specific proteins in tissue samples. This method is a crucial tool in biological research and disease diagnosis, particularly in oncology [49]. Immunohistochemistry relies on the antigen-antibody binding principle, where antibodies are used to recognize and attach to specific antigens (proteins or peptides) in tissue samples. After the primary antibody binds to the target antigen, a label, such as an enzyme, fluorochrome, or luminescent marker, is introduced for detection and observation under a microscope.

The process begins with tissue preparation, where thin sections of tissue are cut and mounted on slides. The tissue is then fixed using formalin or other fixatives to preserve its structure and protein integrity. Next, endogenous enzymes within the tissue, which could cause nonspecific reactions, are inactivated to avoid interference. The tissue sample undergoes an antigen retrieval step, commonly involving heat or enzymatic treatment, to expose the antigens and improve antibody access. Following this, a primary antibody specific to the target antigen is applied, binding to the antigen if present. Subsequently, a secondary antibody, linked to a detectable label, is added to bind to the primary antibody. The label is then visualized using various detection methods depending on its type, with the final results observed under a microscope [66]. Figure 1.5 shows the detailed protocol of immunohistochemistry.

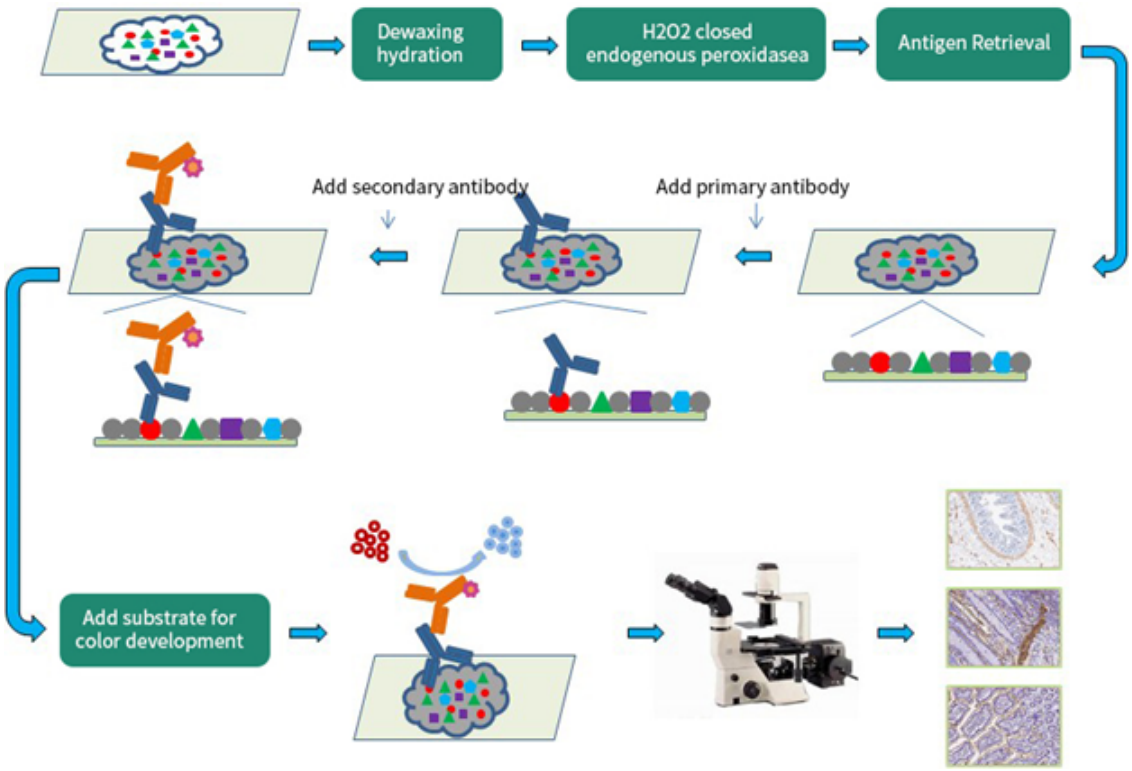

Figure 1.5: Immunohistochemical protocol (Source: internet)

Immunohistochemistry has significant applications in medicine and research. It allows for identifying and localizing cancer-related proteins within tissue samples, aiding in cancer diagnosis and classification. For example, overexpression of the HER2/neu protein detected via IHC can indicate a specific breast cancer subtype and guide treatment choices [111]. IHC also helps determine cells' origin in tumors with unknown origins by detecting tissue-specific markers. Additionally, IHC is a valuable tool in studying the biological mechanisms of diseases, allowing researchers to assess protein expression and localization within tissues. Moreover, IHC can aid in evaluating patient prognosis and monitoring treatment efficacy. For instance, the expression of the Ki-67 protein is used to assess cell proliferation in cancer and to help predict disease [23].

Currently, IHC techniques are widely applied in biopsy testing. After sampling, tissue specimens are tested using immunoassays in which antibodies labeled with fluorescent or chromogenic agents are employed to identify target proteins. Following the dyeing process, image analysis software is utilized to measure the area of the stained region and signal intensity, providing further insights into the expression level of pro-

teins within the tissue. However, this method faces limitations when detecting proteins at very low concentrations, which reduces detection accuracy. Additionally, the optical signal intensity requires normalization to ensure consistency, yet such standardization poses challenges in practical applications.

Although quantitative image processing software is available, it has not been widely adopted and often lacks standardized application in clinical diagnostics. These tools are primarily used to differentiate specific target regions from other tissue areas rather than accurately quantify protein concentration [47, 121, 11]. Consequently, in IHC, the limit of detection (LOD) is commonly defined based on the percentage of the target area rather than by measuring the actual protein concentration within the tissue sample.

1.2.2 Immunoaffinity Chromatography

Immunoaffinity chromatography (IAC) is a highly specific and powerful technique widely applied in biochemistry and biotechnology to purify or isolate proteins, peptides, and other biomolecules that exhibit binding affinity to a specific antibody. The technique utilizes the selective interaction between an antigen and an antibody, enabling the effective separation of target molecules from complex mixtures. The principle of immunoaffinity chromatography is based on antigen-antibody interactions, where the antibody is immobilized on the chromatographic column substrate and serves to selectively bind the target antigen, such as a particular protein in the sample. When the sample is introduced to the column, target antigens bind specifically to the antibody, while non-specific components are washed out. The bound target antigen is then eluted by adjusting conditions—such as pH, ionic strength, or by introducing a specific solvent—to disrupt the antigen-antibody interaction, as illustrated in Figure 1.6.

Immunoaffinity chromatography involves five main steps, including chromatographic column preparation, sample loading, column washing, antigen elution, and antigen analysis, as depicted in Figure 7. In the initial step, a specific antibody is immobilized onto a matrix to prepare the chromatographic column. This immobilized antibody is configured to selectively recognize and bind the target antigen in the sample.

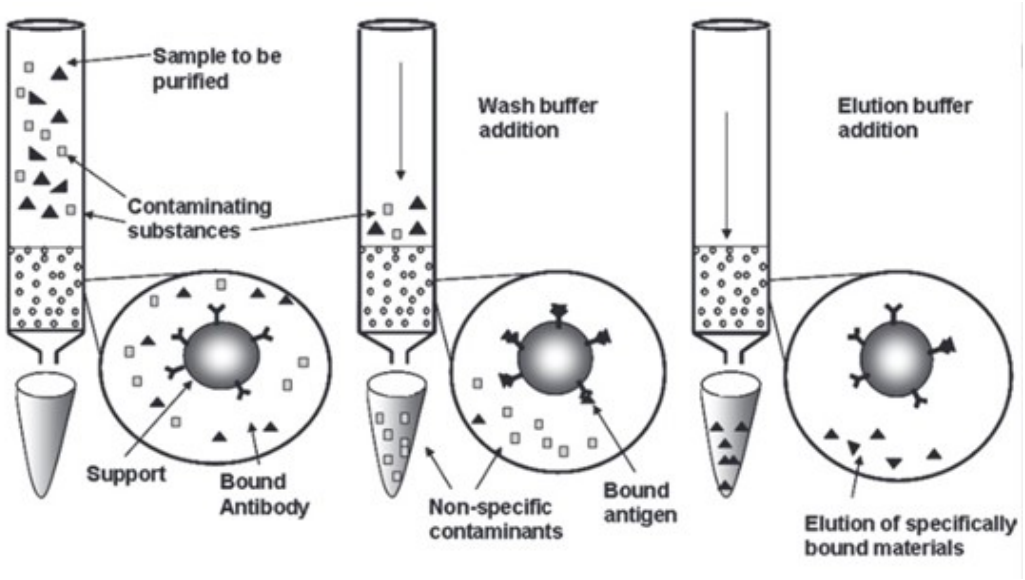

Figure 1.6: Operating model of Immunoaffinity chromatography [136]

In the sample loading phase, the sample containing the target antigen is introduced onto the column. Here, the target antigens selectively bind to the immobilized antibodies, while unbound components are washed through the column and discarded. In the third step, a suitable buffer solution is applied to wash the column, removing residual non-specific substances without eluting the target antigen. The target antigen is subsequently eluted from the column by adjusting specific environmental conditions, such as pH, salt concentration, or by introducing a specialized solvent, to disrupt the antigen-antibody interaction. Finally, after elution, the isolated target antigen is collected for further analysis using advanced methods such as electrophoresis, mass spectrometry, or other molecular biology techniques.

IAC can be employed to purify target proteins from complex mixtures, such as cell culture supernatants or serum, achieving both high purity and efficiency. This technique is also applicable for separating and analyzing antigens or antibodies in biological samples, thereby supporting disease diagnostics and biological research. Additionally, IAC can be combined with other methods, such as ELISA, to detect and quantify proteins, peptides, or other small molecules within biological samples. It is also valuable for studying protein interactions, allowing for the identification and analysis of protein-antibody complexes or other molecular interactions. The LOD of this tech-

nique generally ranges from 9 to 800 pg/mL (ppm) [74]. A primary requirement for antibodies used in IAC is a very high affinity for the target protein, providing IAC with high specificity and separation efficiency [136]. However, this stringent requirement for highly selective, high-affinity antibodies, as well as the need for an effective elution solution, presents a limitation of this method. Additionally, the rigorous conditions required to maintain antibody stability within the chromatography column often pose challenges for users.

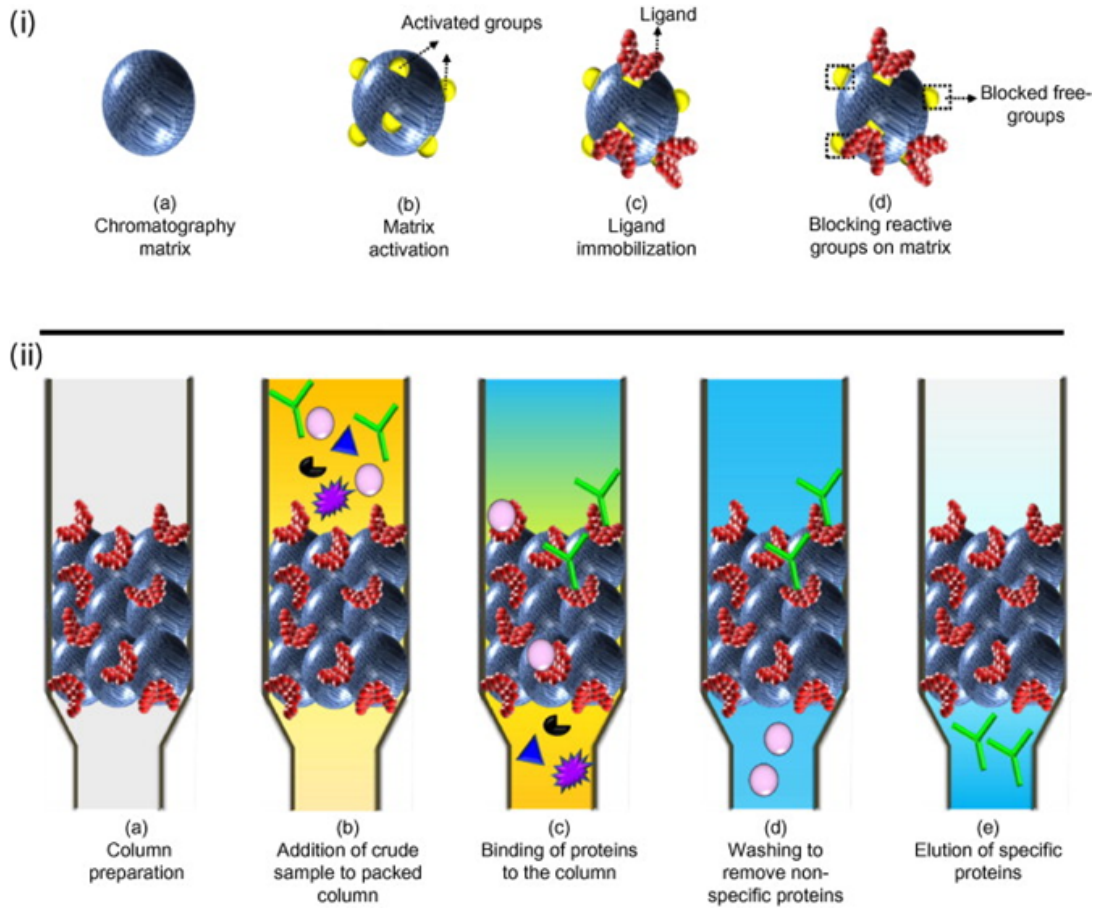

Figure 1.7: Immunoaffinity chromatography process [7]

1.2.3 High-performance liquid chromatography combined mass spectrometry

High-performance liquid chromatography (HPLC) coupled with mass spectrometry (MS) is a powerful analytical technology widely used in fields such as analytical chem-

istry, pharmaceuticals, biology, and environmental science. The combination of HPLC and MS enables the separation, identification, and quantification of compounds with high sensitivity and accuracy. HPLC is an advanced liquid chromatography technique that uses a high-pressure pump to push a solvent containing the sample through a chromatography column packed with a stationary phase capable of separating the sample components based on their physicochemical properties, such as polarity, molecular size, or chemical interactions. Different components of the sample travel through the column at varying speeds, resulting in their separation as they exit the column. Mass spectrometry is an analytical technique used to measure the molecular masses of compounds. In MS, the sample separated by HPLC is ionized, converting it into charged ions. These ions are then analyzed based on their mass-to-charge ratio (m/z) in a mass spectrometer. The result is a mass spectrum that allows for the identification and quantification of the compounds [152].

The HPLC-MS technique involves a five-step process, including sample preparation, chromatography (HPLC), sample transfer to mass spectrometry (MS), mass spectrum analysis, and data processing (Figure 1.8). Firstly, the sample to be analyzed is prepared and dissolved in an appropriate solvent for injection into the HPLC system. The sample is then pumped through the HPLC column, where its components are separated based on interactions with the stationary and mobile phases. After separation, the components are transferred directly into the MS system. Ionization techniques such as electrospray ionization (ESI) or atmospheric pressure chemical ionization (APCI) are commonly used to generate ions from the sample. These ions are analyzed in the mass spectrometer to determine their mass-to-charge ratio (m/z), enabling the identification and quantification of the compounds. Finally, the data obtained from HPLC and MS are processed to generate a mass spectrum, which facilitates the identification of molecular structures and the quantification of substances in the sample.

HPLC-MS is applied in various fields, including pharmaceutical analysis, biological analysis, environmental research, and food analysis. In pharmaceutical analysis, HPLC-MS is a crucial tool for drug analysis and quality control, helping identify active ingredients, impurities, and degradation products in drug samples. In biological sciences,

HPLC-MS is utilized to analyze proteins, peptides, lipids, and other biomolecules. It enables the study of protein interactions, metabolite profiling, and the identification of biomolecules in complex samples. In environmental research, HPLC-MS aids in detecting and quantifying pollutants, pesticides, and persistent organic compounds in the environment. For food analysis applications, HPLC-MS is used to evaluate food quality and safety by detecting additives, preservatives, and contaminants. The detection limit of this technique typically ranges from 0.02 to 0.9 pg/mL [118].

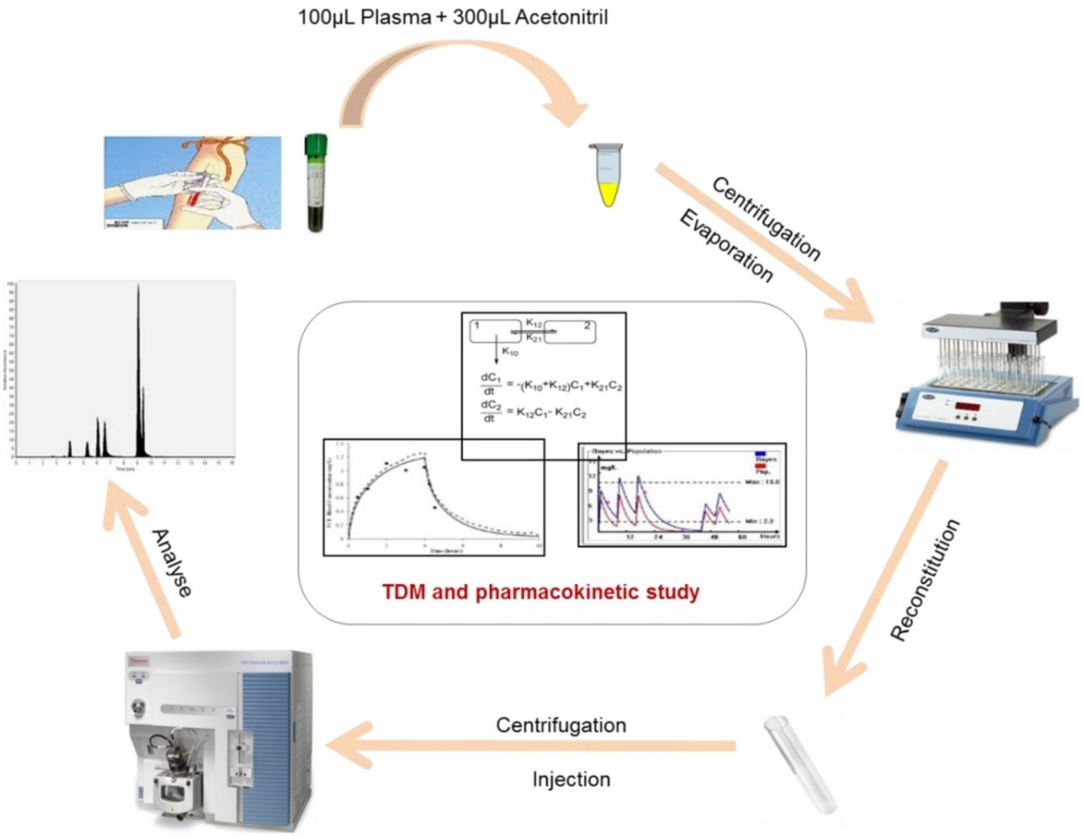

Figure 1.8: Steps of High-Performance Liquid Chromatography (HPLC) combined with Mass Spectrometry (MS) [152]

For protein analysis, performing HPLC to separate proteins often requires running calibration standards first to accurately determine the peak positions associated with the sample before analyzing the sample solution. This technique can also be used for quantification when peak intensity is calibrated for each standard sample or when combined with mass spectrometry, necessitating technical training for operators. Although

HPLC provides highly accurate results, designing a compatible chromatography column system and concentration detection system poses a significant challenge.

1.2.4 Enzyme-Linked Immunosorbent Assay

Enzyme-Linked Immunosorbent Assay is a widely used and essential technique in molecular biology and medicine for detecting and quantifying antigens, antibodies, proteins, and other biomolecules in biological samples. This technique plays a vital role in disease diagnosis, scientific research, and quality control in the food and pharmaceutical industries [119, 53, 94].

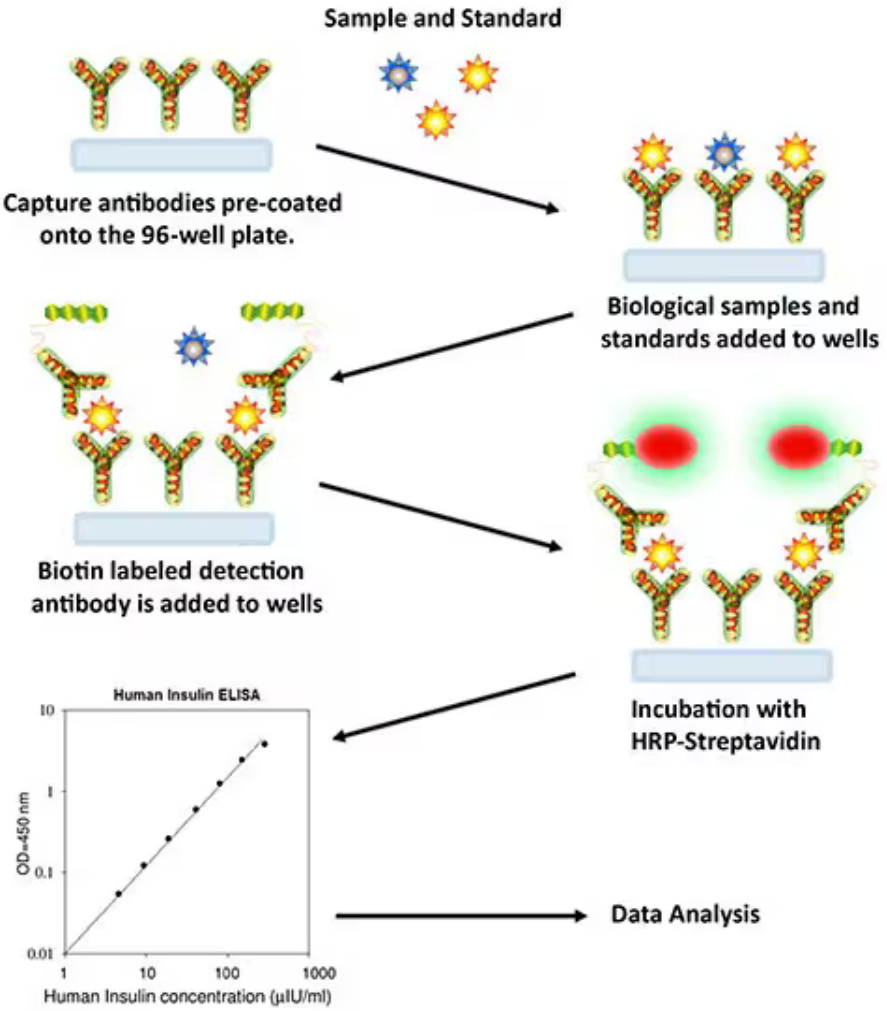

Figure 1.9: ELISA protocol (Source: Sigmaaldrich)

ELISA relies on the specific interaction between an antigen and an antibody. During

the assay, the antigen or antibody is immobilized on the surface of a microplate well. The biological sample containing the target antigen or antibody is then added, followed by the addition of a secondary antibody conjugated with an enzyme to detect the antigen-antibody complex, as shown in Figure 1.9. Upon addition of an appropriate substrate, the enzyme catalyzes a reaction that generates a color signal, with the color intensity directly proportional to the concentration of the target molecule in the sample [32, 19].

The ELISA technique is classified into four main types, including direct ELISA, indirect ELISA, sandwich ELISA, and competitive ELISA, as shown in Figure 1.10. In direct ELISA, the antigen is directly immobilized onto the microplate well, and an enzyme-conjugated antibody is added to detect the antigen. This method is often used for qualitative ELISA and is less commonly applied for quantitative analysis. Its main advantage is that it requires only a single incubation step, which saves time and minimizes the need to control various conditions during the procedure (such as temperature and buffer changes for each incubation, and timing). However, it has the drawback of high background staining due to the nonspecific binding of the antibody to the solid surface and the proteins immobilized on it. Additionally, labeling each type of antibody for each antigen can be costly, especially when diagnosing a large number of different antigens.

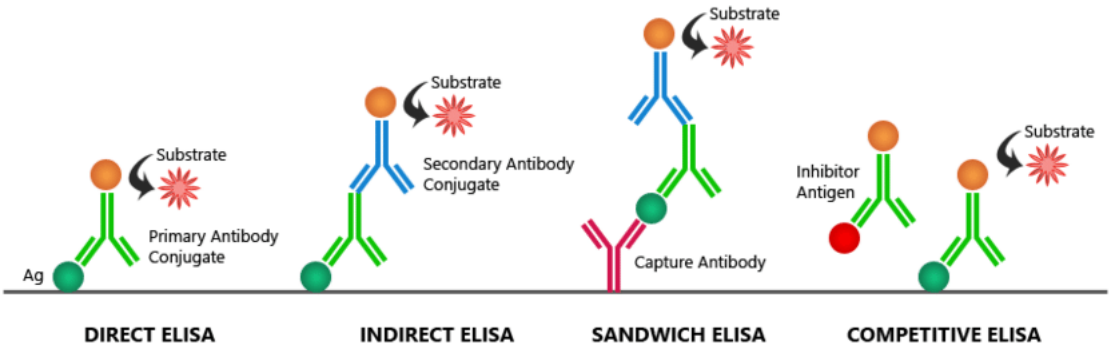

Figure 1.10: Classification of ELISA methods [57]

In indirect ELISA, the antigen is immobilized onto the microplate well. Then, a primary antibody is added to recognize the antigen. A secondary antibody conjugated

with an enzyme is then added to detect the primary antibody. This method offers higher sensitivity because multiple secondary antibodies can bind to each primary antibody [62]. However, its drawback is the increased number of procedural steps, which necessitates additional control of conditions and prolongs the assay process, extending the diagnostic time.

Sandwich ELISA employs two specific antibodies to 'sandwich' the antigen. A capture antibody is immobilized onto the microplate well, followed by the addition of the antigen and then a detection antibody. This method provides high specificity and sensitivity, making it suitable for analyzing complex samples [98]. For competitive ELISA, it is used to detect small molecules or antigens present in very low concentrations. Competitive ELISA is particularly effective for quantifying trace elements in samples. It involves adding a known amount of antigen (the competing antigen) similar to the target antigen in the sample, which competes for binding to a specific antibody immobilized on a solid surface. The quantity of competing antigen is measured via the enzyme activity linked to it. A higher presence of competing antigen indicates a lower concentration of the target antigen in the sample, and vice versa. Thus, the color signal intensity is inversely proportional to the antigen concentration in the sample [142].

The biological sample for ELISA testing typically involves venous blood, collected in clean test tubes, either with or without anticoagulants (Heparin/EDTA), depending on the specific requirements of the assay. Each blood sample is placed in individually labeled test tubes with barcodes and complete identification details, secured with tightly sealed caps. Samples are then placed in secure containers and transported to the laboratory as soon as possible. Typically, blood samples for ELISA tests remain stable at room temperature (20-25 ^{o}C) for up to 12 hours or between 2-8 ^{o}C for 24-48 hours. At the laboratory, the samples are sorted according to the specific tests required and assigned unique codes to prevent cross-contamination or sample misidentification.

The ELISA testing procedure consists of seven steps. Firstly, patient samples, along with positive and negative controls, are added to plastic wells pre-coated with the specific antigen or antibody. Incubation is conducted at room temperature or 37 ^{o}C for a duration specified by the manufacturer. In the second step, the wells are washed

with PBS-Tween 20 buffer solution and blotted dry. The third step involves adding a conjugate to each well, followed by incubation at room temperature or 37 ^{o}C as per the manufacturer's instructions.

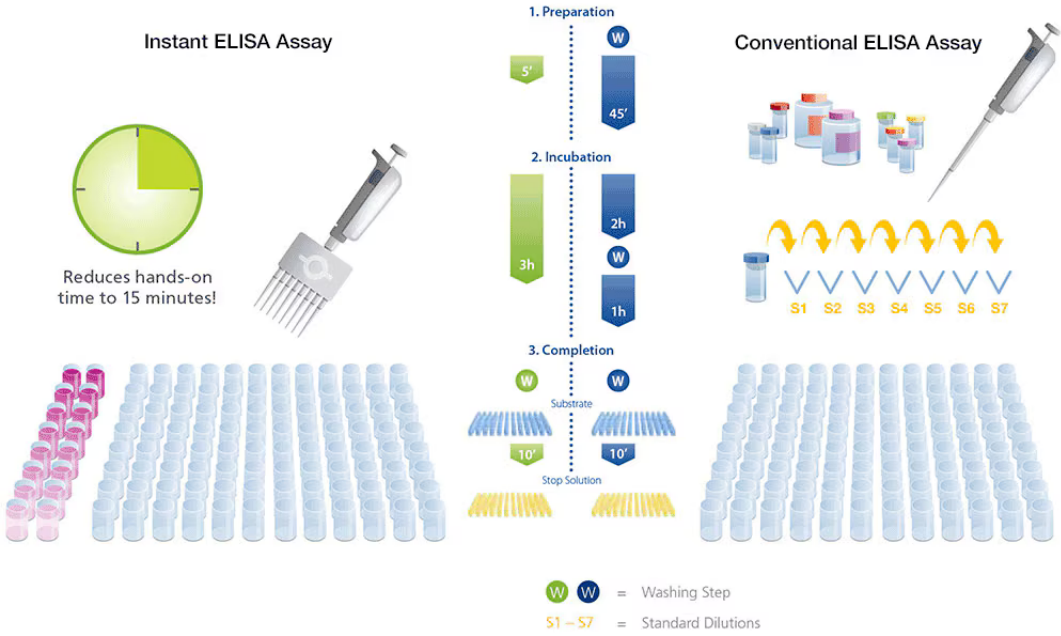

Figure 1.11: The ELISA testing procedure using conventional ELISA and Invitrogen instant ELISA kits (Source: Thermofisher)

The fourth step repeats the washing process with PBS-Tween 20 and blotting the wells dry. In fifth step, a substrate is added to each well, allowing color development (15-30 minutes). In the sixth step, a stopping solution is added to terminate the reaction. Finally, results are read using an automated ELISA reader. Figure 1.11 shows the ELISA testing procedure using conventional ELISA and Invitrogen instant ELISA kits. The ELISA method is currently widely used in healthcare facilities due to its advantages, including lower cost and ease of implementation, which facilitate rapid sample testing. However, ELISA testing requires relatively large sample volumes, typically at least several tens of microliters, and has limited sensitivity for detecting low-concentration proteins. The washing steps in ELISA are crucial to remove non-specifically bound substances, preventing false-positive results. However, this also adds complexity to the procedure, requiring a high level of technical skill [20].

Results from ELISA performed on equipment from major companies, such as Life

Technology, Abcam, eBiosensor, Enzolife Sciences, and Thermo Scientific, report a minimum limit of detection ranging from 2 to 8 pg/mL [149]. Compared to commonly used measurement techniques, the application of micro-nano technology has been explored in two main directions to enhance sensor sensitivity: (i) employing nanomaterials as biomarkers or porous electrodes, and (ii) designing micro-electromechanical systems (MEMS) for measurements. Figure 1.12 presents an overview of LODs published in studies utilizing micro-nano technology over time. From 2008 onward, LODs have steadily decreased, with each year showing an approximate reduction by one order of magnitude. Beginning in 2012, published LOD values have reached the sensitivity threshold of the HPLC method. By 2017, detection limits fell below the threshold achieved by HPLC.

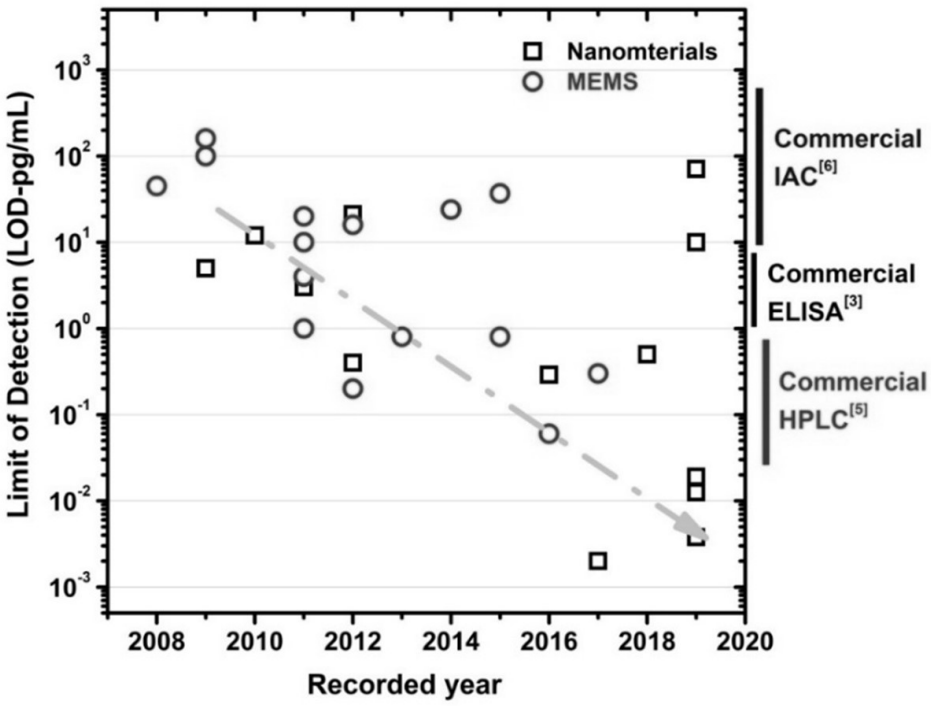

Figure 1.12: Investigation of some critical limits of measurement (LOD) on applied studies of nanomaterials (□) [97, 70, 149] and on microelectromechanical systems (MEMS) (○) [69, 8, 105, 134, 150] compared with commonly used methods such as IAC [74], HPLC [118] and ELISA, respectively [149].

Although detection signals are all electrical, MicroElectroMechanical Systems (MEMS)

technology is still developing somewhat independently from the application of nanomaterials. This may be due to the complexity of designing nano-structured electrodes on microfluidic channels. Additionally, the specific nature of antigen-antibody binding, where each protein target can only pair with a single antibody immobilized on the electrode surface within the microchannel, limits the use of nanoparticles for signal enhancement in electrical measurements within microchannels. This mechanism is similar to that of ELISA, where enzymes are replaced by nanoparticles.

ELISA is widely applied in medical diagnostics, biological research, the food industry, and pharmaceutical development. ELISA plays a crucial role in diagnosing diseases such as HIV, hepatitis, and other infectious diseases. Its high sensitivity and specificity allow for the accurate detection of antigens and antibodies, facilitating disease progression monitoring and evaluation of treatment effectiveness [1, 36, 131]. In scientific research, ELISA is used to measure cytokines, hormones, and other proteins in biological samples, providing essential insights into physiological and pathological processes in the body [18, 61]. Additionally, ELISA is employed to ensure food quality and safety by detecting allergens, preservatives, and contaminants. This contributes to consumer health protection and compliance with food safety regulations [54]. Furthermore, ELISA plays an important role in pharmaceutical development, especially in evaluating immune responses to biologic therapies and assessing product quality. This technique aids in determining the efficacy and safety of biological products before they are brought to market [98, 35].

1.2.5 Protein microarrays

Protein microarrays are an advanced technology that enables the simultaneous analysis of numerous proteins and their interactions in a single experiment. This technology is widely utilized in fields such as biological research, medicine, and biomarker discovery, owing to its capability to identify and quantify proteins in complex samples [24].

Protein microarrays are constructed by immobilizing proteins or antibodies on a solid surface, such as glass or nitrocellulose. When a biological sample, such as serum, is introduced to the microarray, the proteins or antibodies in the sample interact with

the molecules on the microarray, allowing for the detection and analysis of target proteins (1.13). Detection is typically achieved through fluorescent or luminescent signals, enabling the identification of protein-protein interactions or interactions with other molecules [29]. Protein microarrays are classified into three types: functional microarrays, antibody microarrays, and capture microarrays. Functional microarrays contain proteins with intact functions, aiding in the study of protein-protein or enzyme-substrate interactions. This type of microarray is highly useful in investigating cellular signaling networks and drug development [104]. Antibody microarrays are employed to detect antigens in biological samples and hold particular value in disease diagnosis and immunology research [109]. Capture protein microarrays use immobilized proteins or other molecules on the array to capture target proteins from biological samples. This type is commonly used to study interactions between proteins and other molecules, such as DNA or drugs [67].

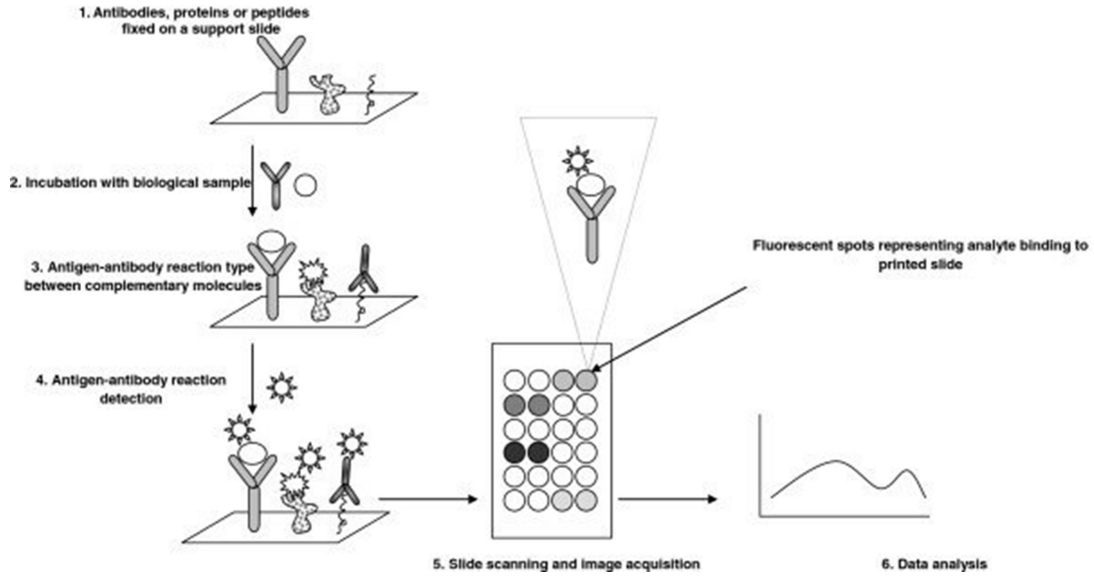

Figure 1.13: Protein microarray technology principle [72]

1.2.6 Lab-on-chip system

The techniques mentioned above are widely applied in medical centers and hospitals, playing a vital role in testing and disease treatment through analyses of urine, blood, and cell biopsy samples. However, to enhance disease detection capabilities, it is nec-

essary to detect proteins at lower concentrations with smaller sample volumes and to reduce testing time. Increasing automation to simplify operations is also a key objective. Finally, reducing costs and improving convenience in testing processes are additional goals that need to be addressed.

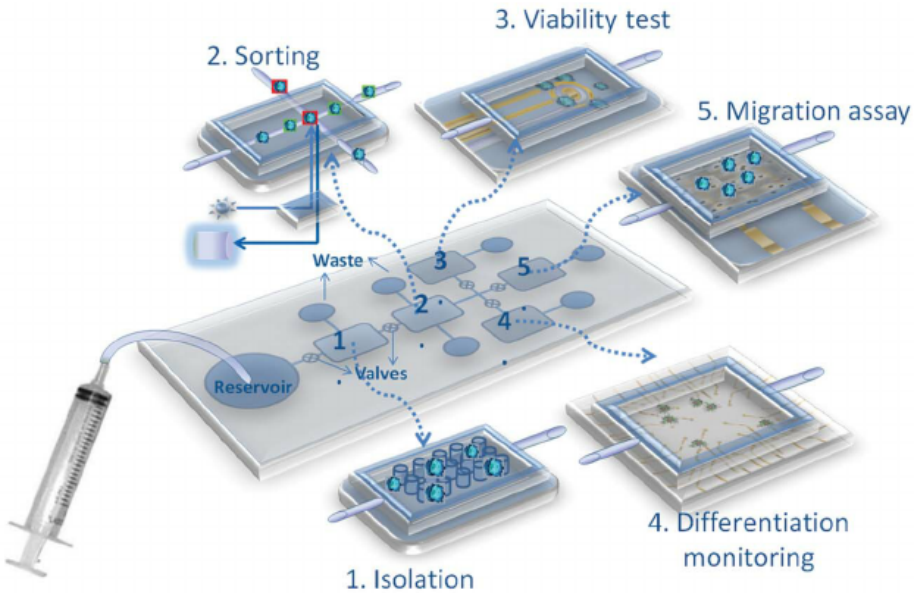

Figure 1.14: Example of Lab-on-a-chip system [100]

To meet these demands, research into biochips (Lab-on-a-Chip) based on microfluidic chip platforms is being actively explored to develop compact testing devices that fulfill the requirements of diagnostic applications. Lab-on-a-Chip (LOC) is a technology that integrates multiple functions of a traditional laboratory into a compact device, typically only a few centimeters in size (Figure 1.14). LOC allows for biological and chemical analyses on a microchip, which is capable of processing samples and performing analyses on a micro- and nano-liter scale. This technology is revolutionizing fields such as molecular biology, medicine, and analytical chemistry by minimizing sample and reagent volumes, reducing processing time, and enhancing the accuracy and automation of experiments [120, 10].

A typical LOC includes a network of microchannels, known as microfluidics, fabricated onto a microchip made from materials like glass, silicon, or polymer. These channels enable precise control over fluid flow, allowing biological, chemical, or physical processes like mixing, reaction, or sample separation to occur on a miniature scale. Inte-

grated sensors on the chip detect and analyze results, including signals such as fluorescence, electrochemical signals, or mass spectrometry [71]. Microfluidic-based bioassays with advantages such as small sample requirements and automation are increasingly being developed for biological applications. These microfluidic chips can incorporate established methods like ELISA, immunohistochemistry, or flow cytometry by scaling down into micro-sized channels.

One significant advantage of microfluidics is that it allows for the separation and concentration of biological targets with minimal sample volume. The process can be automated, simplifying procedures for operators. Due to their compact size, microfluidic-based biochips present a promising research direction in the development of portable diagnostic devices that meet the demands of disease detection and on-site monitoring [4].

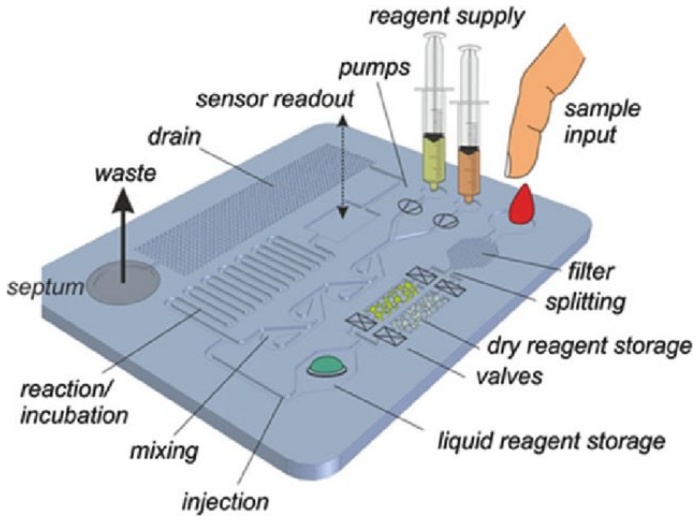

Figure 1.15: Lab-on-a-chip devices for point-of-care applications [12]

Typically, a biosensor chip is integrated with one or more functions, such as concentrating, separating biological entities, selecting, and detecting targets. Biological entities with different physical properties, such as particle size, electric charge, or susceptibility to electromagnetic fields, are utilized in particle concentrating and separation methods. Microfluidic structures are commonly fabricated from PDMS (polydimethylsiloxane). Due to the advantages of micro-scale structures, testing requires only a small sample volume of just a few microliters, which is sufficient for diagnostic analysis [4, 10].

Figure 1.15 shows a LOC device for point-of-care applications comprising a number of passive or active structures. Depending on the application, such chips are designed to include integrated features for handling sample liquids and reagents. These may encompass on-chip reagent storage, channels or chambers for precise mixing, separation, or filtering of fluids, and specialized structures to facilitate analytical readouts. Additionally, storage areas for used reagents and waste liquids are typically incorporated to maintain a clean and efficient workflow within the chip. These features contribute to a self-contained microfluidic platform, enabling streamlined and automated sample processing and analysis [12].

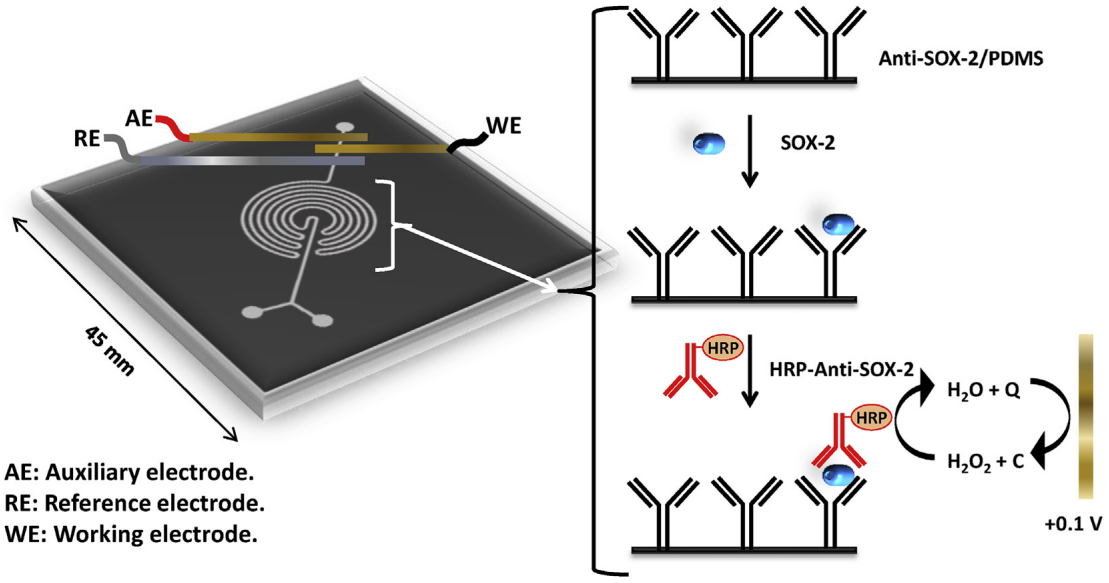

Figure 1.16: The electrochemical microfluidic chip for SOX-2 detection [108]

For protein detection, LOC systems or microfluidic chips are often developed based on antibody-antigen interactions, combining microfluidic technology with various detection techniques such as fluorescence, chemiluminescence, surface-enhanced Raman spectroscopy (SERS), and electrochemical methods [141]. Among them, the integration of microfluidic technology with electrochemical methods is particularly promising due to its low detection limit, rapid response, and simple assay process. Regiart et al. developed an electrochemical microfluidic chip to detect SOX-2 cancer biomarkers [108]. The chip was divided into two main parts: a polydimethylsiloxane (PDMS) device with microchannels and a glass substrate with electrodes, as shown in Figure 1.16. The gold

electrode surface was modified using the dynamic hydrogen bubble template (DHBT) method, which leverages the simultaneous production of hydrogen bubbles to form a nanoporous gold (NPAu) layer. Then, Zhang et al. proposed a miniaturized electrochemical microfluidic chip for the detection of interleukin-6 (IL-6) [151]. In the design, the gold electrode was integrated within a microfluidic chamber, and its surface was modified with graphene and gold nanoparticles to enhance the surface area and facilitate electron transfer, as shown in Figure 1.17. Besides, magnetic beads were employed to enrich IL-6 on the electrode surface.

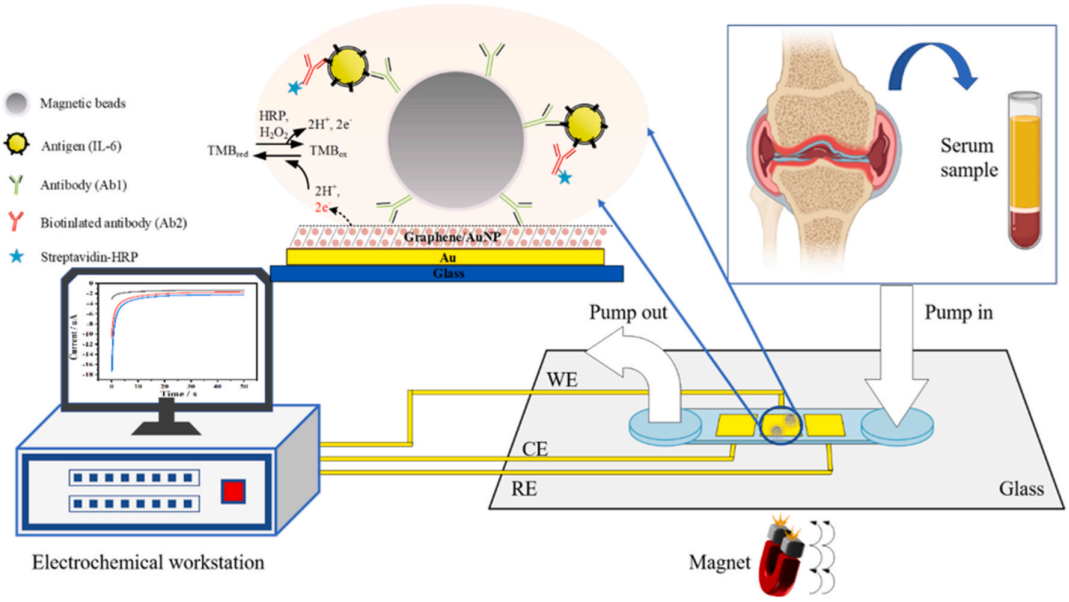

Figure 1.17: The design of a microfluidic chip for interleukin-6 detection [151]

1.3 Protein preconcentration and protein preconcentration methods

As mentioned above, proteins are large biomolecules and macromolecules that comprise one or more long chains of amino acid residues. Protein plays an important role in the human body. Protein is also a tumor marker used to diagnose cancer [75]. Protein tests are mainly based on immunoassay methods, such as IHC, ELISA, and flow cytometry [133, 28, 103, 73]. These methods are commonly used in hospitals and health facilities. However, they have the disadvantages of the LOD, processing time, and expensive

equipment. Recently, research groups have been focusing on developing LOC systems based on the microfluidic structure to address the disadvantages of conventional methods [55]. One of the most significant advantages of microfluidic channels comprises biological object separation and concentration with a tiny sample volume [120, 10]. With compact size, the bio-chip based on microfluidic channel structures opens up a promising research direction in the development of compact testing devices that still meet the problem of on-site disease detection and monitoring [99, 37, 56]. A normal bio-chip is integrated with one or several functions, including protein separation, concentration, and detection. The preconcentration process of low-concentration proteins plays a crucial role in increasing the sensitivity and accuracy of biochemical analyses. Because there is a huge number of protein types in a small sample, the protein concentration can be lower than the LOD of the conventional biosensors after several separation steps in the protein detection process [5]. Therefore, the proteins need to be sorted out and enriched in a particular channel region to address these problems.

Although polymerase chain reaction (PCR) is a powerful and widely used technique for the exponential amplification of specific DNA or RNA sequences, it is not directly applicable to the amplification of proteins. This is primarily due to the inherent complexity of proteins, which are composed of intricate three-dimensional structures formed by amino acid sequences. Unlike nucleic acids, proteins do not have a simple, linear sequence that can be easily amplified through a process like PCR. The amplification of proteins presents additional challenges, such as the need to preserve their functional structure and the difficulty in replicating the diverse chemical modifications that proteins undergo.

To address these challenges, various methods have been developed to enrich or amplify specific proteins from complex biological samples, including electrokinetic trapping [76, 14, 63], field amplification stacking (FAS) [143], isotachophoresis [26, 68] isoelectric focusing [115], micellar electrokinetic sweeping [15] and chromatographic preconcentration [92]. These techniques are designed to regulate and enhance the local concentration of proteins near the biosensor surface, enabling the detection of even low-abundance biomarkers.

1.3.1 Field amplification stacking

The FAS method uses enhanced electric fields to concentrate biological molecules, as shown in Figure 1.18. When the electric field is amplified in a specific region, the biological molecules are drawn toward this area and concentrated. This technique is particularly useful for concentrating molecules with low charge and for high-sensitivity bioanalytical applications. In FAS, a sample with a low analyte concentration is placed in a region with lower conductivity than the buffer solution. Upon applying an electric field, ions in the sample move more quickly through the low-conductivity region due to the conductivity gradient. As the analytes enter the higher-conductivity buffer region, their migration velocity suddenly decreases, leading to ion concentration at the boundary between regions with differing potentials. This effect "compresses" the analytes at a single point, significantly enhancing their detectability post-separation. FAS enhances detection the sensitivity of the system by exploiting differences in ion migration velocity across regions with varying electric fields, thereby concentrating analytes into a smaller region for improved analysis in techniques such as capillary electrophoresis (CE), and mass spectrometry.

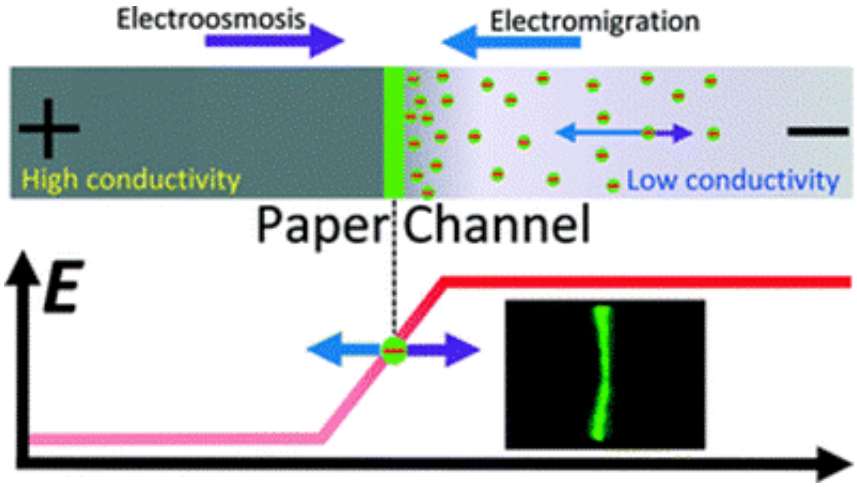

Figure 1.18: Field Amplification Stacking method [65]

1.3.2 Isotachophoresis

Isotachophoresis (ITP) is a technique for separating ions based on differences in their electrophoretic mobility, as shown in Figure 1.19. This technique is commonly used to separate and concentrate ions within complex samples. ITP can achieve high concentration efficiency in a short time, enhancing the sensitivity of bioassays. In ITP, the sample is placed between two buffer solutions, a leading electrolyte (LE) and a terminating electrolyte (TE) within a capillary or microchannel. The leading electrolyte contains ions with higher electrophoretic mobility, while the terminating electrolyte contains ions with lower mobility. Under an applied electric field, ions migrate at different speeds depending on their mobility. However, ITP establishes conditions where all ions reach the same velocity. The ions arrange into distinct zones, with the highest-mobility ions following the leading electrolyte and the lowest-mobility ions preceding the terminating electrolyte. Because the ions move at the same velocity, the boundaries between different ion types become clearly defined. This effect makes ITP particularly effective for separating and analyzing analytes at low concentrations.

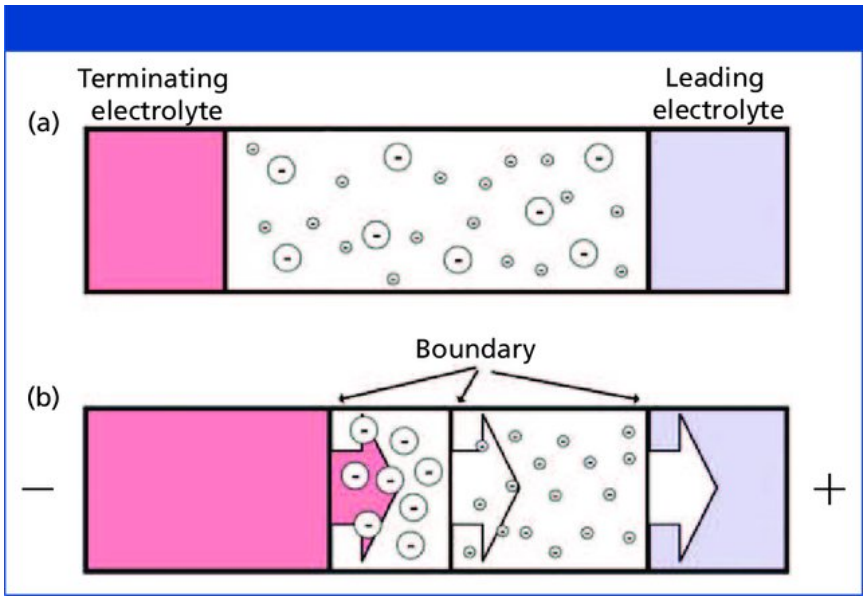

Figure 1.19: Isotachophoresis method (a) initial conditions with sample injection between leading and terminating electrolytes, (b) isoelectric region at steady state [128]

1.3.3 Isoelectric focusing

Isoelectric focusing (IEF) is a method for separating and concentrating molecules based on their isoelectric point (pI), as illustrated in Figure 1.20. When an electric field is applied, molecules migrate to the location with a pH that corresponds to their pI and stop moving there. This technique is commonly used to concentrate and separate proteins in biological applications. In IEF, molecules are separated by applying an electric field across a pH gradient within a gel or capillary. The main steps of the process include creating a pH gradient, protein migration in the electric field, focusing at the isoelectric point, and separation based on pI.

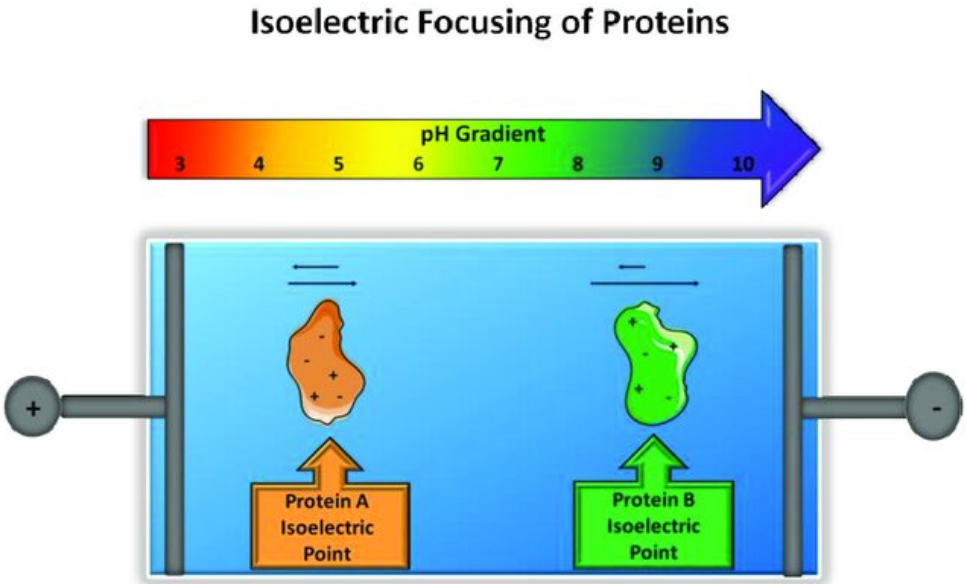

Figure 1.20: Principle of isoelectric focusing. Two proteins with varying isoelectric points will migrate in the presence of a pH gradient and electric field until the net charge of a protein is zero, in which migration will cease [96]

First, a stable pH gradient is established in the medium (such as polyacrylamide gel or capillary) using ampholytes—small molecules that create a pH range from acidic to basic. When the protein sample is introduced and an electric field is applied, proteins move through the medium based on their net charge. Positively charged proteins move toward the cathode (negative electrode), while negatively charged proteins move toward the anode (positive electrode). As proteins migrate, they encounter different pH regions

in the gradient. Each protein stops moving and focuses when it reaches the pH matching its pI. At this pH, the protein has no net charge and is no longer influenced by the electric field, so it remains at that position. Proteins with different isoelectric points (pI) accumulate at specific positions along the gradient, enabling their separation based on pI differences.

1.3.4 Micellar electrokinetic sweeping

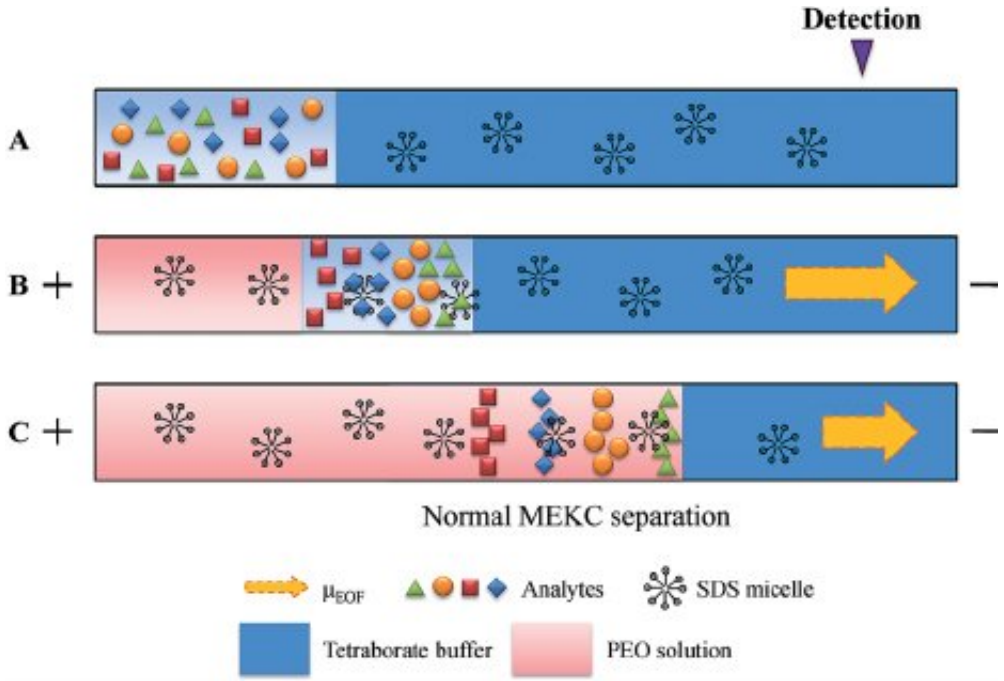

Figure 1.21: Schematic of the sweeping-MEKC method using a polymer solution. (A) The samples (in deionized water) are hydrodynamically injected for 90 s once the capillary is filled with tetraborate buffer containing sodium dodecyl sulfate (SDS), (B) the SDS micelles sweep the analytes present in the sample zone once a positive high voltage is applied, and both the SDS micelles and analytes migrate against EOF and enter the PEO zone during stacking, and (C) the analytes are stacked in a narrow band, migrate into the poly(ethylene oxide) (PEO) zone and are separated by MEKC [130]

This method combines electrophoresis and micellar sweeping to concentrate biological molecules. It enables the separation and concentration of small molecules and can

be applied to a wide range of samples, including complex biological ones. When an electric field is applied, micelles act as a "mobile stationary phase," concentrating and transporting analytes according to three principles, including micellar electrokinetic chromatography (MEKC), sweeping and micellar electrokinetic sweeping.

In MEKC, micelles create a separation environment by absorbing or encapsulating analytes through hydrophobic and electrostatic interactions. The analytes interact with the micelles and move with them under the influence of the electric field, resulting in separation based on the interaction between the analytes and micelles. The sweeping process is a preconcentration technique where low-concentration analytes are concentrated into a narrow zone within the capillary prior to separation. This is achieved by creating a migration velocity difference between the background solution and the analytes. In micellar electrokinetic sweeping, sweeping and MEKC are integrated (see Figure 1.21). Low-concentration analytes are introduced into the capillary, followed by the injection of a micellar solution driven by the electric field. As the micelles encounter the analytes, they absorb or interact with them, concentrating the analytes into a narrow zone. This process increases analyte concentration at a specific location before separation, enhancing measurement sensitivity.

1.3.5 Chromatographic preconcentration

Chromatographic concentration methods use chromatographic columns to concentrate and separate biological molecules based on their interactions with the column packing material. This technique is commonly employed in chemical and biological analysis applications that require high sensitivity and reproducibility. Chromatographic concentration works by trapping and concentrating the analyte in a small region within the column or a similar environment before separation and detection. Low-concentration analytes are concentrated at a specific location in the system and are subsequently separated in the usual manner. The process consists of three main steps. Firstly, the analyte is passed through a trapping stage in the column or similar device, where it is retained by physical or chemical interactions, such as adsorption or affinity to the stationary phase. After the analyte has been concentrated, a change in conditions (e.g.,

temperature or solvent gradient) is applied to release the analyte and introduce it into the separation process. After concentration and release, the analyte is separated using standard chromatographic methods and detected using techniques such as UV-Vis, MS, or fluorescence detection.

1.3.6 Electrokinetic trapping

The methods mentioned above have several disadvantages, including the need for specialized equipment, time-consuming procedures, high costs, and reproducibility issues.

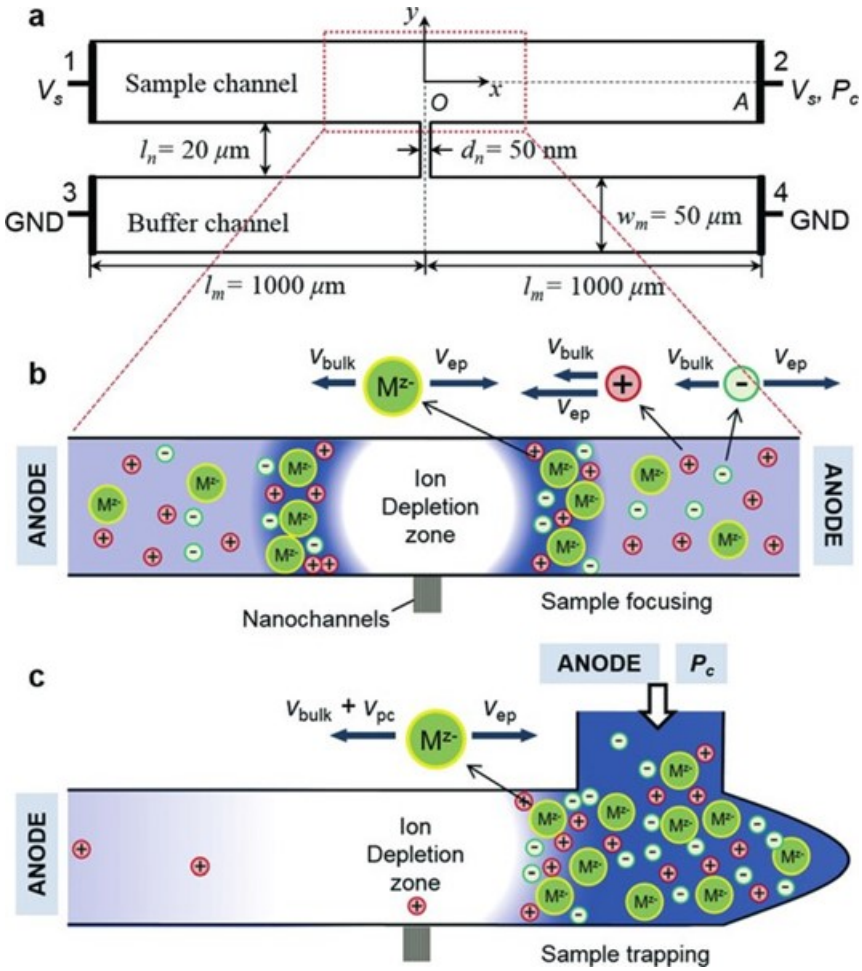

Figure 1.22: (a) Image of a microfluidic system using ion concentration polarization to deplete and concentrate biological particles; (b) Mechanism of ion concentration polarization using nanochannels; (c) Concentration of biological particles [147]

Electrokinetic trapping is a widely applied technique for concentrating charged

molecules. Electrokinetic trapping offers several advantages, including high sensitivity, low detection limits, rapid and real-time preconcentration. Notably, it can be easily integrated into lab-on-a-chip devices, enabling portable and miniaturized analytical systems while reducing sample and reagent consumption. This method utilizes nanoporous ion-selective membranes to create ion concentration polarization (ICP) at nano-interfaces. The ICP phenomenon generates ion depletion and ion enrichment zones, allowing the concentration of biological molecules at specific locations within the microchannel, as shown in Figure 1.22. ICP phenomenon occurs at the macro/micro–nano interface of the nanofluidic structures due to strong concentration gradients of ionic species generated through a perm-selective ion current [46, 137, 30, 138, 122]. Under the impact of ICP, the ion depletion zone and the ion enrichment zone are formed on the anodic side and cathodic side of the junction, respectively. For nanofluidic channels, the suitable dimensions for ion perm-selectivity were reported ranging from 10 nm to 100 nm [139, 43, 34, 25]. The optimal nanochannel size for this effect typically ranges from 10 nm to 100 nm. These channels can be fabricated through various methods, including electrical breakdown, nanoparticle deposition, and the use of Nafion membranes.

Jeong et al. proposed a method using the junction-gap electrical breakdown between two PDMS microchannels to fabricate nanofractures [40]. Nanogaps were created by applying a high direct-current voltage of up to 1 kV between microchannels. The results showed that a concentration factor of 104 was obtained within 1 hour. Similarly, Hui Yu et al. also developed a disposable microfluidic device for rapid protein concentration with a concentration factor ranging from 10^3 to 10^5 utilizing the structure of two printed V-shaped microchannels, as shown in Figure 1.23 [148]

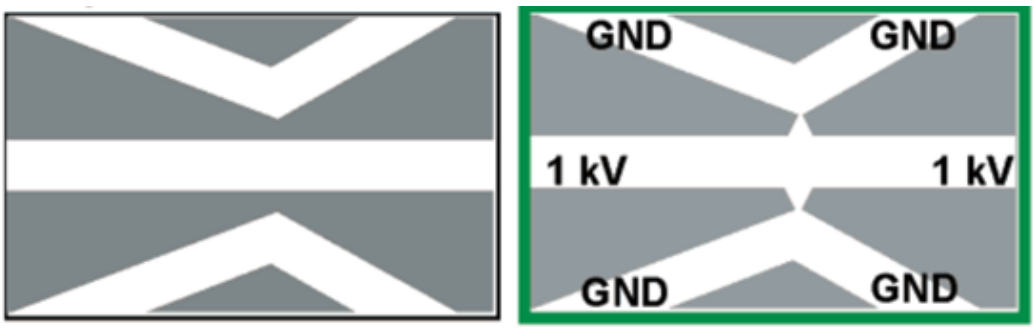

Figure 1.23: Mechanism of nanochannel formation using high voltage [148]

Chun-Ping et al. proposed a method for nano-fracture formation employing nanoparticle deposition at the junction gap between microchannels to reduce the required electric breakdown voltage (1.24) [41, 135]. Proteins were concentrated with the preconcentration factor of 1.5×104 after 60 minutes. However, while effective, this method comes with certain limitations. A primary issue is the inconsistent bonding strength between the glass substrate and the PDMS microchannel substrate, which can lead to variable results across different experiments. Another limitation is the restricted perm-selectivity of the nano-junctions, which may limit the efficiency and applicability of this method in certain experimental conditions. To overcome these challenges, researchers have explored the use of Nafion, a perfluorinated ionomer known for its robust ion-selective properties, to create a more stable and effective ion-selective membrane within a planar microfluidic structure. This Nafion membrane can be integrated into microfluidic devices to enable the preconcentration of microbeads and proteins with improved performance and reproducibility [42, 58, 45, 13, 27]. The use of Nafion addresses the limitations associated with nanoparticle deposition by offering a stable membrane with high ion selectivity that can withstand the bonding process to glass substrates more reliably than PDMS-glass interfaces.

In addition to offering improved selectivity and robustness, the fabrication of ion-selective membranes using Nafion is also simpler and more accessible than the high-voltage electrical breakdown method. Two principal techniques, microflow patterning and microstamping, have been developed and optimized for depositing Nafion membranes onto glass substrates in microfluidic devices [59, 44, 123, 50]. Microflow patterning allows for controlled deposition of Nafion by directing a flow of the Nafion solution over the desired area, which facilitates precise pattern formation and minimal material waste. Microstamping, on the other hand, involves creating predefined patterns on a stamp, which is then coated with Nafion solution and pressed onto the glass substrate, transferring the ion-selective layer. Both techniques offer distinct advantages in terms of pattern precision and reproducibility, making them valuable for the integration of Nafion membranes in microfluidic systems for biomolecule concentration and analysis.

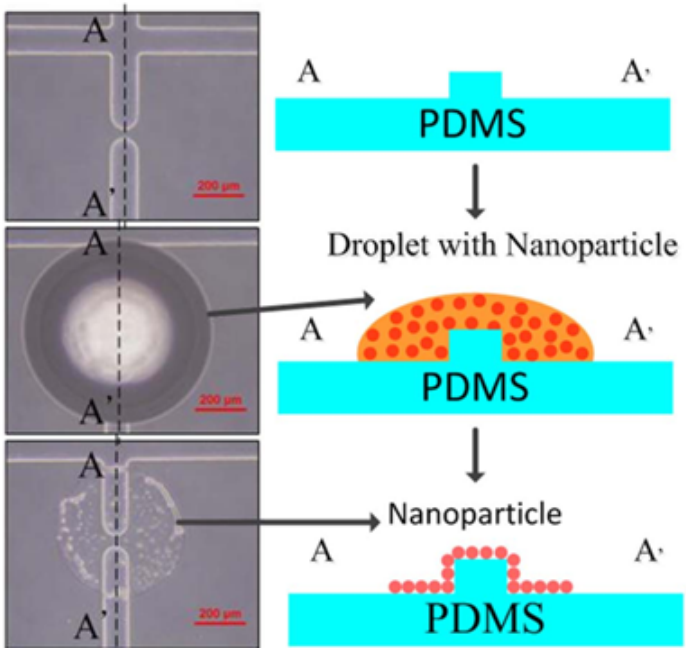

Figure 1.24: Nanoparticle attachment mechanism for on-chip nanofracture formation [41]

1.4 Electrostatic interaction and ion concentration polarization in nanofluidic channels

When a solid surface is exposed to an aqueous solution, specific electric charges develop at the liquid-solid interface. This surface charge refers to the electric charge that forms on any surface in contact with a polar fluid, such as water. Various processes contribute to surface charging, including ion adsorption, ion association or dissociation, and the influence of external electric fields [106]. Surface charge formation is commonly observed when an oxide or hydroxide surface is immersed in an aqueous environment, primarily due to protonation or deprotonation reactions. For example, the interface between a silica surface and water typically acquires a negative charge at pH values $\geqslant 2$, resulting from the dissociation of silanol groups.

$$SiOH \rightleftharpoons SiO^- + H^+ \tag{1.1}$$

The binding and release of protons from silanol groups are strongly affected by

the electrolyte's pH level. Under alkaline conditions, deprotonation of initially neutral surface groups drives the equilibrium to the right in the associated reaction, resulting in a negatively charged silica surface. There is a specific pH at which the surface has no net charge, known as the pI, which for SiO_2 ranges between 1.7 and 3.5 [93]. The resulting electrostatic forces of attraction and repulsion among ions, due to the surface charge, lead to various significant physical phenomena in nanofluidic systems.

The electric double layer (EDL) plays an increasingly significant role in determining physical properties such as ion selectivity, viscosity, and proton mobility within a nanofluidic channel. When a solid surface contacts a liquid electrolyte, it acquires a surface charge, attracting a layer of oppositely charged ions (counterions) at the interface. This initial layer, known as the Stern layer, is closely bound to the surface [124]. To maintain electroneutrality, additional counterions form a secondary, more diffuse layer, creating the complete EDL structure, which consists of the immobile Stern layer and a mobile diffuse layer [2]. The structure of the EDL is illustrated in Figure 1.25.

The first model for EDL was introduced by Hermann von Helmholtz, who proposed that surface charge is neutralized by a layer of counterions located a fixed distance d from the surface, as illustrated in Figure 1.26 (a).

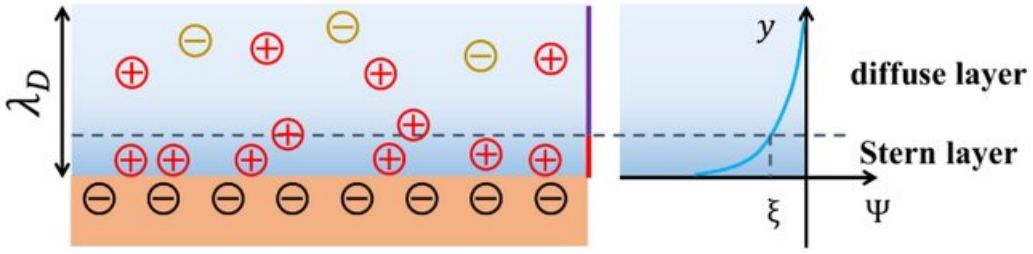

Figure 1.25: Illustration of electrical double layer consisting of a Stern layer and diffuse layer at the solid interface [2]

In this model, the surface potential ψ decreases linearly from the charged surface to the counterions. Although Helmholtz's model was pivotal in explaining solid-liquid interactions, it lacked key considerations, such as ion diffusion and adsorption. To address these limitations, the Gouy-Chapman model was later developed, suggesting that counterions form a diffuse layer at the liquid-solid interface rather than being

fixed. As shown in Figure 1.26 (b), counterions in this diffuse layer follow a Boltzmann distribution (1.2, where ψ is the electric potential, kT represents the thermal energy, and z is the ionic charge. The Gouy-Chapman model predicted an exponential drop in the electric potential perpendicular to the charged plane. However, further refinements were needed to improve accuracy in predicting EDL thickness.

$$c = c_{bulk}.exp(\frac{ze\psi}{kT}) \tag{1.2}$$

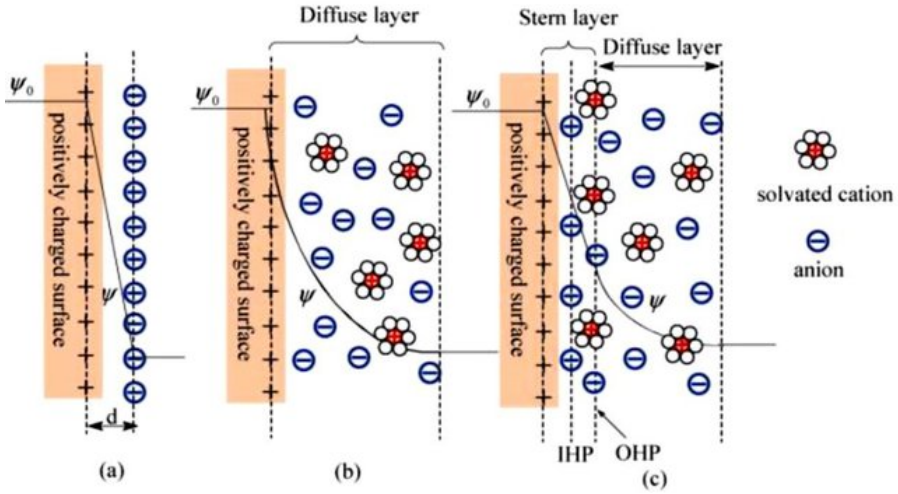

Figure 1.26: Models of the electrical double layer at a positively charged surface. (a) In the Helmholtz model, the charge is stored solely at the electrode surface within a fixed double layer distance d. (b) The Gouy-Chapman model introduces a diffuse layer of ions but omits the Helmholtz region. (c) The Stern model combines both, showing charge stored in the Helmholtz region as well as within a diffuse layer. Here, ψ_0 represents the electrode potential, while ψ denotes the potential at the electrode/electrolyte interface [106]

The Gouy-Chapman-Stern model advanced the understanding of counterion distribution by proposing a two-tiered structure, adding a layer known as the Stern layer, which remains closely bound to the charged surface. This Stern layer can be further divided into two sublayers: the inner Helmholtz plane (IHP) and the outer Helmholtz plane (OHP), as shown in Figure 1.26 (c). In the IHP, counterions are unhydrated,

while in the OHP, they are hydrated. Additionally, this model introduces the concept of a slip plane, which separates the immobile Stern layer from the mobile diffuse layer.

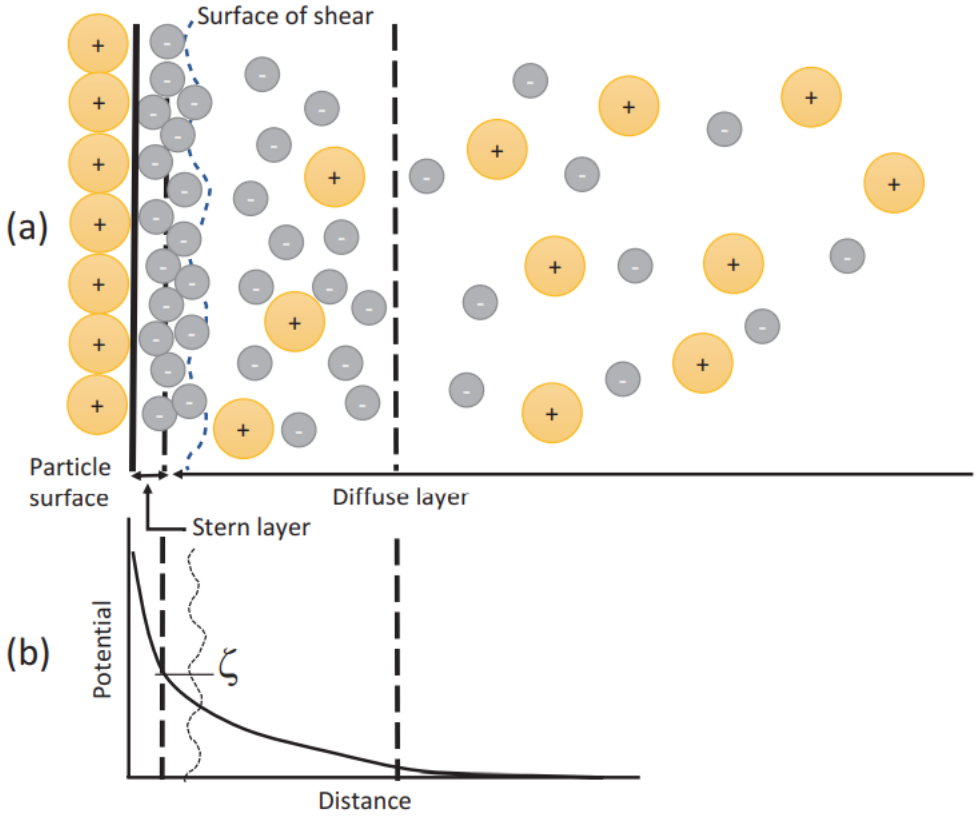

Figure 1.27: (a) Illustration of the charge distribution at the surface/liquid interface of a particle according to Gouy-Chapman-Stern model. (b) the potential drops as the distance from the particle surface increases. The zeta potential (ζ) is measured at the interface between the Stern's and diffuse layer [33]

Figure 1.27 provides a detailed view of the distinct layers in the Gouy-Chapman-Stern model and illustrates the potential distribution across the solid-liquid interface. The potential generated by the surface charge, represented as ψ_0, dissipates in two stages. Firstly, the potential drops across the Stern layer, with thickness δ, from ψ_0 to ψ_δ. The remaining potential drop occurs across the diffuse layer, with ψ_δ, often referred to as the zeta potential (ζ).

The Debye length is a characteristic length representing the distance in the bulk solution from the Stern layer, where the magnitude of the zeta potential decreases to

approximately 36.8% of its original value. It can be expressed as Equation 1.3, where ε is the dielectric constant, k_B is the Boltzmann constant, T is the temperature, e is the elementary charge, N_A is Avogadro's number, and c is the ionic strength of the electrolyte. The Debye length depends on electrolyte concentration rather than the zeta potential (ζ). Within the Debye length, the electric potential at a distance x from the interface between the Stern and diffuse layers can be described by Equation 1.4.

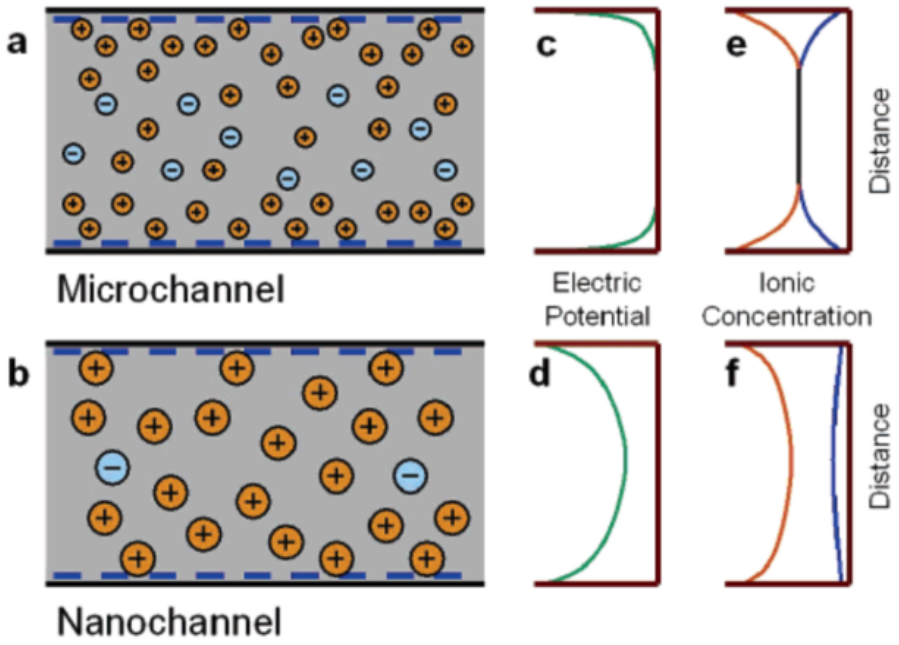

Figure 1.28: Schematic representation of the electric double layer (EDL) in microchannels and nanochannels. (a) In a microchannel, the Debye length is typically much smaller than the channel dimensions, resulting in a largely neutral solution across most of the channel. (b) In a nanochannel, when the Debye length is greater than the channel dimensions, the solution becomes charged. (c) The electric potential in the microchannel decays rapidly to reach bulk conditions beyond the Debye length. (d) In the nanochannel, however, the electric potential at the channel center is still influenced by the surface charge and does not reach the bulk potential. (e) In the microchannel, the concentrations of cations (orange) and anions (blue) are equal to the bulk concentrations. (f) In the nanochannel, the counterion concentration (orange) is significantly higher than that of coions (blue) [48]

$$\lambda_D = \sqrt{\frac{\varepsilon k_B T}{2e^2 N_A c}} \tag{1.3}$$

$$\psi = \zeta exp(\frac{-x}{\lambda_D}) \tag{1.4}$$

The boundary where the Debye length terminates is defined at x=λ_D, at which point the electric potential is 36.8% of the zeta potential (ζ). The zeta potential is directly proportional to the surface charge density; therefore, an increase in ζ corresponds to a higher electric potential at the outer edge of the Debye length.

When the critical dimension of a channel approaches the Debye length, the electrostatic effects generated by surface charge begin to significantly affect ion distribution across the channel [48]. Figure 1.28 (a) illustrates a typical microchannel, where the Debye length is negligible in comparison to the channel size. In contrast, Figure 1.28 (b) demonstrates that the EDL occupies a substantial portion across the cross-section of a nanofluidic channel.

Figures 1.28 (c) and (d) show the electric potential distribution within the cross-sections of a microchannel and a nanochannel, respectively. As the Debye length becomes comparable to the height of the nanochannel, a higher concentration of counterions than coions is needed within the channel to maintain electroneutrality. Figures 1.28 (e) and (f) depict the concentration profiles within the cross-sections of a microchannel and a nanochannel, respectively. Due to their high surface area-to-volume ratio, nanochannels with a sufficiently large Debye length can have the EDL occupy most of the channel volume. As a result, nanochannels can preferentially transport counterions (opposite to the surface charge), leading to unique physical effects such as ICP.

As mentioned above, the surface charge-induced EDL has been shown to regulate ion transport within nanochannels, particularly at low ionic strengths. When the electrolyte concentration exceeds a certain threshold, EDLs can overlap, causing the nanofluidic channel to become permselective. Under a constant voltage bias applied across the nanochannel, counterions are selectively transported from the anodic to the cathodic side, as illustrated in Figure 1.29.

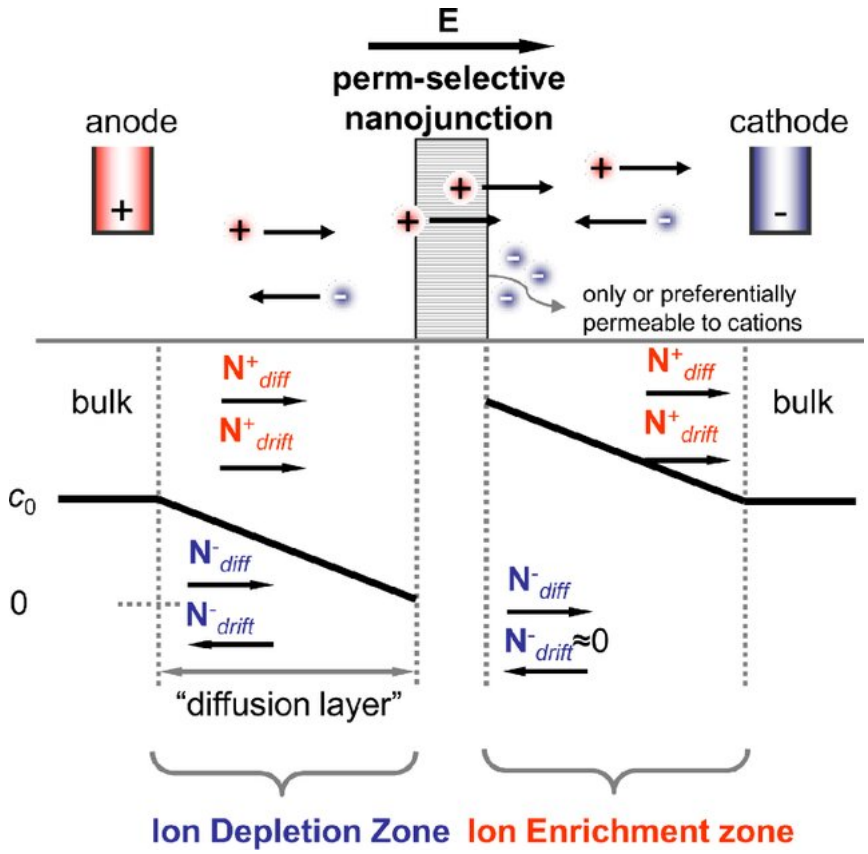

Figure 1.29: The asymmetric concentration profile of ions across an ion-selective membrane results from the preferential transport of counterions, which generates a concentration polarization on either side of the membrane. This polarization arises as counterions are selectively transported, leading to ion enrichment on one side and depletion on the other [44]

Conversely, coions are prevented from entering the nanochannel from the cathodic to anodic side. This selective ion transport creates an asymmetry in ionic concentrations, leading to ion depletion on the cathodic side and enrichment on the anodic side to maintain electroneutrality. This asymmetric concentration distribution, shown in Figure 1.29, results in a phenomenon called ICP. As ion concentrations approach zero in the depletion zone, the system reaches a diffusion-limited current. ICP has been applied in various innovative lab-on-chip applications. For example, it has been used in microfluidic platforms to concentrate biomolecules [44] and in technologies for desalination [51] and biomolecule separation [39].

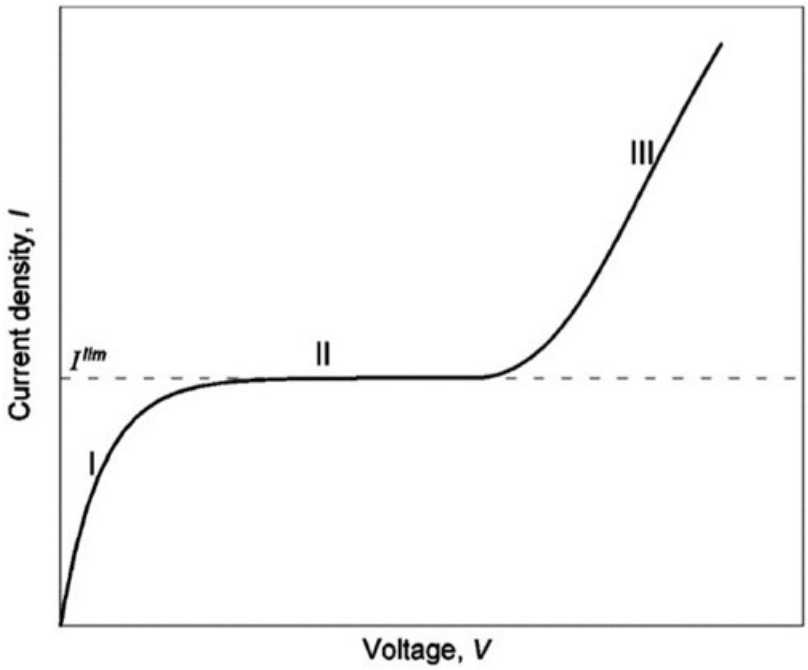

Figure 1.30: Diagram of a typical current-voltage curve for a cation-exchange membrane, showing three distinct regions: I (linear region), II (limiting region), and III (overlimiting region [47]

The characteristics of ICP were first observed in permselective membranes [47], where current density reaches a saturation point beyond a specific voltage threshold, introducing a limiting resistance regime in the current-voltage (I-V) curve. Figure 1.30 illustrates this behavior, showing three distinct regions in the I-V profile: the ohmic region (I), where current increases linearly with voltage; the limiting current regime (II), where current plateaus due to transport limitations; and the over-limiting current regime (III), where current increases once more.

In the limiting regime, ion transport occurs primarily through diffusion, and a diffuse layer forms at the nanochannel entrance as ICP initiates. Later theoretical developments proposed that, as counterions continue to deplete, a space charge layer (SCL), larger than the EDL, can emerge at the nanochannel entrance of the permselective system [145]. Figure 1.31 (a) shows the ion concentration profile along the nanochannel after the onset of the limiting current regime, while Figure 1.31 (b) illustrates the aggregation of the diffuse layer (DL), SCL, and EDL, collectively known as the con-

centration polarization layer (CPL). Following the formation of the SCL, ion currents exceed those in the limiting resistance regime, producing what is termed over-limiting current (OLC) [112, 146].

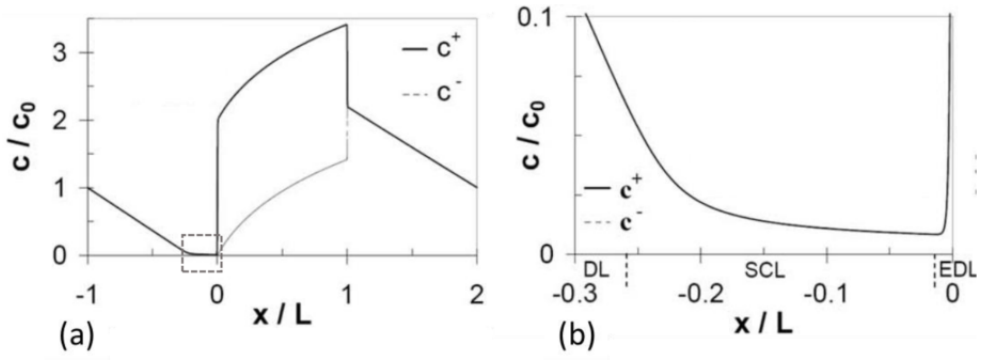

Figure 1.31: (a) Numerical simulation results illustrating the concentration distribution for ion concentration polarization (ICP) in a permselective membrane (0 $\leq$ x $\leq$ L), with a membrane thickness of L, during the limiting current regime. (b) A zoomed-in view of the region highlighted by the dashed rectangle in (a), showing the ion concentration profiles on the anodic side of the membrane for ICP, along with the various layers of the concentration polarization layer (CPL) [2]

1.5 Conclusion

This chapter presented the overview of protein, the role of protein in the body and protein pre-concentration and detection methods. Proteins are composed of amino acids linked by peptide bonds and play vital roles in the human body, functioning as both structural components of cells and active participants in nearly all biological processes. Beyond their structural and functional roles, proteins are essential biomarkers widely used for the identification, diagnosis, and monitoring of disease progression.

Currently, several methods are available for protein testing, primarily through immunoassays, which include techniques such as IHC, ELISA, flow cytometry, protein microarrays, and LOC systems. Each method has its own advantages and limitations. ELISA remains a common method in hospitals and medical facilities, valued for its robustness and reliability. However, LOC-based technologies are gaining attention from

researchers aiming to develop alternatives to traditional methods, owing to their potential for miniaturization, automation, and rapid analysis. In domestic research, numerous teams are focusing on the development of immunology-based biosensors and microfluidic chips, which are LOC-based platforms. These efforts have shown promising results, highlighting a growing interest and investment in advanced, sensitive protein-detection technologies within the field.

Protein preconcentration is an essential step in biosensing and biomarker analysis, especially when target proteins are present at low concentrations. Effective preconcentration techniques can improve detection sensitivity by increasing the local concentration of proteins near the biosensor surface, making even low-abundance biomarkers detectable. There are some methods for protein preconcentration, including electrokinetic trapping, FAS, isotachophoresis, isoelectric focusing, micellar electrokinetic sweeping and chromatographic preconcentration. Among them, the electrokinetic trapping is the most popular. This method uses ICP effect to create protein depletion and enrichment zones. The combination of a biosensor and pre-concentrator inside a microfluidic chip is a potential direction to develop a protein point-of-care testing system for biomedical diagnostics.

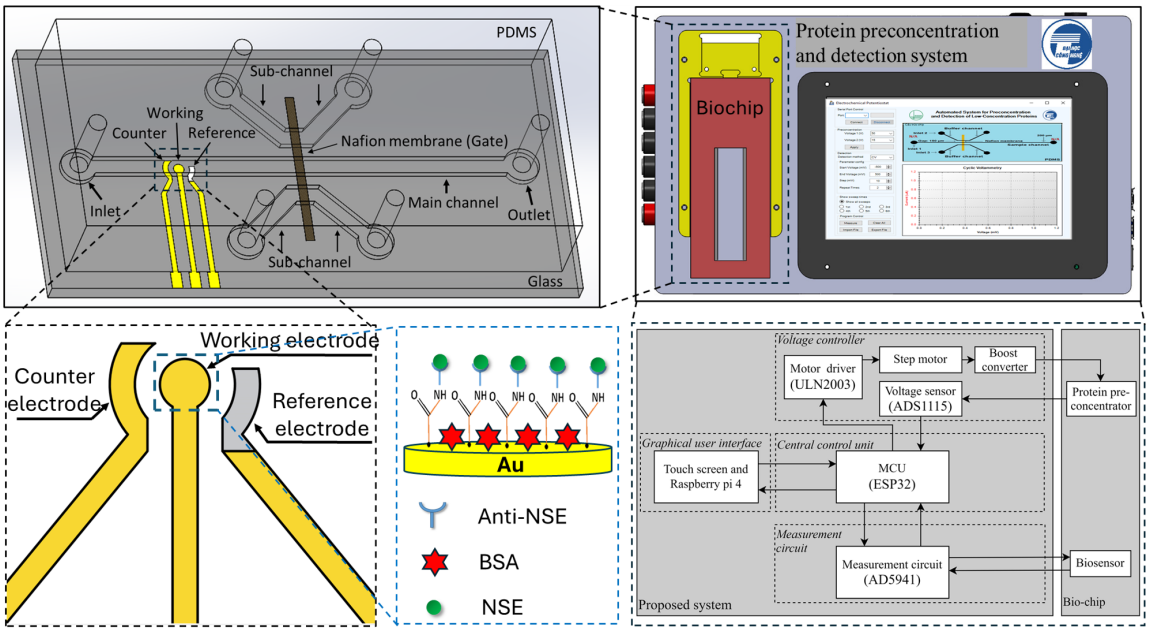

Figure 1.32: The proposed protein preconcentration and detection system

In this study, a protein preconcentration and detection system is developed. The system consists of a microfluidic chip and a control and data acquisition system, as shown in Figure 1.32. The microfluidic chip integrates a protein preconcentrator and an electrochemical immunosensor. The development of the protein preconcentrator using a dual-gate structure and ion-selective nanomembrane is presented in Chapter 2, while the development of the immunosensor for protein detection is introduced in Chapter 3. The result of the combination between them for protein enrichment and detection is presented in Chapter 5. Finally, the development of the control and data acquisition system is provided in Chapter 4.

Chapter 2

Development of a microfluidic chip for protein preconcentration using dual gate structure and ion-selective nanomembrane

In this chapter, the development of a microfluidic chip for protein preconcentration using a dual-gate structure and an ion-selective nanomembrane is described. First, a preconcentrator is designed and modeled to analyze the structure's operation. Then, the chip fabrication process is outlined, utilizing photolithography and soft lithography techniques. Finally, experiments are conducted to assess the functionality and performance of the proposed chip.

2.1 Materials and apparatuses

Bovine serum albumin - fluorescein isothiocyanate conjugate (BSA-FITC) used as a sample protein to evaluate the performance of the proposed preconcentration structure was purchased from Sigma-Aldrich Chemical Co (St.Louis, MO, USA). Polydimethylsiloxane (SYLGARD^{TM} 182, Dow Corning, USA) was utilized to fabricate the proposed microfluidic chip. Microscope glass was used as the substrate of the microfluidic chip

purchased from Duran Group (Germany). The Nafion solution (Nafion^{TM} 117, Sigma-Aldrich) was employed to fabricate the ion-selective membrane. 1X Phosphate-Buffered Saline (PBS) with a pH of 7.4 was employed to dilute the BSA protein solution. The microscope glass was then deposited a thin gold film layer by a standard sputtering coating process. S1813 photoresist and MP 315 developer were used to fabricate the gold electrode purchased from Shipley MicroChem Co., Ltd. (Westborough, MA, USA). AuR-1091 and TIR-8051B chemicals were used to remove the gold and titanium, respectively, purchased from AppliChem Technology Co., Ltd. (Miaoli County, Taiwan).

Some apparatuses were used to fabricate microfluidic chips and investigate the working modes of the preconcentrator. The 3D printing machine (Object 500 Connex 3, Stratasys, USA) was used to fabricate the mold of the chip. An inverted fluorescence microscope IX 71 (Olympus, Melville, NY, USA) equipped with a Phantom VEO 710L high-speed camera (Ametek, USA) was employed for fluorescence imaging using Phantom Camera Control software (PCC). A direct-current voltage supply (TP3H-1S, Twintex) was employed to generate the applied voltage in the preconcentration progress. Besides, a commercial precision impedance analyzer (6630 LCR Meter, Microtest Coporation, New Taipei City, Taiwan) was utilized to measure the impedance of concentration zone.

2.2 Chip design and operational principle

The proposed preconcentration structure was designed with a dual-gate configuration, including three micro-channels of a main channel in the middle and two symmetrical sub-channels, as shown in Figure 2.1 (a). The sub-channels were electrically connected to the main channel through an ion-selective membrane formed from the Nafion solution. The term gate represents the nanomembrane (nanojunction) between the main channel and the sub-channel. The dual gate represents using two nanomembranes to connect the main channel to the sub-channels. In this design, the microchannels were designed with a width of 50 µm and a height of 40 µm. The distance between the main channel and sub-channels was 150 µm. The main channel was filled with the protein

solution through inlet 1, while the sub-channels were filled with PBS solution through inlet 2 and inlet 3. The dual gate structure allows symmetrically forming the depletion region at both sides of the main channel faster and more stable than the single gate structure, which employs only one single sub-channel parallel to the main channel [52]. The proposed structure can be modeled as an N-channel Junction Field Effect Transistor (JFET), a common semiconductor device in electronic circuits (Figure 2.1 (b)). Here, the main channel was represented as n-type semiconductor with Drain and Source terminals at its two ends, while gate terminals were the nanomembranes, as mentioned above.

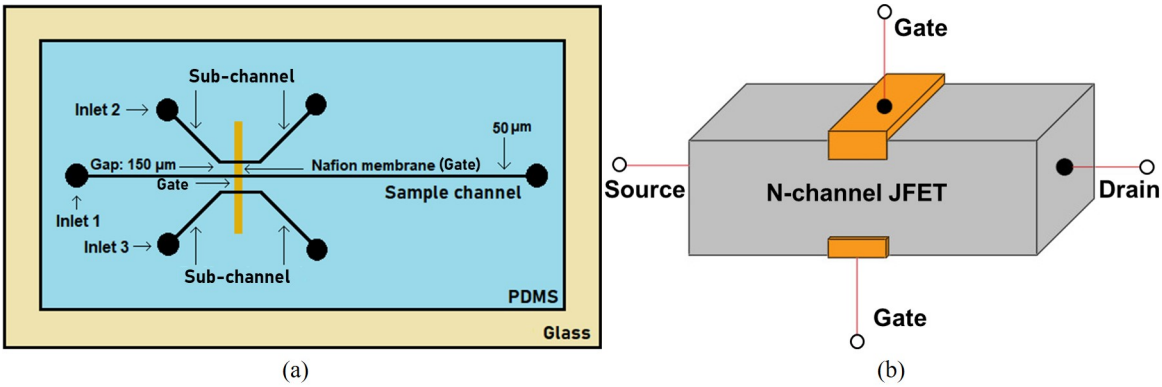

Figure 2.1: (a) Design of protein preconcentration chip with a dual-gate structure; (b) Equivalence diagram of the structure as an N-channel JFET component

The proposed preconcentration procedure includes depletion and enrichment modes, as shown in Figures 2.2 (a) and (b). At first, the main channel and the sub-channels were filled with the protein and the buffer solution, respectively. The concentration of protein was considered uniform distribution in the whole main channel. In the depletion mode, $V+$ and 0 V voltages were applied to inlets of both the main channel and sub-channels, respectively, aiming to create a voltage difference between the channels, as shown in Figure 2.2 (a). This configuration forms two external electric fields (E_N) in opposite directions through the planar Nafion ion-selective membranes and initiates the ion concentration polarization. Under the ion concentration polarization effect, the negatively charged protein molecules and anions in the buffer solution were repelled from the middle region of the main channel near the Nafion membrane and moved

toward the terminals of the main channel, where the higher voltage was applied ($V+$), while the cations in the solution passed the ion-selective membrane and moved to the sub-channels, where the lower voltage was applied (GND). This phenomenon caused the depletion zone with the disappearance of protein molecules and ions from the middle region of the main channel near the Nafion membrane's position. This mode was quite similar to the operation of N-channel JFET in the case that the Drain and Source terminals were applied a positive voltage, while the Gate terminals were both grounded or the voltage difference between them was less than zero ($V_{GS} < 0$). The two PN junctions became reverse bias, forming and expanding the depletion zone in the junctions (yellow areas in Figure 2.2 (a)). The depletion regions extending to the channel were equal in thickness and symmetrical. If the value of V_{GS} was large enough, the depletion regions would touch each other and block the channel (pinch-off condition). Besides, the voltage between the Drain and Source terminals (V_{DS}) was equal to zero, so there was no current flowing through the transistor, or the transistor was in cut-off mode.

In the enrichment mode, the voltages applied to the two ends of the main channel were adjusted to create a voltage difference between the two sides of the main channel, leading to the formation of a tangential electric field (E_T) along the main channel, as shown in Figure 2.2 (b). Under the influence of the tangential electric field, the sample fluids, including proteins and ions, were pushed toward the depletion region along the main channel by the influence of the electroosmotic flow force (EOF). The iso-electric point of BSA is at a pH of 4.5 – 5.0, resulting in the negative charge of BSA molecules in PBS 1X solution at pH 7.4. As a consequence, proteins accumulated in front of the depletion zone at the higher voltage ($V++$) side in the main channel. This zone was known as the electro-kinetically trapping zone or concentration zone. By contrast, on the lower-voltage side of the ion-selective membrane, proteins were pushed toward the reservoir, where a slightly lower voltage was applied ($V+$). However, these results were different from those on N-channel JFET. In this case, the voltage of the Drain terminal was higher than the Source voltage while the Gate terminals were still grounded. This results in the junction region near the Drain terminal being

more reverse-biased than the region near the Source terminal. Therefore, the depletion was extended towards the Drain terminal, where a slightly higher voltage was applied ($V++$). Furthermore, the operating point and the depletion size depended on the V_{DS} and V_{GS} values. The depletion regions could not block the channel, and there was still current flowing through the channel when the transistor operated at the ohmic or saturation modes.

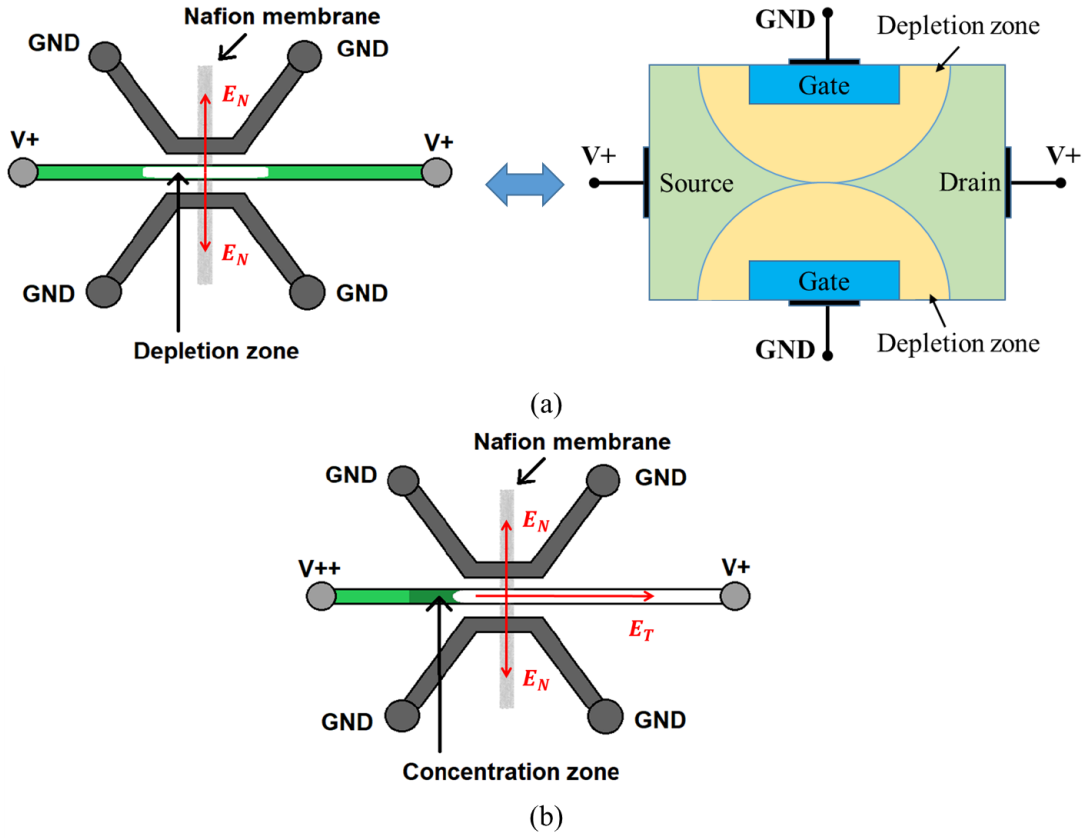

Figure 2.2: Operation principle of proposed preconcentrator with two modes: depletion (a) and enrichment (b)

2.3 Chip fabrication

The fabrication process of the proposed chip consisted of 12 steps combining the soft-lithography technique and the micro-flow patterning technique, as shown in Figure 2.3. At first, the surface of microscope glass slides with the dimensions of 26 mm × 76 mm (width × length) was cleaned with acetone and isopropanol solution in an ultrasonic

cleaner before being dried using nitrogen gas. Consequently, a layer of dry film was placed on top of the cleaned glass and fixed using a laminator at 120°C, as shown in Figure 2.3. Then, a mask with the printed channel structure was placed on top of the dry film. With a positive mask style, the film area below the channels was exposed to UV light for 20 seconds (Figure 2.3 (b)). The patterned microchannel mold was realized by dipping the exposed glass substrate in the developer solution (Na_2CO_3 0.1 mM), as shown in Figure 2.3 (c). Following this, the glass substrate with the single channel mold was placed in a 3D-printed rectangular mold, and the mixture of PDMS pre-polymer with a curing agent at a weight ratio of 10:1 was poured inside the 3D-printed mold to form the single microfluidic channel substrate (Figure 2.3 (d)).

Then, the mold with the PDMS mixture was placed in a vacuum chamber for 15 minutes to remove air bubbles in the PDMS solution and was hardened in the oven at 70°C for 1 hour before being peeled off from the mold, as shown in Figure 2.3 (e). The inlets of the microfluidic structure were created at the two ends of the channel for filling the solution and electrode connection, as shown in Figure 2.3 (f). As a result, a PDMS microfluidic channel was successfully fabricated based on the soft-lithography technique with dry film. Although this approach exhibited a limitation on the dependence of the channel depth on the dry film thickness, it is still a simple microfluidic chip fabrication method without the requirement of a clean room. In this study, two PDMS microchannel structures were fabricated, including a single straight channel for creating the Nafion membrane (Figure 2.3 (f)) and a three-channel structure for the preconcentration chip (Figure 2.3 (j)). The microflow patterning method was employed to create the Nafion membrane. Firstly, the single-channel PDMS substrate with a height of 40 µm and a width of 50 µm was placed on the cleaned glass. Then, 3 µl of Nafion solution was filled into the channel through the inlet of the main channel, as shown in Figure 2.3 (g). With properties like good water uptake ($\approx 27\%$) and ionic conductivity ($1.23 \times 10^{-2}\Omega^{-1}cm^{-1}$), it was straightforward to flow the Nafion solution into the microchannel for surface patterning. After that, the pipette was directly used to generate a negative pressure applied on one end of the channel to suck the liquid resin completely in the micro-channel, as shown in Figure 2.3 (h). After being sucked, the

thin layer of Nafion membrane remained on the surface of the glass slide, and the chip was then heated at 95°C for 10 minutes to achieve the cured ion-selective membrane in a stripe shape on the glass, as shown in Figure 2.3 (i). The thickness of the membrane mainly depends on the magnitude of applied negative pressure.

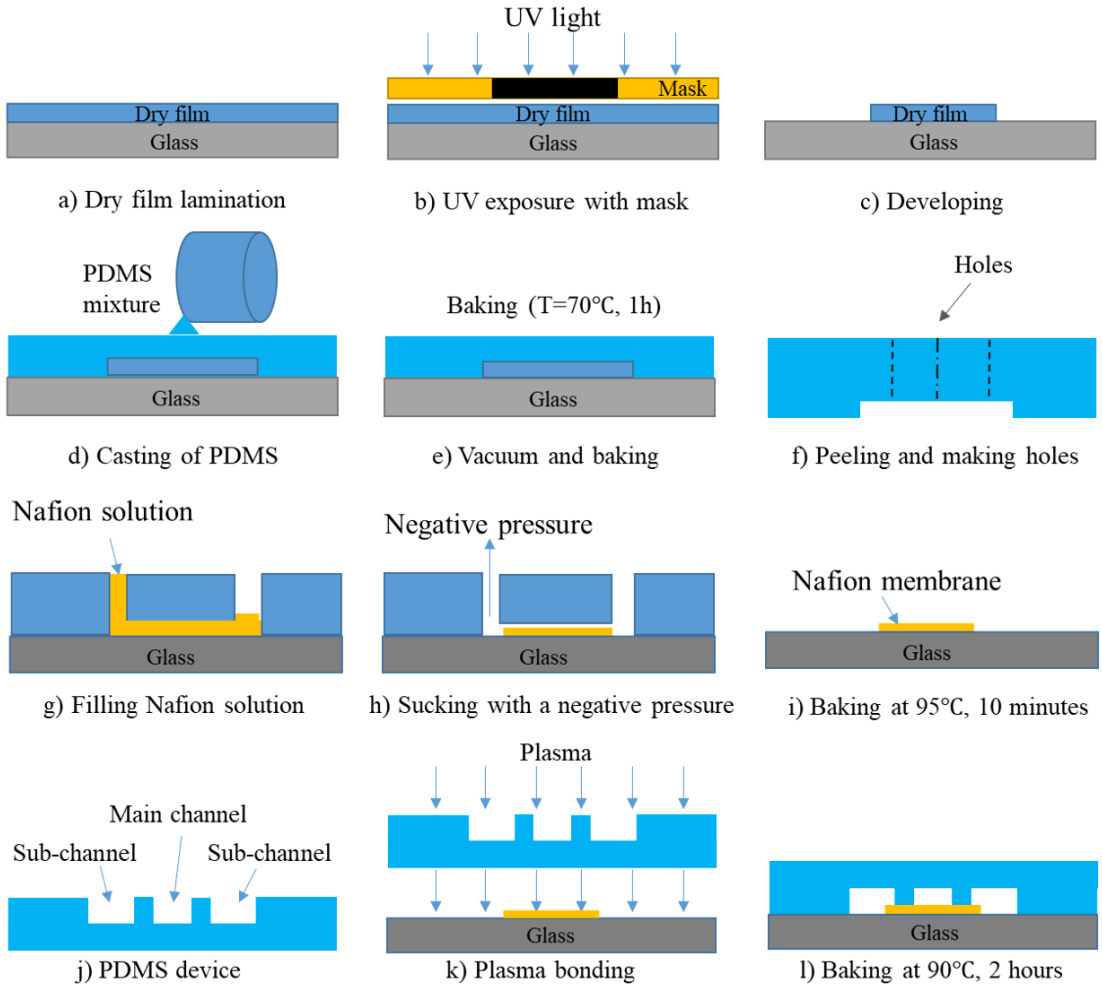

Figure 2.3: Fabrication process of the proposed structure using soft-lithography and micro-flow patterning techniques

Following the formation of the Nafion membrane on the glass slide, the PDMS substrate with three micro-channels was bonded on the patterned glass substrate using the standard oxygen plasma bonding technique, as shown in Figures 2.3 (j) and (k). Finally, the assembled device was heated on a hot plate at 90°C for 2 hours to enhance bonding performance, as shown in Figure 2.3 (l).

2.4 Experimental setup

An inverted microscope system integrated with a high-speed camera was used to observe and record the fluorescence image of the microfluidic channel. A personal computer coupled with PCC software from Vision Research Company was connected to a high-speed camera for data acquisition and analysis, as shown in Figure 2.4.

After being filled with proteins and the buffer solution, the fabricated microfluidic chip was placed on the inverted microscope system and connected to the direct-current voltage supply to apply the electrical voltage to microchannels through the copper electrodes. The experiments were conducted at room temperature and in low-light conditions to ensure the protein's functional activity and the conjugated fluorescence molecules.

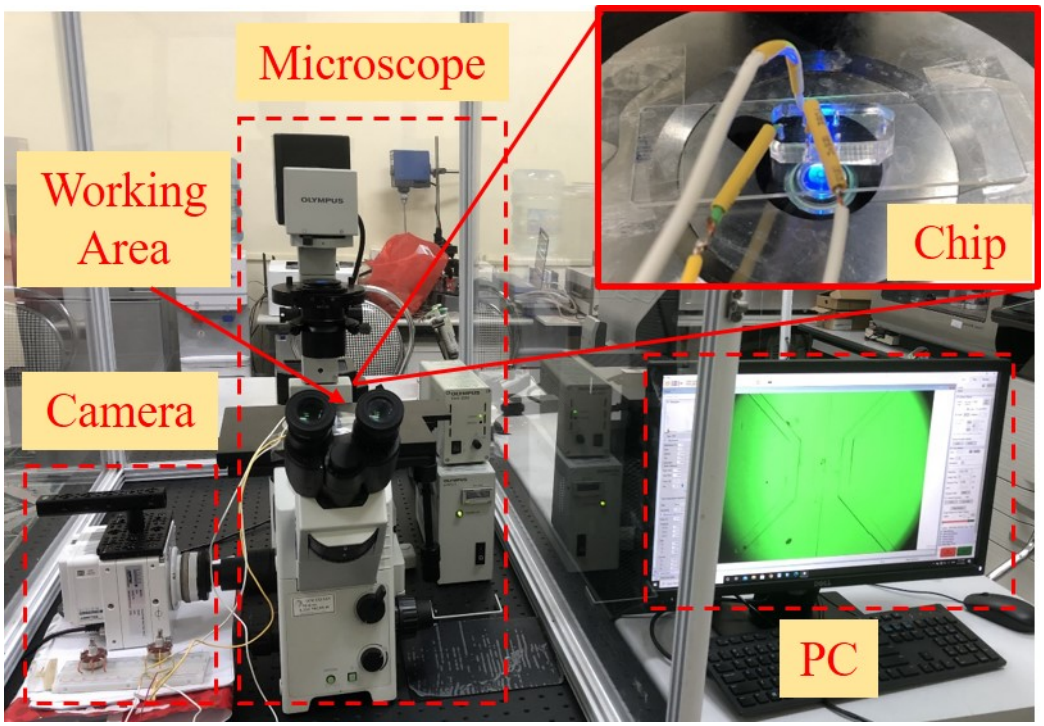

Figure 2.4: Experimental setup for protein pre-concentration

2.5 Results and Discussions

2.5.1 Depletion mode operation

The protein sample was first prepared by diluting the BSA-FITC in PBS 1X, pH 7.4 solution. In this experiment, the protein concentration of 50 µM was utilized to investigate the depletion progress of the proposed structure. 5 µl of prepared protein sample was injected into the main channel by the pipette, while the sub-channels were filled with PBS 1X solution. Consequently, the preconcentration chip was placed on the microscope and connected to the voltage supply via copper electrodes. Initially, the BSA protein molecules were evenly distributed throughout the main channel, which was observed by the uniform intensity of the fluorescence signal, as shown in Figure 2.5 (a). The slight difference in brightness in the obtained image was solely due to the irregularity of the fluorescent excitation lamp's light beam. Afterward, a voltage difference of 50 V was applied between the main channel and the two sub-channels from the direct-current voltage supply. The experimental results show that the fluorescence signal at the middle region of the main channel, where the Nafion membrane was patterned for electrical connection between the sub-channels and the main channel, decreased significantly, called the depletion zone. In contrast, the fluorescence intensity of the region at the two ends of the channel was enhanced, as shown in Figure 2.5 (b). This can be explained that the BSA protein molecules and anions were repelled from the depletion region and moved to the two ends of the main channel due to the impact of electrophoresis force (EPF). The velocity of molecules was represented by the following Equation 2.1.

$$\nu = \frac{Eq}{f} \tag{2.1}$$

Where ν is the velocity of the molecules (m/s), E is the electric field (V/m), q is the net charge on the molecules, and f is the frictional coefficient, which depends on the mass and shape of the molecules. By contrast, cations moved to the sub-channels through the ion-selective membrane to create an ion depletion zone. In addition, the

results also demonstrate that the depletion region was formed on both sides of the main channel because of the advantage of the dual-gate structure utilization.

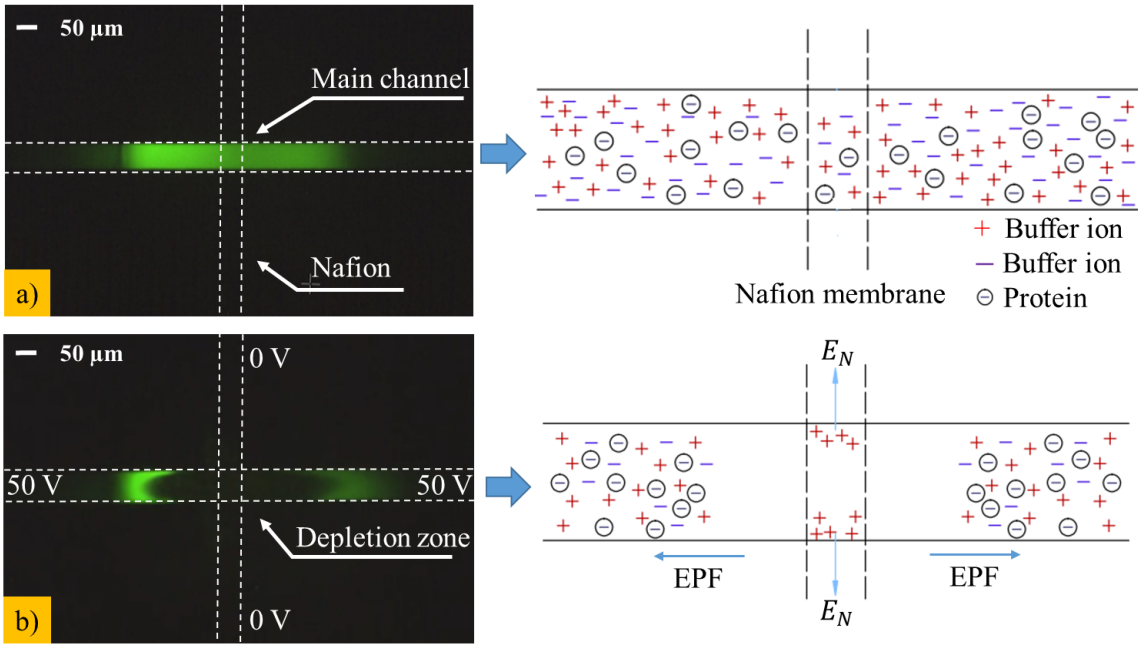

Figure 2.5: Depletion zone concentration result. (a) Before applying voltages; (b) After 20 seconds of applying a voltage of 50 V at the two ends of the main channel and 0 V at the two ends of each sub-channel

2.5.2 Enrichment mode operation

In the enrichment mode, the applied voltage on one end of the main channel was lowered to a voltage of 40 V in order to create the voltage difference between the two ends of the main channel. Figure 2.6 demonstrates the fluorescence image of the main channel during the protein concentration progress. The experimental results show that the higher voltage region of the main channel in front of the depletion zone exhibited a higher fluorescence signal intensity. In comparison, the lower voltage region of the channel demonstrated a decrease in the fluorescence signal, as shown in Figure 2.6. By applying a voltage difference between the two ends of the main channel, the EOF flow appeared and drove both proteins and ions along the electric field direction E_T, from the higher voltage region to the lower voltage region along the main channel. On

the higher voltage side, the proteins were affected by two opposing forces consisting of EOF and EPF. When the electroosmotic force was in balance with the electrophoresis force, a stable concentration region of proteins was formed at a distance Δd from the Nafion membrane, called the protein concentration zone. On the lower voltage side, the two forces were in the same direction toward the lower voltage region along the main channel, so proteins were pushed to the lower voltage reservoir.

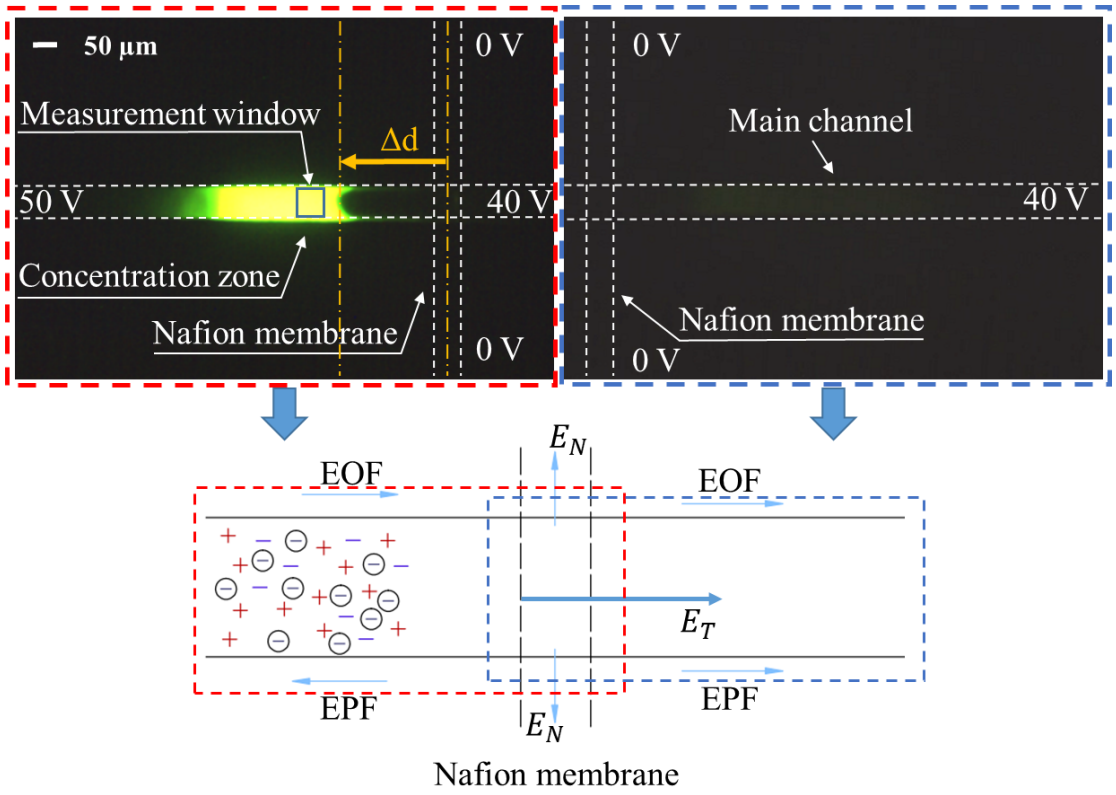

Figure 2.6: Protein preconcentration results, proteins were accumulated in the concentration zone

In this study, five BSA protein concentrations were used to quantitatively evaluate the proposed chip's preconcentration factor and speed. Besides, ten different protein concentrations ranging from 0.5 µM to 150 µM were filled into the main channel, and fluorescence measurement was implemented to achieve the fluorescence intensity of the reference protein concentrations. The fluorescence intensity measurements were performed on ImageJ software, a Java-based image processing program developed by the National Institutes of Health and the Laboratory for Optical and Computational

Instrumentation (LOCI, University of Wisconsin). Fluorescence intensity was represented by the mean value of a square measurement window located within the protein concentration region, as shown in 2.6. The dimensions of this measurement window were 50 µm x 50 µm, and its position adjacent to the end of the depletion region at a distance of Δd + 50 µm from the Nafion membrane, providing specific context for the data analysis. This information allows the accurate interpretation and comparison of the fluorescence intensity results.

Here, the preconcentration factor (PF) is defined as the ratio of the protein concentration after being concentrated (C_e) and the protein concentration of the initial solution (C_i):

$$PF = \frac{C_e}{C_i} \tag{2.2}$$

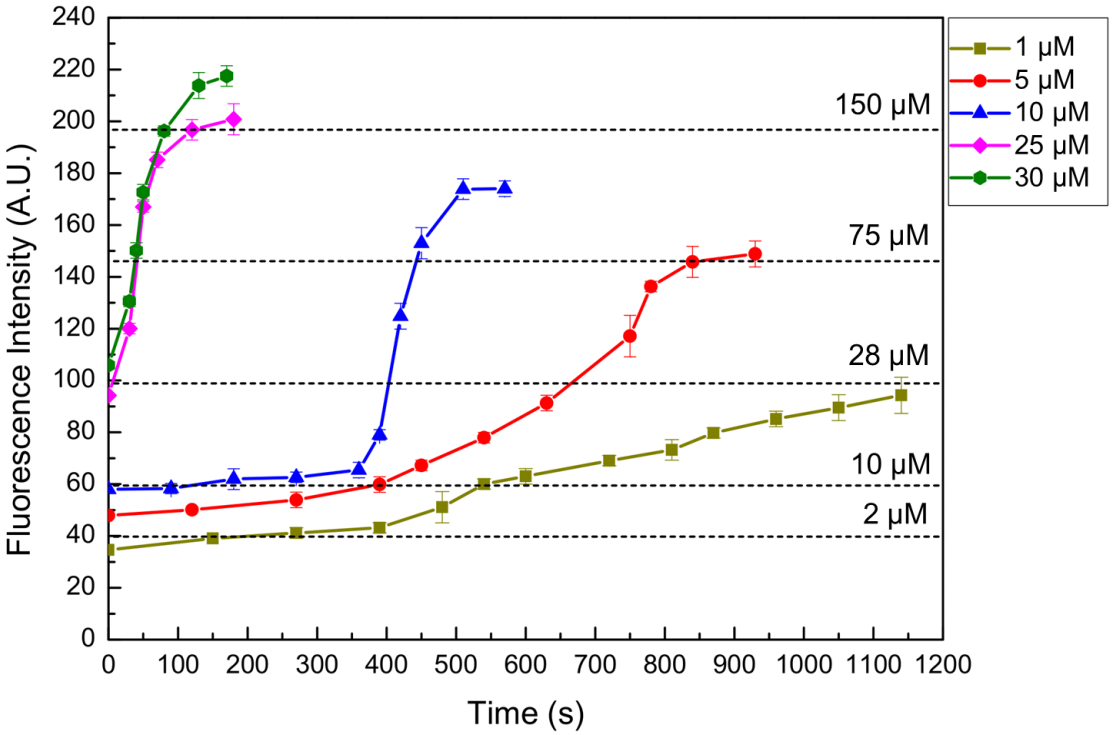

Figure 2.7: The protein concentration increases over time in the concentration zone

The experimental results indicated that the protein preconcentration speed at the high initial concentration group, including 25 µM and 30 µM, was much faster than the lower initial concentrations, as shown in Figure 2.7. At the higher concentration group,

the intensity increased sharply right after applying the voltage and reached the saturation values after approximately two minutes. In the case of the protein concentration of 30 µM, the concentration rose to the reference intensity of 150 µM, i.e., the PF is about 5 after 80 seconds. For the lower concentration group, the period for protein preconcentration was markedly lower. There was a slight increase in intensity in the early stage, while the intensity grew significantly in the later stage. At an initial concentration of 10 µM, the fluorescence intensity increased slightly from 59 A.U to 65 A.U in the first 6 minutes. However, it rose strongly and reached 170 A.U in the next 2 minutes. The corresponding PF was approximately 7.5 after 7.5 minutes. In addition, for the initial concentrations of 1 µM and 5 µM, the preconcentration factors were around 28 and 15 after 19.5 minutes and 14 minutes, respectively. The results were acceptable compared with previous studies in the high initial protein concentration range. The low protein concentration samples can be carried out to further evaluate the performance of the proposed chip in the subsequent research.

2.5.3 Preconcentration operation

In this study, a BSA protein solution at a concentration of 10 µM was used to examine the preservation of proteins with two distinct structures featuring main channel widths of 50 µm and 100 µm. After that, voltages were applied to the channels to concentrate proteins at the specified zone, as mentioned above. Once the fluorescence intensity of the concentration zone reached a stable level, indicating that the protein concentration had saturated during the manipulation process, the electrodes were then disconnected from the power supply. The results show that the fluorescence intensity of the concentration zone gradually decreased after the voltage disconnection, as shown in Figure 2.8.

The discontinuation of applied voltage resulted in the disappearance of the external electric field, eliminating the electrical force acting on the proteins. Concequently, the proteins diffused back into the solution through the main channel. The duration of this process can vary depending on the width of the channel, ranging from approximately 1 to 3 minutes. Eventually, the protein concentration at the specified zone could be

either larger or smaller than the original concentration of 10 µM due to the non-specific binding of proteins at the concentration zone, or proteins being trapped and retained at the lower voltage terminal of the main channel. The integration of microelectrodes into the channel to facilitate the detection and recognition of the protein concentration zone through electrical measurement techniques is a promising approach, especially for non-fluorescently labeled proteins. The utilization of electrical impedance measurement can take advantage of the fact that proteins are negatively charged, leading to a decrease in impedance in the protein concentration zone. To ensure accurate electrical measurements, the voltage maintaining the concentration zone must be disconnected to prevent any interference. Since the protein will be diffused into the surrounding area after the voltage is disconnected, conducting electrical measurements promptly is crucial to accurately detect and recognize the protein concentration zone.

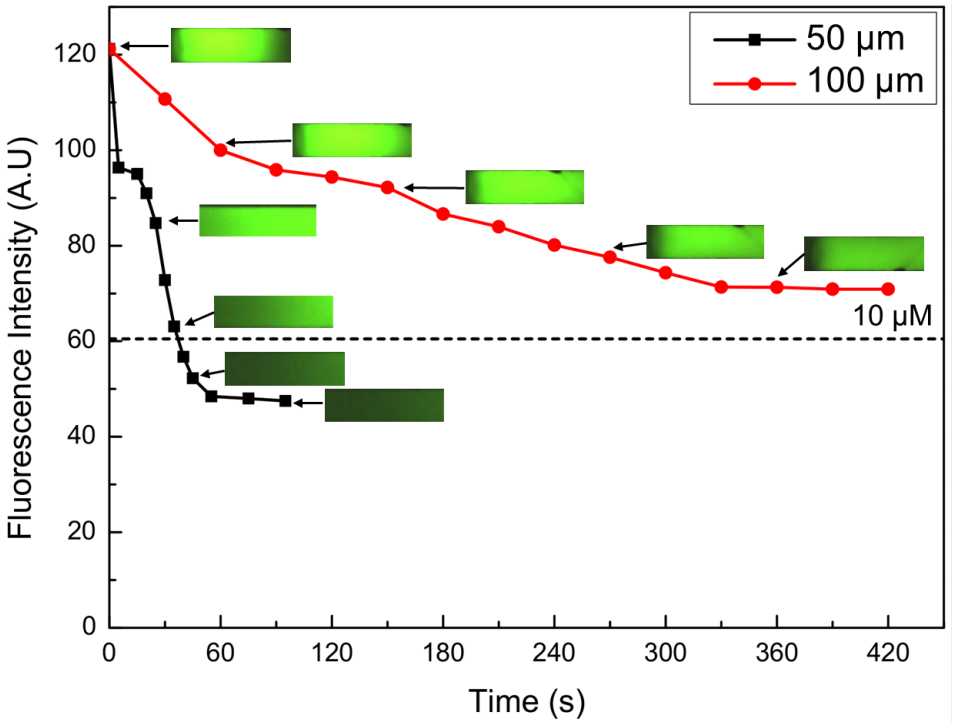

Figure 2.8: The fluorescence intensity of the concentration zone was reduced according to the disruption of the applied voltage

In the enrichment mode, the proteins were influenced by two opposing forces: EOF and EPF. The position of the concentration region can be adjusted by altering the

voltage difference between the two terminals of the main channel. This adjustment influences the EOF and EPF within the channel. As described in the previous study conducted by Nhu et al., changes in the voltage difference can manipulate the behavior of these flows, thereby causing the concentration region to either move closer to or further away from the Nafion membrane [76].

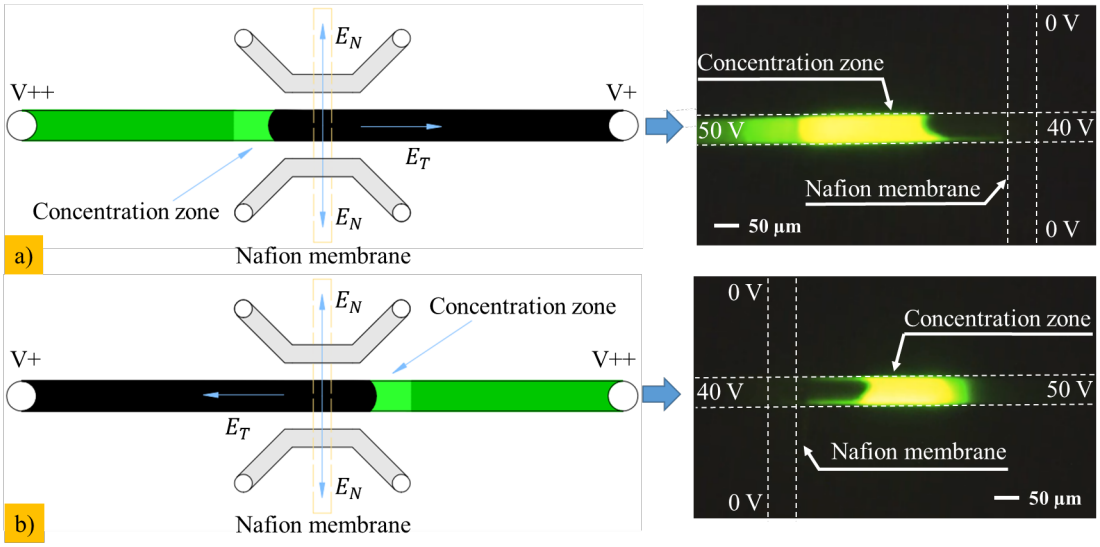

Figure 2.9: Manipulation of protein concentration zone at the two sides of the main channel by the voltage difference alternation; (a) Concentration zone is on the left of the main channel; (b) Concentration zone is on the right of the main channel

In this study, as the next step of the investigation process with the initial protein concentration of 50 µM, after the proteins were enriched at the concentration zone of the main channel with the higher voltage terminal of 50 V and the lower voltage terminal of 40 V (Figure 2.9 (a)), the polarity of the applied voltages was reversed. The results indicate that the protein concentration zone disappeared on the lower voltage side of the main channel, while the concentration zone gradually formed on the higher voltage side of the main channel, i.e., the right side in Figure 2.9 (b). A new concentration zone formed in approximately 38 seconds when the voltage was reversed under the condition of an initial protein concentration of 50 µM. This can be explained by the change in the polarization of the voltages, which altered the direction of the electrical field and the EOF flow. Consequently, the proteins in the concentration zone of the

right-side terminal of the main channel were pushed toward the Nafion nanomembrane and concentrated in front of the depletion zone. On the left side, the proteins moved to the lower voltage region under the effect of the EOF and the EPF. The research results also indicate the potential to create two preconcentrators in a chip, allowing the manipulation of multiple types of proteins in the same microfluidic structure.

2.5.4 Investigation of protein concentration zone impedance change

Two gold micro−electrodes were integrated into the main channel to measure the impedance of the protein sample after the pre−concentration stage. The width of each electrode and the distance between them are both 30 µm. The micro−electrodes were fabricated utilizing the soft photolithography technique. The electrode fabrication process was divided into 6 steps, as shown in Figure 2.10 (a).

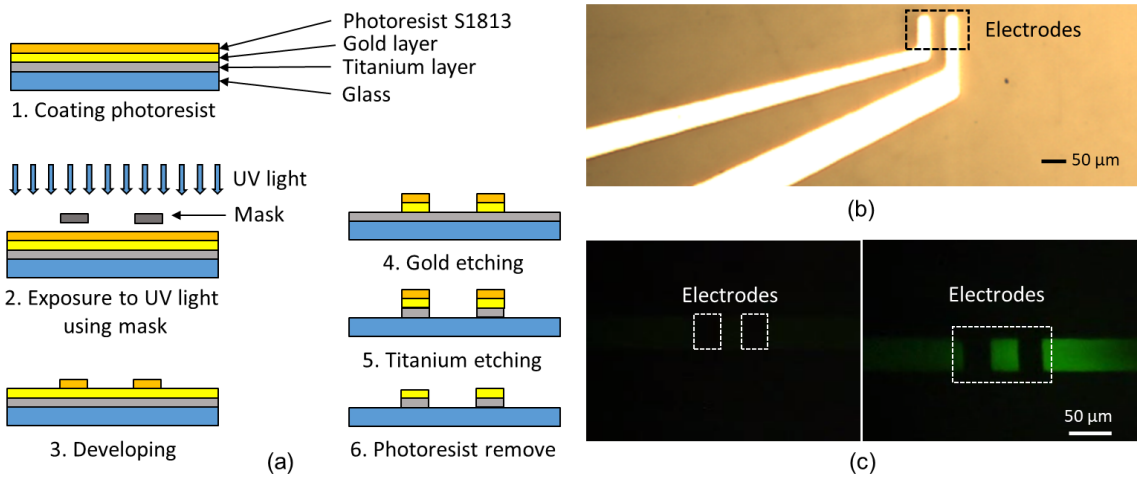

Figure 2.10: (a) The gold electrode fabrication process using photolithography technique; (b) The actual image of the electrode under the microscope; (c) The change of fluorescence signal of electrode area before and after protein pre-concentration in the main channel

Firstly, the clean gold-sputtered glass was coated with an S1813 photoresist layer using a spin coater. Subsequently, the gold-sputtered glass was placed on a hot plate machine at the temperature of 90 ^{o}C for 2 minutes to dry the photoresist layer. In

the second step, a mask with the printed electrode structure was placed on top of the photoresist layer and both were exposed to UV light for 30 seconds. Following this, the glass was immersed in MP 351 developer solution to remove photoresist areas exposed to UV light and retain the desired electrode-shaped photoresist layer on the glass substrate, as depicted in step 3 of Figure 2.10 (a). After that, exposed gold and titanium areas were corroded by AuR-1091 and TIR-8051B chemicals, respectively (steps 4 and 5 in Figure 2.10 (a)). Finally, the covering photoresist layer was removed by acetone solution and the gold electrodes were clearly visible on the glass (step 6 in Figure 2.10 (a)). Figure 2.10 (b) shows the actual image of the gold electrode observed under the microscope. The microscope with the gold electrode was then used as a substrate to fabricate the microfluidic chip as mentioned above. The Nafion ion-selective membrane was printed on the glass substrate using the micro-flow patterning method. After the electrodes and Nafion membrane were fabricated on the glass substrate, the PDMS chip was bonded on the substrate integrated the gold electrodes through the oxygen plasma treatment technique. The bonding process was performed under the microscope to ensure the electrode and Nafion membrane were in the desired position.

The concentration zone impedance change was investigated with the initial protein concentration of 5 µM. Initially, the main channel was filled with 5 µM BSA-FITC solution. The color of the main channel and the electrode region were quite dark due to the initial low protein concentration, as shown in Figure 2.10 (c). After applying the potentials to the ends of micro-channels, proteins were manipulated and concentrated at the sensing electrode area, as shown in Figure 2.10 (c). The impedance between two electrodes was measured before and after the protein pre-concentration process. The parameters of the impedance analyzer were set up, including the voltage of 10 mV, and the frequency ranged from 10 kHz to 100 kHz.

The experimental results show the impedance has been decreased significantly after pre-concentrating protein to the sensing area, as shown in Figure 2.11 (a). The two impedance curves are clearly separated in the frequency range from 10 kHz to 100 kHz. Besides, the impedance at high frequency range is lower and more stable than low frequency range. These change in the impedance can be explained by the simplified

Randles, as illustrated in Figure 2.11 (b). R_S represents the resistance of the protein solution, while R_{ct} and C_{dl} were the charge transfer resistance and the double-layer capacitance between the gold electrode surface and the protein solution, respectively.

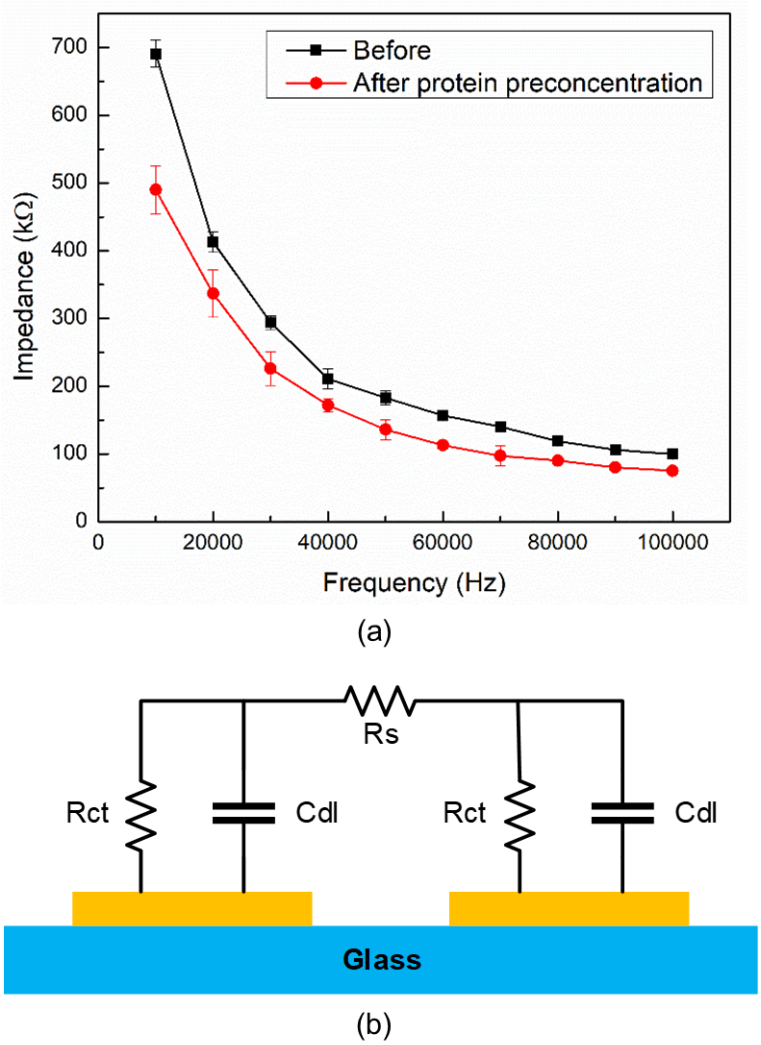

Figure 2.11: (a) The change of impedance between two electrodes before and after protein pre-concentration; (b) The simplified Randles model was used to explain the impedance change of concentration zone

At the low frequency, the impedance of the double layer capacitance, so the total impedance was high. In contrast, the influence of C_{dl} diminished at higher frequencies, resulting in a decrease in the total impedance. Furthermore, during protein preconcentration, proteins, which act as negative ion, along with anions from the buffer

solution, migrated toward the electrode area. This enrichment of ions at the electrode area contributed to an increase in solution conductance within the main channel surrounding the electrode, consequently resulting in a decrease in solution resistance, R_S. At the high frequencies, the total impedance is mainly contributed by the resistance of the solution. With the achieved results, the position of the concentration zone can be recognized through impedance measurements conducted on the integrated electrode within the channel.

2.6 Conclusion

This chapter presented the development and experimental validation of a microfluidic structure with a dual-gate configuration for protein-preconcentrating applications. The fabrication of the proposed structure was achieved through soft-lithography and micro-flow patterning techniques. The performance of the microfluidic chip was rigorously assessed in the context of protein enrichment. The experimental analysis, utilizing varying concentrations of BSA protein, demonstrated a preconcentration factor of 28 after 19.5 minutes for an initial protein concentration of 1 µM. Upon removal of the applied voltage, the concentrated protein zone was transiently maintained before gradual dispersion and even distribution throughout the main channel. In addition, manipulation of the concentration zone was effectively achieved by varying the voltage difference across the main channel. These results unequivocally confirm the efficacy and feasibility of the proposed dual-gate structure, showcasing its potential in manipulating, concentrating, and enriching proteins within designated regions. Moreover, a two gold-electrode configuration was integrated inside the main channel of the preconcentrator for impedance measurement purposes. The impedance of the concentration zone decreased considerably after the protein pre-concentration. The results have been explained by the simplified Randles model. The achieved results clearly indicate that the efficiency and position of the protein concentration zone can be reliably determined by the impedance measurement. This innovative approach not only underscores the simplicity of its fabrication technique but also highlights its significant implica-

tions for advancing lab-on-chip systems in protein enrichment and detection. In the future, the proposed microfluidic chip is potential for distinguishing various types of proteins based on their conductivity differences. In addition, the gold electrode surface can be functionalized to detect and quantify the protein concentration through specific bonds between antibodies and antigens. The research findings have been published in high-impact journals and presented at prominent international conferences [77, 78, 76].

Chapter 3

Electrode surface functionalization and development of protein detection immunosensors

This chapter describes the functionalization process of gold and carbon electrode surfaces for the attachment of antibodies, facilitating the development of immunosensors for protein detection. The experiments are conducted using commercially available screen-printed electrodes. Various parameters, including incubation time, electrode type, and thiol species, are systematically evaluated. Additionally, the performance of immunosensors employing both two-electrode and three-electrode configurations is compared. Finally, proteins captured on the electrode surface are detected using both fluorescence and electrochemical measurement techniques

3.1 Materials and apparatuses

11-Mercaptoundecanoic acid (11-MUA, 95%) and HS-PEG7500-COOH (7500 mol.g^{-1}) were used to create a self-assembled monolayer on the gold electrodes. N − (3 − Dimethylaminopropyl) − N − ethylcarbodiimidehydrochloride (EDC, 98%) and N - Hydroxysuccinimide (NHS, 98%) were mixed to activate the carboxyl acid terminated group of the self-assembled monolayer (SAM). Bovine serum albumin–fluorescein isoth-

iocyanate conjugate and anti-albumin antibody (anti-BSA) were used as the antigen-antibody pair to assess the performance of the functionalization process. Three types of gold electrodes were employed in the experiments: the sputtered gold electrode created by sputtering titanium and gold on a glass slide with a gold layer thickness of 20 nm, the screen-printed gold electrodes and screen-printed carbon electrodes (ER-N DEP chip, Biodevice Technology, Ltd, Japan). Aniline, chloroauric acid ($HAuCl_4$) were used to modify the carbon electrode surface and purchased from Sigma-Aldrich (St. Louis, Missouri, USA). Apart from HS-PEG7500-COOH, BSA-FITC, and anti-BSA, the remaining chemicals used in the experiment can cause skin irritation upon direct contact. Therefore, it is essential to wear laboratory gloves and protective equipment during the experiment.

An inverted microscope system (CKX41, Olympus, Melville, NY, USA) was employed to observe the fluorescence signal on the electrode surface. Cyclic voltammetry (CV) measurements were performed by the wireless potentiostat device (ECWP100plus, Zensor R and D, Taichung City, Taiwan) and µStat 200 Bipotentiostat (Metrohm DropSens, Oviedo, Spain), while electrochemical impedance spectroscopy (EIS) measurements were performed by PalmSens4 (PalmSens BV, 3995 GA Houten, Netherlands). Both measurements were used to detect and quantify the protein concentration.

3.2 The structure of commercial screen-printed electrode

There are three electrodes in a screen-printed gold electrode used in the experiments, including working, counter and reference, as shown in Figure 3.1 (a). The working electrode was made of gold or carbon material, while the counter and reference electrodes were carbon and Ag/AgCl, respectively. The working electrode is modified to immobilize biomolecules and it is where the reactions occur. The working electrode is designed to be small in size, making it suitable for handling small-volume samples. Before the surface modification, the electrode was cleaned by the isopropyl alcohol solution (IPA), deionized water (DI) and dried by nitrogen to remove a dust layer on the

electrode surface, as shown in Figure 3.1 (b). After cleaning, the electrode was placed inside an Eppendorf tube and stored at room temperature.

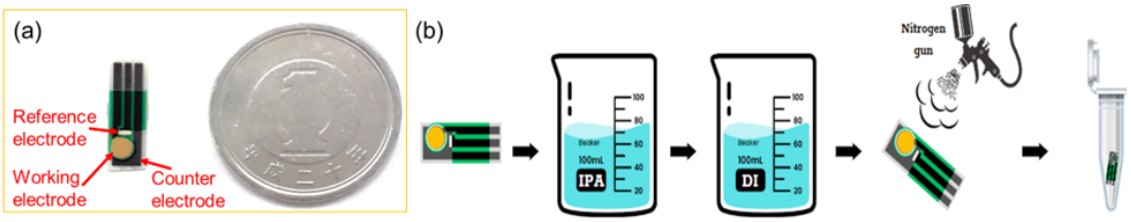

Figure 3.1: (a) Actual image of a screen-printed gold electrode used in the experiments, including working, counter and reference electrodes; (b) Electrode cleaning process

3.3 Gold electrode surface functionalization process

11-MUA is a commonly used type of SAM in research on electrode surface functionality and biosensors. It has the molecular formula of $HS(CH_2)_{10}COOH$, featuring a thiol group (-S-H) at one head and a carboxyl functional group (-COOH) at the other, which allows it to form a nanomembrane-like layer capable of bonding with gold electrodes and antibodies. This facilitates the immobilization of antibodies on the electrode surface. In comparison with other SAM types, 11-MUA exhibits several advantages, including its affordability, ease of storage at room temperature, and its ability to bond quickly with antibodies due to its concise structure.

The screen-printed gold electrode surface functionality process was divided into five main steps, as shown in Figure 3.2. The screen-printed gold electrode included working, counter, and reference of gold material, carbon, and Ag/AgCl, respectively. During the SAM layer formation stage, a 5 mM 11-MUA and 4 µM HS-PEG7500-COOH solutions were prepared in ethanol and PBS 1X, respectively. The cleaned electrode was then incubated in 1 ml of the 11-MUA solution for 16 – 60 hours, depending on the specific experiments. Meanwhile, the electrode was immersed in a 4 µM HS-PEG7500-COOH solution for 12 hours, following the procedure described in our previous publication [102]. During incubation, the thiol group (-S-H) of 11-MUA and HS-PEG7500-COOH reacted with the gold electrode to create a stable Au-S bond on the gold surface.

This resulted in the generation of carboxyl (-COOH) groups on the electrode surface, where the hydrogen atom in the thiol group of SAM was replaced by the gold atom on the electrode surface. To prevent ethanol evaporation, the incubation process was conducted inside an Eppendorf tube, tightly closed with the cap-covered parafilm. After incubation, the electrode was removed and washed with ethanol and DI water. The electrode was then placed in a Petri dish with a damp cloth at the bottom to maintain humidity and prevent solution evaporation from its surface.

In the second stage, EDC and NHS were dissolved in PBS 1X solution to create solutions with concentrations of 0.4 M and 0.2 M, respectively. Subsequently, EDC/NHS solution was prepared by mixing these two solutions in a 1:1 volume ratio. Then, 5 µl of the EDC/NHS solution was dripped onto the electrode surface and incubated for approximately 30 minutes to activate the carboxyl (-COOH) group of 11-MUA, forming NHS ester groups. These ester groups allowed efficient conjugation to the antibody's amine group (NH2). Afterward, the electrode was gently washed with PBS 1X solution to remove any residual EDC/NHS solution from the surface.

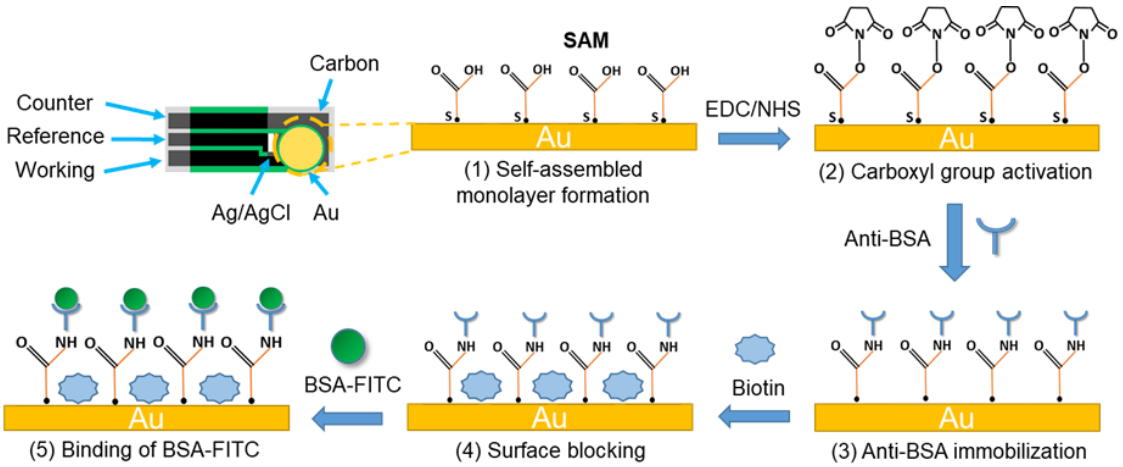

Figure 3.2: The screen-printed gold electrode surface functionality process for immobilizing anti-BSA and detection of BSA

During the anti-BSA immobilization stage, a 0.5 µM anti-BSA solution was prepared by mixing anti-BSA with PBS 1X (pH 7.4). Then, 5 µl of the 0.5 µM anti-BSA solution was added to the electrode and incubated for 2 hours at room temperature. After that, the electrode was washed with PBS 1X solution to remove unbound molecules.

During the incubation of anti-BSA, the NHS ester groups covalently coupled with the amine group (NH_2) of anti-BSA, forming stable amide bonds. In order to prevent the nonspecific bonds between antigens and residual ester groups, 1 µM biotin solution was used to block the electrode surface. Finally, 5 µl of BSA-FITC 5 µM protein solution was dripped onto the gold electrode surface to bind to anti-BSA specifically. After each step in the process, the electrode was gently washed with PBS 1X solution to remove unbound biomolecules. The incubation process of BSA-FITC was carried out for 2 hours at 4 ^{o}C and under low light conditions.

Various protein concentrations were prepared by dissolving the proteins in PBS 1X solution. BSA-FITC molecules were captured on the electrode surface through the specific bond between anti-BSA and BSA, while unbound molecules were removed using PBS 1X solution. There were no non-specific interactions between the self-assembled monolayer (SAM) and the target (BSA) because several controls were implemented in the experimental design. Firstly, rigorous washing steps were employed after each stage of the SAM and BSA interaction. This ensured the removal of any weakly bound molecules, minimizing non-specific interactions. Secondly, blank experiments were conducted where the SAM was exposed to various proteins other than BSA, and the response was monitored. The consistent lack of response in these cases further supports the specificity of the BSA interaction.

To confirm the specificity of the immunosensor, experiments were performed involving successive additions of BSA-FITC directly onto the surface without the presence of antibodies (Gold/11-MUA). This approach was taken to assess any non-specific interactions of the fabricated immunosensor. The absence of significant signal change in these experiments indicates the high specificity of the immunosensor for BSA-FITC.

Experiments were also conducted similarly on the sputtered gold electrode created by sputtering titanium and gold on a glass slide with a gold layer thickness of 20 nm. Before the surface modification, a standard procedure was applied to clean the sputtered gold electrode on the glass slides. The gold electrode was immersed in acetone, IPA, and subjected to ultrasonic shaking for approximately 5 minutes, followed by rinsing with DI water and drying with nitrogen airflow. Acetone and IPA are strong cleaning

agents combined with ultrasonic vibration to completely remove dirt on the electrode surface. Since acetone evaporated quickly, the electrode was promptly transferred from the acetone beaker to the IPA beaker to prevent acetone evaporation, which could lead to a dust layer on the electrode surface. After cleaning, the electrodes were stored at room temperature.

3.4 Carbon electrode surface functionalization process

As mentioned above, there were three components in the screen-printed carbon electrode, including working, counter and reference electrodes. The working and counter electrodes were carbon, while the reference electrode was Ag/AgCl. Before being modified, The electrode was immersed in isopropyl IPA and sonicated for five minutes to clean the electrode surface. The electrode was rinsed with DI water and dried with nitrogen. The electrode was stored in an Eppendorf tube to prevent dust formation until functionalization.

The modified process included the formation of a conducting polymer layer on the carbon electrode (CE) with aniline, gold nanoparticle coating, the formation of a self-assembled monolayer using 11-MUA acid, the carboxyl group activation, and protein immobilization as shown in Figure 3.3. The electrode was subjected to electrolysis using cyclic voltammetry in 0.1 M aniline and 0.5 M H_2SO_4 to form a polyaniline film on the surface. The applied voltage ranged from -0.2 V to 1.0 V with a scan rate of 50 mV/s for 10 cycles. Electrochemical deposition was used to reduce gold nanoparticles onto the electrode surface under an applied potential. This method facilitated precise control over the size, shape, and density of AuNPs by adjusting the potential, deposition time, and electrolyte composition. The electrode was electrolyzed in 0.2 mM $HAuCl_4$ and 0.5 M H_2SO_4. The applied voltage ranged from -0.4 V to 1.2 V at a scan rate of 50 mV/s for 20 cycles.

The following steps involved the functionalization of gold nanoparticles to enable protein immobilization. The 11-MUA solution was prepared in ethanol, while

EDC/NHS and BSA solutions were prepared in PBS 1X solution. The electrode was immersed in a 5 mM 11-MUA solution for 24 hours to create a SAM layer on the gold nanoparticle surface. SAM is a layer with a thickness of a few nanometers. In 11-MUA, the head contains a thiol group (S-H), allowing the formation of stable bonds on the gold nanoparticle surface. Next, the electrode was gently washed with ethanol to remove unbound molecules.

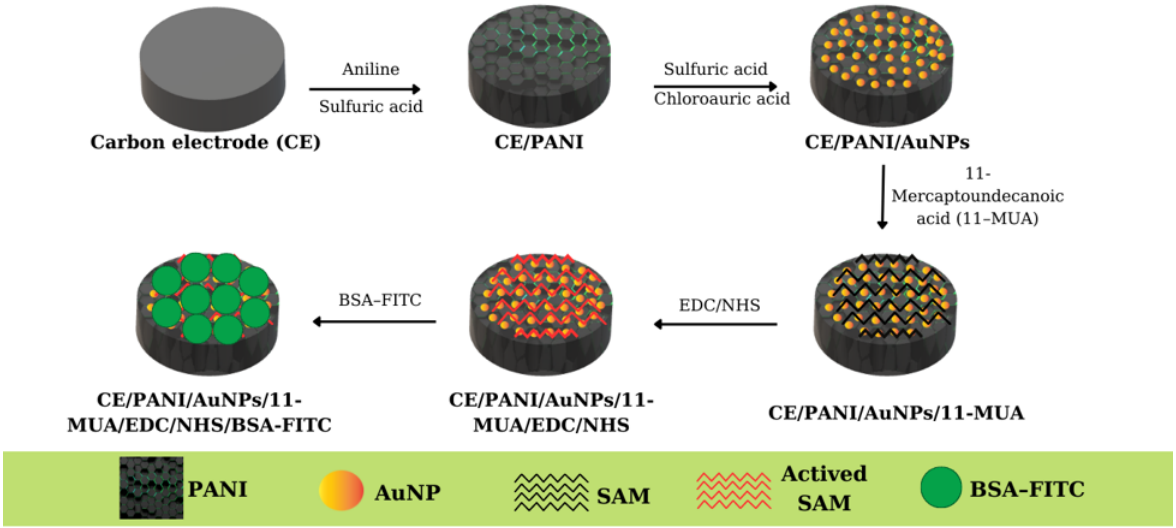

Figure 3.3: Carbon electrode functionalization using aniline and gold nanoparticles. Definitions: PANI: polyaniline; SAM: self-assembled monolayer; EDC: N-(3-dimethylaminopropyl)-N′-ethyl carbodiimide hydrochloride; NHS: N-hydroxysuccinimide; BSA−FITC: bovine serum albumin–fluorescein isothiocyanate conjugate

The electrode was subsequently incubated with the EDC and NHS solution for 30 minutes to activate the carboxyl (-COOH) groups and form ester functionalities. These readily bind to the amine groups (NH_2) of antibodies and antigens. In the final step, the electrode was incubated with 5 µM BSA-FITC for 2 hours at 4 ^{o}C. During the incubation, BSA was captured through the bonds between the amine functionalities of BSA-FITC and ester groups on the electrode. After each step, the electrode was gently washed with PBS 1X.

3.5 Results and discussion for gold electrodes

3.5.1 Results of specific binding performance between different electrodes and thiols

Both types of gold electrodes were functionalized by the proposed modification procedure, as mentioned above. The incubation time for 11-MUA and BSA-FITC protein solution concentrations were 24 hours and 5 µM, respectively.

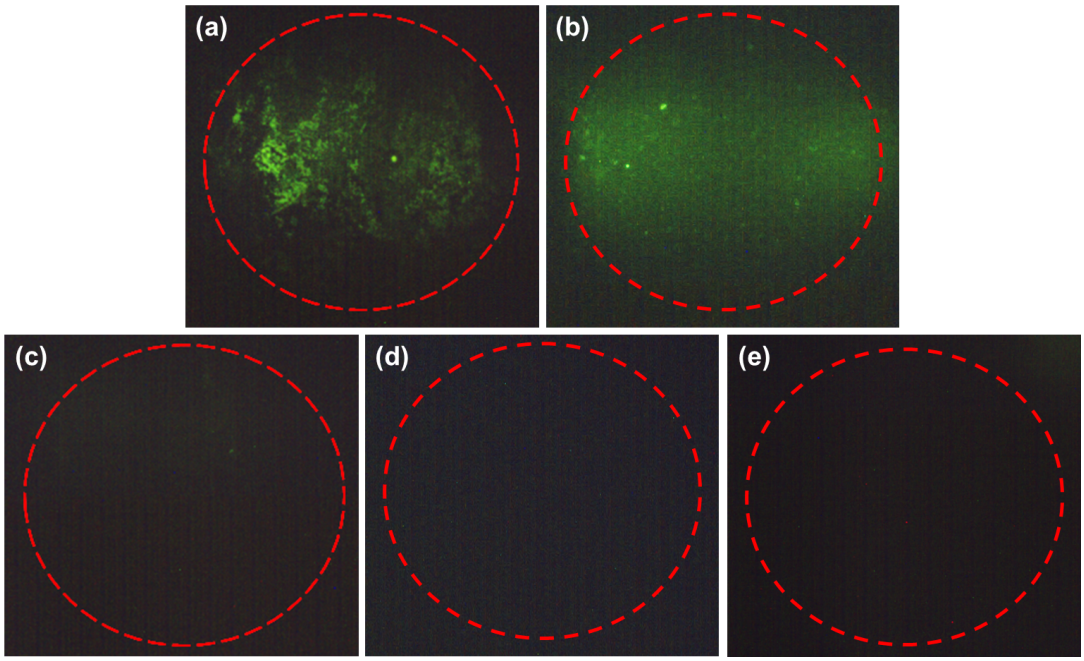

Figure 3.4: Experimental results demonstrating the proposed gold surface functionalization procedure on various electrodes at a BSA-FITC concentration of 5 µM; (a) The sputtered gold electrode; (b) The gold screen-printed electrode; (c) Control result on the sputtered gold electrode without the step of 11-MUA incubation; (d) Control result on the screen-printed gold electrode without the step of 11-MUA incubation; (e) Control result on the screen-printed gold electrode without the steps of the carboxyl activation and anti-BSA incubation

Figure 3.4 shows the fluorescence image of the different gold electrodes functionalized with BSA protein following the proposed procedure. The fluorescence signal

observed in Figures 3.4 (a) and (b) confirm the presence of BSA-FITC protein immobilized on the electrode surface. In other words, BSA-FITC protein was specifically bound to anti-BSA immobilized on both the sputtered and gold screen-printed electrodes. In contrast, the fluorescence signal did not appear on the control electrodes skipped the step of 11-MUA incubation, as shown in Figures 3.4 (c) and (d). BSA-FITC proteins were not successfully immobilized on the control electrodes after cleaning. Similar results were also observed on the other control electrodes that skipped the steps of EDC/NHS and anti-BSA incubation, as shown in Figure 3.4 (e). The electrode surface only exhibits a background signal level, confirming that no protein was retained. In other words, there was no non-specific interaction between BSA-FITC and the carboxyl group of 11-MUA.

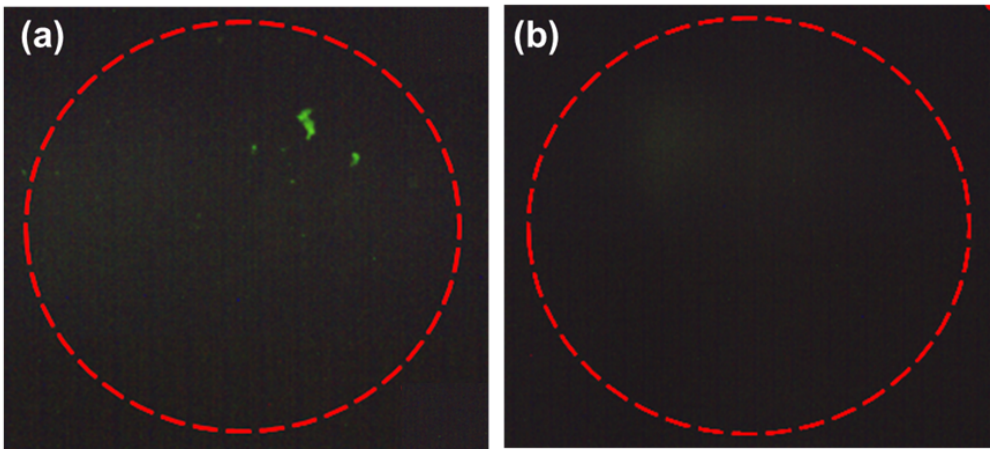

Figure 3.5: (a) The experiment result with HS-PEG7500-COOH functionalization on the sputtered gold electrode; (b) Control result of HS-PEG7500-COOH without the step of HS-PEG7500-COOH incubation on the sputtered gold electrode

Additionally, the experiments were conducted using HS-PEG7500-COOH, another type of SAM used in the electrode surface functionalization process, as shown in Figures 3.5 (a) and (b). The results show that a small amount of protein remained on the electrode surface, while no protein appeared on the control electrode. Comparatively, 11-MUA exhibited a significantly better effect than HS-PEG7500-COOH, which can be attributed to the fact that the structure of HS-PEG7500-COOH is much longer than that of 11-MUA, making it more challenging for HS-PEG7500-COOH to directly

immobilize on the electrode. Many carboxyl radicals may not be favorably positioned to bind with proteins.

3.5.2 Investigation results of 11-Mercaptoundecanoic acid incubation time

The influence of 11-MUA incubation time on performance was investigated to determine the optimal value. The experimental procedure was performed on both types of gold electrodes as described above, with the BSA-FITC concentration of 5 µM. Four 11-MUA incubation times were implemented: 16, 24, 48, and 60 hours, all conducted at room temperature. The experimental results on both types of gold electrodes indicated protein retention in all four cases, but the performance varied among the electrodes. The fluorescence intensity increased significantly when the 11-MUA incubation time was extended from 16 to 24 hours for both electrode types, as shown in Figure 3.6.

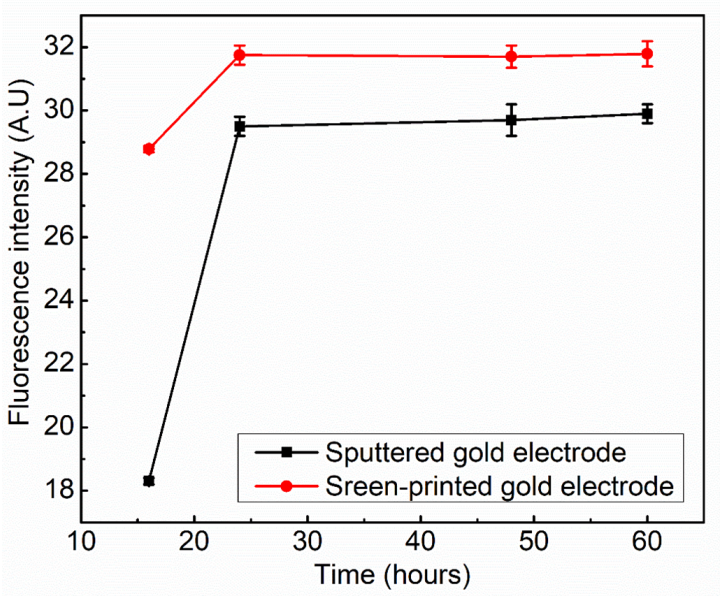

Figure 3.6: Investigation results of 11-MUA incubation time on the sputtered gold electrode and the screen-printed gold electrode using the proposed gold surface functionalization procedure with a BSA-FITC concentration of 5 µM

The fluorescence intensity remained stable between 24 and 60 hours of 11-MUA incubation. This can be explained by the significant influence of 11-MUA incubation

time on forming the SAM layer. Prolonger incubation time enhances the durability of the bond between the thiol group and the gold electrode surface, facilitating the increase in carboxyl radicals for protein binding. The amount of protein retained on the electrode surface increased gradually as the incubation time approached the limit point.

3.5.3 Investigation results of BSA protein concentration

The concentration of BSA-FITC protein was also investigated to determine the optimal value. The experiments were performed according to the proposed functionality process with five different BSA protein concentrations, including 0.5 µM, 1 µM, 5 µM, 20 µM, and 50 µM.

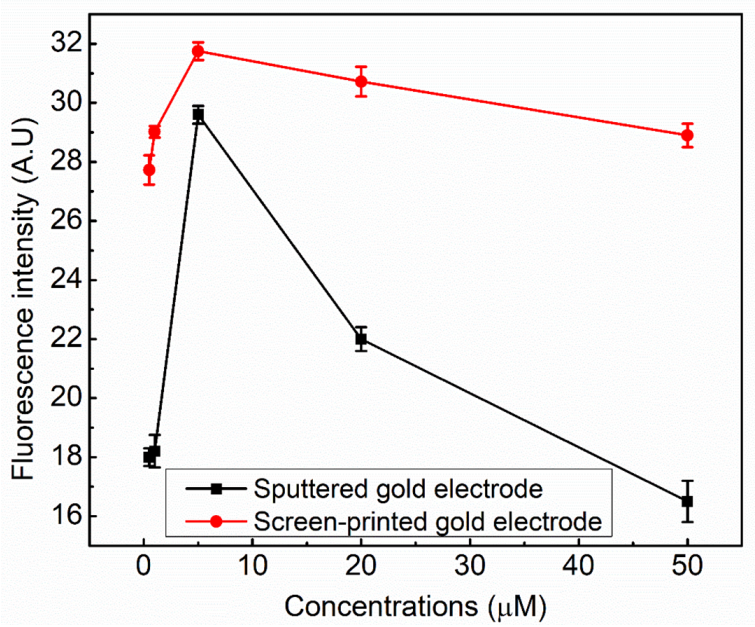

Figure 3.7: Investigation results of various BSA protein concentrations on the sputtered gold electrode and the screen-printed gold electrode using the proposed gold surface functionalization procedure, with a 24-hour 11-MUA incubation time.

The electrodes were incubated in a 5 mM 11-MUA solution for 24 hours. The results showed that proteins were retained at the concentrations of 0.5 µM, 1 µM, 20 µM, and 50 µM with low performance, while a large amount of protein was retained at the concentration of 5 µM, resulting in the highest fluorescence intensity (Figure 3.7). This

indicates that high protein concentrations during incubation lead to worse performance in capturing the target protein.

3.5.4 Investigation results of electrode surface using Raman spectroscopy measurements

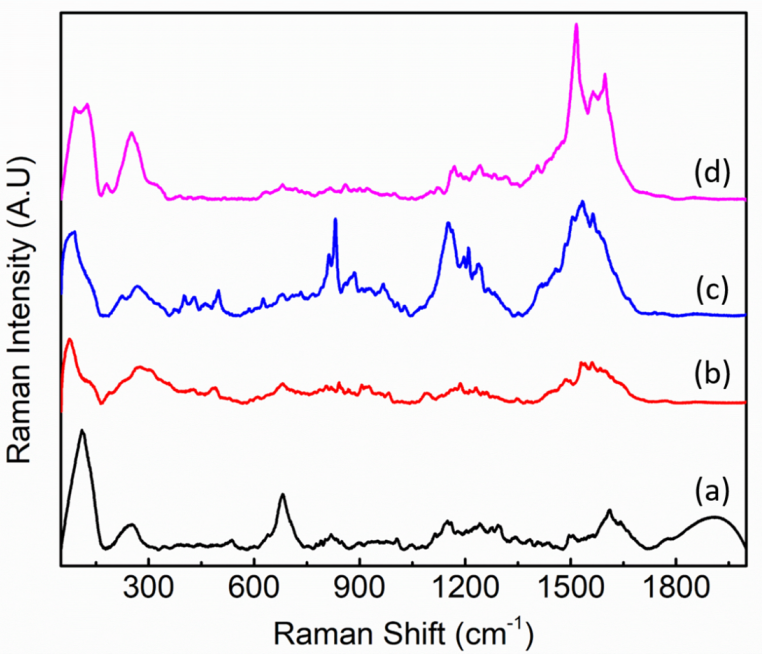

Figure 3.8: Raman spectra corresponding to different stages of the proposed gold surface functionality process on the screen-printed gold electrode, with a 24-hour incubation time of 11-MUA and a BSA-FITC concentration of 5 µM; (a) Bare gold electrode (Au); (b) 11-MUA-functionalized gold electrode (11-MUA/Au; (c) Anti-BSA/11-MUA-functionalized gold electrode (Anti-BSA/11-MUA/Au); (d) BSA/Anti-BSA/11-MUA-functionalized gold electrode (BSA/Anti-BSA/11-MUA/Au)

To further validate the performance of the proposed process, Raman spectroscopy measurements were conducted at each step of the gold electrode surface functionality on the screen-printed gold electrode. The results showed the changes in the Raman signal after each step. The bare electrode exhibited five peaks in the Raman signal

(Figure 3.8 (a)), while the 11-MUA/Au electrode displayed only two low peaks at the Raman shift signals of 137 cm-1 and 156 cm-1 (Figure 3.8 (b)).

After incubation with anti-BSA, two new peaks emerged at the Raman shift signals of 885 cm-1 and 1151 cm-1 (Figure 3.8 (c)). Finally, these two peaks disappeared during the BSA incubation step (Figure 3.8 (d)). These changes confirmed the success of each step in the gold electrode functionality process.

3.5.5 Investigation results using electrical measurements

The experiments were conducted on the screen-printed gold electrode for the electrical measurement method. The electrode structure included a working electrode (gold electrode), along with two other carbon and Ag/AgCl electrodes, referred to as counter and reference electrodes, respectively.

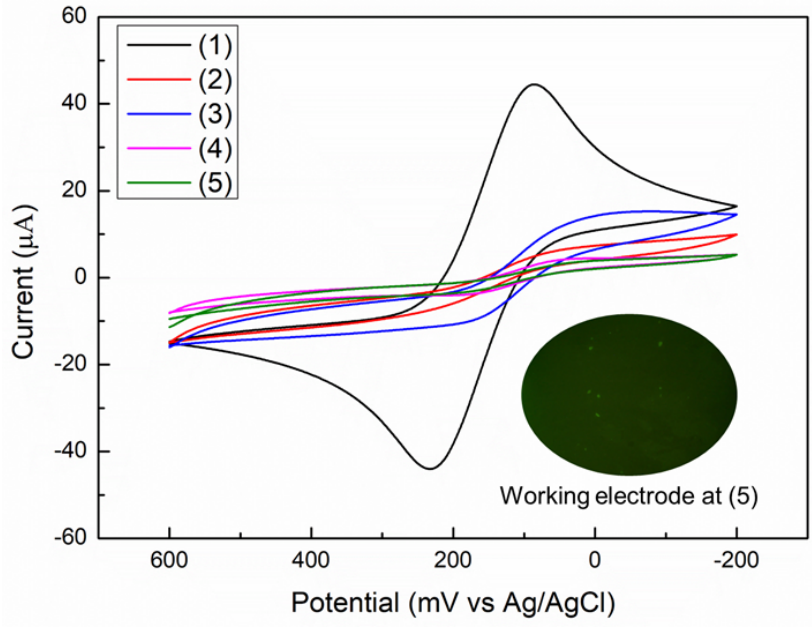

Figure 3.9: The change of CV signal after each step of gold electrode surface functionalization process; (1) Bare (Au); (2) 11-MUA/Au; (3) EDC/NHS/11-MUA/Au; (4) Anti-BSA/EDC/NHS/11-MUA/Au; (5) BSA/Anti-BSA/EDC/NHS/11-MUA/Au. The inset shows the appearance of a fluorescent green BSA-FITC signal on the working electrode

This electrode structure allowed for easy evaluation of the proposed process's per-

formance using electrical methods, such as EIS and CV. A standard redox solution containing 5 mM Fe(II)/Fe(III) and 0.1 mM KCl (ferry/ferrocyanide redox) was used in these two measurements. The CV measurement parameters were configured with a starting voltage of 600 mV, an ending voltage of -200 mV, and a scan rate of 50 mV/s.

The results indicate the appearance of a fluorescent green BSA-FITC signal on the working electrode, and significant changes in the CV signal were observed after each step of the process, as illustrated in Figure 3.9. Specifically, the amplitude of the reduction peak decreased strongly from 50.4 µA to 6.89 µA after the step of 11-MUA incubation. This result shows that a self-assembled monolayer was formed on the electrode surface, prohibiting the transfer of electrons to reduce Fe^{3+} to Fe^{2+}. Subsequently, the amplitude of the reduction peak further decreased to 3.17 µA, confirming the presence of BSA-FITC protein on the electrode surface. As a consequence, both fluorescence and CV measurements demonstrated the success of the proposed process. BSA proteins are specifically bound to anti-BSA and kept on the gold electrode surface.

For the EIS measurement, some parameters were set up, including the frequency ranging from 0.1 Hz to 200 kHz, and the applied voltage of 10 mV. Besides, the Randles circuit model was used for EIS measurements to fit the impedance data, with R_s representing the dynamic solution resistance, R_{ct} representing the charge transfer resistance of the immobilized recognition layer, C_{dl} indicating the capacitance measured between the gold electrode and the electrolyte solution on a double-layer basis. Here, the charge transfer resistance is a crucial parameter reflecting the electrical resistance linked to the transfer of charge at the electrode-electrolyte interface. This interface plays a pivotal role in electrochemical immunosensors, where the binding of biomolecules, such as antibodies and antigens, induces alterations in charge transfer kinetics. The results show that R_{ct} changed significantly after each step of the proposed process, as shown in Figure 3.10. However, the trend is opposite to the amplitude of the reduction peak observed in the CV measurements. R_{ct} increased slightly from 32.92 kΩ to 37.74 kΩ after the electrode was incubated with the 11-MUA solution. Then, the charge transfer resistance increased considerably to 64.01 k kΩ and 206.9 kΩ at the steps of anti-BSA and BSA incubation, respectively. The results reaffirmed the success of the gold elec-

trode surface functionalization process. The formation of anti-BSA and BSA layers on the electrode surface leads to the increase of the charge transfer resistance.

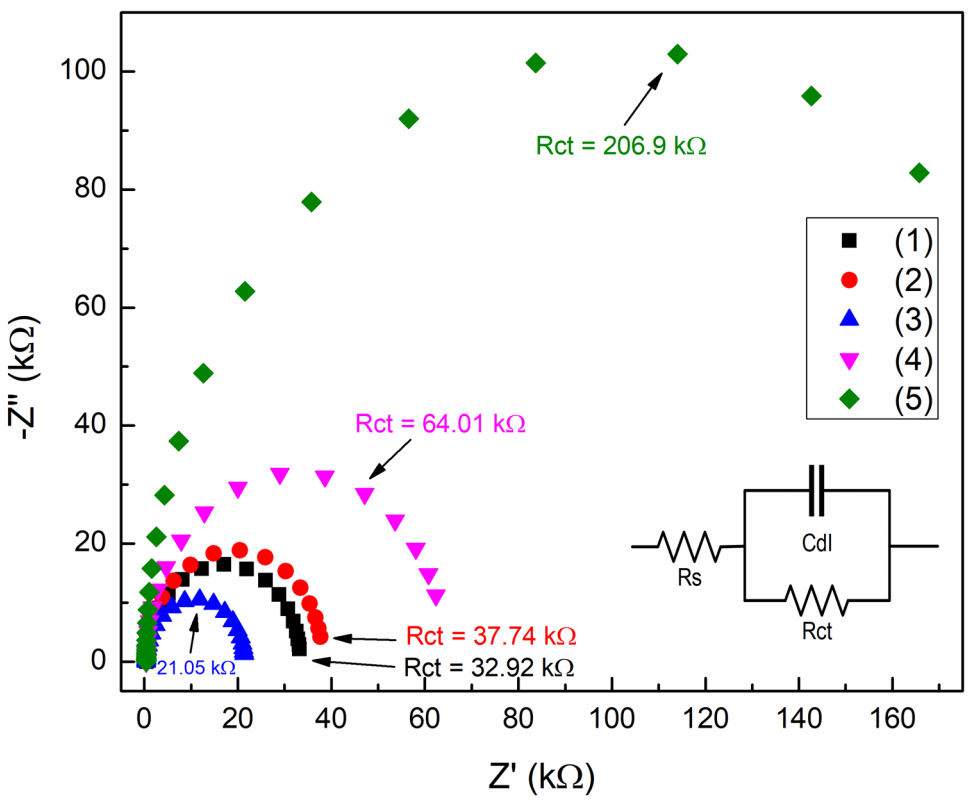

Figure 3.10: The change of EIS signal after each step of the gold electrode surface functionalization process; (1) Bare (Au); (2) 11-MUA/Au; (3) EDC/NHS/11-MUA/Au; (4) Anti-BSA/EDC/NHS/11-MUA/Au; (5) BSA/Anti-BSA/EDC/NHS/11-MUA/Au

By contrast, BSA-FITC proteins were not kept on the control electrode surface that has not undergone incubation with 11-MUA. Only a dark color was observed on the working electrode surface, indicating no BSA-FITC proteins were captured (the inset image in Figure 3.11 (a)). CV signals were almost unchanged after each process step, as shown in 3.11 (a). Similarly, the charge transfer resistance of the EIS signal exhibited minimal change, as depicted in 3.11 (b). The absence of signal change indicates that no layer was formed on the gold electrode surface. These results follow the theoretical predictions that a self-assembled monolayer was not formed, resulting in the absence of active carboxyl groups capable of binding with Anti-BSA.

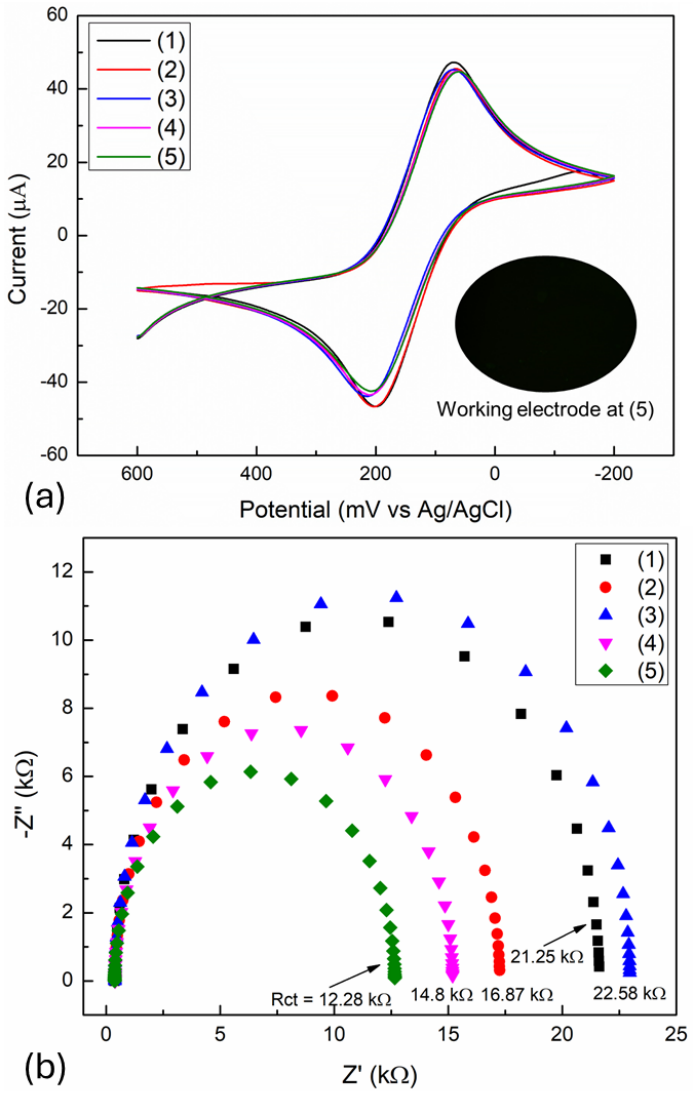

Figure 3.11: The change of CV (a) and EIS (b) signals on the control electrode that has not undergone incubation with 11-MUA; (1) Bare (Au); (2) EDC/NHS/Au; (3) Anti-BSA/EDC/NHS/Au; (4) Biotin/Anti-BSA/EDC/NHS/Au; (5) BSA/Biotin/Anti-BSA/EDC/NHS/Au. The inset shows only a dark color was observed on the working electrode surface, indicating no BSA-FITC proteins were captured

Five different BSA protein concentrations were investigated to determine the relationship between the BSA concentration and the amplitude of the reduction peak. For the CV measurement, the experimental results show that the amplitude of the reduction peak decreased gradually when the BSA concentration increased, as shown

in Figure 3.12 (a). The amplitude of the reduction peak decreased from 3.41 µA to 2.7 µA as the BSA concentration increased from 0.1 µM to 5 µM.

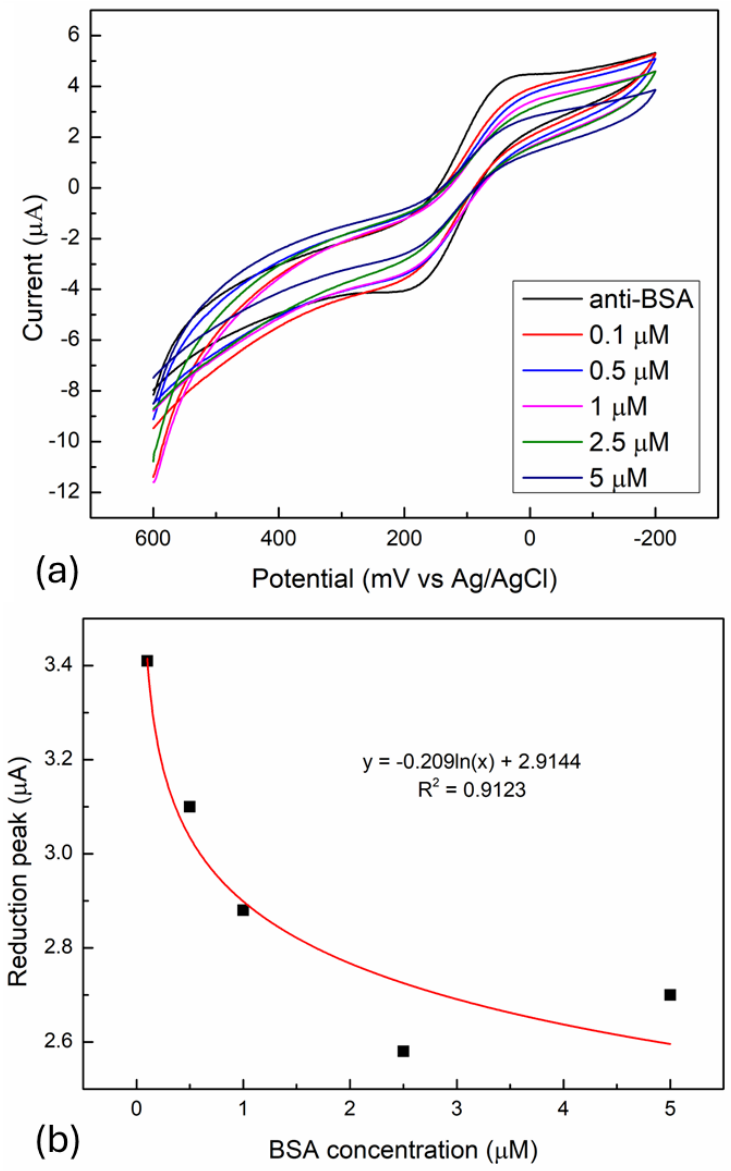

Figure 3.12: (a) The change of CV signals at the different BSA concentrations; (b) The relationship between the amplitude of reduction peak and BSA concentration

The result can be explained that higher protein concentrations lead to the formation of a thicker protein layer, which hinders the exchange of electrons between the electrode and the redox solution. This results in a decrease in the redox current. The formula expressed the relationship between the amplitude of the reduction peak and

BSA concentration: $reductionpeak = -0.209ln[BSA] + 2.9144 (R2 = 0.9123)$, as shown in Figure 3.12 (b). As can be seen, the BSA concentration can be quantified based on the amplitude value of the reduction peak from CV signals.

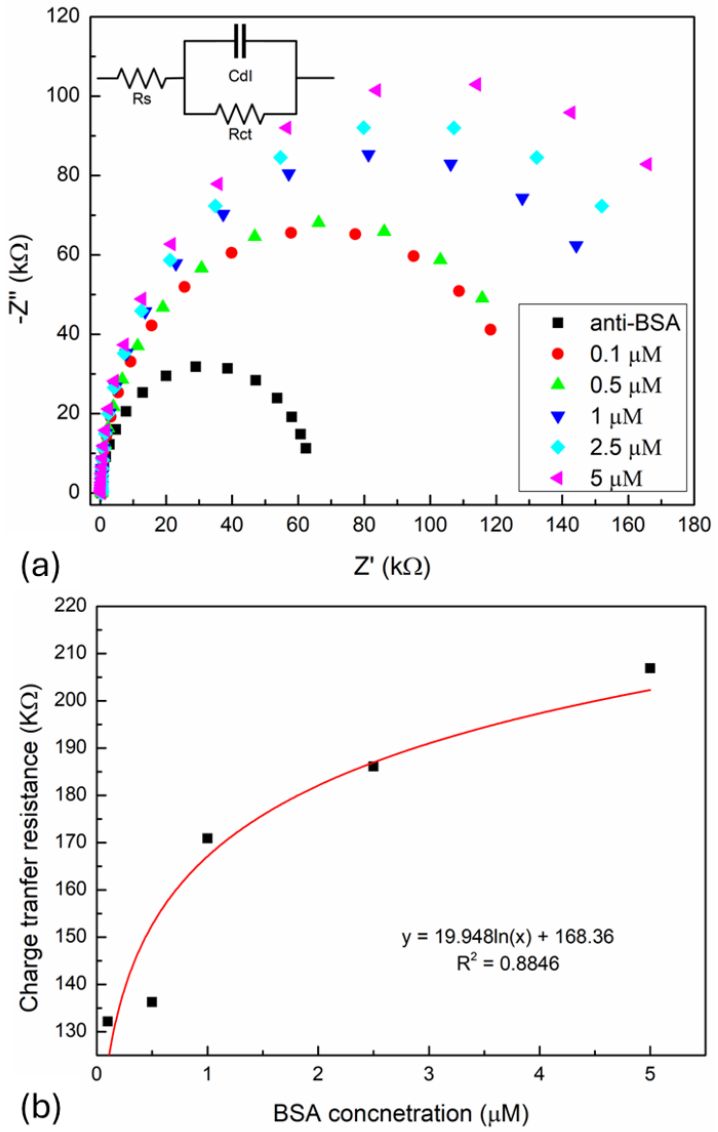

Figure 3.13: (a) The change of EIS signals at the different BSA concentrations; (b) The relationship between the change of the charge transfer resistance (ΔR_{ct}) and BSA concentration

For the EIS measurement, the results show that the charge transfer resistance was proportional to the BSA concentration. When the BSA concentration increased from 0.1 μM to 5 μM, the charge transfer resistance also rose from 132.2 kΩ to 206.9 kΩ,

respectively, as shown in Figure 3.13 (a). At first, there was a slight increase in the charge transfer resistance at the BSA concentration of 0.5 µM, from 68.19 kΩ to 72.29 kΩ. Subsequently, the charge transfer resistance exhibited a sharp increase at higher concentrations. These results indicate that more proteins specifically bond and are retained on the electrode at high BSA protein concentrations, leading to the formation of a thicker protein layer on the electrode. This hindered the exchange of electrons between the electrode and the solution, significantly affecting the charge transfer resistance. The relationship between the BSA protein concentration and the charge transfer resistance was fitted as a logarithm function $Rct = 19.948[BSA] + 168.36(R^2 = 0.8846)$, as depicted in Figure 3.13 (b). Therefore, the BSA concentration can be quantified based on the change in charge transfer resistance obtained from the EIS measurement.

3.5.6 Performance comparison results between sensors based on 2-electrode and 3-electrode configurations

The 2-electrode and 3-electrode configuration-based biosensors are modeled into equivalent circuits based on the Randles circuit, as shown in Figure 3.14. The model of the 2-electrode configuration-based biosensor is depicted in Figure 3.14 (a), comprising a series combination of the Randles circuit. The impedance is measured between the working and counter electrodes over a wide range of frequencies to analyze the impedance changes associated with the modification of the electrode surface. The biochemical event such as antigen-antibody interactions occurring on the surface of the electrodes causes the impedance change.

The contact of the solution with the electrode surface results in the formation of a double-layer capacitance (C_{dl}). Furthermore, a small leakage current could be observed between the solution and electrodes, contributing to the creation of charge transfer resistance (R_{ct}). Hence, the surface impedance comprises C_{dl} and R_{ct} connected in parallel. The model includes two electrodes, resulting in two surface impedances connected in series through the solution resistance (R_S). In this model, the solution resistance has a negative effect, reducing the sensitivity of the biosensor. Because R_S is much larger than the surface impedance, there is only a small change in the total impedance

when the electrode surface is immobilized with the analyte. Cause of that reason, the 3-electrode configuration-based biosensor is studied to enhance the sensitivity.

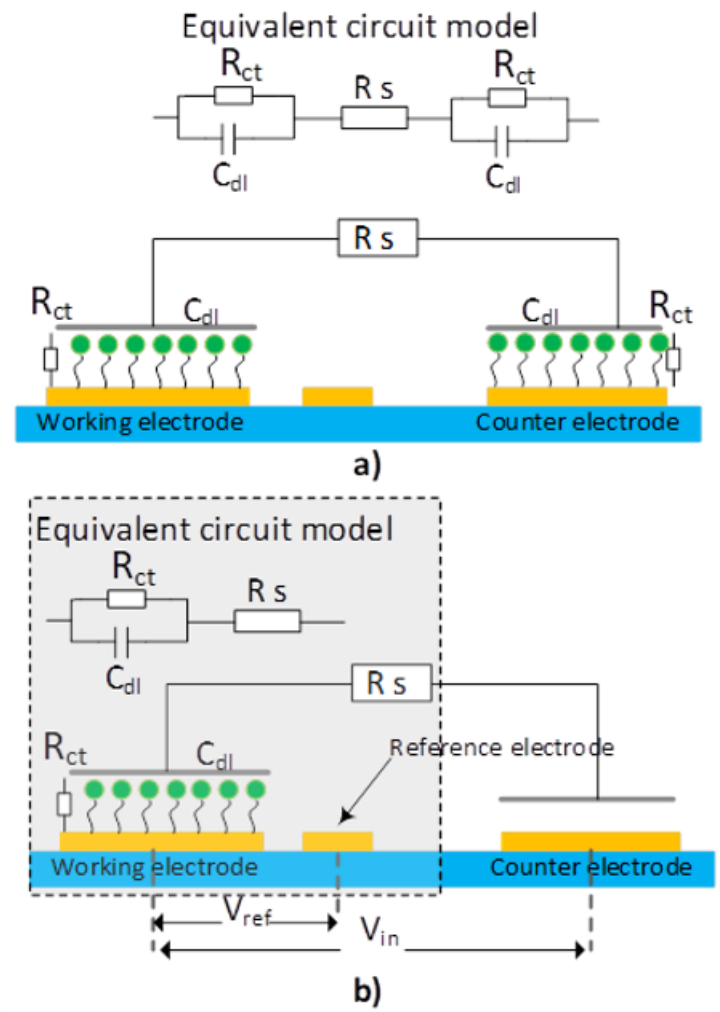

Figure 3.14: The model of electrode in the solution; (a) 2-electrode configuration; (b) 3-electrode configuration

For the 3-electrode configuration-based biosensor, a reference electrode with a stable and well-known electrode potential is added to maintain a constant voltage (V_{ref}) between the reference and working electrodes, as shown in Figure 3.14 (b). The current flowing to the working electrode is measured to determine the surface impedance accurately. The equivalent circuit model of the sensor is illustrated in Figure 3.14 (b). As can be seen, the solution resistance (R_S) is very small because the reference electrode is in close proximity to the working electrode. As a result, the measured impedance pre-

dominantly comprises the surface impedance component, contributing to the enhanced sensitivity of the sensor. Through the model, the total impedance (Z) is calculated by Equation 3.1, where Z is the sum of surface resistance ($Z_{surface}$) and solution resistance (R_S) and it approximates the surface impedance since the solution impedance is negligible in this case. The surface impedance is determined based on the impedance of the double-layer capacitance ($Z_{C_{dl}}$) and the charge transfer resistance R_{ct}, as shown in Equation 3.2. The impedance of the double-layer capacitance is calculated by Equation 3.3, where ω is the angular frequency of the exciting signal to the biosensor.

$$Z = Z_{surface} + R_S \approx Z_{surface} \tag{3.1}$$

$$Z_{surface} = \sqrt{Z_{C_{dl}}^2 + R_{ct}^2} \tag{3.2}$$

$$Z_{C_{dl}} = \frac{1}{j\omega C_{dl}} \tag{3.3}$$

The gold electrode surface functionalization process is similar to the section mentioned above and performed on the screen-printed gold electrode. There were five different BSA-FITC protein concentrations used to investigate the performance of both types of the sensor, including 0.1 µM, 0.5 µM, 1 µM, 2.5 µM and 5 µM. The measurements were conducted on the same modified electrodes, and a detailed comparison will be presented. While the performance of the 2-electrode configuration-based biosensor was evaluated based on the change of impedance at a specific frequency range, the 3-electrode configuration-based-biosensor employed the Randle model with fitting curves to estimate alterations in the surface impedance. The electrode was immersed in a solution containing 5 mM Fe(II)/Fe(III) and 0.1 mM KCl to perform the impedance measurements. In the case of the 2-electrode configuration, working and counter electrodes were employed, and the reference electrode was not involved during the measurement.

For the 2-electrode configuration-based biosensor, Figure 3.15 shows the impedance spectroscopy results corresponding to the different concentrations of BSA protein binding on the gold electrode surface. The measurement parameters were configured with an excitation signal magnitude of 50 mV and a frequency range spanning from 10 kHz to 1 MHz.

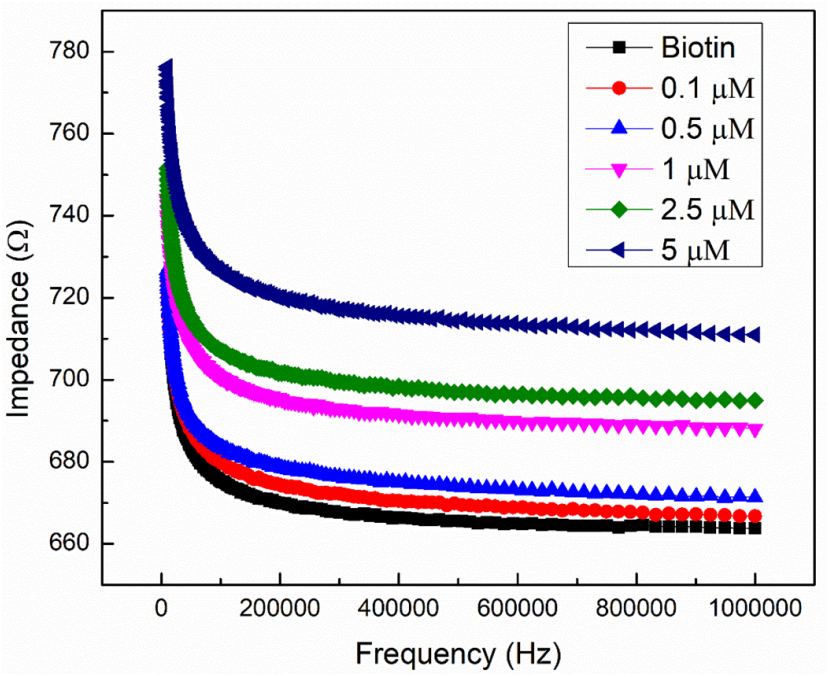

Figure 3.15: Bode plots corresponding to the change of protein concentration from 0.1 µM to 5 µM BSA-FITC binding on the gold electrode

As can be seen, the impedance at the step of biotin incubation shows the lowest value, ranging from 730 to 660 Ω. As the concentration of BSA protein increased, a corresponding rise in impedance was observed. At the BSA concentration of 5 µM, the impedance reached to 780 Ω at 10 kHz and dropped to below 720 Ω at 1 MHz. At lower BSA concentrations, the impedance has been observed to decrease with a high slope. These results can be explained that in the 2-electrode model, total impedance was contributed by surface impedance ($Z_{surface}$) and solution resistance (R_s) with the solution resistance being constant. At the low-frequency range, the double-layer capacitance was high, resulting in an increase in the surface impedance. At the high-frequency range, the surface impedance reduced, and the total impedance was larger than the surface impedance, resulting in a small slope of the impedance change.

The total impedance shows an increase corresponding to the rising protein concentration. At a frequency of 1 MHz, the total impedance is observed to increase from below 670 Ω to 720 Ω with the rising BSA protein concentration from 0.1 to 5 µM. The total impedance increased across the entire frequency range from 10 kHz to 1

MHz, correlating with the rising protein concentration binding on the electrode. Figure 3.16 illustrates the change percentage of total impedance before and after BSA protein binding at various concentrations.

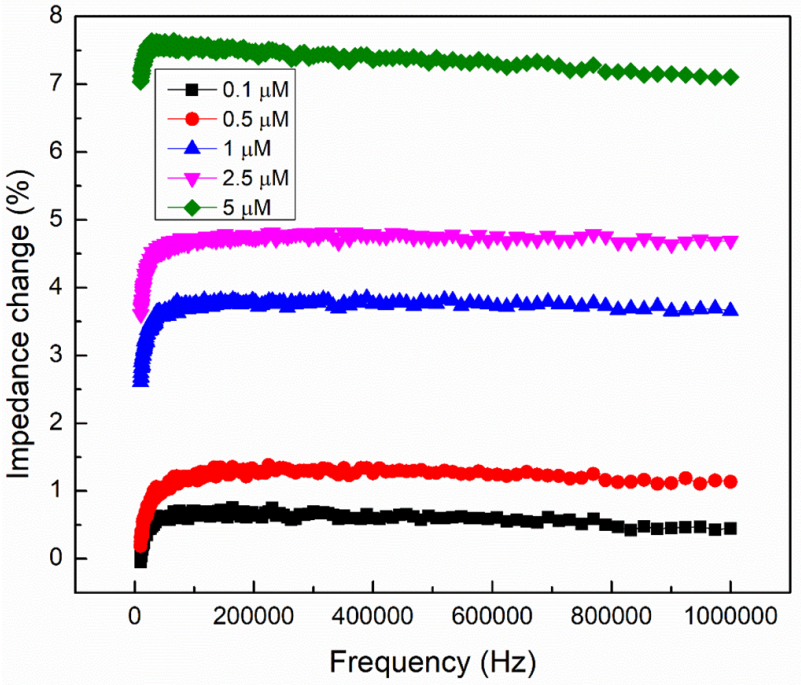

Figure 3.16: The change percentage of total impedance by the frequencies from 10 Hz to 1 MHz before and after BSA protein binding at various concentrations

The results indicate that the total impedance change remained relatively constant within the frequency range of 100 kHz to 1 MHz. It can be assumed that within this frequency range, the impedance was primarily affected by the resistance of the sensor surface, attributed to the interaction between the antibody and antigen. The binding of proteins to the gold electrode altered the surface geometry, leading to a change in the total impedance. Although the change percentage of total impedance was small, the protein concentration was clearly distinguished based on this change.

Figure 3.17 shows the impedance change percentage according to the different protein concentrations binding on the gold electrodes at the frequency of 300 kHz. For the fluorescence measurement, the results show fluorescence intensity was proportional to BSA protein concentration. The blue fluorescence was more obvious at high concentrations, indicating that more proteins were specifically bound to anti-BSA on the

electrode surface.

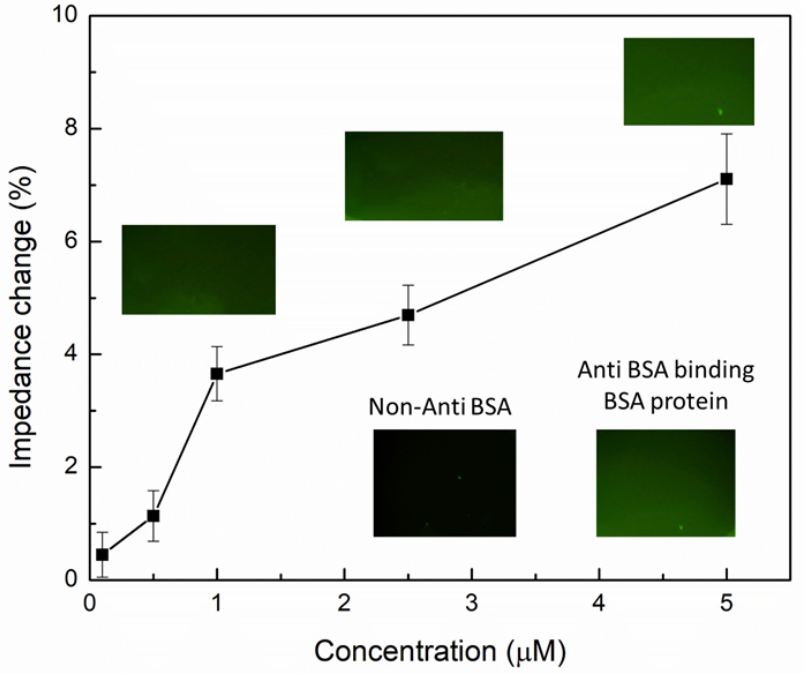

Figure 3.17: The relationship between the impedance changes percentage at the frequency of 300 kHz and different protein concentrations was confirmed by the fluorescent images of non-anti BSA binding and different concentrations of BSA binding

Furthermore, experiments were also performed on the control electrode skipped the step of anti-BSA incubation. In the final step, the electrode was incubated with 5 µM BSA-FITC solution. The fluorescent image results reveal only black color observed on the control electrode, in contrast to the clear fluorescent green results on the electrode with the complete procedure, as shown in Figure 3.17. The sensitivity of 2-electrode configuration-based sensor is around 12 Ω/µM or 1.4 %/µM.

For the 3-electrode configuration-based biosensor, the EIS measurement was conducted on the same electrode to evaluate the performance of the 3-electrode configuration-based biosensor. Due to the proximity of the reference electrode to the working electrode, the surface impedance can be accurately measured through the EIS measurement. The Randles circuit model was used fitted the impedance data of five protein concentrations, as shown in Figure 3.18. Similar to the 2-electrode configuration-based

sensor, the surface impedance was proportional to the protein concentration. The solution resistance is also much smaller than the surface impedance at the low-frequency range.

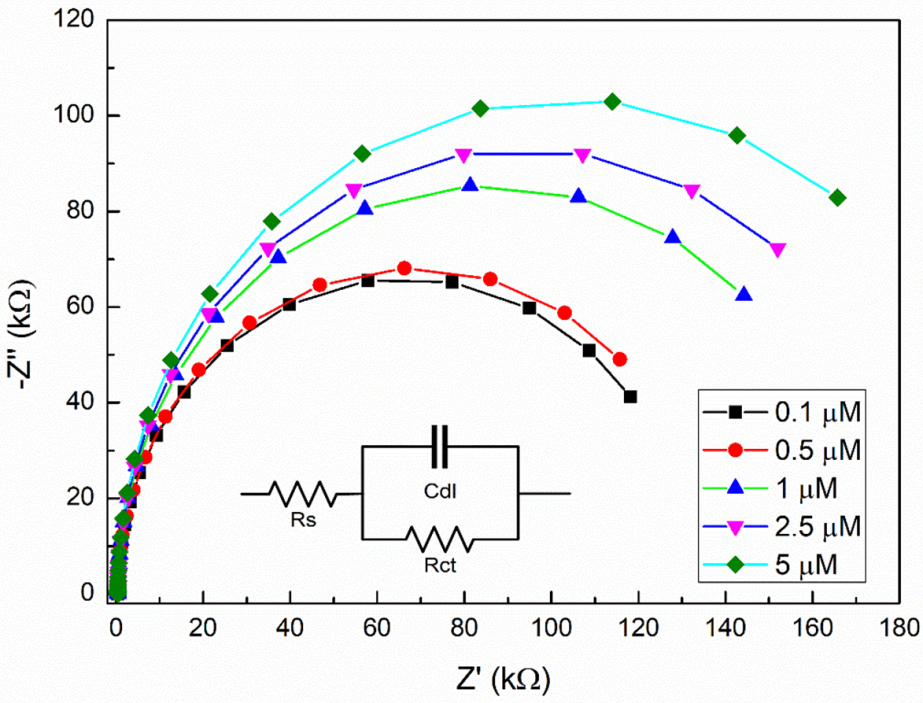

Figure 3.18: The Nyquist plot of different BSA concentrations, including 0.1 µM, 0.5 µM, 1 µM, 2.5 µM and 5 µM based on Randles circuit model

A PSTrace 5.9 software (PalmSens BV, 3995 GA Houten, Netherlands) was utilized to calculate Rct corresponding to various BSA concentrations based on the measured data. Figure 3.19 shows the relationship between the concentration of BSA binding on the electrodes and the change of Rct before and after protein binding. Rct before protein binding is estimated to be 75.4 kΩ. When the BSA concentration increased from 0.1 µM to 5 µM, the change in the charge transfer resistance became larger, from 13.22 kΩ to 20.69 kΩ. In the concentration range of 1 µM to 5 µM BSA, the sensor exhibited a sensitivity of approximately 7.2 kΩ/µM, corresponding to 7.5 %/µM within this measurement range.

As can be seen, the experimental results showed the performance of both 2-electrode and 3-electrode configuration-based sensors in protein detection. While the 2-electrode configuration-based sensor measured total impedance at a fixed frequency range to esti-

mate the concentration of protein binding on gold electrode, the 3-electrode configuration-based sensor utilized the EIS measurement and Randles circuit model to calculate Rct, revealing the concentration of BSA protein. Additionally, the results are also further confirmed through the fluorescence measurement. In the case of the 2-electrode configuration-based sensor, the observed increase in total impedance highlighted the sensor's capability in protein detection. The sensor demonstrated a sensitivity of 12 Ω/µM at a fixed frequency of 300 kHz. Due to the absence of a reference probe in the 2-electrode configuration, the detailed electrical characteristics of surface impedance could not be precisely investigated.

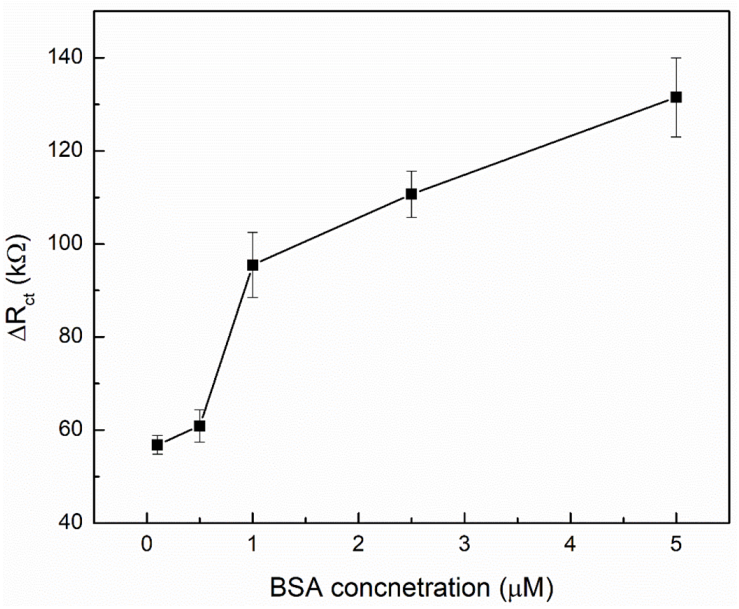

Figure 3.19: The relationship between BSA concentration binding on the electrodes and the change of the charge transfer resistance

To enhance the sensitivity of the 2-electrode configuration sensor based on non-faradaic method, Tanak et al. has used semiconductor materials as zinc oxide (ZnO) to transduce physicochemical changes with biomolecular binding in electrochemical biosensors [127]. Based on those approaches, the biosensor demonstrated the capability to detect C-reactive protein (CRP) with a molecular weight of 24 kD. The sensitivity is estimated, showing a roughly 22% increase in total impedance at 10 µg/ml (approximately 0.42 µM) in whole blood samples. Although this sensor shows high

sensitivity when incorporating a ZnO layer on the electrodes, the fabrication of the sensor becomes more intricate, demanding additional facilities. Based on our simple sensor structure, the sensitivity within the range below 1 µM (BSA protein with a molecular weight of 66.5 kD) demonstrates a 4 %/µM increase in total impedance. Through the non-faradaic method, protein detection can be achieved with varying impedance corresponding to different protein concentrations. With the proposed 3-electrode configuration-based sensor using the faradaic method, the sensitivity of the sensor in the range from 1 µM to 5 µM BSA is estimated to be 7.5 %/µM. Below 1 µM, the sensitivity is higher, with the Rct increasing by 79.5% after the binding of 0.5 µM BSA.

Despite the identified disadvantage, the 2-electrode configuration-based sensor can still be employed to detect and quantify the concentration of protein. In contrast, the 3-electrode configuration is commonly utilized in biosensor development, demonstrating its advantage of high sensitivity (7.2 kΩ/µM in this report). However, the challenge remains in minimizing the size of the 3-electrode sensor for integration into microfluidic channels. In some cases, the 2-electrode configuration is a good candidate for minimizing the size of the sensor. The advantages of simple structure and low cost are important factors that help the sensor become more potential for the immunosensor and lab-on-a-chip system development.

3.6 Results and discussion for carbon electrodes

3.6.1 Electro-polymerization of aniline on the screen-printed carbon electrode

CV technique was performed to electro-polymerize aniline on the working electrode. The cyclic voltammograms for the formation of polyaniline (PANI) film on the working electrode surface are shown in Figure 3.20 (a). The increased signal peaks at a repeated potential of 0.29 V indicate that PANI was continuously formed on the carbon electrode surface. Furthermore, the color of the working electrode was changed from black to blue

indicating the generation of a conducting emeraldine form of PANI. The relationship between the oxidation peak current and the number of cycles (times) is displayed in Figure 3.20 (b), represented by the equation:

$$peakcurrent = 0.7121 * times + 0.3253 (R^2 = 0.9439). \tag{3.4}$$

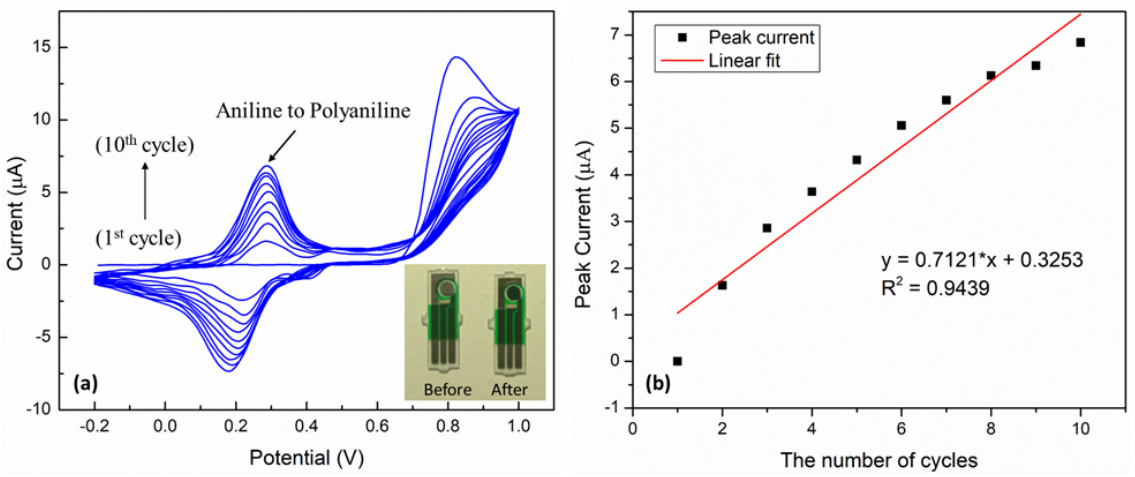

Figure 3.20: (a) Cyclic voltammograms for the electro-polymerization of the PANI film on the carbon electrode in 0.1 M aniline and 0.5 M H2SO4. The applied voltage ranged from -0.2 V to 1.0 V at a scan rate of 50 mV/s and 10 cycles. (b) Relationship between the peak current and the number of cycles

The electro-polymerization process of aniline was represented through Equations from 3.5 to 3.11. At first, aniline reacted with sulfuric acid to form ions in the solution:

$$C_6H_5NH_2 + H_2SO_4 \rightleftharpoons H_3O^+ + C_6H_5NH^{3+} + HSO4^- \tag{3.5}$$

Where, $C_6H_5NH_2$ is aniline. H_3O^+ is an oxonium ion, known as hydroni ions or hydrate proton. Oxonium ions are formed when a water molecule reacts with a hydronium ion or when an acid molecule combines with a water molecule. In this case, oxonium ions were generated when water molecules act on anilinium ion ($C_6H_5NH^{3+}$), a reaction product between aniline and sulfuric acid. These ions facilitate electrolysis by providing protons to anilinium and maintaining charge balance in the electrolyte solution.

At anode:

$$C_6H_5NH^{3+} \rightarrow [C_6H_4NH]^{\bullet} + H^+ + e^- \tag{3.6}$$

$$[C_6H_4NH]^{\bullet} + H^+ \rightarrow [C_6H_4NH]^{2+} \tag{3.7}$$

$$[C_6H_4NH]^{2+} + [C_6H_4NH]^{2+} \rightarrow (C_6H_4NH)_n + 2H^+ \tag{3.8}$$

Anilinium was converted into radical aniline ($[C_6H_4NH]^{\bullet}$) and released an electron. The radical aniline was an activated molecule with an unpaired electron on a carbon atom in the benzene ring. The dot symbol at the end of the molecular formula represents the removal of this electron from the parent aniline molecule. Then, the radical aniline combines with H^+ to make aniline cations and prepares for polyaniline formation. Finally, aniline cations combine to form polyaniline on the carbon electrode surface, as shown in Equation 3.8.

At cathode:

$$H_2SO_4 \rightarrow H^+ + HSO4^- \tag{3.9}$$

$$HSO4^- + 2H^+ + 2e^- \rightarrow SO_4^{2-} + 2H_2O \tag{3.10}$$

Sulfuric acid was electrolyzed into H^+ and $HSO_4^{\breve{}}$. Then, H^+ in the solution combined with $HSO_4^{\breve{}}$ to generate $SO_4^{2\breve{}}$ and water, as shown in Equation 3.10. The general reaction equation for the electro-polymerize of aniline to polyaniline in 0.5 M H_2SO_4 solution was shown in Equation 3.11. Aniline was oxidized to form polyaniline ($(C_6H_4NH)_n$), which n is the number of aniline molecules in the polymer chain. Water and sulfuric acid act as an electrolyte solution and provide protons to facilitate the electrolysis process.

$$2C_6H_5NH_2 + H_2SO_4 + 2H_2O \rightarrow (C_6H_4NH)_n + H_3O^+ + HSO4^- \tag{3.11}$$

3.6.2 Electro-deposition of gold nanoparticles on the electrode surface

Gold nanoparticles were deposited on the electrode surface by cyclic voltammetry in 0.2 mM $HAuCl_4$ and 0.5 M H_2SO_4. The cyclic voltammograms for the deposition of gold nanoparticles on the carbon electrode are shown in Figure 3.21. During the cathodic

half-cycle, Au^{3+} was reduced to Au on the PANI surface due to the application of a negative potential. Meanwhile, Au was oxidized to form Au^{3+} and gold oxide during the anodic half-cycle. The increasing amplitude of the cathodic peak shows that more Au atoms were produced. Subsequently, Au atoms nucleated into gold nanoparticles on the PANI surface.

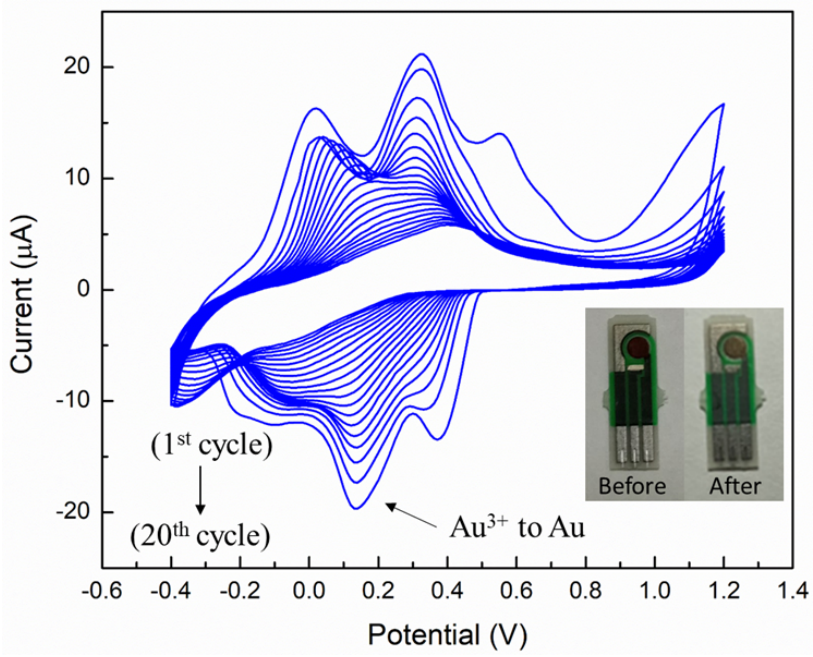

Figure 3.21: The cyclic voltammograms for the electro-deposition of gold nanoparticles on the carbon electrode by electrolyzing in a solution mixture of 0.2 mM $HAuCl_4$ and 0.5 M H_2SO_4 . The applied voltage ranged from -0.4 V to 1.2 V, the scan rate of 50 mV/s and 20 cycles

The color of the working electrode changed from blue to yellow, indicating the presence of gold nanoparticles. The surface coverage of gold nano-particles (Γ) on the PANI/CE electrode during the deposition was determined based on the charge (Q), the number of electrons transferred ($n = 3$) and the area of the electrode surface ($A = 0.026$ cm^2), as shown in Equation 3.12 with $F = 96{,}500$ C/mol [101].

$$\Gamma = \frac{Q}{nFA} \tag{3.12}$$

The quantity of gold on the PANI/CE electrode was determined by [129], as shown in Equation 3.13, with M equal to 196.97 g/mol. The total charge after 20 cycles was

determined using Dropview 200 software to be 2007.39 µC. Therefore, the mass of gold on the PANI/CE electrode was estimated to be 1.364 µg.

$$m = \frac{Q \times M}{n \times F} \tag{3.13}$$

3.6.3 Investigation results of electrode surface morphology

The electrode morphology was examined using scanning electron microscopy (SEM) as shown in Figure 3.22.

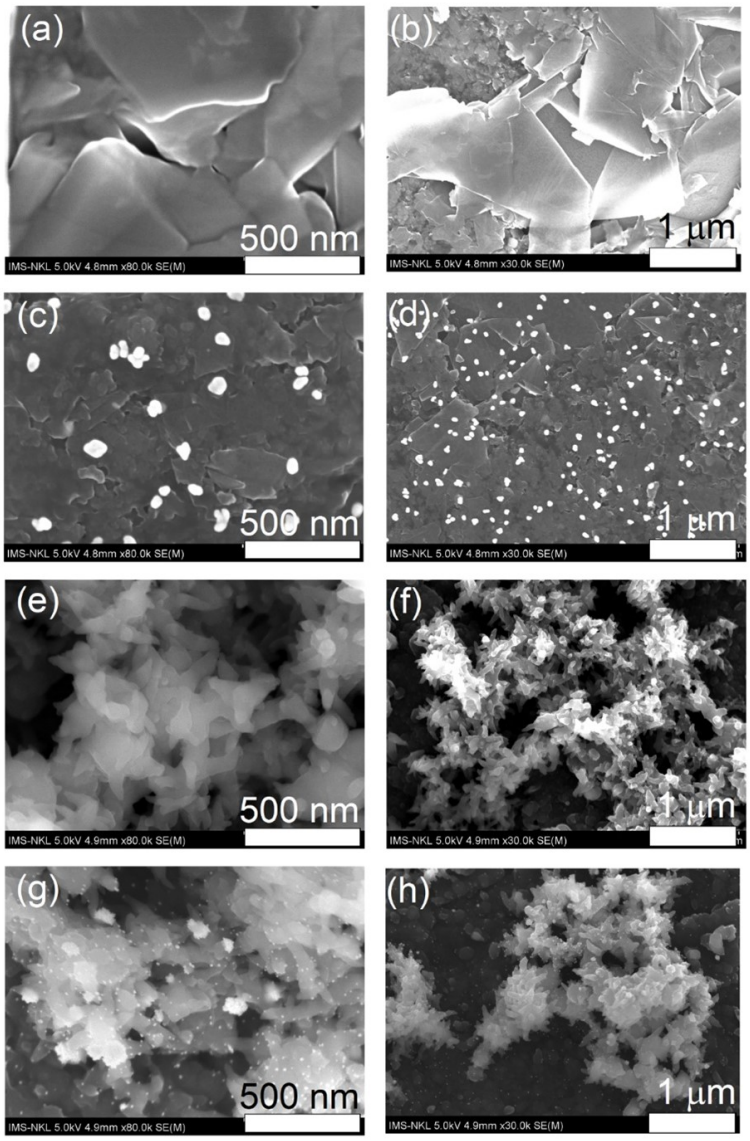

Figure 3.22: Scanning electron micrographs of the (a-b) bare CE; (c-d) AuNP/CE; (e-f) PANI/CE; and (g-h) AuNP/PANI/CE

The unmodified carbon electrode is quite smooth (Figures 3.22 (a) and (b)), while the PANI layer exhibits a pod-like shape with an approximate size in the hundred-nanometer range (Figures 3.22 (e) and (f)). The size of AuNPs was estimated using the ImageJ software. The results show that the gold nanoparticles deposited on the bare electrode and the PANI-modified electrode were 75 nm and 10 nm, respectively (Figures 3.22 (c-d) and (g-h)). This result can be explained because PANI acted as a template for the nucleation and growth of gold nanoparticles on the electrode surface. The PANI matrix provided a confined environment conducive to nanoparticle growth, thereby limiting their size and promoting uniformity. Moreover, PANI is adsorbed onto the nanoparticle surface, preventing agglomeration and facilitating the formation of smaller, well-dispersed nanoparticles. Additionally, the presence of conducting polymers on the surface enhanced the dispersion of gold precursor ions and promoted their interaction with the electrode. This facilitated uniform nucleation and growth of nanoparticles, resulting in the formation of smaller and more homogeneous gold nanoparticles.

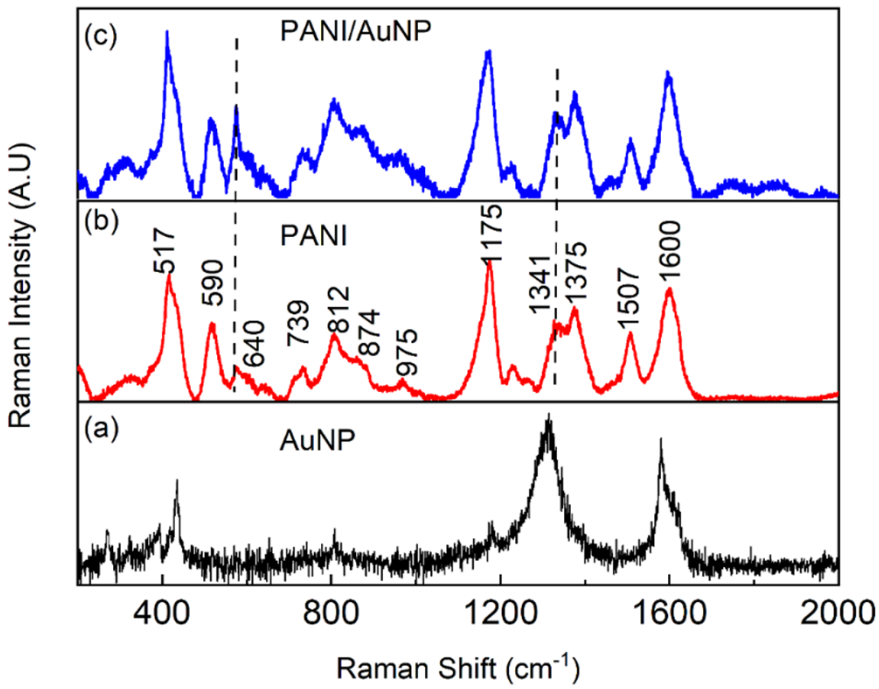

Figure 3.23: Raman spectra corresponding to different electrodes; (a) AuNP/CE; (b) PANI/CE; (c) AuNP/PANI/CE

Figures 3.22 (g) and (h) indicate that the gold nanoparticles are anchored on the PANI layer. Moreover, the number of gold nanoparticles per unit area increases significantly compared to electrodes without a polymer layer, thereby enhancing the surface area of the gold layer for antibody binding. The PANI layer plays a crucial role in ensuring the uniform distribution of gold nanoparticles on the electrode.

The Raman spectra in Figure 3.23 reveal noteworthy observations. Upon the deposition of gold nanoparticles on the bare and PANI-modified electrodes, the vibrational modes characteristic of gold are notably absent. Instead, the Raman spectrum exclusively exhibits the vibrational modes of carbon on the bare electrode and the vibrational mode of PANI on the modified electrode. Specifically, bands from 1100 to 1700 cm^{-1} are indicative of stretching modes, while those from 400 to 1000 cm^{-1} provide insights into the deformation vibrations of the benzene ring [110]. However, the PANI peaks at 640 and 1341 cm^{-1} exhibit greater enhancement compared to others due to the surface-enhanced Raman effect.

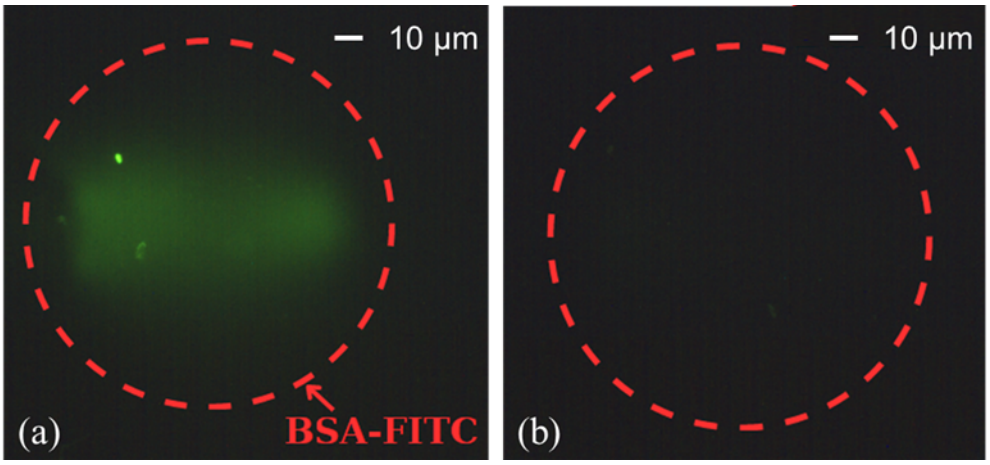

Figure 3.24: Characterization of electrode surface by fluorescence microscopy: (a) the fully modified electrode with 5 µM BSA-FITC and (b) the electrode without gold nanoparticle coating

3.6.4 Electrode surface investigation using fluorescence

After being functionalized and incubated with protein, the electrode was characterized by fluorescence microscopy. The results show that BSA-FITC proteins were present on

the electrode surface due to the fluorescent green color on the modified electrode shown in Figure 3.24 (a). A clear and uniform fluorescent signal across the electrode indicates the efficiency of protein immobilization. The amine groups of BSA-FITC were successfully bonded with the ester group on the electrode. In contrast, no fluorescent response appeared on the control electrode without the gold nanoparticle coating as shown in 3.24 (b). These measurements further validate the successful surface functionalization.

3.6.5 Electrode surface investigation using cyclic voltammetry

In this study, carbon was modified by the combination of PANI and gold nanoparticles to enhance the electrochemical sensitivity of the sensor. Cyclic voltammetry was performed on the AuNP/CE and AuNP/PANI/CE electrodes to compare the electrochemical response.

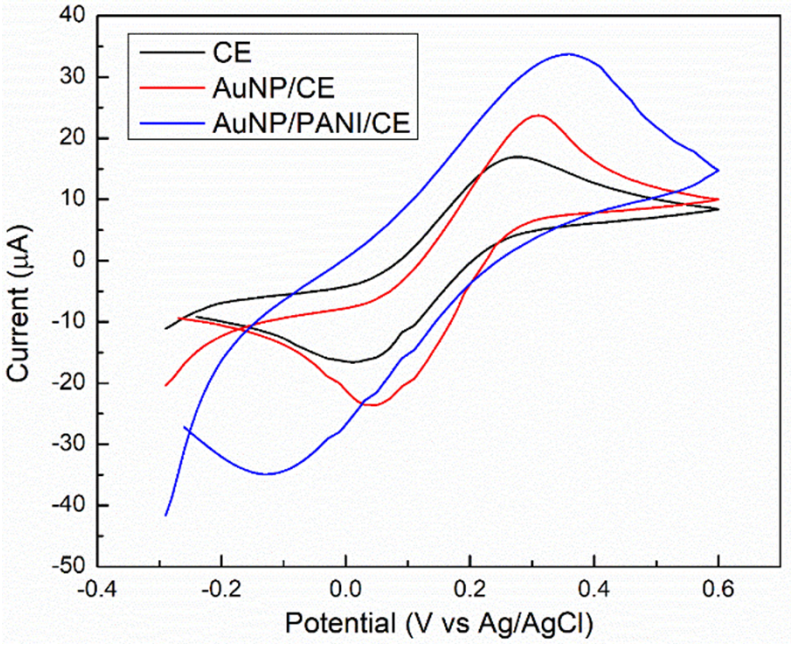

Figure 3.25: Comparison of cyclic voltammograms at bare carbon CE, AuNP/CE and AuNP/PANI/CE in 5 mM Fe(II)/Fe(III) and 0.1 mM KCl (ferry/ferrocyanide redox). The applied potential ranged from -0.4 V to +0.6 V at a scan rate of 0.05 V/s

A standard redox solution containing 5 mM Fe(II)/Fe(III) and 0.1 mM KCl (ferry/ferrocyanide redox) was used in these measurements. The applied potential ranged from

-0.4 V to +0.6 V, and the scan rate was 0.05 V/s. The results in Figure 3.25 show that the amplitude of the oxidation peak on both electrodes increased significantly compared to the bare electrode. The amplitude of the oxidation peak increased from 16.94 µA to 23.74 µA for the AuNP/CE electrode and to 33.76 µA for the AuNP/PANI/CE electrode. The oxidation peak amplitude of the AuNP/PANI/CE electrode was double that of the bare electrode and substantially higher than that of the AuNP/CE electrode. The results demonstrate that the combination of the PANI layer and the gold nanoparticles enhanced the electrode contact area and current transmission. Furthermore, the results reveal a significant change in the redox peak potential separation at the AuNP/PANI/CE electrode compared to the bare and AuNP/CE electrodes, which were 0.49 V, 0.27 V, and 0.26 V, respectively. This phenomenon is due to the modifications on the electrode surface morphology and conductivity that results in shifts in peak potential and an augmentation in peak-peak potential separation.

Cyclic voltammetry was performed to evaluate the success after each step of the carbon electrode surface functionalization. The setting parameters were the same as in the above discussion. The cyclic voltammograms changed significantly after each step as shown in Figure 3.26 (a). The amplitude of the oxidation peak increased after the PANI and gold nanoparticles were incorporated on the electrode. The amplitude of the oxidation peak was decreased in the subsequent steps. The cyclic voltammetry amplitude was especially small for the BSA-FITC incubation.

Figure 3.26 (b) provides a quantitative comparison of the oxidation peak amplitude for each step. The oxidation peak amplitude doubled upon the formation of the PANI and gold nanoparticle composite on the electrode. Subsequently, the peak amplitude experienced a decrease of approximately 5 µA with the formation of the SAM on the gold nanoparticles. At this step, the oxidation peak amplitude decreased by nearly 6 times. Lastly, for the BSA incubation, the amplitude was low, approximately 1 µA. This result occurred because a large quantity of protein covered the electrode surface, preventing the redox reactions and reducing the peaks.

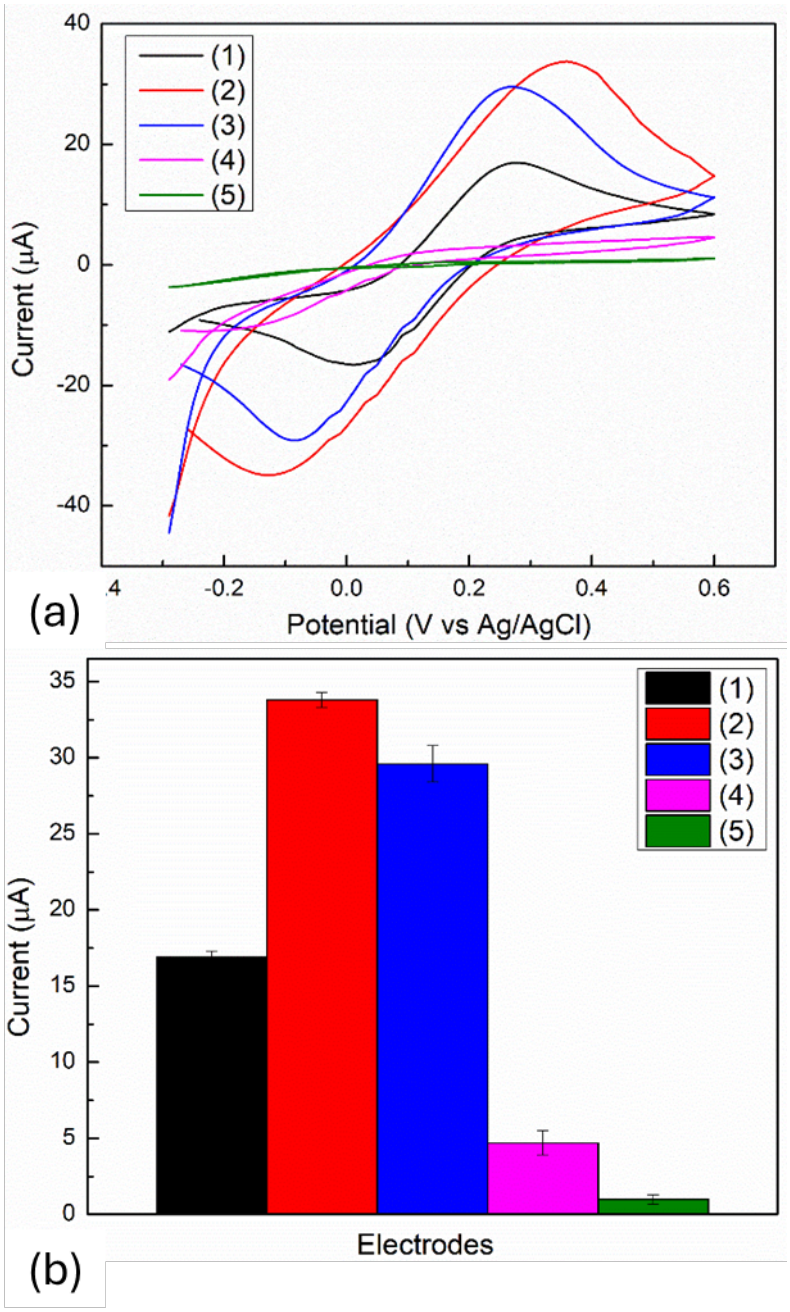

Figure 3.26: (a) Cyclic voltammograms after each step of carbon electrode surface functionalization. (b) Amplitude of the oxidation peak at each step in the functionalization. Plot identification: (1) bare (CE); (2) AuNP/PANI/CE; (3) 11-MUA/AuNP/PANI/CE; (4) EDC/NHS/11-MUA/AuNP/PANI/CE; and (5) BSA/NHS/11-MUA/AuNP/PANI/CE

The observation indirectly confirms the effectiveness of anti-BSA binding to the

electrode. Bovine serum albumin and anti-bovine serum albumin both contain amine groups that readily bind to ester groups formed after the EDC/NHS incubation. The increased binding of anti-BSA on the electrode surface is significant for developing electrochemical immunosensors based on specific antigen-antibody interactions which facilitates the formation of specific bonds, thereby improving the sensor sensitivity and performance. Furthermore, the significant changes in peak-peak potential separation observed after each step also indicate the successful progression of each stage in the functionalization process.

Temperature and pH affect the performance of functionalization processes. Temperature influences the rate of chemical and biological reactions, while pH changes the charge properties of the sensor surface, impacting the electrostatic interactions between the sensor and biomolecules. The literature has shown that room temperature and pH 7.4 are optimal for electrochemical biosensors. Moreover, the formation of the polyaniline layer and gold nanoparticles on the electrode surface also requires attention. The formation of layers can be recognized through the change in the color of the electrode and SEM. To confirm the presence of protein immobilized on the electrode, fluorescence and electrical measurement methods need to be used. When proteins are not labeled with color indicators, the electrochemical measurements are critical for assessing the efficacy of each step. This method provides essential insights into the success of protein immobilization on the electrode surface, offering a reliable means of confirmation. Besides, surface investigation methods such as Raman and surface plasmon resonance may also be utilized for further confirmation.

3.7 Conclusion

This chapter proposed an immunosensor based on the screen-printed gold electrode to detect and quantify BSA concentration by electrochemical measurements. The sensor was developed by functionalizing the screen-printed gold electrode surface. The functionalization process included five main steps to attach anti-BSA on the gold electrode and specifically bind to BSA. The effectiveness of this process was examined on

two types of gold electrodes: sputtered gold electrodes on glass slides and commercial screen-printed gold electrodes. Electrical measurements, Raman spectroscopy, and fluorescence observations were employed to validate the performance of the process. Experimental results confirmed the successful specific binding and immobilization of BSA proteins on the electrode surface, as evidenced by the fluorescent signal. Furthermore, a gradual decrease in surface impedance of the working electrode was observed after each step of surface functionalization and protein immobilization. Besides, the influences of the 11-MUA incubation time and the protein concentration on the performance were also investigated, revealing that an incubation time of 24 hours and a protein concentration of 5 µM resulted in optimal SAM binding. Additionally, The experimental results confirm that BSA-FITC proteins have been successfully immobilized on the gold electrode surface, as indicated by fluorescence, CV, and EIS measurements. Furthermore, the control electrode results further confirmed the proposed process's success. The results revealed the relationship between BSA concentration and the reduction peak in the CV signal, as well as with the charge transfer resistance in the EIS signal. Therefore, the BSA concentration can be determined through the reduction peak of the CV signal or the charge transfer resistance of the EIS signal.

Furthermore, the performance of 2-electrode and 3-electrode configuration-based sensors was also compared through experiments for BSA protein detection. The experimental results confirmed the performance of both sensor configurations. The sensors can detect and quantify various concentrations of BSA protein from 0.1 µM to 5 µM based on impedance measurement methods. The sensitivity of the sensors was 12 Ω/µM and 7.2 kΩ/µM, respectively. As can be seen, the sensitivity of the 3-electrode configuration-based sensor was much better than 2-electrode configuration-based sensor the 2-electrode configuration-based sensor. However, the 2-electrode configuration-based sensor remains a potential candidate for various applications. Notably, this configuration allows for straightforward exploration of miniaturization, making it suitable for integration into microdevices.

Moreover, a carbon electrode surface functionalization process was successfully developed for the immobilization of proteins. The process utilized a combination of PANI

conducting polymer and gold nanoparticles to enhance the electrode contact area and current transmission. The electrode surface morphology, as well as the presence of PANI and AuNPs, were verified by SEM and Raman spectroscopy. The results show that gold nanoparticles were uniformly distributed on the electrode through the PANI film. This combination facilitated the formation of a nanocomposite on the electrode. The cyclic voltammograms exhibited a significant increase when PANI film and gold nanoparticles were incorporated, indicating the enhanced current transmission of the nanocomposite layer. The presence of BSA on the electrode was verified by fluorescence and cyclic voltammetry. The PANI layer ensured the uniform distribution of gold nanoparticles, reducing the particle size and increasing the surface area of the gold on the carbon electrode surface as well as the protein immobilization. In the future, high-sensitivity immunosensors may be developed to quantify proteins for disease diagnosis. The research findings have been disseminated through publications in prestigious journals and presentations at leading conferences [79, 80, 81, 82, 16, 17, 83, 84]

Chapter 4

Development of a preconcentration control system and electrochemical measurement circuit

This chapter details the research and development of an embedded system that integrates a preconcentrator and an electrochemical measurement circuit for the concentration and detection of proteins in a microfluidic chip. The system is fabricated using multilayer printed circuit board (PCB) and monolithic aluminum processing techniques. Embedded software is developed for the microcontroller, and a graphical user interface (GUI) is designed to enable user interaction, thereby facilitating the execution of system functions. Finally, the system is thoroughly evaluated to assess the protein preconcentration and the accuracy of electrical measurements.

4.1 Materials and apparatuses

Bovine serum albumin–fluorescein isothiocyanate conjugate was purchased from Sigma-Aldrich Chemical (St. Louis, Missouri, USA). A 1X phosphate-buffered saline solution was obtained from Sigma-Aldrich Chemical Co (St. Louis, Missouri, USA). Polydimethylsiloxane (SYLGARD™ 182, Dow Corning, USA) was utilized to fabricate the proposed microfluidic chip. Microscope glass was used as the substrate of the microflu-

idic chip purchased from Duran Group (Germany). The Nafion solution (Nafion™ 117, Sigma-Aldrich) was used to fabricate the ion-selective membrane.

The components used in the system include the AD5941 integrated circuit (IC) procured from Digi-Key Electronics Corp., Minnesota, United States, serving as a high-precision impedance and electrochemical front-end. The ESP32 Wi-Fi and Bluetooth module, acquired from Espressif Systems, Ltd., Shanghai, China, served as the central processor for measurement configuration and data acquisition. Commercially printed electrodes, specifically the ER-N DEP Chip from BioDevice Technology, Ltd., Ishikawa, Japan, were utilized in the experimental setup. For comparative purposes, the BDTminiSTAT100 commercial potentiostat and LMP91000 commercial evaluation module, obtained from BioDevice Technology, Ltd., Ishikawa, Japan, and Texas Instruments Inc., Texas, United States, respectively, were used to perform CV measurements and evaluate device performance. Resistance measurements were carried out using the DT4256 digital multimeter from HIOKI E.E. Corp., Nagano, Japan. The device case was fabricated using the Objet 500 Connex 3 3D printer from Stratasys, Ltd., Minnesota, United States. The printer utilizes PolyJet Technology to print models simultaneously with different model materials. An inverted fluorescence microscope IX 71 (Olympus, Melville, NY, USA) equipped with a Phantom VEO 710L high-speed camera (Ametek, USA) was employed for fluorescence imaging using Phantom Camera Control software (PCC).

4.2 Design and fabrication of electrochemical and impedance measurement circuit

Figure 4.1 shows block diagram of the proposed system, including center processing block, measurement circuit, sensors, and communication. In the center processing block, ESP32 Wi-Fi and Bluetooth module was utilized to configure the parameters and registers of the AD5941 measurement circuit.

Additionally, the ESP32 module received data from the AD5941 via SPI communication, analyzed and processed the data, and then transmitted it to a PC. The

incorporation of the ESP32 module facilitated extended wireless communications due to the built-in Wi-Fi and Bluetooth circuits available on the module.

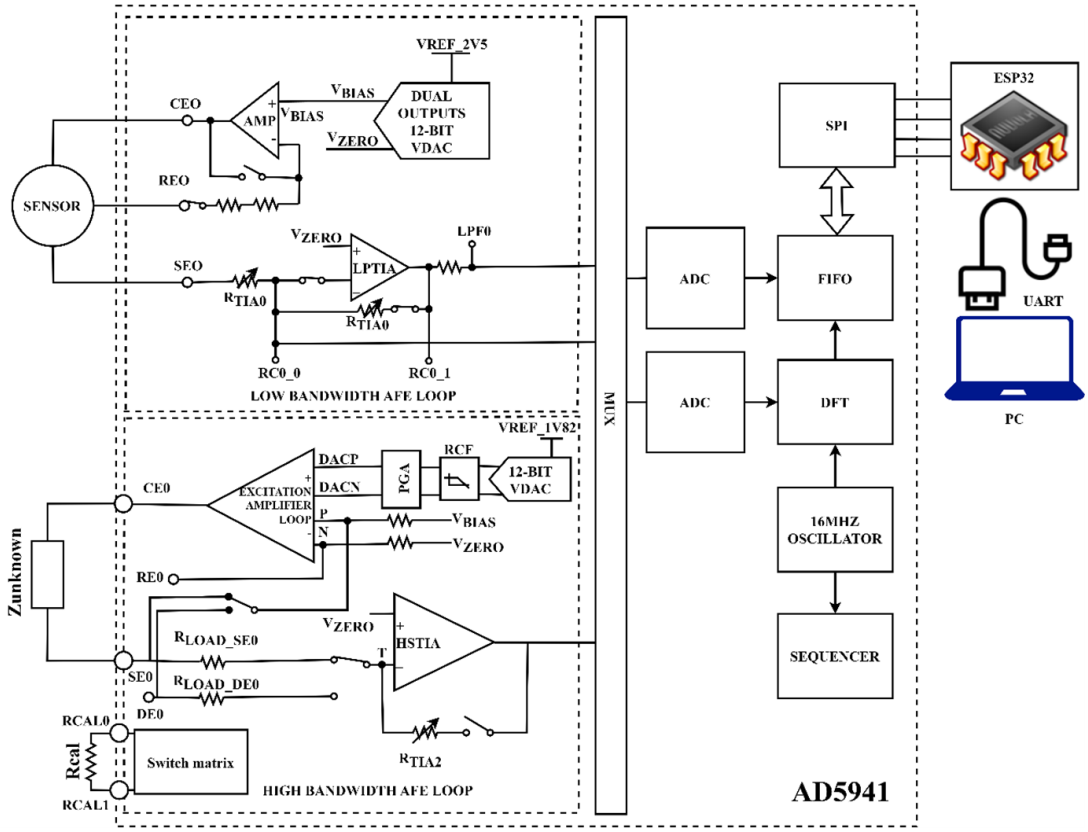

Figure 4.1: Block diagram of the proposed system with 4 main blocks, including processing block, measurement circuit, sensors, and communication

The measurement circuit block primarily consisted of an AD5941 analog integrated circuit, which performed electrochemical and impedance measurements. The AD5941 facilitated electrochemical-based measurement techniques and supported both 2-wire and 3-wire impedance measurement configurations. It incorporated a discrete fourier transform (DFT) hardware block to determine the magnitude and phase of object impedance. The sensor block primarily consisted of commercial gold-printed electrodes used in the experiments of this study. These electrodes were directly connected to the measurement circuit block via connectors. In the system, alongside SPI communication between the center processing block and the measurement circuit, Universal Asynchronous Receiver/Transmitter (UART) was employed to transmit data to the computer. A graphical user interface was developed using the C sharp language, en-

abling users to select measurements, configure parameters, and receive and display results. Additionally, the system was powered by two voltage levels: 5V and 3.3V. The 5V voltage was directly obtained from the USB connector, while the 3.3V voltage was generated as the output of the LM1117 linear voltage regulator.

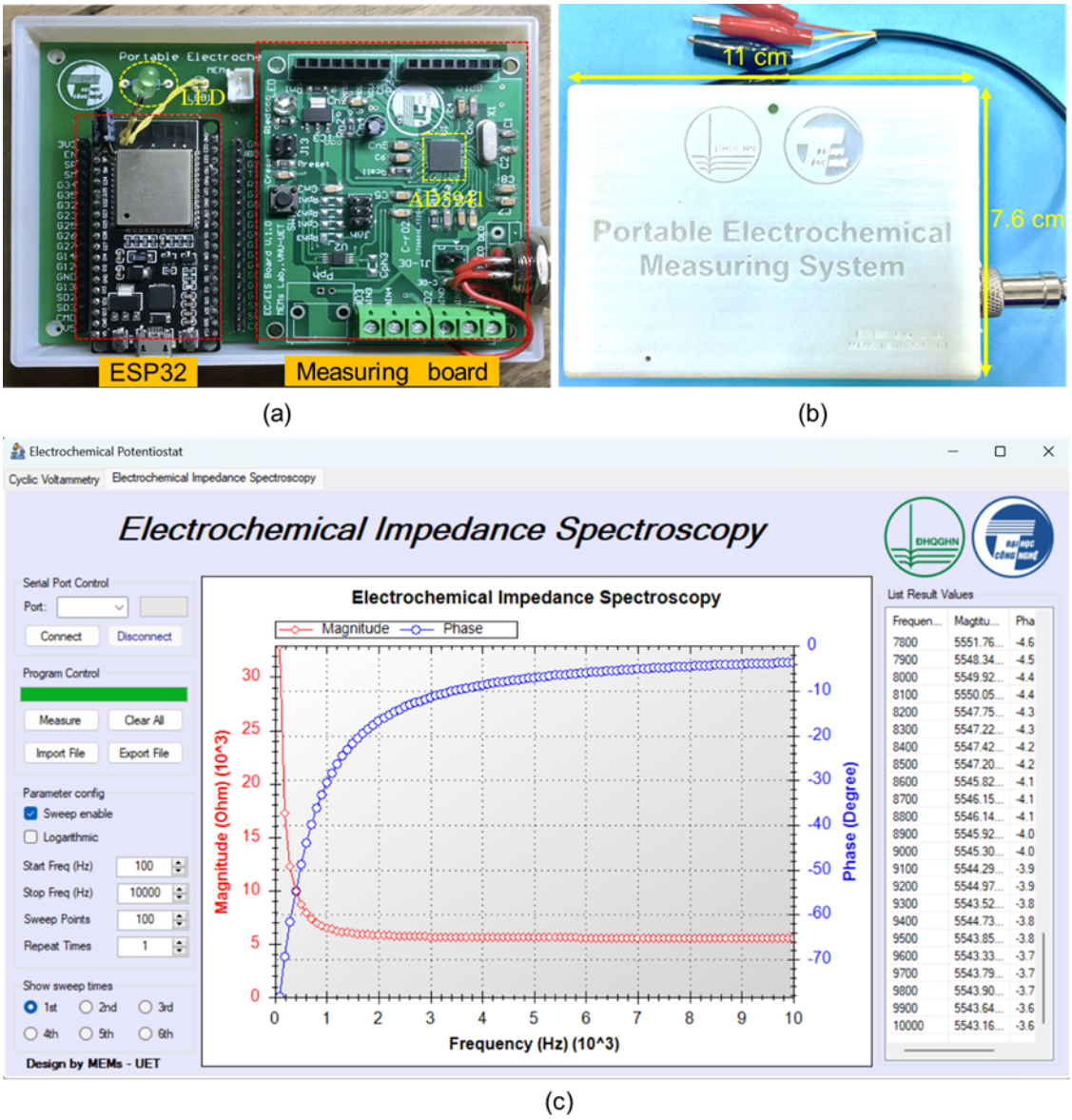

Figure 4.2: Image of the system after being manufactured and packaged. (a) Inside the system; (b) Outside the system; (c) Graphical user interface (GUI)

The system circuit was designed and fabricated using a multi-layer printed circuit board technique. It comprised a measurement circuit based on AD5941 and a mother-

board intended to connect the ESP32 module to the measurement circuit, as depicted in Figure 4.2 (a). After soldering, the circuits were enclosed within a 3D-printed box fabricated using 3D printing technology, as illustrated in Figure 4.2 (b). The system dimensions measured 11 cm x 7.6 cm x 4 cm (length x width x height). USB and connectors were positioned at the edge of the box for easy user access to connect to the computer and sensor. The graphical user interface (GUI) is depicted in Figure 4.2 (c), showcasing parameter configuration options, control panels, and a display screen.

4.3 Design and fabrication of system integrating preconcentrator and electrochemical measurements

The proposed system executed two primary tasks, including protein pre-concentration at low concentrations and employing electrochemical measurement techniques for target protein detection. Figure 4.3 shows the overall design and the block diagram of the proposed system. The proposed system was divided into five main blocks, including the central control unit, measurement circuit, voltage controller, bio-chip and graphical user interface (GUI). The central control module utilized the ESP32 DevKit V1 development board, was responsible for automating the testing process.

The ESP32 module communicated with the graphical user interface to receive configuration commands and transmit measurement results. Moreover, it interfaced with the voltage controller and measurement circuit blocks to establish the requisite voltages for protein pre-concentration and the parameters of electrochemical measurements, respectively. Specifically, the measurement circuit block integrated an AD5941 analog integrated circuit tailored for conducting electrochemical measurements on the biosensor. This functionality encompasses EIS and CV, thereby offering a comprehensive analytical framework within the system. The results obtained from the measurements were transmitted to the central control unit block via the serial peripheral interface (SPI) communication protocol. Within the voltage controller block, a voltage boost

circuit module was implemented to convert the 12 V power supply into higher voltages necessary for protein preconcentration. The output voltage was acquired via a closed-loop controller system. Feedback regarding the voltage output was relayed to the central control unit block using a 16-bit analog-to-digital converter, employing the inter-integrated circuit (I2C) communication protocol.

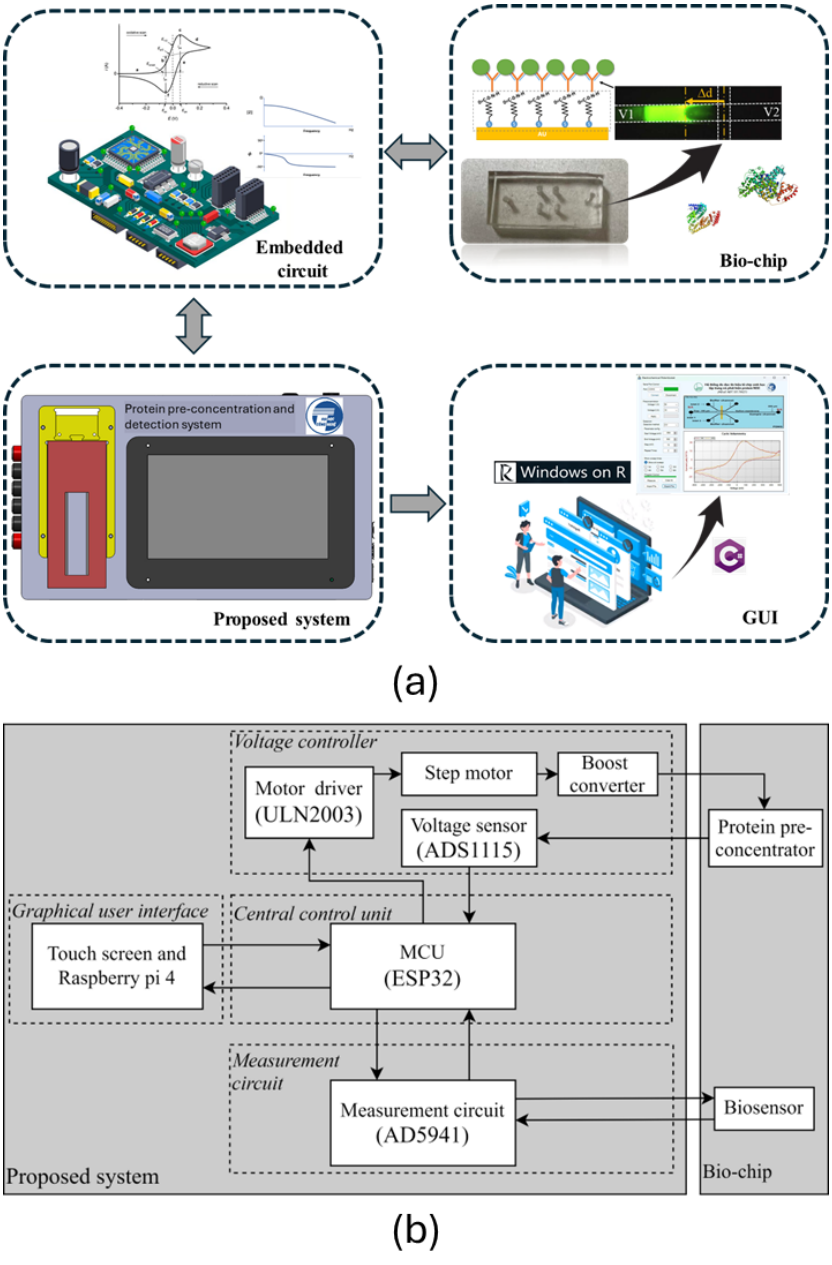

Figure 4.3: System design; (a) Overall design; (b) Block diagram of the proposed system

A ULN2003 motor driver and step motor combination were employed as the ac-

tuator mechanism to adjust the output voltage. The bio-chip featured both protein pre-concentration and an integrated biosensor. The pre-concentrator was designed utilizing a dual-gate structure, incorporating three micro-channels and a Nafion membrane [77], while the biosensor was configured as an electrochemical sensor comprising three electrodes: working, counter, and reference electrodes.

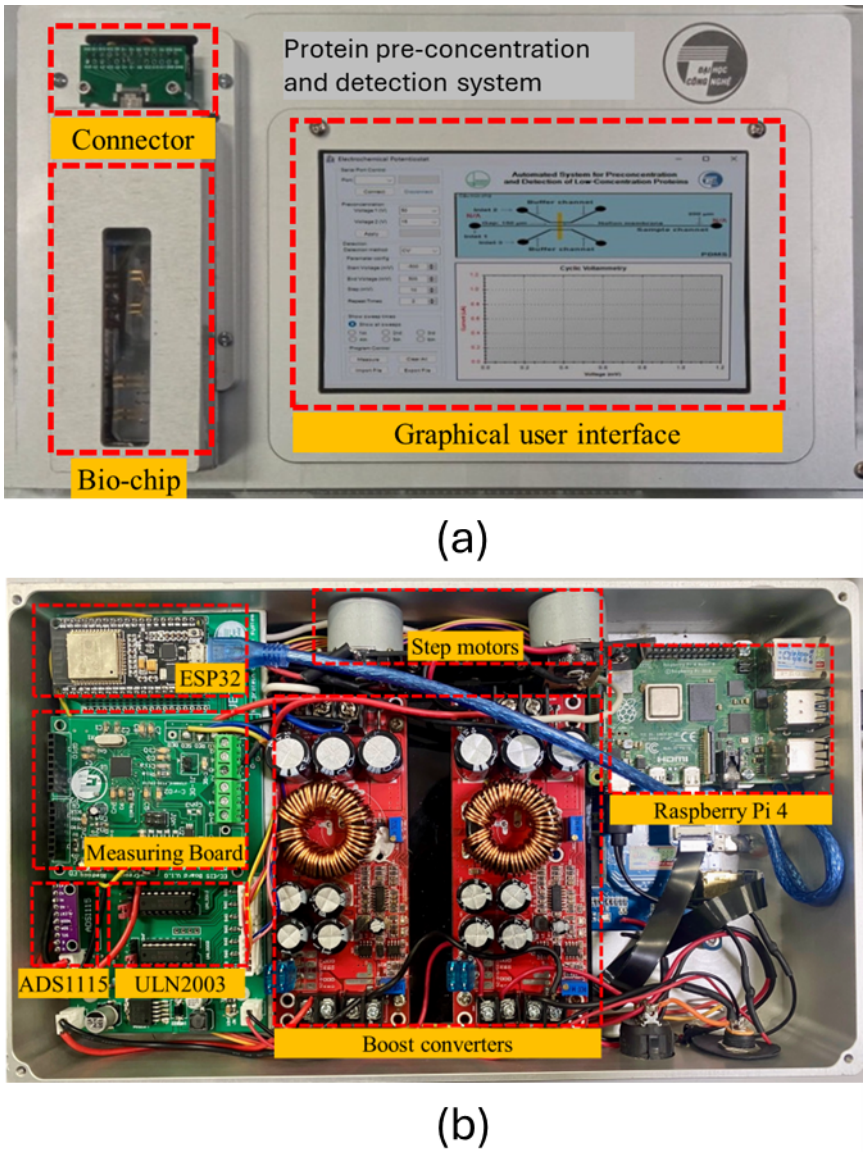

Figure 4.4: Actual image of the proposed system after designing and fabricating. (a) Outside the system; (b) Inside the system

Finally, a graphical user interface was created using the C Sharp language and

operated on the Windows platform. The Windows operating system was installed on the Raspberry Pi 4 (ARMv8) using the Windows on Raspberry project (WoR). The user interface software enabled users to configure parameters for both the voltage control function and the electrochemical measurement function. The system shell was designed by Solidwork 3D CAD design software (Dassault Systèmes SolidWorks Corp., Vélizy, France).

Following the design phase, the system circuit and shell were fabricated by the multilayer layer printed circuit board (PCB) and monolithic aluminum processing techniques, respectively. Two SZ-BT07CCCV-D1 1500W 30A DC-DC boost converter step-up power supply modules were utilized to provide the voltages for the protein pre-concentration. The output voltage of the boost converter circuit can be adjusted within the range of 15V to 90V and was regulated using a potentiometer. This potentiometer was controlled by a stepper motor mechanism. Figure 4.4 shows the actual images of the proposed system after designing and fabricating.

The outside of the proposed system included a bio-chip, connector and graphical user interface, as shown in Figure 4.4 (a). The bio-chip was connected to the system circuit via a USB connector. Users could adjust applied voltages, configure parameters, and observe the results via the screen. Within the system, the internal components included a measurement circuit incorporating the AD5941, along with a motherboard facilitating connections among various modules. These modules comprised the power module, ESP32 module, ULN2003 driver, ADS1115 module, and AD5941 measurement circuit. The measurement outcomes were transmitted to the Raspberry Pi 4 for display on the screen, as shown in Figure 4.4 (b).

4.4 Embedded algorithm on microprocessor and GUI for electrochemical and impedance measurement circuit

Two measurements, including CV and EIS, were built into the program. An embedded algorithm was developed for the ESP32 module to execute these measurements, outlined in Algorithm 1. Initially, the system established a connection to the PC via the COM Port at a baud rate of 9600 bps to await information transmission from the PC. Subsequently, the system read the setting parameters through UART communication once the serial register received transmitted data. Based on the retrieved data, the system determined the measurement and its associated parameters. Finally, the measurement was conducted, and the data was transmitted to the PC. For CV measurement, the current response of a redox-active solution was measured to a linearly cycled potential sweep. The step in the measurement represented the change of voltage amplitude applied to V_{bias}. The output voltage ranges from 0.2 V to 2.4 V for the 12-bit output of the low-power DAC. Therefore, the least significant bit (LSB) value of the 12-bit output was 537.2 μV. Moreover, the start voltage and end voltage were also important parameters in this measurement.

Algorithm 1 Firmware for measurements and data acquisition

```
Begin serial communication at 9600 bps
while true do
    if Serial.Available = true then
        Read the setting parameters from UART
        Configure the parameters for measurement
        Make measurement
        Send data to PC
    end if
end while
```

For impedance measurement, the process comprised two steps. Initially, a voltage

signal was administered to the R_{CAL} reference resistor (200 kΩ) via the RCAL0 and RCAL1 pins and the switch matrix within the measurement circuit. Subsequently, the resultant current I_{RCAL} was gauged through the trans-impedance amplifier and 16-bit ADC. The real (r_c) and the imaginary (i_c) components of the Impedance were computed using the DFT hardware accelerators and stored in the data FIFO. In the subsequent step, the identical voltage signal was applied to the unknown impedance ($Z_{unknown}$) and the process was reiterated to ascertain the real value (r_z) and the imaginary value (i_z) of $Z_{unknown}$. Upon storing all four parameters in the data FIFO, the magnitude and phase of the unknown impedance were calculated using Equations 4.1 and 4.2, respectively [153].

$$|Z_{unknown}| = \frac{\sqrt{r_c^2 + i_c^2}}{\sqrt{r_z^2 + i_z^2}} \times R_{TIA} \tag{4.1}$$

$$\angle Z_{unknown} = tan^{-1}\frac{-i_c}{r_c} - tan^{-1}\frac{-i_z}{r_z} \tag{4.2}$$

On the PC side, an algorithm was developed to read and exhibit the data received from the ESP32 module via the COM Port, as delineated in Algorithm 2. Initially,

Algorithm 2 Software on PC

```
Begin serial communication at 9600 bps
Set parameters to sample measurements
Wait for the measurement to complete
if Serial.Available = true then
    Read data
end if
Average filter
Display data
```

the software established communication by opening the COM port on the computer, operating at a baud rate of 9600 bps. Subsequently, users could define the type of measurement and its parameters through a GUI. The program remained in a waiting state until data from the measurement circuit was transmitted. Upon reception, the acquired data was read and stored in an array before undergoing averaging to smooth

the dataset. Finally, the data was depicted graphically on the PC screen. Additionally, the digital data could be archived on the PC for subsequent processing endeavors.

4.5 Graphical user interface and embedded software for system integrating preconcentrator and electrochemical measurements

The graphic user interface was designed and developed using Visual Studio IDE, a software development environment provided by Microsoft, based in the USA, employing the C sharp programming language. GUI included a control panel and a graphing area, as shown in Figure 4.5. The control panel contained three functional control groups, including serial port control, pre-concentration and measurement groups.

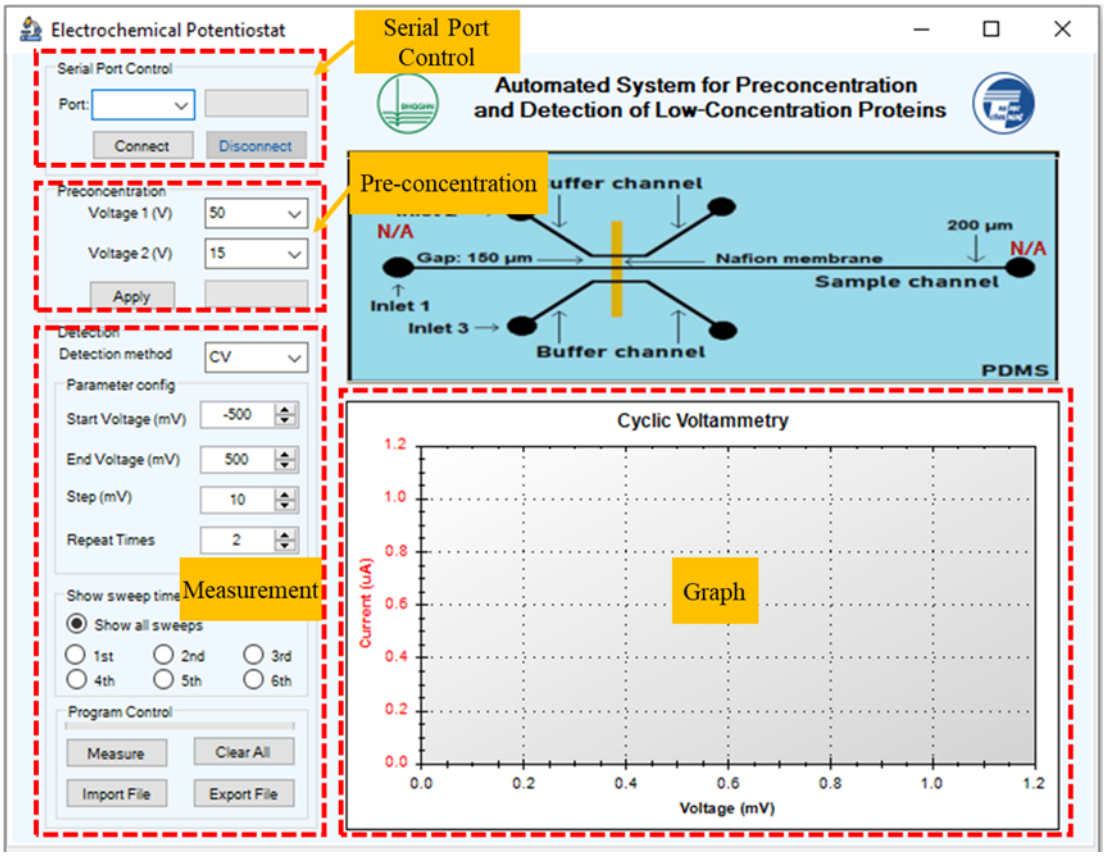

Figure 4.5: The image of graphical user interface developed using C sharp language

Within the serial port control group, available ports were automatically scanned to establish a connection with the ESP32 module. This connection facilitated the transmission of control commands and receipt of results. The pre-concentration control group provided users with the ability to configure two voltage values applied to the ends of the micro-channels within the microfluidic chip for protein pre-concentration. Meanwhile, the measurement group allowed users to conduct CV or EIS measurements and set corresponding parameters for each measurement. Upon pressing the "Apply" button in the pre-concentration block or the "Measure" button in the measurement block, the user interface transmitted control commands to the central control unit to execute the designated tasks. Subsequently, upon task completion, the central control unit relayed the results back to the Raspberry Pi for visualization on the interface. These results included adjusted voltage values displayed on the image of the chip structure for the voltage control function and measurement data drawn on the graph for the measurement function.

The algorithm for voltage control is shown in Algorithm 3. Firstly, the system read the input setting voltage from the user through the GUI. Then, the system read the current voltage through ADS1115 module and calculated the difference between them. When this difference exceeded the expected voltage error, the ESP32 module engaged in

Algorithm 3 Implementation of the voltage control function

```
Read the input voltage received from the serial port
Read the actual voltage from ADS1115 and calculate the voltage error
while the voltage error > the expected voltage error do
    Control the stepper motor to achieve the desired voltage
    Read the feedback voltage and update the voltage error
    Send the results back to the GUI
end while
```

communication with the stepper motor via the ULN2003 driver. This action facilitated the rotation of the potentiometer within the boost converter, thereby adjusting the voltage to match the desired values. Following this adjustment, the system obtained the feedback voltage, updated the voltage error, and transmitted the results to the

GUI. This iterative process persisted until the desired voltage value was achieved.

The electrochemical measurements were conducted utilizing the AD5941 analog IC. For CV measurements, a cyclic voltage waveform was applied to the sensor, and the resulting current was recorded and plotted on a graph. The V_{bias} was adjusted following each increment in the input voltage, with a minimum resolution of 537 µV. The sample delay, denoting the duration before transitioning to the subsequent step, was set to a default value of 7 ms. Measurement time was determined based on the duration of these wait cycles before progressing to the next sequential step. The measurements comprised steps, starting voltage, and ending voltage parameters. For EIS measurement, two distinct procedures were incorporated into the measurement process. Initially, the system was calibrated with the RCAL reference resistor (200 kΩ). Subsequently, the system was connected to the object to determine its impedance. The actual and imaginary components of the impedance were determined utilizing the hardware accelerators for DFT. The algorithm for the electrochemical measurement function is outlined in Algorithm 4. Initially, the system obtained the type of measurement and configuration parameters from the user through the serial port. Subsequently, the ESP32 module configured the AD5941 and executed either CV or EIS measurements. The resulting measurement data was then transmitted back to the GUI and plotted on the graph.

Algorithm 4 Implementation of the Electrochemical measurement function

```
Receive the measurement method and configuration parameters from the serial port
if method = CV then
    Configure the AD5941 and set up params to perform CV
else if method = EIS then
    Configure the AD5941 set up params to perform EIS
end if
Perform the measurement
Send the results back to the GUI
```

4.6 Experimental setup

For the investigation of protein pre-concentration, the protein pre-concentration chip was positioned under the microscope and connected to the system via wires. The voltages were configured on the screen of the device. The protein pre-concentration process was observed on a computer screen connected to the high-speed camera of the microscope system, as shown in Figure 4.6.

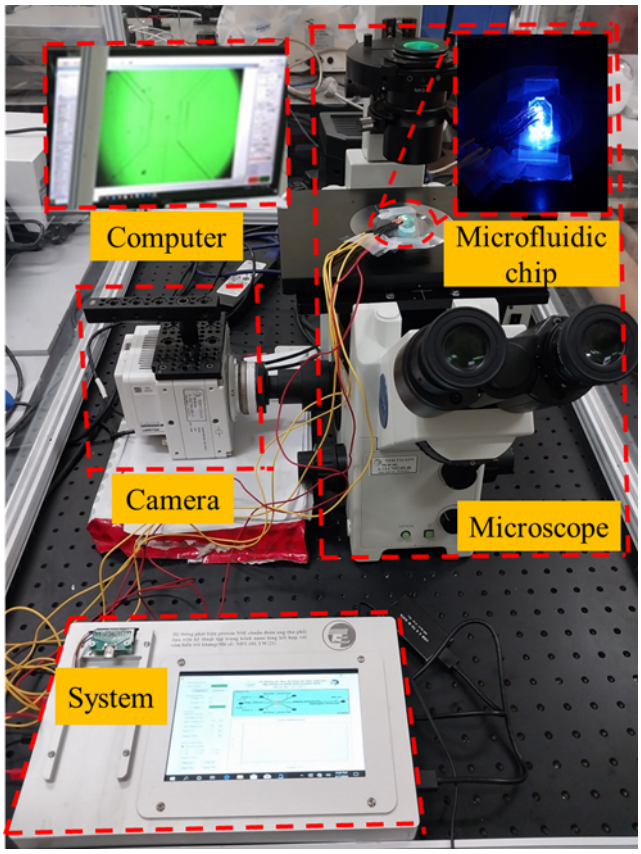

Figure 4.6: The experimental setup for protein pre-concentration

Experiments were conducted on a microfluidic chip engineered with a dual-gate structure, featuring three micro-channels, as mentioned in chapter 2 above. Among these, one main channel was positioned at the center, while two sub-channels were symmetrically located as side channels. The connection between the sub-channels and the main channel was established via an ion-selective membrane crafted from a Nafion solution. These micro-channels were designed with dimensions of 50 µm in width and

40 µm in height. The separation between the main channel and the sub-channels was maintained at 150 µm. The main channel was filled with the BSA-FITC protein solution, while the sub-channels was filled with PBS 1X solution.

For the investigation of CV measurement, experiments were conducted using commercial gold screen-printed electrodes immersed in a solution mixture containing the Ferro/Ferri 5M ($K_4Fe(CN)_6/K_3Fe(CN)_6$) redox couple and 0.1M KCl. Regarding the EIS measurement, experiments were performed using a Randles equivalent circuit. This circuit model is widely recognized in electrochemistry and electrochemical impedance spectroscopy for understanding the intricate processes occurring at the electrochemical interface.

4.7 Results and discussion

4.7.1 Investigation of voltage controller

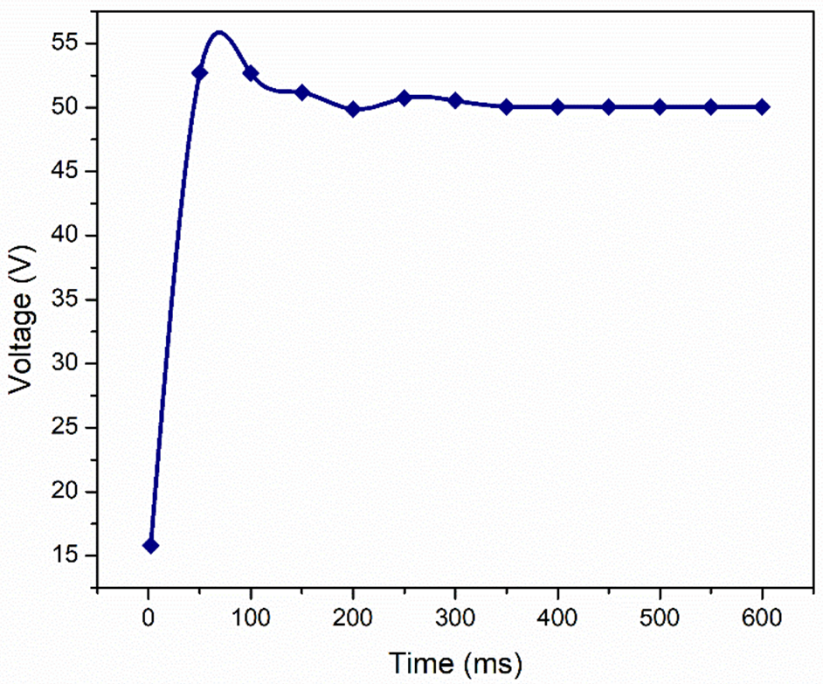

Figure 4.7: The change of output voltage over time when setting the system to 50 V from the initial voltage of 15 V

The voltage controller facilitated the adjustment of the output voltage to supply the protein pre-concentrator chip, with a range spanning from 15 V to 90 V. To assess the voltage controller's performance, the system was set to a voltage of 50 V from an initial value of 15 V, and the output voltage was continuously monitored over time.

The results demonstrated an immediate change in the output voltage upon transmission of the command from the screen to the ESP32 module, as illustrated in Figure 4.7. Initially, the output voltage exhibited a rapid increase to reach 50 V within the first 100 ms, accompanied by an overshoot of 5.4%. Subsequently, the output voltage stabilized at 50 V after 300 ms. This rapid response time indicates the system's efficient performance.

4.7.2 Investigation of protein preconcentration

Firstly, the main channel and sub-channels were filled 10 µM BSA-FITC and PBS 1X solutions, respectively. The main channel appeared uniformly green, indicating the even distribution of protein molecules within the main channel. The main channel exhibited a uniform green appearance, indicating the even distribution of protein molecules within it. Subsequently, a voltage difference of 50 V was applied between the main channel and the sub-channels using the proposed system. The experimental results illustrate that the middle region of the main channel darkens as proteins and anions are expelled, while the regions near the ends of the channel brighten, as depicted in Figure 4.8 (a).

This can be explained that the voltage difference between the micro-channels induced ion concentration polarization, resulting in the generation of an electrophoresis force (EPF) near the Nafion membrane located between the ends of the main channel. This force exerted an influence on negatively charged protein molecules, directing them away from the middle zone of the main channel, known as the depletion zone, and towards the ends of the main channel.

In enrichment mode, a voltage difference of 10 V was applied to the two ends of the main channel. This generated a tangential electric field in the main channel, accompanied by a co-directional EOF. The EOF propelled negatively charged protein molecules towards the vicinity of the Nafion membrane. Upon achieving a balance

between the forces of EOF and EPF, a stable protein concentration zone was established within the main channel. Fluorescence imaging revealed that the concentration zone appeared on the left side of the main channel, exhibiting a brighter green color, while the right side became darker, as demonstrated in Figure 4.8 (b). The fluorescence intensity increased from 28 A.U to 55 A.U after seven minutes.

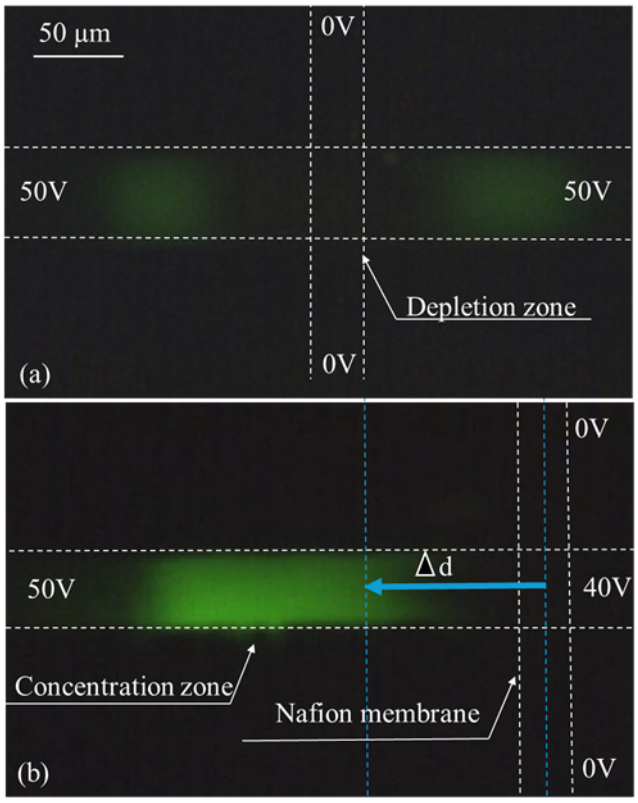

Figure 4.8: The investigation result of protein pre-concentration chip with the proposed system; (a) Depletion mode; (b) Enrichment mode

4.7.3 Investigation of CV measurement

After being designed and fabricated, the proposed system was connected to the commercial screen-printed gold electrode to perform the CV measurement. The electrode structure included the working, counter and reference electrodes. The working electrode was made of gold material, while the counter and reference electrodes were made of carbon and Ag/AgCl, respectively. Then, the electrodes were dripped with a 5 mM potassium ferro/ferricyanide solution. A PC with pre-installed software was connected

to the system through COM port to configure the parameters and display the data.

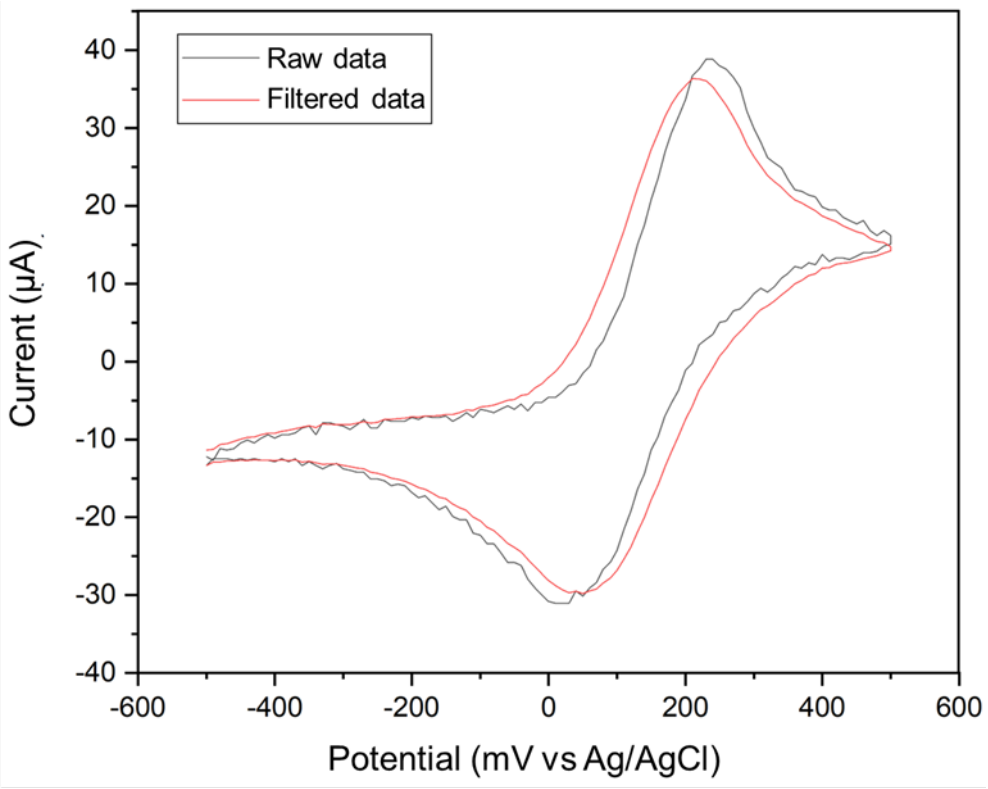

Figure 4.9: The result data of the CV measurement in the unfiltered and average filtered cases in a 5 mM potassium ferro/ferricyanide solution. The start voltage, end voltage, and step are -500 mV, 500 mV and 10 mV

For CV measurement, four parameters need to be set, including start voltage, end voltage, step, and repeat times. The start voltage must be less than the end voltage. In this study, the setting parameters were -500 mV, 500 mV, 10 mV, and two repeat times, respectively. Here, the data was taken at the second measurement to ensure that the system was stable. The results show the obtained signal had a standard duck shape characterizing for CV measurement with a standard redox solution, as shown in Figure 4.9. Before being passed the average filter, the raw data had high-frequency noises exhibited by the serrations in the black line in Figure 4.9. These noises were eliminated when being passed the average filter with a window size of three and the signal became smoother, as shown in the filtered data in Figure 4.9. The acquired results demonstrate that the average filter played an important role in the signal processing process in the

software on the PC. The same experiments were carried out on the BDTminiSTAT100 commercial potentiostat device (BDT device) and LMP91000 module to compare the performance between devices. The obtained results indicate that all three devices exhibit the characteristic duck shape for CV measurements in redox solutions, as depicted in Figure 4.10.

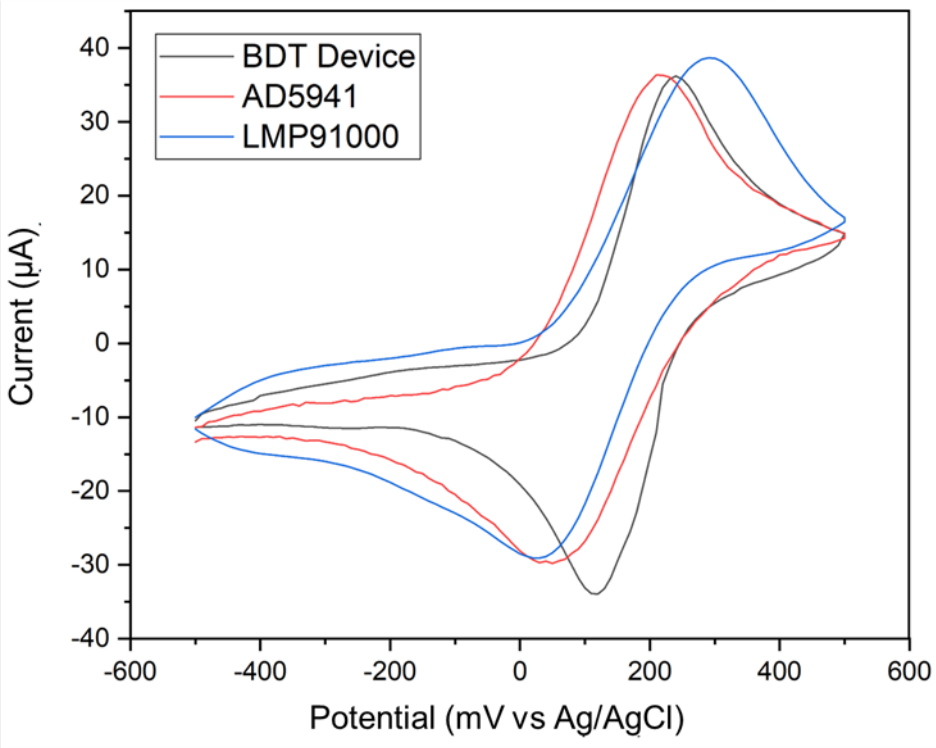

Figure 4.10: The comparison of CV measurement results between the proposed system with BDTminiSTAT100 commercial potentiostat device and LMP91000 module in a 5 mM potassium ferro/ferricyanide solution. The start voltage, end voltage, and step are -500 mV, 500 mV and 10 mV

As can be seen, the obtained signal from the AD5941-based system was more similar to the signal acquired from the BDTminiSTAT100 commercial device (BDT device) rather than the signal from the LMP91000 module in terms of the amplitude and position of redox peaks. The positive peak represented the oxidation of Fe^{2+} to Fe^{3+}, while the negative peak represented the reduction of Fe^{3+} to Fe^{2+}. In comparision to CV signal from the BDT device, the CV signal of the proposed device had the same oxidation peak amplitude at 36 µA. The difference in oxidation peak positions

of these two signals was very small, around 10 mV. The experimental results indicate the outstanding efficiency of AD5941 IC compared to LMP91000 IC. The resulting similarity between the proposed system and the commercial device demonstrated the potential of the device in the electrochemical measurements.

4.7.4 Investigation of impedance spectroscopy measurement

In impedance speactroscopy mesurement configuration, the CE0 and SE0 pins in AD5941 IC were carried out to perform the 2-electrode impedance spectroscopy measurement. On the software, the impedance measurement option was selected with the configurations of fixed or sweep frequency. Five main parameters were utilized in the sweep frequency configuration, including start frequency, stop frequency, the number of sweep points, repeat times, and the display mode (linear or logarithmic). To evaluate the performance of the proposed system, several different experiments were conducted. The measurement results were then analyzed to determine the values of resistance (R) and capacitance (C) in the RC circuit. Subsequently, the acquired values were compared to those measured by the HIOKI multimeter. The experiments were conducted five times, and the results were then averaged.

Firstly, a resistor with a value of 5.6 kΩ was measured in a frequency range from 100 Hz to 10 kHz. The results show a slight fluctuation in the measured amplitude and phase values, ranging from 5.523 kΩ to 5.529 kΩ and from - 0.1° to 0.13°, respectively, with the increase in frequency from 100 Hz to 10 kHz, as depicted in Figure 4.11 (a). It is clear that the amplitude and phase values remained stable despite the change in the frequency. The average error of the proposed system compared to the multimeter was 1.53%.

In the subsequent experiment, the proposed system was investigated with a basic series RC circuit. The circuit used a resistor of 5.6 kΩ, a capacitor of 47 nF, and a sweep frequency ranging from 500 Hz to 10 kHz. Figure 4.11 (b) depicts the data concerning the amplitude and phase in the series RC circuit. The data reveals a notable impedance value at the low-frequency range attributed to the effect of the capacitor. As frequency increases, the impact of capacitors decreases, resulting in a decline in the

magnitude and phase of the circuit impedance towards the value of the resistor (5.6 kΩ) and 0 degree, respectively. The measured results were in accordance with the theory of the circuits. The obtained results were then analyzed to identify the R and C values measured at different frequencies. As shown in Figures 4.11 (c) and (d), the error of R was below 2% and C was below 4% across the full frequency range from 500 Hz to 10 kHz. Hence, the experiment results confirm that the customized AD5941 module is capable of accurately determining the values of R and C in a series RC circuit.

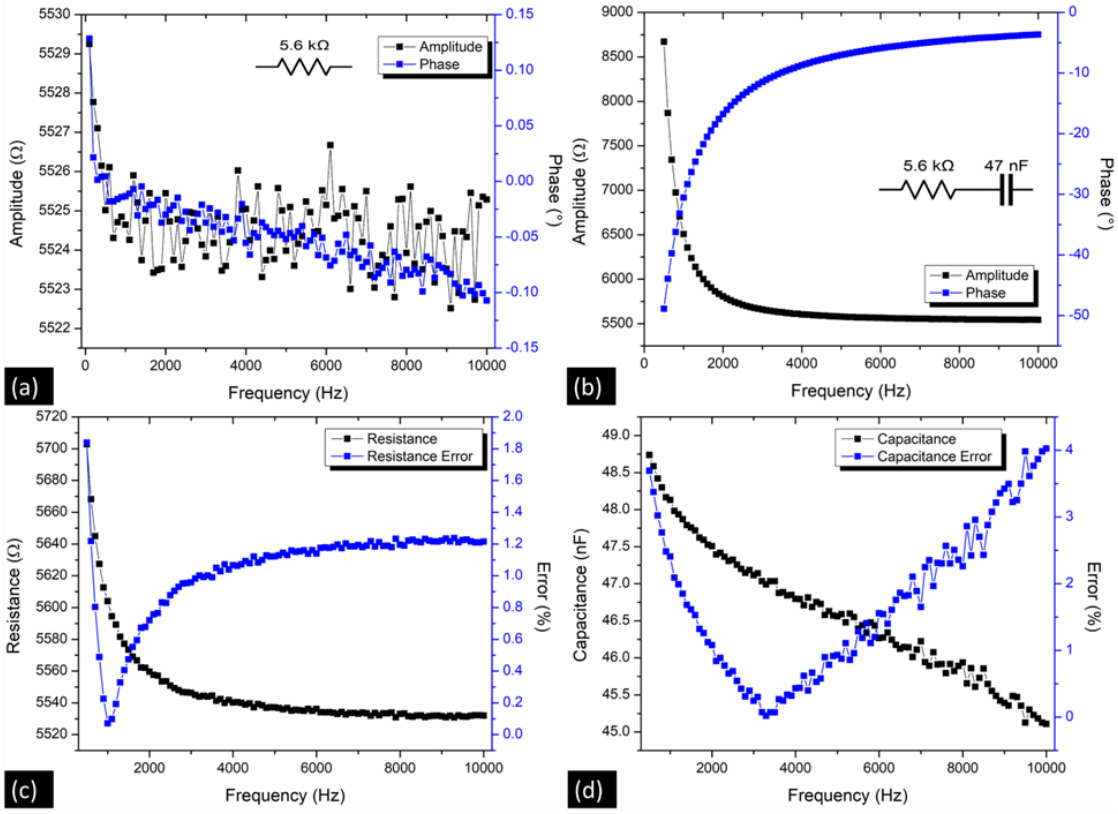

Figure 4.11: Measurement results of the AD5941 module on the resistor R and series RC circuit, a) measured resistance of 5.6 kΩ, b) Bode plots of amplitude and phase corresponding to the series RC circuit, c) Estimated resistance of the 5.6 kΩ resistor in the series RC circuit at full frequency range, d) Estimated capacitance of 47 nF capacitor at full frequency range

To prove the ability of electrical impedance spectroscopy applied for biosensors, a Randles circuit was set to investigate the performance of the proposed system. The Randles equivalent circuit is a popular model used in electrochemistry and electrochem-

ical impedance spectroscopy to describe the processes at the electrochemical interface, including an active electrolyte resistance (R_S) in series with the parallel combination of the double-layer capacitance (C_{dl}) and the charge transfer resistance (R_{ct}). In this circuit, the values of R_S, C_{dl} and R_{ct} were 5.6 kΩ, 47 nF and 4 kΩ respectively. The system was set with a scan frequency ranging from 100 Hz to 10 kHz. Figure 4.12 displays the Bode and Nyquist plots corresponding to this circuit configuration. As the frequency increases, the amplitude decreased from 10 kΩ to approximately 5.6 kΩ, while the phase initially shifted from 0 degrees toward -90 degrees before returning to 0 degrees, as depicted in the Bode plot (Figure 4.12 (a)).

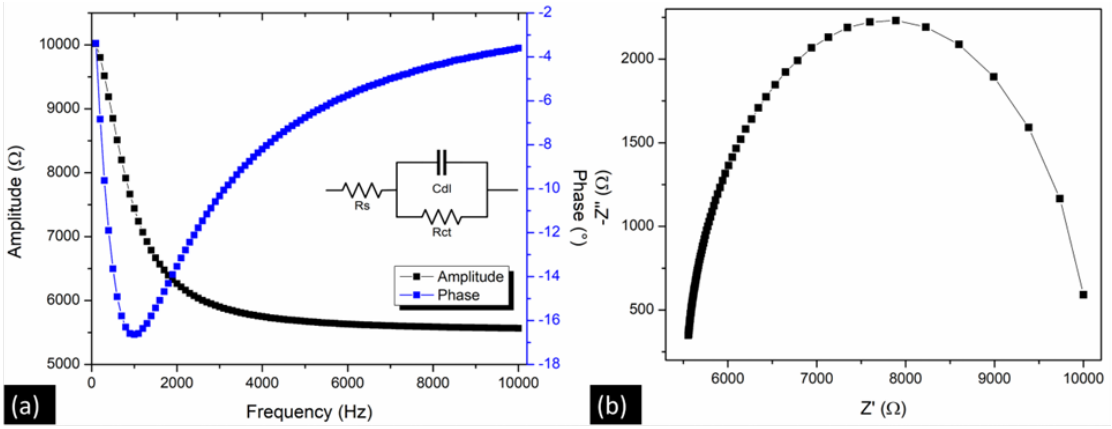

Figure 4.12: The investigation result of the proposed system with the Randles circuit; (a) Bode plot; (b) Nyquist plot. The values of R_S, C_{dl} and R_{ct} are 5.6 kΩ, 47 nF and 4 kΩ respectively. The scan frequency ranges from 100 Hz to 10 kHz

Similar results were also observed on the Nyquist plot in Figure 4.12 (b). This can be explained that at high frequencies, C_{dl} had an impedance close to zero and the circuit impedance mainly came from R_S. Therefore, the beginning of the semi-circle was R_S with a resistance value of 5.6 kΩ. In range of low frequencies, the impedance of C_{dl} was very high and all the current flowed through R_{ct}. So, the impedance of the circuit at the right end of the semi-circle was $R_S + R_{ct}$, nearly 10 kΩ. Therefore, it is easy to determine the elements of the Randles circuit through the Nyquist plot.

4.8 Conclusion

This chapter presents the development of a novel and compact system for electrochemical and impedance measurements based on AD5941 IC. The system was designed and fabricated based on the multi-layer PCB technique combined with 3D printing technology. The experimental results show the system was suitable to perform the CV and impedance measurements. The performance of the proposed system was comparable to commercial devices, while its cost was significantly lower. Besides, a low-cost and compact system integrating a preconcentrator and electrochemical measurements for protein preconcentration and detection was also developed. The system was designed and manufactured using a combination of multilayer printed circuit board and monolithic aluminum processing techniques. Experimental results show that the system can generate a voltage ranging from 15 V to 90 V with high accuracy and fast response time. These output voltages were supplied to the preconcentration chip to concentrate BSA-FITC proteins. The result shows the chip exhibited successful operation in both depletion and enrichment modes. Specifically, fluorescence intensity increased from 28 A.U to 55 A.U within seven minutes of applying voltages, confirming the efficacy of the proposed system in protein pre-concentration. Besides, CV and EIS electrochemical measurements were investigated using the standard redox solution and Randles equivalent circuit, respectively. The results indicate that the performance of the proposed system was comparable to that of commercial devices while offering significantly lower costs. In the future, this system holds potential for use in the medical field to detect the presence of biological molecules and diagnose diseases through electrochemical and impedance measurements. This presents promising prospects for the system's application in medical research and diagnosis, facilitating improvements in disease diagnosis processes, particularly for conditions such as cancer and other diseases related to the body's biology and chemistry. The research findings have been disseminated through publications in prestigious journals and presentations at leading conferences [85, 86, 87, 88].

Chapter 5

Development of integrated microfluidic chip for protein concentration and detection

This chapter presents the development of microfluidic chips for BSA and NSE detection. For BSA detection, the chip integrates a preconcentrator and an immunosensor, as discussed in Chapters 2 and 3, respectively. The chapter begins with the proposed chip design, followed by a detailed explanation of the fabrication processes for the electrochemical biosensor and the microfluidic channels. Finally, experimental procedures and results are presented to evaluate the performance of the developed chip.

5.1 Materials and apparatuses

The gold substrate was produced by successively depositing a thin layer of titanium and gold on microscope glass (Duran Group, Huntington Beach, California, USA) through a standard sputtering coating process. S1813, SU-8 50 photoresists, and MP-315 developer were used to fabricate gold electrodes purchased from Shipley MicroChem Co., Ltd. (Westborough, MA, USA). Gold Etchant (AuR-1091) and Titanium Etchant (TIR-8051B) chemicals purchased from AppliChem Technology Co., Ltd. (Miaoli County, Taiwan) were used to remove the gold and titanium, respectively. Polydimethylsilox-

ane (SYLGARD™ 182, Dow Corning, USA) was utilized to fabricate the microfluidic chip. Silver nitrate ($AgNO_3$) was purchased from Sigma-Aldrich Chemical Co (St. Louis, Missouri, USA). Ammonia water (NH_4OH, Choneye Pure Chemicals, 25%) and potassium chloride (KCl, Shimakyu Company Limited) were used to form Ag and AgCl layers on the reference electrode. 11-Mercaptoundecanoic acid (11-MUA), N-(3-Dimethylaminopropyl)-N′-ethyl carbodiimide hydrochloride, N-Hydroxysuccinimide and bovine serum albumin (BSA) were purchased from Sigma-Aldrich Chemical Co (St. Louis, Missouri, USA). Neuron-specific enolase (NSE) and anti-neuron-specific enolase (anti-NSE) were employed as the antigen-antibody pair, purchased from Sigma-Aldrich Chemical Co (St. Louis, Missouri, USA).

The bonding process and filling of the solution were supported by a micro-inspection zoom lens system (ZOOM 125C, OPTEM, Japan) equipped with a Moticam 2000 microscope camera (Motic Microscopes Company, San Antonio, US) and a light source (LSH-150, Taiwan Fiber Optics, Inc., Taiwan). The experimental results were observed under an inverted microscope system (CKX41, Olympus, Melville, NY, USA) equipped with a DP71 Olympus digital camera. A portable instrument (PalmSens4, PalmSens BV, 3995 GA Houten, Netherlands) was used to perform electrochemical impedance spectroscopy (EIS) measurements.

5.2 Electrochemical biosensor design for NSE detection

The proposed biosensor consists of three main electrodes, including working, counter, and reference electrodes, as shown in Figure 5.1. The working and counter electrodes were made of gold-sputtered material, while the reference electrode was made of Ag/AgCl. The working electrode played a crucial role as the site for electrochemical reactions. This electrode had a circular shape with a radius of 30 µm and was positioned between the counter and reference electrodes. It was also 30 µm away from the other two electrodes. All these electrodes were situated within a straight microfluidic channel, which had a width of 150 µm and a height of 40 µm. Chemicals and solutions for the

electrode surface functionalization process were introduced into the channel through an inlet. The electrodes were fabricated on the microscope glass, while the channel was fabricated on PDMS material using photolithography and soft lithography.

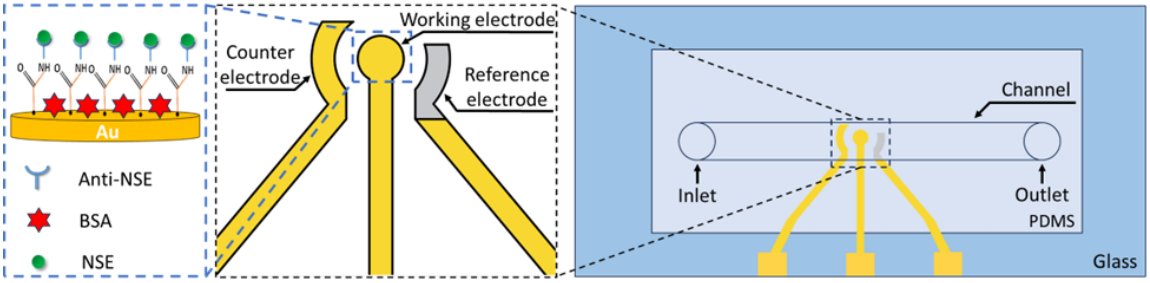

Figure 5.1: Microfluidic chip design, including an electrochemical biosensor integrated inside the miro-channel

5.3 Electrochemical biosensor design for BSA pre-concentration and detection

The microfluidic chip design was divided into two main parts, including a protein pre-concentrator and a bioelectrochemical sensor, as shown in Figure 5.2. The protein pre-concentrator had a dual-gate configuration with a main channel in the middle and two symmetrical sub-channels. The two sub-channels were connected to the main channel through a Nafion membrane. The dual gate represented two Nafion membrane layers connecting between the main channel and sub-channels. The micro-channel had dimensions of 100 µm in width and 40 µm in height. The main channel was 150 µm away from the sub-channels. The main channel was filled with target proteins, i.e., BSA-FITC, while the two sub-channels were filled with PBS 1X, pH 7.4. A bioelectrochemical sensor was designed to integrate within the channel at the designated enrichment area. The biosensor consisted of three electrodes, including working, counter, and reference electrodes. The working and counter electrodes were made of gold materials, while the reference electrode was made of Ag/AgCl. The working electrode was circular in shape with a diameter of 30 µm and positioned 30 µm away from other electrodes.

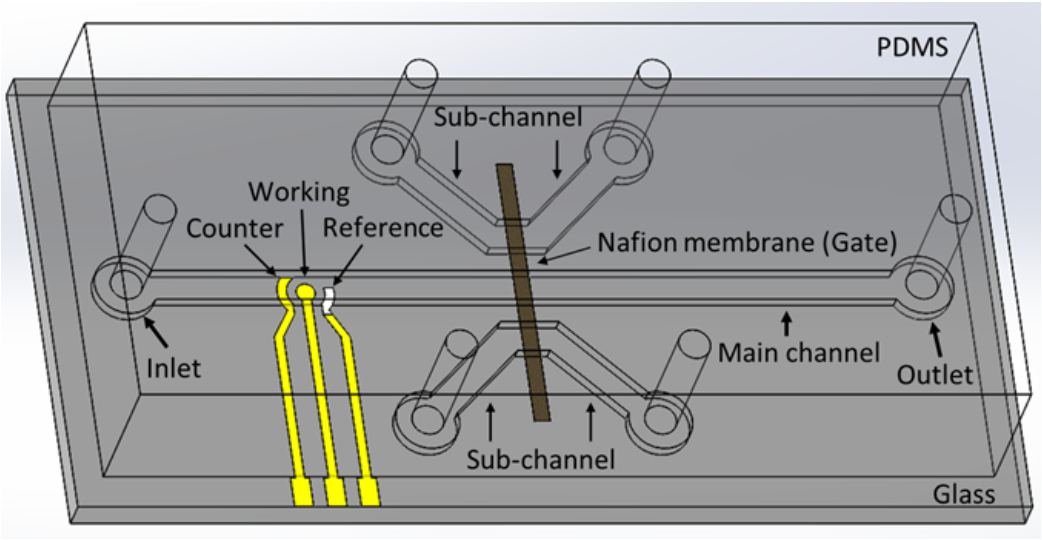

Figure 5.2: Design of the proposed microfluidic chip featuring a protein pre-concentrator and an bioelectrochemical sensor

5.4 Electrochemical biosensor fabrication process

The fabrication process of the electrode structure consists of six main steps, including coating photoresist, exposure to UV light using the mask, developing, gold etching, titanium etching, and photoresist removal, as shown in Figure 5.3. At first, the gold-sputtered glass was cleaned by an IPA solution, and DI water in an ultrasonic vibration tank before being dried by nitrogen. Then, the clean gold-sputtered glass was coated with an S1813 photoresist layer using a spin coater. The photoresist layer was cured and dried at 90 ^{o}C for 2 minutes. In the second step, a mask featuring the printed electrode structure was aligned and placed over the photoresist layer. Subsequently, both the mask and the photoresist layer were exposed to UV light for 30 seconds. Then, the glass substrate was immersed in MP-351 developer solution to remove the photoresist areas exposed to UV light, leaving behind the desired electrode-shaped photoresist layer on the glass substrate. In the next steps, exposed gold and titanium areas were corroded by AuR-1091 and TIR-8051B chemicals, respectively. Finally, the covering photoresist layer was removed using an acetone solution, revealing a clear gold electrode structure on the glass substrate.

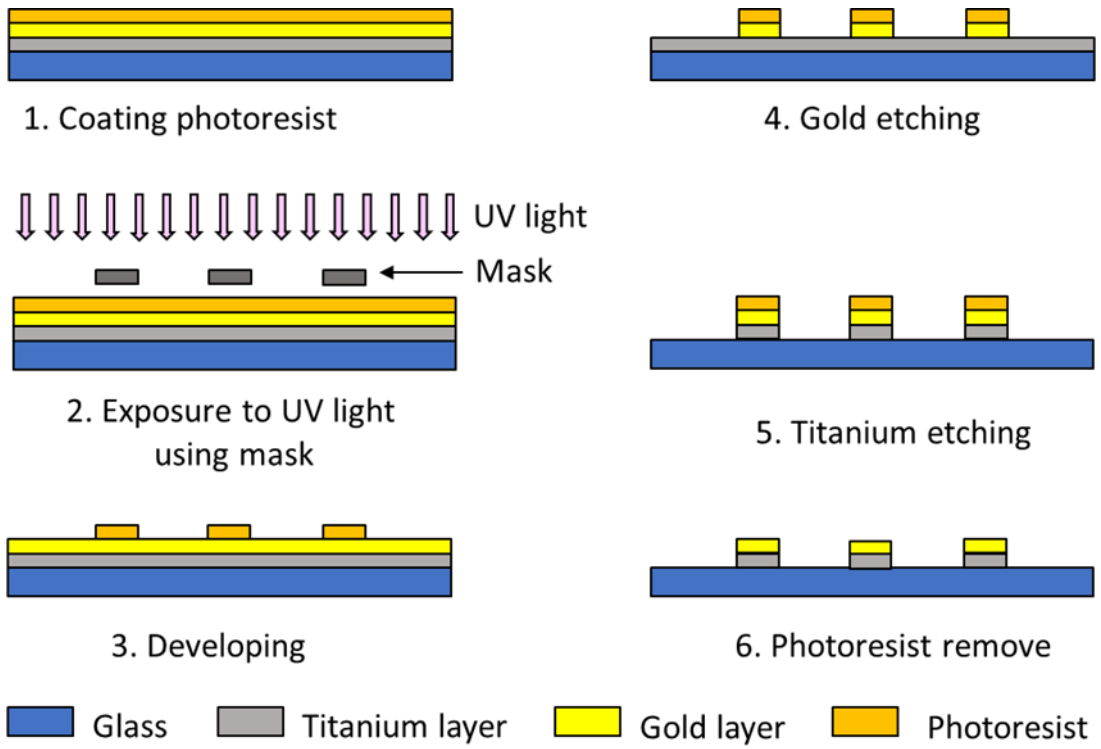

Figure 5.3: The gold electrode fabrication process on the glass substrate using the photolithography technique

After being fabricated, the gold electrodes were cleaned with IPA solution, DI water, and nitrogen-dried. Subsequently, the initial three steps in the aforementioned process were reiterated using another mask to selectively expose only the reference electrode, covering the remaining electrodes with a photoresist layer. The fabrication process of the reference electrode involved two phases: silver electroplating and silver chloride coating, as depicted in Figure 5.4.

In the initial phase, the electrodes were immersed in the silver nitrate solution containing 0.3 M $AgNO_3$ and 1M NH_3. Subsequently, a potential difference of -0.2 V was applied to the reference electrode and a silver bar, both of which were immersed in the silver nitrate solution for 1 minute, as shown in 5.4 a. During the silver electroplating process, at the reference electrode surface, Ag^+ was converted into Ag (Equation 5.1). Meanwhile, at the silver bar surface, water (H_2O) was electrolyzed into hydrogen ions (H^+) and oxygen (O_2), as shown in Equation 5.2. Figure 5.5 (a) illustrates the experimental result, wherein a silver layer has been deposited onto the surface of the

reference electrode.

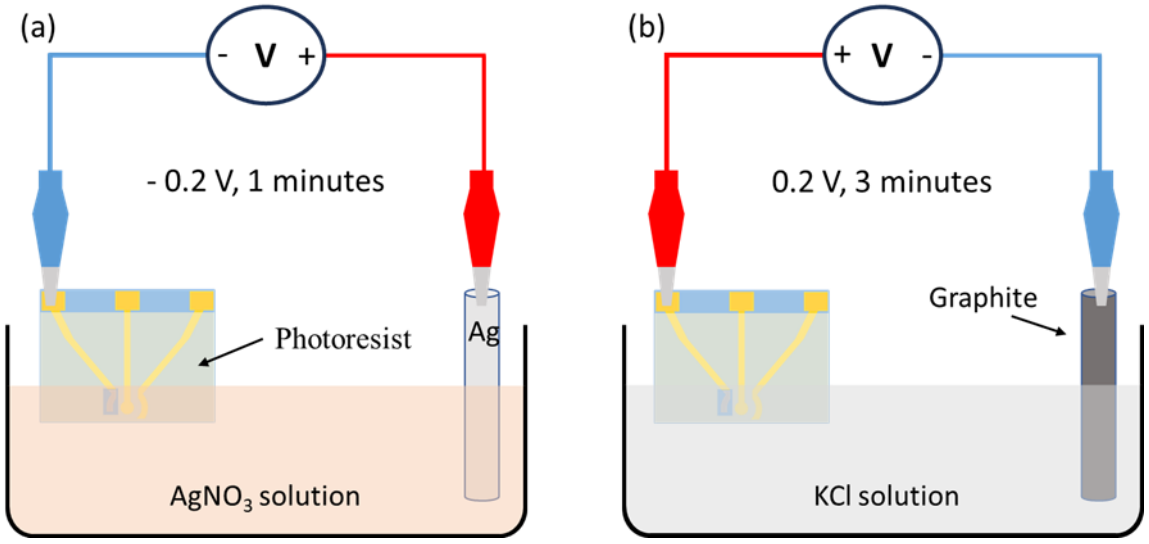

Figure 5.4: The reference electrode fabrication process: (a) silver electroplating; (b) silver chloride coating

At anode:

$$Ag^{+} + 1e \rightarrow Ag \tag{5.1}$$

At cathode:

$$2H_2O \rightarrow 4H^{+} + O_2 + 4e \tag{5.2}$$

In the second phase, the silver nitrate solution was replaced by 0.1 M KCl solution, and the Ag bar was replaced by a graphite bar, as shown in Figure 5.4 (b). Following this, a potential difference of +0.2 V was applied to the reference electrode and the graphite bar for 3 minutes. During this period, at the reference electrode surface, Ag was oxidized to Ag^{+} and released one electron (Equation 5.3).

Then, Ag^{+} combined with Cl^{-} in the solution to form AgCl on the electrode surface (Equation 5.4). At the graphite electrode surface, water underwent electrolysis to produce hydrogen gas (H_2) and hydroxide ions (OH^{-}) according to Equation 5.5. The experimental results demonstrated the formation of an AgCl layer on the reference electrode, resulting in a smoother and more uniform electrode surface, as illustrated in Figure 5.5 (b). Figure 5.5 (c) presents the actual image of electrodes after fabrication.

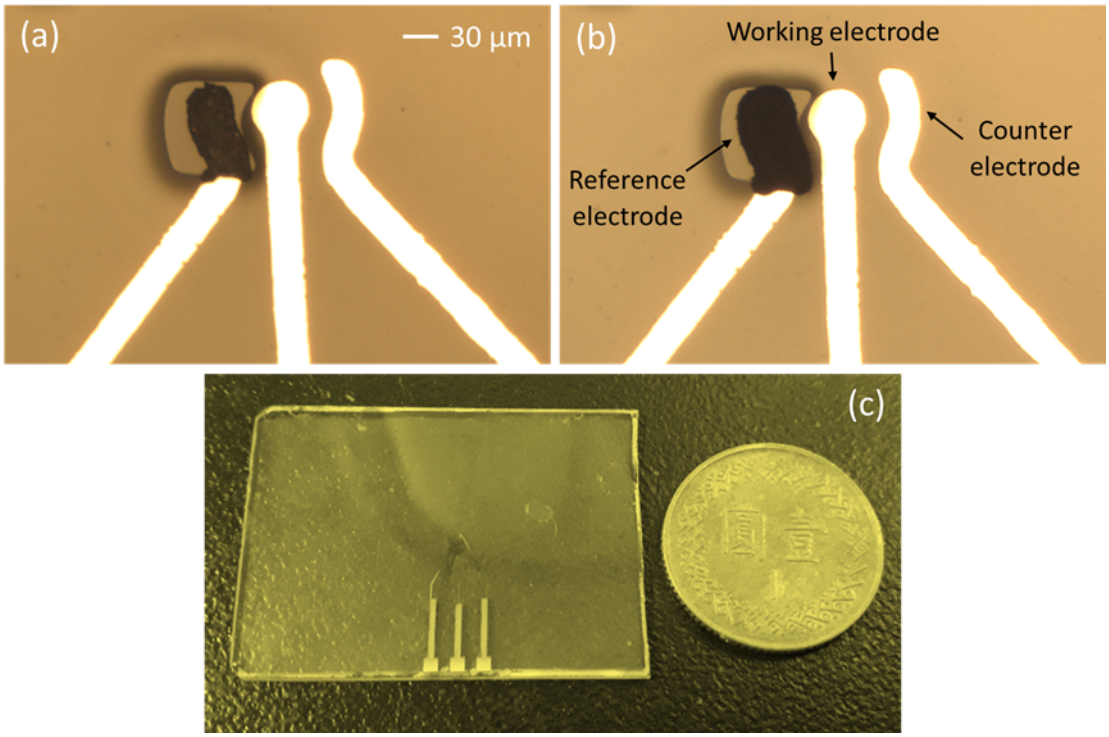

Figure 5.5: The fabricated electrode structure: (a) After silver electroplating; (b) After silver chloride coating; (c) Actual image of electrodes

At anode:

$$Ag \rightarrow Ag^{+} + 1e \tag{5.3}$$

$$Ag^{+} + Cl^{-} \rightarrow AgCl \tag{5.4}$$

At cathode:

$$2H_2O + 2e \rightarrow H_2 + 2OH^{-} \tag{5.5}$$

5.5 Microfluidic channel fabrication process

The microfluidic channel and microfluidic chip were fabricated based on photolithography and soft lithography techniques, as shown in Figure 5.6. The photolithography was implemented on a silicon wafer to produce a micro-channel mold, comprising four primary steps as depicted in Figure 5.6 (a). Firstly, the silicon wafer was cleaned with IPA solution, DI water in an ultrasonic vibration tank, and dried nitrogen. Then, the clean silicon wafer was coated with an SU-8 50 photoresist layer using a spin coater.

The photoresist was cured and dried by positioning the silicon wafer on a hot plate at 65 degrees for 10 minutes, then at 90 degrees for 20 minutes. A mask outlining the channel structure was subsequently aligned on top of the wafer. UV light exposure was then administered to the silicon wafer and mask assembly. Finally, a gentle washing with acetone solution was employed to eliminate undesired photoresist from the wafer surface. Unlike the S1813 photoresist, SU-8 50 served as a positive photoresist, wherein UV-irradiated areas of the photoresist remained intact while the unirradiated areas were removed.

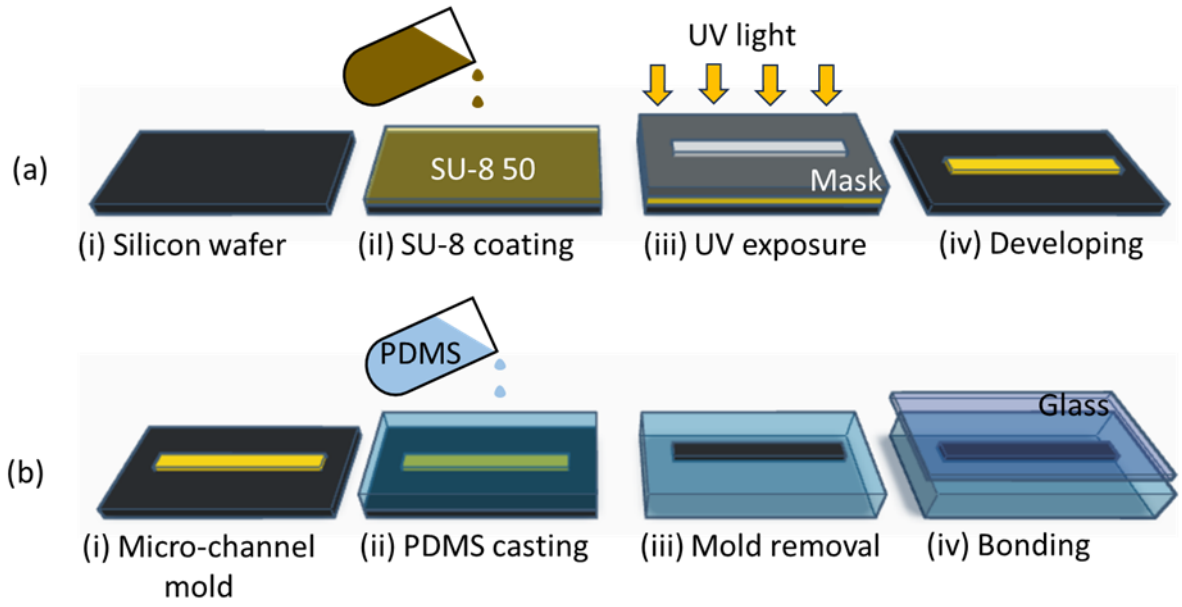

Figure 5.6: Microfluidic channel and microfluidic chip fabrication process using (a) photolithography and (b) soft lithography techniques

After the micro-channel mold fabrication, the microfluidic channel or microfluidic device was realized according to the process shown in Figure 5.6 (b). At first, a micro-channel mold was gently cleaned with IPA solution, DI water and dried with nitrogen. Subsequently, a mixture of PDMS and its curing agent was poured into the dish to achieve a certain thickness. The dish was then transferred to a vacuum chamber for 30 minutes to remove air bubbles and subsequently placed on a hot plate set to 90 degrees for 1 hour to cure the PDMS. Finally, the PDMS region containing the microchannel was carefully bonded to the glass substrate containing the fabricated gold electrode

using the plasma bonding technique, forming a microfluidic chip.

Figure 5.7 displays the fabrication result of the proposed chip with the electrochemical electrode positioned inside the main channel of the pre-concentrator. The left inset displays a close-up of the electrochemical electrode configuration, with annotations identifying the reference, working, and counter electrodes. These electrodes are strategically positioned within the main channel, enabling electrochemical detection through redox reactions, which facilitate the quantification or identification of target analytes. The right inset focuses on the membrane region and sub-channels, illustrating the structural configuration surrounding the Nafion membrane.

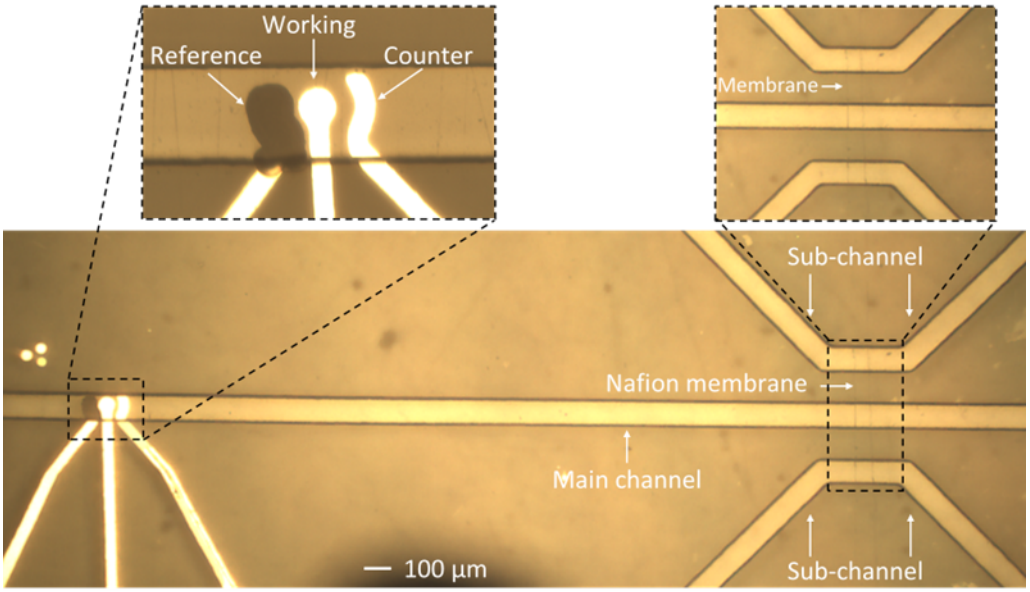

Figure 5.7: The proposed microfluidic chip for BSA pre-concentration and detection after fabrication

5.6 Gold electrode surface functionalization process

After the fabrication of the microfluidic chip, the gold electrode surface underwent functionalization following the process outlined in Figure 5.8. This process aimed to immobilize anti-NSE onto the electrode surface and enable the detection of NSE through specific binding interactions between the antibodies and the target antigen. The process was divided into five main steps, including self-assembled monolayer formation,

carboxyl group activation, anti-NSE immobilization, surface blocking, and the binding of NSE. 11-MUA was dissolved in ethanol, while other chemicals were dissolved in PBS 1X solution. The solutions were injected into the micro-channel through a 20 µl pipette connected to a silicon tube.

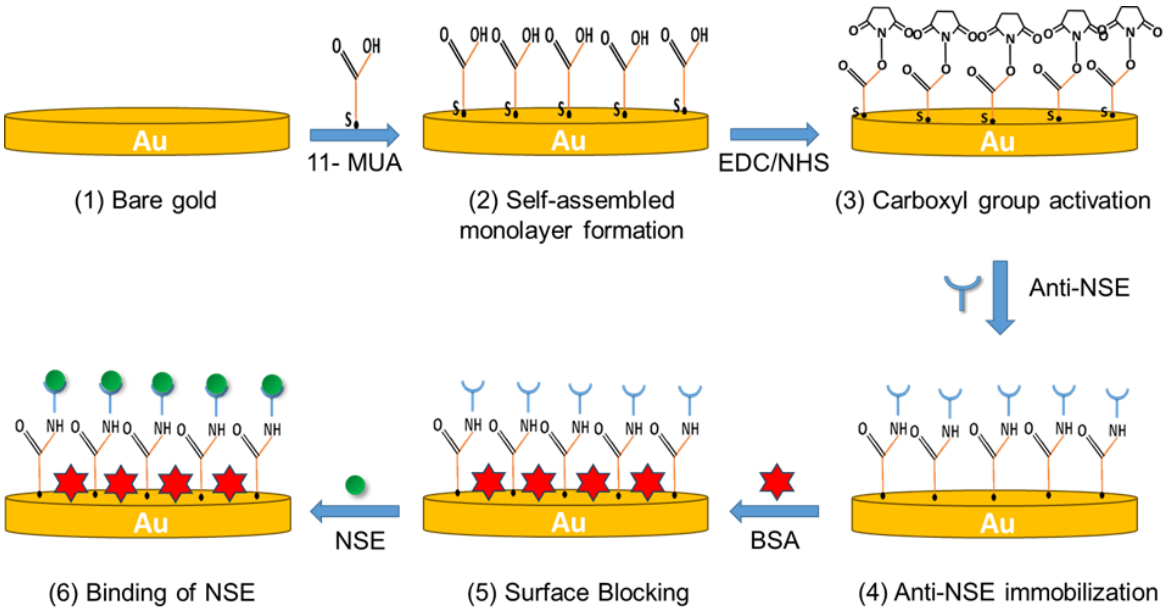

Figure 5.8: Gold electrode surface functionalization process in microchannels for anti-NSE immobilization and NSE protein detection

Firstly, 10 µl of 5 mM 11-MUA solution was introduced into the electrode area inside the micro-channel and incubated for 24 hours. The inlet and outlet of the microchannel were tightly sealed with tape to prevent water evaporation. During incubation, the thiol group (S-H) of 11-MUA combined with the gold atom to form a stable Au-S bond, creating a self-assembled monolayer on the electrode surface. After incubation, the electrode was cleaned gently with ethanol and DI water to remove unbound 11-MUA molecules from the electrode surface. In the next step, the carboxyl (–COOH) group of 11-MUA was activated by the mixture solution of 0.4 M EDC and 0.2 M NHS. The activation process took 30 minutes to form NHS ester groups on the electrode surface. Subsequently, the electrode was incubated in a 50 µg/ml anti-NSE solution for 2 hours. During this period, the ester groups readily bonded to the antibody's amine group (NH_2). 5 µM BSA protein was utilized to bind to residual ester groups or block

the electrode surface, thereby preventing nonspecific binding of NSE to the electrode surface. Finally, the electrode was incubated in NSE protein solution at different concentrations for 2 hours to facilitate the formation of specific bindings between NSE and anti-NSE. After each step, PBS 1X solution was injected into the micro-channel to remove unbound molecules from the electrode surface.

For the microfluidic chip for BSA protein pre-concentration and detection, the gold electrode surface functionalization process was repeated with anti-BSA. Biotin was used to block the electrode and prevent nonspecific binding between antigens and the electrode surface. Then, the pre-concentration process was used to obtain a high local protein concentration at the electrode surface and enhance the protein binding efficiency on it.

5.7 Experimental setup

For the microfluidic chip for NSE detection, The electrode was connected to the Palmsen 4 device according to each implemented NSE concentration to perform EIS measurements in PBS 1X solution. Several measurement parameters were set up, including the applied voltage of 10 mV, the frequency ranging from 0.1 Hz to 200.000 kHz.

A simplified Randles circuit model was also utilized to fit the data from the measurement results. Here, R_S, R_{ct}, and C_{dl} were the solution resistance, the immobilized recognition layer's charge transfer resistance, and the capacitance measured between the gold electrode and the electrolyte solution, respectively. In order to confirm the success of the gold electrode surface functionalization process in binding target NSE protein, control experiments were conducted with the fabricated electrode that omitted the 11-MUA incubation step.

For the microfluidic chip for BSA pre-concentration and detection, the main channel was filled with 10 µM BSA-FITC solution, while the sub-channels were filled with PBS 1X solutions using the 10 µl pipette. The proposed chip was placed on the microscope. Then, the two terminals of the main channel were connected to the potentials of 30 V and 25 V, respectively, while the sub-channels were connected to 0 V to activate the

enrichment mode of the pre-concentrator. The protein concentration was then pushed to the biosensor area by adjusting the potential difference between the two ends of the main channel. The pre-concentration process was sustained for 1 hour before gently cleaning the main channel with PBS 1X solution to eliminate unbound molecules from the micro-channel, facilitating EIS measurements. The pre-concentration process was recorded by a digital camera integrated into the microscope and displayed on a monitor screen, as shown in Figure 5.9.

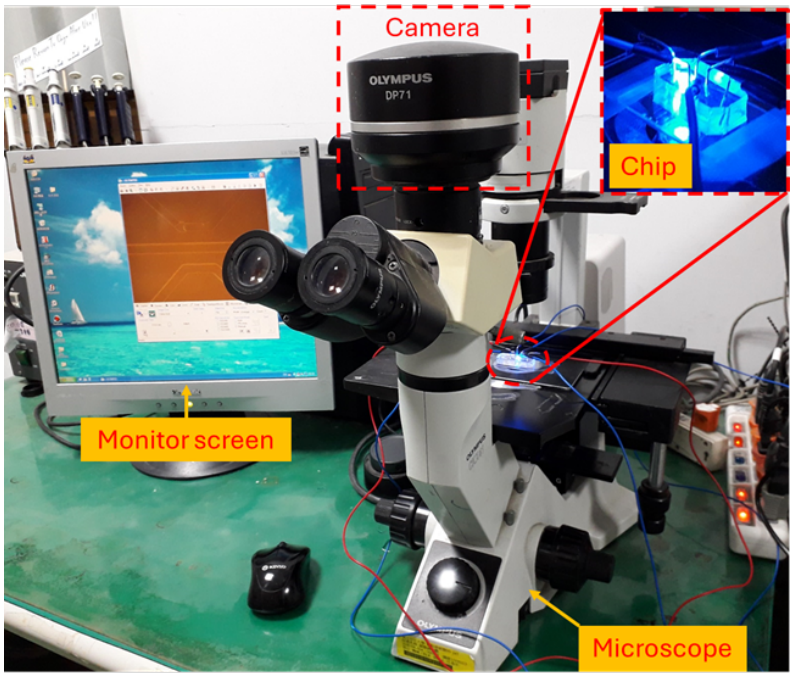

Figure 5.9: Experimental setup for protein pre-concentration process

5.8 Results of BSA protein pre-concentration and detection

For the protein pre-concentration process, the concentration zone was gradually formed after applying the potentials to the ends of the micro-channels. The fluorescence intensity of the protein concentration zone increased rapidly over time, as shown in Figure 5.10. The protein concentration increased 6 times, from 10 µM to 60 µM after 30 seconds. The concentration continued to increase to 100 µM and 250 µM after 45 seconds

and 80 seconds, respectively.

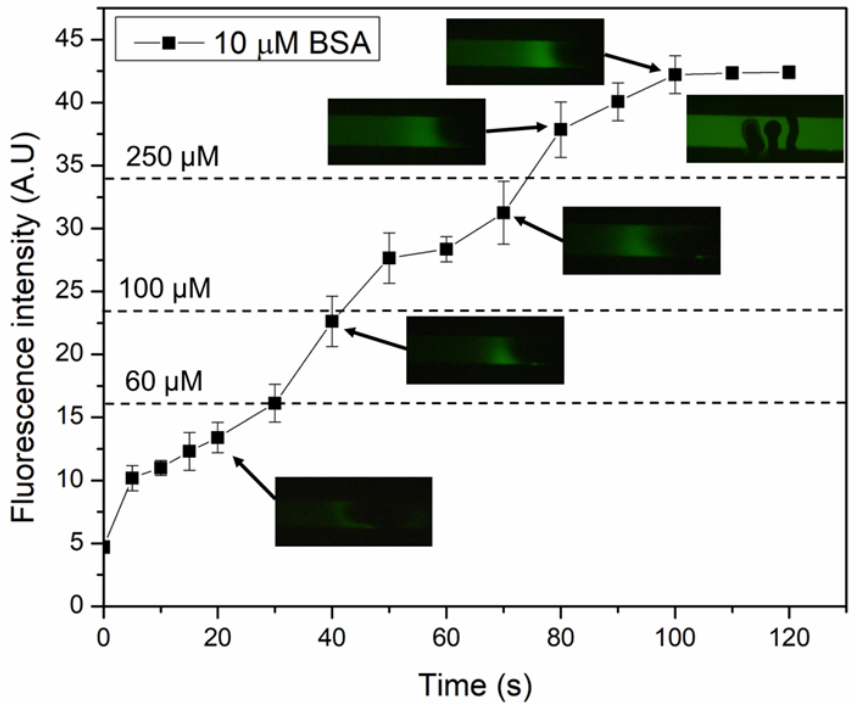

Figure 5.10: The fluorescence intensity change of the protein concentration zone during the protein pre-concentration process at the initial BSA protein of 10 µM

After 100 seconds, the fluorescence intensity of the protein concentration zone reached a saturation state. At this time, the protein concentration zone was pushed to the biosensing area and kept here for 1 hour. After 1 hour, PBS 1X solution was filled to the main channel to remove unbound BSA proteins from the microelectrode and micro-channel. The conjugation between anti-BSA and BSA is strong and highly specific. Anti-BSA selectively binds to BSA due to the unique epitopes (specific regions) on the BSA molecule that are recognized by the anti-BSA. The Palmsen 4 portable instrument was then connected to the biosensor to perform EIS measurements. Some measurement parameters were set up, including the applying voltage of 10 mV, a frequency range from 0.1 Hz to 200 kHz. The obtained impedance data was fitted using the Randles circuit model with R_s, R_{ct}, and C_{dl}, being the dynamic solution resistance, the charge transfer resistance, and the double-layer capacitance formed between the sensor surface and the electrolyte solution, respectively. In which, R_{ct} and C_{dl} represented the surface impedance of the biosensor.

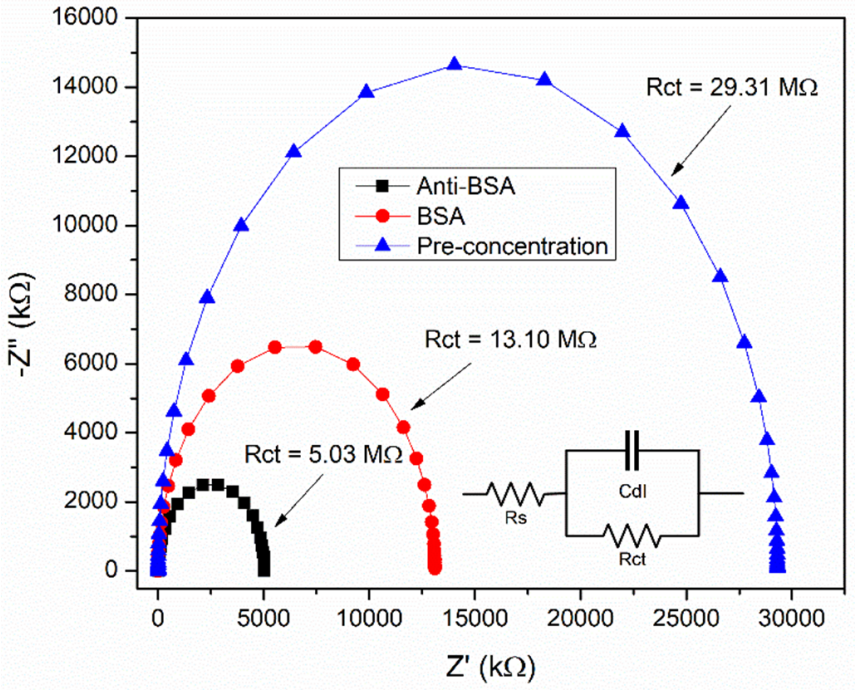

Figure 5.11: The change of EIS signal after the steps of anti-BSA immobilization, BSA incubation without preconcentration, and BSA preconcentration

The EIS measurements results are depicted in Figure 5.11, illustrating the EIS signals following the step of anti-BSA immobilization (black curve), after BSA protein pre-concentration (blue curve), and after BSA-FITC immobilization for 2 hours without the pre-concentration process (red curve). Here, the semi-circle corresponded to the surface impedance of the biosensor. As can be seen, the charge transfer resistance increased significantly after BSA-FITC proteins were concentrated and immobilized, demonstrating that BSA proteins were specifically bound to anti-BSA on the working electrode surface. The BSA protein layer hindered the exchange of electrons between the solution and the working electrode, resulting in an increase in the electrode surface impedance. Besides, the results also show that the charge transfer resistance in the case of protein pre-concentration (29.31 MΩ) was significantly higher compared to BSA immobilization without protein pre-concentration (13.10 MΩ). In other words, more proteins were specifically captured on the electrode surface during the protein pre-concentration process. This result also demonstrates the remarkable effectiveness of the protein pre-concentration process in signal amplification and protein detection.

The control experiment has been performed to confirm the success of the proposed process, as mentioned in our previous publication [79].

5.9 Results of NSE protein detection

Figure 5.12 illustrates the change in EIS signals before and after incubating 1000 ng/ml NSE at both the fully prepared and the control electrodes. The surface impedance for the fully prepared electrode increased sharply after NSE specifically bound to the electrode, as shown in Figure 5.12. The charge transfer resistance increased from 4.83 MΩ to 89.18 MΩ after NSE incubation, demonstrating the success of the proposed process. NSE antigens specifically bound to anti-NSE immobilized on the gold electrode surface, resulting in a decrease in surface impedance. By contrast, the EIS signal remained almost unchanged after the step of NSE incubation in the case of the control electrode (Figure 5.12 (b)). The surface impedance mostly remained unaffected without specific binding between NSE and anti-NSE on the electrode surface.

For different NSE concentrations, the experimental results show that the EIS signal changed significantly when NSE concentration increased, as shown in Figure 5.13 (a). The expansion of the semi-circle diameter in the EIS signal correlated with the concentration increase, signifying a corresponding rise in surface impedance. In other words, as the concentration of protein captured on the electrode increases, the charge exchange between the electrode and the solution is inhibited. As a consequence, this inhibition leads to an escalation of the electrode surface impedance. Figure 5.13 (b) shows the relationship between the charge transfer resistance and NSE concentrations. As can be seen, charge transfer resistance increased from 24.54 MΩ to 89.18 MΩ when the NSE concentration increased from 10 ng/ml to 1000 ng/ml. The relationship between them was modeled by a logarithmic function, expressed as equation:

$$R_{ct} = 12.82 * ln[NSE]\breve{}3.3181(R^2 = 0.9791) \tag{5.6}$$

The LOD of sensor was calculated using Equation 5.7, where S represented the standard deviation and D denotes the slope. The result show the LoD of sensor was approximately 1.005 ng/ml, with the standard deviation of 0.0212 MΩ.

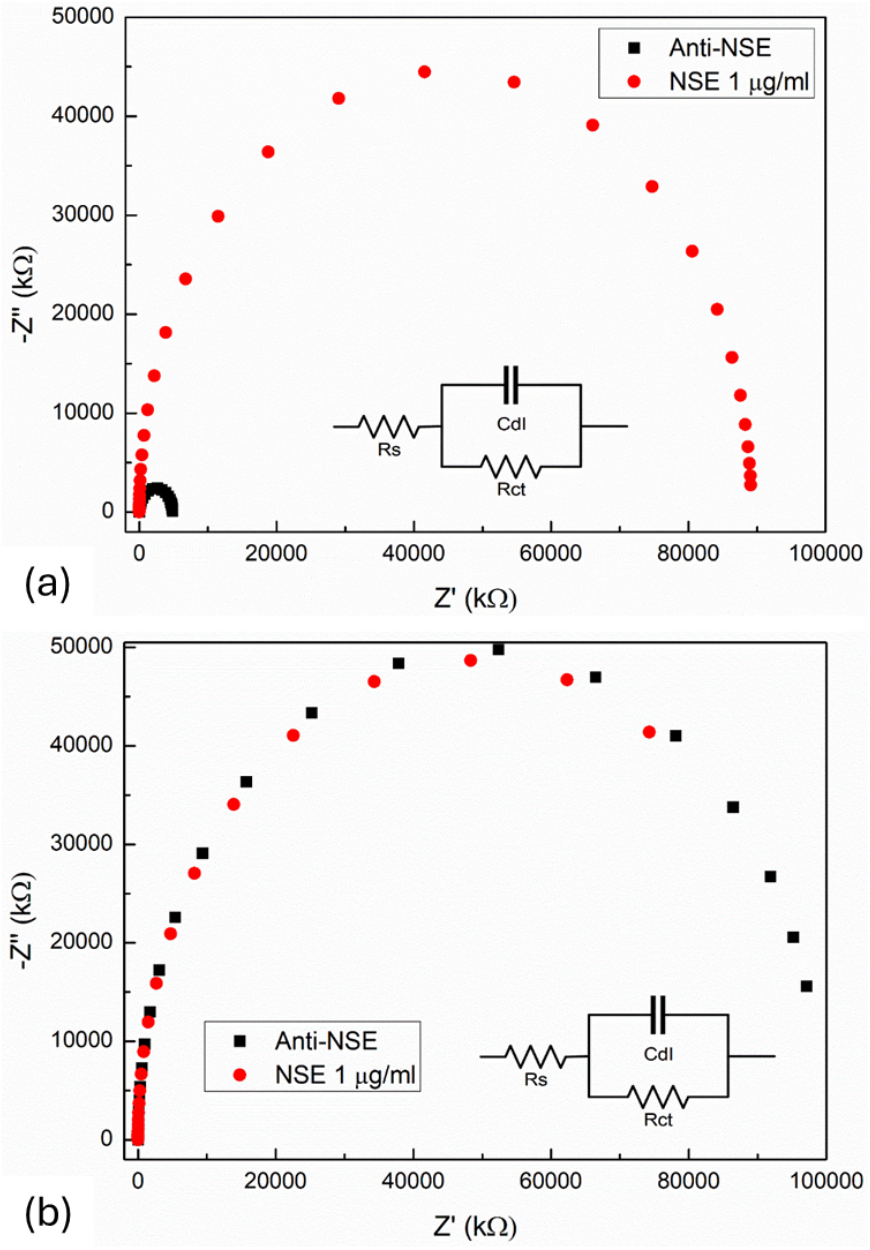

Figure 5.12: The change of EIS signals after anti-NSE 1 µg/ml NSE incubation steps at different electrodes to confirm the success of the gold electrode surface functionalization process in binding target NSE protein; (a) the fully prepared electrode and (b) the control electrode without the 11-MUA incubation step.

Utilizing this established relationship, the NSE concentration can be readily quantified through the charge transfer resistance derived from EIS measurements. Significantly, the NSE concentration threshold for small cell lung cancer, particularly at 35

ng/ml, falls within the testing range as well as the LOD of the proposed microfluidic chip. Hence, the microfluidic chip can be effectively utilized for NSE protein testing to diagnose lung cancer.

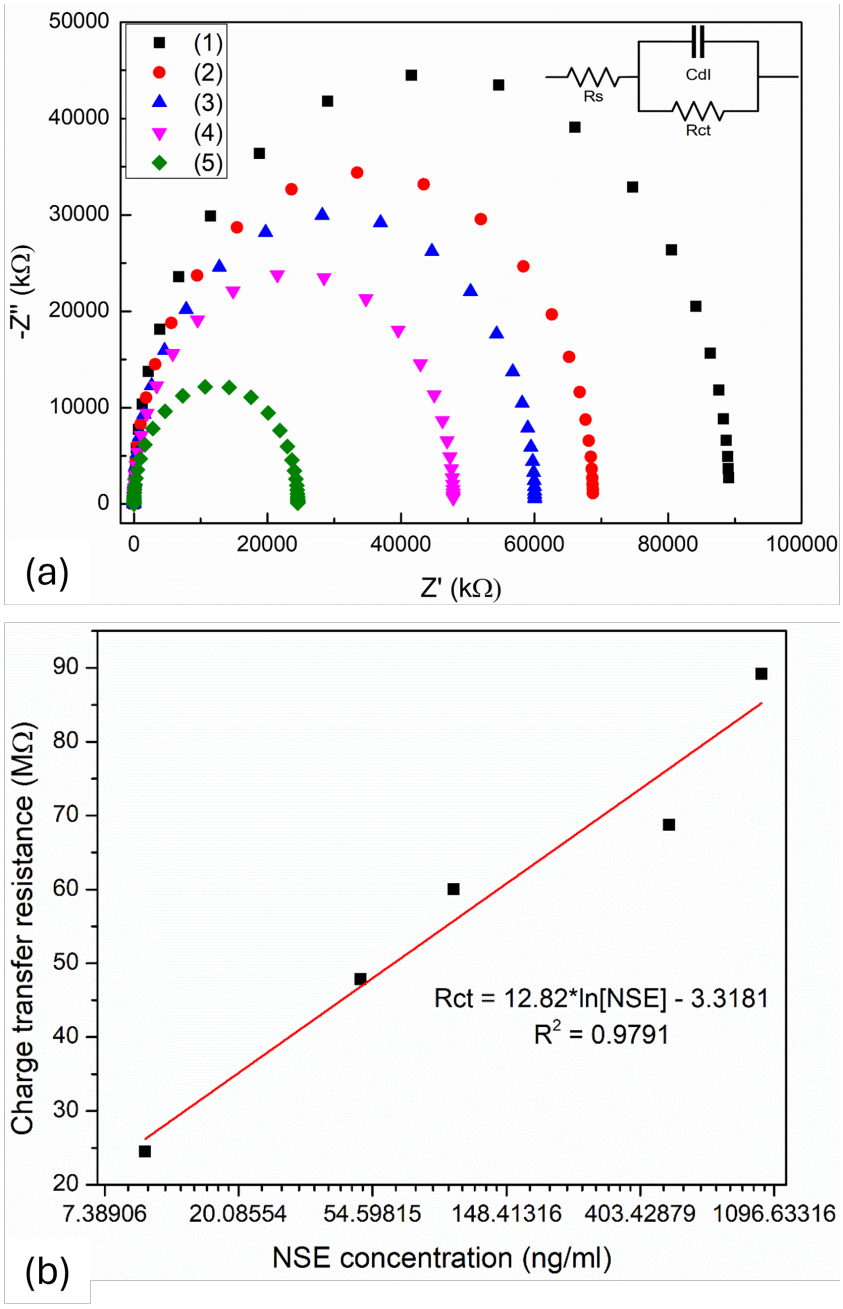

Figure 5.13: (a) The change of EIS signals at different NSE concentrations: (1) 1000 ng/ml, (2) 500 ng/ml, (3) 100 ng/ml, (4) 50 ng/ml (5) 10 ng/ml; (b) The relationship between the charge transfer resistance and the NSE concentration

$$LOD = \frac{3 \times S}{D} \tag{5.7}$$

Table 5.1 presents a performance comparison between different NSE detection systems. It is evident that the LOD achieved by the proposed microfluidic chip surpassed that of the Enzyme-linked Immunosorbent Assay Kit using the colorimetric method and other systems. This highlights the potential of the chip to replace traditional NSE protein testing systems in the future.

Table 5.1: Performance comparision table between different NSE detection system

Detection methods	**Sensitivity/ Linear Range**	**Limit of detection (ng/ml)**	**Refs**
Colorimetric, ELISA kit	5.0–178 (ng/ml)	1.2	[6]
Imaging Ellipsometry	19.6 (grayscale value/ log(ng/ml))	2	[91]
Aptamer based surface plasma resonance assay	0.0945 (relative response unit/nM)	183.3	[126]
Electrochemical	12.82 (MΩ/ln(ng/ml)])	1.005	This work

5.10 Conclusion

In this chapter, a microfluidic chip was proposed and developed to detect and quantify NSE concentrations for lung cancer diagnosis. The proposed chip included an electrochemical biosensor integrated inside a straight micro-channel. The electrode was fabricated on gold glass using the photolithography technique, while the microchannel was created using photolithography and soft lithography techniques. This study also proposed a process for depositing Ag and AgCl layers onto the gold material for reference electrode fabrication. Following fabrication, the working electrode underwent modification to attach anti-NSE to its surface. Five different NSE concentrations ranging from 10 ng/ml to 1000 ng/ml were used to specifically bind to anti-NSE, and the resulting change in surface impedance was recorded through EIS measurements. The

result shows that the electrode surface impedance increased when NSE concentrations increased. The relationship between the charge transfer resistance and the NSE concentration was a logarithmic equation, as $R_{ct} = 12.82 * ln[NSE]\check{}3.3181 (R^2 = 0.9791)$. Furthermore, this chapter also presents the development of a microfluidic platform for protein pre-concentration and detection. The proposed chip consisted of a bioelectrochemical sensor integrated inside the main channel of a protein preconcentrator with a dual-gate structure. The microfluidic chip was fabricated by photolithography and soft lithography techniques. The reference electrode was formed by electroplating Ag and AgCl layers on the gold electrode. The gold electrode surface underwent a functionalization process to attach anti-BSA before the preconcentration of BSA protein on the sensing area. The proposed microfluidic platform has been demonstrated for the first time. The experimental results show that BSA proteins were successfully concentrated after applying the electrical potentials to the pre-concentrator. Besides, EIS measurements demonstrated the presence of BSA protein on the electrode surface and the outstanding efficiency of the protein pre-concentration process in signal amplification for protein detection. Though optimizations and in-depth experiments, including testing with real samples need to be implemented in subsequent research, the obtained results verify the effectiveness and feasibility of the integration of the protein manipulation and detection technique for the future development of a Lab-on-a-Chip platform. The research findings have been disseminated through publications in prestigious journals [89, 90].

Conclusions and future works

In this study, a protein detection system has been successfully developed, presenting a promising platform for point-of-care testing in biomedical diagnostics. This system consisted of a microfluidic chip integrated with a protein pre-concentrator, an electrochemical immunosensor, and measurement and control circuits. The pre-concentrator featured a dual-gate structure, with a main microchannel for sample actuation and two sub-microchannels to generate depletion regions. These channels were connected through a sub-micron thick ion-selective membrane formed from Nafion solution using a micro-flow patterning technique. A model of an N-channel junction field-effect transistor was applied to clarify the chip's operational principles. Fabrication of the pre-concentrator relied on a straightforward soft-lithography process using dry film photoresist, eliminating the need for a cleanroom. Impedance within the concentration zone was also analyzed by integrating a gold configuration inside the main channel, with changes in impedance explained using the Randles model.

The electrochemical immunosensor was designed with a three-electrode configuration, including gold working and counter electrodes, and an Ag/AgCl reference electrode. The working electrode surface was modified to immobilize antibodies, creating the biosensor. Specific antigen-antibody binding on the sensor surface was detected through fluorescence (for BSA-FITC) and electrochemical techniques, such as cyclic voltammetry and electrochemical impedance spectroscopy. The combination of the immunosensor with the pre-concentrator in the microfluidic chip enhances both the selectivity and the limit of detection of the biosensor. Additionally, a portable device was developed to integrate the microfluidic chip with measuring and control circuits, creating a practical point-of-care device. This device provides voltage potentials for

protein pre-concentration and performs electrochemical measurements to detect and quantify protein levels, displaying results on-screen.

The outcomes demonstrated the system's robust performance and highlighted numerous advantages. This platform holds significant potential for future medical applications, enabling the detection of biological molecules and disease diagnosis via electrochemical and impedance measurements. It promises to advance diagnostic capabilities, particularly for cancer and other biologically complex diseases, paving the way for enhanced disease detection and monitoring.

List of publications concerning dissertation

1. **Chi Tran Nhu**, Phu Nguyen Dang, Loc Do Quang, Trinh Chu Duc, Chun-Ping Jen, Tung Bui Thanh (2023) "Development of a microfluidic chip for protein preconcentration using dual gate structure and nanomembrane", *Microsystem Technologies* vol. 29, no. 12, pp. 1757-1767 (WoS, Q3)

2. **Chi Tran Nhu**, Loc Do Quang, Chun-Ping Jen, Trinh Chu Duc, Tung Bui Thanh (2024) "Development of a Protein Enrichment and Detection Microfluidic Platform based on Ion Concentration Polarization (ICP) and Electrochemical Impedance Spectroscopy (EIS) Techniques", *IEEE Sensors Letters* vol. 8, no. 9, pp. 1-4 (WoS, Q2)

3. **Chi Tran Nhu**, Tuan Vu Quoc, Loc Do Quang, Phu Nguyen Dang, Jen Chun-Ping, Trinh Chu Duc, Tung Bui Thanh (2024) "Comparison of faradaic and non-faradaic impedance biosensors using 2-electrode and 3-electrode configurations for the determination of bovine serum albumin (BSA)", *Analytical Letters* vol. 57, no. 17, pp. 2959–2971 (WoS, Q3)

4. **Chi Tran Nhu**, Tuan Vu Quoc, Loc Do Quang, Phu Nguyen Dang, Son Nguyen Hong, Trinh Chu Duc, Tung Bui Thanh (2024) "Novel, compact electrochemical and impedance instrumentation", *Instrumentation Science and Technology* pp. 1-16 (WoS, Q3)

5. **Chi Tran Nhu**, Phu Nguyen Dang, Manh Pham Tien, Trinh Chu Duc, Tung Bui Thanh, Loc Do Quang (2024) "Functionalization of Carbon Electrode Surface

Using Polyaniline and Gold Nanoparticles for Protein Immobilization", *Analytical Letters* pp. 1–15 (WoS, Q3)

6. **Chi Tran Nhu**, Bui Thanh Tung, Chu Duc Trinh, Nguyen Dang Phu (2023) "Development of a Non-Enzyme Sensor to Detect Glucose Based on the Modification of Copper Electrode", *Arabian Journal for Science and Engineering* vol. 49, pp. 9849–9858 (WoS, Q1)

7. **Chi Tran Nhu**, Phu Nguyen Dang, Linh Huynh Thi Thuy, Loc Do Quang, Thuy Nguyen Tran, Trung Le Thanh, Thanh Le Ngoc, Trinh Chu Duc, Tung Bui Thanh (2024) "An evaluation of a gold surface functionalization procedure for antibody binding and protein detection using 11-mercaptoundecanoic acid (11-MUA)", *Biomedical Engineering: Applications, Basis and Communications* vol. 36, no. 02, pp. 2450002 (WoS, Q4)

8. **Chi Tran Nhu**, Anh Phan Hoang, Tuan Vu Quoc, Loc Do Quang, Phu Nguyen Dang, Trinh Chu Duc, Tung Bui Thanh (2024) "Development of a Low-Cost and Compact Medical Image Reconstruction Platform Based on EIT Technique", *IETE Journal of Research* vol. 70, no. 08, pp. 7044–7057 (WoS, Q3)

9. **Chi Tran Nhu**, Huynh Thi Thuy Linh, Nguyen Canh Viet, Do Quang Loc, Vu Quoc Tuan, Tran Thi Thuy Ha, Vu Ngoc Trung, Jen Chun-Ping, Chu Duc Trinh, Bui Thanh Tung, Nguyen Dang Phu (2024) "Development of an immunosensor based on the screen-printed gold electrodes for bovine serum albumin detection", *International Journal of Nanotechnology (IJNT)* Accepted (WoS, Q4)

10. **Chi Tran Nhu**, Trung Vu Ngoc, Jen Chun-Ping, Loc Do Quang, Trinh Chu Duc, Tung Thanh Bui (2024) "NSE protein detection in a microfluidic channel integrated an electrochemical biosensor", *Biomedical Physics and Engineering Express* Vol 11, No. 1, pp. 1-10 (WoS, Q3)

11. **Chi Tran Nhu**, Nguyen Tran Thuy, Nguyen Cong Huu, Le Thanh Trung, Do Quang Loc, Bui Thanh Tung (2024) "Development of a Compact System Integrating Pre-Concentrator and Electrochemical Measurements for Protein Pre-

Concentration and Detection", in *The 10th IEEE International Conference on Communications and Electronics - IEEE ICCE 2024* pp. 178-183

12. **Chi Tran Nhu**, Loc Do Quang, Chun-Ping Jen, Thuy Nguyen Tran, Huu Nguyen Cong, Trinh Chu Duc, Tung Thanh Bui (2023) "A Novel Approach to Detect Protein Utilizing the Microfluidic Pre-Concentrator Based on The Impedance Measurement Method", in *2023 1st International Conference on Health Science and Technology (ICHST)* pp. 1-5

13. **Chi Tran Nhu**, Phu Nguyen Van, Loan Do Thi, Loc Do Quang, Chun-Ping Jen, Trinh Chu Duc, Tung Bui Thanh (2023) "Research and Development of A Portable Impedance Measurement System Utilizing AD5941 Analog Integrated Circuit for A549 Lung Cancer Cell Detection", in *2023 1st International Conference on Health Science and Technology (ICHST)* pp. 1-6

14. **Chi Tran Nhu**, Phu Nguyen Dang, Hang Tran Thanh, Thom Vu Thi, Loc Do Quang, Tung Bui Thanh (2022) "A protein preconcentration platform utilizing dual gate structure and ion-selective membrane", in *2022 IEEE Ninth International Conference on Communications and Electronics (ICCE)* pp. 195-198

15. **Chi Tran Nhu**, Huynh Thi Thuy Linh, Nguyen Canh Viet, Do Quang Loc, Le Van Chieu, Vu Ngoc Trung, Jen Chung Ping, Chu Duc Trinh, Bui Thanh Tung (2023) "Detection and quantification of bovine serum albumin using screen-printed gold electrodes and electrochemical measurements", in *The 8th International Workshop on Nanotechnology and Application (IWNA 2023)* pp. 254-257

16. **Chi Tran Nhu**, Do Quang Loc, Nguyen Dang Phu, Nguyen Cong Huu, Nguyen Tran Thuy, Chu Duc Trinh, Bui Thanh Tung (2023) "A novel surface functionalization process for carbon electrodes based on the combination of conducting polymer and gold nanoparticles for protein detection", in *The 8th International Workshop on Nanotechnology and Application (IWNA 2023)* pp. 258-261

17. **Chi Tran Nhu**, Do Quang Loc, Jen Chung Ping, Chu Duc Trinh, Bui Thanh Tung (2023) "Research and Detection of Bovine Serum Albumin using the Screen-

Printed Gold Electrode", in *The 4th International Workshop on Advanced Materials and Devices (IWAMD 2023)* pp. 52-55

.

References

[1] D. S. Aga, R. Goldfish, and P. Kulshrestha, "Application of ELISA in determining the fate of tetracyclines in land-applied livestock wastes," *Analyst*, vol. 128, no. 6, pp. 658–662, Jan. 2003, doi: 10.1039/B301630G.

[2] Z. Ahmed, "Ion concentration polarization based on 1-D nanocapillaries," *Doctoral dissertation, Hong Kong University of Science and Technology*, 2019, doi: 10.14711/THESIS-991012753759803412.

[3] B. Alberts, A. Johnson, J. Lewis, M. Raff, K. Roberts, and P. Walter, "The Shape and Structure of Proteins", *Molecular Biology of the Cell. 4th edition*, Garland Science, 2002.

[4] P. Alicia, D. Powers and Sean P. Palecek, "Choosing Treatment for Cancer Patients," *J Heal. Eng.*, vol. 3, no. 4, pp. 503–534, 2014, doi: 10.1260/2040-2295.3.4.503.Protein.

[5] N. L. Anderson and N. G. Anderson, "The Human Plasma Proteome: History, Character, and Diagnostic Prospects," *Mol. Cell. Proteomics*, vol. 1, no. 11, pp. 845–867, Nov. 2002, doi: 10.1074/MCP.R200007-MCP200.

[6] E. B. Aydın, M. Aydın, and M. K. Sezgintürk, "Selective and ultrasensitive electrochemical immunosensing of NSE cancer biomarker in human serum using epoxy-substituted poly(pyrrole) polymer modified disposable ITO electrode," *Sensors Actuators B Chem.*, vol. 306, p. 127613, Mar. 2020, doi: 10.1016/J.SNB.2019.127613.

[7] B. V. Ayyar, S. Arora et al. “Affinity chromatography as a tool for antibody purification,” *Methods*, Vol. 56, Issue 2, February 2012, pp. 116-129.

[8] A. I. Barbosa and N. M. Reis, “A critical insight into the development pipeline of microfluidic immunoassay devices for the sensitive quantitation of protein biomarkers at the point of care,” *Analyst*, vol. 142, no. 6, pp. 858–882, 2017, doi: 10.1039/c6an02445a.

[9] R. C. Bast et al., “Early Detection of Ovarian Cancer: Promise and Reality,” *Cancer Treat. Res.*, vol. 107, pp. 61–97, 2002.

[10] J. P. Beech, "Microfluidics Separation and Analysis of Biological Particles" *Lund University*, 2011.

[11] C. L. Boujon, S. Selimovic-Hamza, I. Bouzalas, and T. Seuberlich, “Development and validation of an immunohistochemistry procedure for the detection of a neurotropic bovine astrovirus,” *J. Virol. Methods*, vol. 239, pp. 26–33, Jan. 2017, doi: 10.1016/J.JVIROMET.2016.10.013.

[12] J. Castillo-León, W. E. Svendsen, “Lab-on-a-Chip Devices and Micro-Total Analysis Systems,” *Springer Cham*, Lab-on-a-Chip Devices Micro-Total Anal. Syst., 2015, doi: 10.1007/978-3-319-08687-3.

[13] C. C. Chao, P. H. Chiu, and R. J. Yang, “Preconcentration of diluted biochemical samples using microchannel with integrated nanoscale Nafion membrane,” *Biomed. Microdevices*, vol. 17, no. 2, pp. 1–9, Apr. 2015, doi: 10.1007/S10544-015-9940-2/METRICS.

[14] Q. Chen, X. Liu, Y. Lei, and H. Zhu, “An electrokinetic preconcentration trapping pattern in electromembrane microfluidics,” *Phys. Fluids*, vol. 34, no. 9, Sep. 2022, doi: 10.1063/5.0109394/2844589.

[15] S. Y. Chen, W. C. Chen, and S. Y. Chang, “Cyclodextrin-assisted dispersive liquid–liquid microextraction for the preconcentration of carbamazepine and

clobazam with subsequent sweeping micellar electrokinetic chromatography," *J. Sep. Sci.*, vol. 41, no. 8, pp. 1871–1879, Apr. 2018, doi: 10.1002/JSSC.201701096.

[16] T. N. Chi, H. T. T. Linh, N. C. Viet, D. Q. Loc, V. Q. Tuan, T. T. T. Ha, V. N. Trung, J. C. Ping, C. D. Trinh, B. T. Tung, N. D. Phu, "Development of an immunosensor based on the screen-printed gold electrodes for bovine serum albumin detection" *International Journal of Nanotechnology (IJNT)*, 2024, Accepted.

[17] T. N. Chi, H. T. T. Linh, N. C. Viet, D. Q. Loc, L. V. Chieu, V. N. Trung, J. C. Ping, C. D. Trinh, B. T. Tung, "Detection and quantification of bovine serum albumin using screen-printed gold electrodes and electrochemical measurements" *The 8th International Workshop on Nanotechnology and Application (IWNA 2023)*, pp. 254-257, 2023.

[18] E. L. Chiswick, E. Duffy, B. Japp, and D. Remick, "Detection and Quantification of Cytokines and Other Biomarkers," *Methods Mol. Biol.*, vol. 844, p. 15, 2012.

[19] J. R. Crowther, "Basic Principles of ELISA," *ELISA*, pp. 35–61, Nov. 1995, doi: 10.1385/0-89603-279-5:35.

[20] J. R. Crowther, "The ELISA Guidebook," *Springer Science & Business Media*, vol. 516, 2009, doi: 10.1007/978-1-60327-254-4.

[21] N. Davidenko, R. Cameron, and S. Best, "Natural Biopolymers for Biomedical Applications", *Encycl. Biomed. Eng.*, vol. 1–3, pp. 162–176, Jan. 2019, doi: 10.1016/B978-0-12-801238-3.11026-8.

[22] M. J. Duffy, "Circulating cancer biomarkers: current status and future prospects," *Cancer Biomarkers Clin. Asp. Lab. Determ.*, pp. 409–443, Jan. 2022, doi: 10.1016/B978-0-12-824302-2.00009-6.

[23] L. Eliasson, B. Kallin, M. Patarroyo, G. Klein, H. Fujiki, and T. Sugimura, "Activation of the EBV-cycle and aggregation of human blood lymphocytes by the tumor promoters teleocidin, lyngbyatoxin a, aplysiatoxin and debromoaplysiatoxin," *2Int. J. Cancer*, vol. 31, no. 1, pp. 7–11, Jan. 1983, doi: 10.1002/IJC.2910310103.

[24] V. Espina et al., "Protein microarrays: Molecular profiling technologies for clinical specimens," *Proteomics*, vol. 3, no. 11, pp. 2091–2100, Nov. 2003, doi: 10.1002/PMIC.200300592.

[25] J. Fu, R. B. Schoch, A. L. Stevens, S. R. Tannenbaum, and J. Han, "A patterned anisotropic nanofluidic sieving structure for continuous-flow separation of DNA and proteins," *Nat. Nanotechnol.*, vol. 2, no. 2, pp. 121–128, Feb. 2007, doi: 10.1038/nnano.2006.206.

[26] P. Gebauer, Z. Malá, and P. Bocček, "Recent progress in analytical capillary isotachophoresis," *Electrophoresis*, vol. 32, no. 1, pp. 83–89, Jan. 2011, doi: 10.1002/ELPS.201000304.

[27] M. Gholinejad, A. Jabari Moghadam, D. T. Phan, A. K. Miri, and S. A. Mousavi Shaegh, "Design and application of ion concentration polarization for preconcentrating charged analytes," *Phys. Fluids*, vol. 33, no. 5, May 2021, doi: 10.1063/5.0038914/992176.

[28] L. Grimwade, E. Gudgin, D. Bloxham, M. A. Scott, and W. N. Erber, "PML protein analysis using imaging flow cytometry," *J. Clin. Pathol.*, vol. 64, no. 5, pp. 447–450, May 2011, doi: 10.1136/JCP.2010.085662.

[29] B. B. Haab, M. J. Dunham, and P. O. Brown, "Protein microarrays for highly parallel detection and quantitation of specific proteins and antibodies in complex solutions," *Genome Biol.*, vol. 2, no. 2, pp. 1–13, Feb. 2001, doi: 10.1186/GB-2001-2-2-RESEARCH0004/FIGURES/7.

[30] S. I. Han, K. S. Hwang, R. Kwak, and J. H. Lee, "Microfluidic paper-based biomolecule preconcentrator based on ion concentration polarization," *Lab Chip*, vol. 16, no. 12, pp. 2219–2227, Jun. 2016, doi: 10.1039/C6LC00499G.

[31] S. M. Hanash, S. J. Pitteri, and V. M. Faca, "Mining the plasma proteome for cancer biomarkers," *Nat. 2008 4527187*, vol. 452, no. 7187, pp. 571–579, Apr. 2008, doi: 10.1038/nature06916.

[32] H. Hayrapetyan, T. Tran, E. Tellez-Corrales, and C. Madiraju, "Enzyme-Linked Immunosorbent Assay: Types and Applications," *Methods Mol. Biol.*, vol. 2612, pp. 1–17, 2023.

[33] A. J. Hickey and S. Giovagnoli, "Physical Properties Characterization," *Pharmaceutical Powder and Particles (2018)*, pp. 21–30, 2018.

[34] A. Höltzel and U. Tallarek, "Ionic conductance of nanopores in microscale analysis systems: Where microfluidics meets nanofluidics," *J. Sep. Sci.*, vol. 30, no. 10, pp. 1398–1419, Jul. 2007, doi: 10.1002/JSSC.200600427.

[35] P. V. Hornbeck, "Enzyme-Linked Immunosorbent Assays," *Curr. Protoc. Immunol.*, vol. 110, no. 1, pp. 2.1.1-2.1.23, Aug. 2015, doi: 10.1002/0471142735.IM0201S110.

[36] S. Hosseini, P. Vázquez-Villegas, M. Rito-Palomares, and S. O. Martinez-Chapa, "General Overviews on Applications of ELISA," *SpringerBriefs Appl. Sci. Technol.*, no. 9789811067655, pp. 19–29, 2018.

[37] H. Y. Hsieh et al., "A nanofluidic preconcentrator integrated with an aluminum-based nanoplasmonic sensor for Epstein-Barr virus detection," *Sensors Actuators B Chem.*, vol. 355, p. 131327, Mar. 2022, doi: 10.1016/J.SNB.2021.131327.

[38] F. B. Hu, "Protein, body weight, and cardiovascular health," *Am. J. Clin. Nutr.*, vol. 82, no. 1, pp. 242S-247S, Jul. 2005, doi: 10.1093/AJCN/82.1.242S.

[39] H. Jeon, H. Lee, K. H. Kang, and G. Lim, "Ion concentration polarization-based continuous separation device using electrical repulsion in the depletion region," *Sci. Reports*, vol. 3, no. 1, pp. 1–7, Dec. 2013, doi: 10.1038/srep03483.

[40] H. L. Jeong, S. Chung, J. K. Sung, and J. Han, "Poly(dimethylsiloxane)-based protein preconcentration using a nanogap generated by junction gap breakdown," *Anal. Chem.*, vol. 79, no. 17, pp. 6868–6873, Sep. 2007.

[41] C. P. Jen, T. G. Amstislavskaya, C. C. Kuo, and Y. H. Chen, "Protein Preconcentration Using Nanofractures Generated by Nanoparticle-Assisted Electric Breakdown at Junction Gaps," *PLoS One*, vol. 9, no. 7, p. e102050, Jul. 2014, doi: 10.1371/JOURNAL.PONE.0102050.

[42] M. Jönsson and U. Lindberg, "A planar polymer microfluidic electrocapture device for bead immobilization," *J. Micromechanics Microengineering,*, vol. 16, no. 10, p. 2116, Aug. 2006, doi: 10.1088/0960-1317/16/10/027.

[43] S. J. Kim, L. D. Li, and J. Han, "Amplified electrokinetic response by concentration polarization near nanofluidic channel," *Langmuir*, vol. 25, no. 13, pp. 7759–7765, Jul. 2009.

[44] S. J. Kim, Y. A. Song, and J. Han, "Nanofluidic concentration devices for biomolecules utilizing ion concentration polarization: theory, fabrication, and applications," *Chem. Soc. Rev.*, vol. 39, no. 3, pp. 912–922, Feb. 2010, doi: 10.1039/B822556G.

[45] M. Kim, M. Jia, and T. Kim, "Ion concentration polarization in a single and open microchannel induced by a surface-patterned perm-selective film," *Analyst*, vol. 138, no. 5, pp. 1370–1378, Feb. 2013, doi: 10.1039/C2AN36346A.

[46] A. Krishnamurthy and R. K. Anand, "Recent advances in microscale extraction driven by ion concentration polarization," *TrAC Trends Anal. Chem.*, vol. 148, p. 116537, Mar. 2022, doi: 10.1016/J.TRAC.2022.116537.

[47] K. Jensen, R. Krusenstjerna-Hafstrøm, J. Lohse, K. H. Petersen, and H. Derand, "A novel quantitative immunohistochemistry method for precise protein measurements directly in formalin-fixed, paraffin-embedded specimens: analytical performance measuring HER2," *2Mod. Pathol.*, vol. 30, no. 2, pp. 180–193, Feb. 2017, doi: 10.1038/MODPATHOL.2016.176.

[48] R. Karnik, R. Fan, M. Yue, D. Li, P. Yang, and A. Majumdar, "Electrostatic control of ions and molecules in nanofluidic transistors," *Nano Lett.*, vol. 5, no. 5, pp. 943–948, May 2005.

[49] A. M. Kelly, B. A. Fricker, and K. J. Wallace, "Protocol for multiplex fluorescent immunohistochemistry in free-floating rodent brain tissues," *STAR Protoc.*, vol. 3, no. 4, p. 101672, Dec. 2022, doi: 10.1016/J.XPRO.2022.101672.

[50] S. H. Ko, Y. A. Song, S. J. Kim, M. Kim, J. Han, and K. H. Kang, "Nanofluidic preconcentration device in a straight microchannel using ion concentration polarization," *Lab Chip*, vol. 12, no. 21, pp. 4472–4482, Nov. 2012, doi: 10.1039/C2LC21238B/.

[51] S. J. Kim, S. H. Ko, K. H. Kang, and J. Han, "Direct seawater desalination by ion concentration polarization," *Nat. Nanotechnol.*, vol. 5, no. 4, pp. 297–301, Mar. 2010, doi: 10.1038/nnano.2010.34.

[52] S. J. Kim, Y. C. Wang, J. H. Lee, H. Jang, and J. Han, "Concentration polarization and nonlinear electrokinetic flow near a nanofluidic channel," *Phys. Rev. Lett.*, vol. 99, no. 4, p. 044501, Jul. 2007, doi: 10.1103/PHYSREVLETT.99.044501/FIGURES/3/MEDIUM.

[53] G. N. Konstantinou, "Enzyme-Linked Immunosorbent Assay (ELISA)," *Methods Mol. Biol.*, vol. 1592, pp. 79–94, 2017.

[54] E. Kurstak, P. Tijssen, C. Kurstak, and R. Morisset, "Enzyme immunoassays and related procedures in diagnostic medical virology," *Bull. World Health Organ.*, vol. 64, no. 3, p. 465, 1986.

[55] T. Lakshmipriya, U. Hashim, S. C. B. Gopinath, and N. Azizah, "Microfluidic-based biosensor: signal enhancement by gold nanoparticle," *Microsyst. Technol.*, vol. 22, no. 10, pp. 2389–2395, Oct. 2016, doi: 10.1007/S00542-016-3074-1/METRICS.

[56] T. Lakshmipriya, S. C. B. Gopinath, and U. Hashim, "Influenza viral detection on microfluidic delivery assisted biosensors," *Microsyst. Technol.*, vol. 24, no. 2, pp. 823–830, Feb. 2018, doi: 10.1007/S00542-017-3555-X/TABLES/1.

[57] A. E. Larsen, "A Paper-Based Elisa Device for the Rapid Detection of Ischemic Stroke," *Master's Theses*, Jun. 2019.

[58] D. Lee et al., "Highly efficient and scalable biomarker preconcentrator based on nanoelectrokinetics," *Biosens. Bioelectron.*, vol. 176, p. 112904, Mar. 2021, doi: 10.1016/J.BIOS.2020.112904.

[59] J. H. Lee, Y. A. Song, and J. Han, "Multiplexed proteomic sample preconcentration device using surface-patterned ion-selective membrane," *Lab Chip*, vol. 8, no. 4, pp. 596–601, Mar. 2008, doi: 10.1039/B717900F.

[60] H. J. Leidy et al., "The role of protein in weight loss and maintenance," *Am. J. Clin. Nutr.*, vol. 101, no. 6, pp. 1320S-1329S, Jun. 2015, doi: 10.3945/AJCN.114.084038.

[61] S. X. Leng, J. E. McElhaney, J. D. Walston, D. Xie, N. S. Fedarko, and G. A. Kuchel, "ELISA AND MULTIPLEX TECHNOLOGIES FOR CYTOKINE MEASUREMENT IN INFLAMMATION AND AGING RESEARCH," *J. Gerontol. A. Biol. Sci. Med. Sci.*, vol. 63, no. 8, p. 879, 2008, doi: 10.1093/GERONA/63.8.879.

[62] R. M. Lequin, "Enzyme immunoassay (EIA)/enzyme-linked immunosorbent assay (ELISA)," *Clin. Chem.*, vol. 51, no. 12, pp. 2415–2418, Dec. 2005, doi: 10.1373/CLINCHEM.2005.051532.

[63] D. Li et al., "On-site preconcentration of pesticide residues in a drop of seawater by using electrokinetic trapping, and their determination by surface-enhanced Raman scattering," *Microchim. Acta*, vol. 185, no. 1, pp. 1–10, Jan. 2018, doi: 10.1007/S00604-017-2580-X/METRICS.

[64] L. Lo Conte, C. Chothia, and J. Janin, "The atomic structure of protein-protein recognition sites", *J. Mol. Biol.*, vol. 285, no. 5, pp. 2177–2198, Feb. 1999, doi: 10.1006/JMBI.1998.2439.

[65] B. Ma, Y. Z. Song, J. C. Niu, and Z. Y. Wu, "Highly efficient sample stacking by enhanced field amplification on a simple paper device," *Lab Chip*, vol. 16, no. 18, pp. 3460–3465, Aug. 2016, doi: 10.1039/C6LC00633G.

[66] S. Magaki, S. A. Hojat, B. Wei, A. So, and W. H. Yong, "An Introduction to the Performance of Immunohistochemistry," *Methods Mol. Biol.*, vol. 1897, pp. 289–298, 2019.

[67] G. MacBeath and S. L. Schreiber, "Printing Proteins as Microarrays for High-Throughput Function Determination," *Science (80-.)*, vol. 289, no. 5485, pp. 1760–1763, Sep. 2000.

[68] Z. Malá and P. Gebauer, "Analytical isotachophoresis 1967–2022: From standard analytical technique to universal on-line concentration tool," *TrAC Trends Anal. Chem.*, vol. 158, p. 116837, Jan. 2023, doi: 10.1016/J.TRAC.2022.116837.

[69] R. Malhotra et al., "Ultrasensitive detection of cancer biomarkers in the clinic by use of a nanostructured microfluidic array," *Anal. Chem.*, vol. 84, no. 14, pp. 6249–6255, 2012, doi: 10.1021/ac301392g.

[70] B. D. Mansuriya and Z. Altintas, "Graphene Quantum Dot-Based Electrochemical Immunosensors for Biomedical Applications," *Materials (Basel).*, vol. 13, no. 1, p. 96, 2019, doi: 10.3390/ma13010096.

[71] D. Mark, S. Haeberle, G. Roth, F. Von Stetten, and R. Zengerle, "Microfluidic Lab-on-a-Chip Platforms: Requirements, Characteristics and Applications," *NATO Sci. Peace Secur. Ser. A Chem. Biol.*, pp. 305–376, 2010.

[72] C. Matei et al., "Protein microarray for complex apoptosis monitoring of dysplastic oral keratinocytes in experimental photodynamic therapy," *Biol. Res.*, vol. 47, no. 1, 2014, doi: 10.1186/0717-6287-47-33.

[73] K. M. McKinnon, "Flow Cytometry: An Overview," *Curr. Protoc. Immunol.*, vol. 120, no. 1, pp. 5.1.1-5.1.11, Jan. 2018, doi: 10.1002/CPIM.40.

[74] A. C. Moser and D. S. Hage, "Immunoaffinity chromatography: an introduction to applications and recent developments," *Bioanalysis*, vol. 2, no. 4, pp. 769–790, Apr. 2010, doi: 10.4155/bio.10.31.

[75] M. Nagpal, S. Singh, P. Singh, P. Chauhan, and M. A. Zaidi, "Tumor markers: A diagnostic tool," *Natl. J. Maxillofac. Surg.*, vol. 7, no. 1, p. 17, 2016, doi: 10.4103/0975-5950.196135.

[76] C. T. Nhu, P. N. Dang, H. T. Thanh, T. V. Thi, L. Do Quang, and T. B. Thanh, "A Protein Preconcentration Platform Utilizing Dual Gate Structure and Ion-Selective Membrane," *ICCE 2022 - 2022 IEEE 9th Int. Conf. Commun. Electron.*, pp. 195–198, 2022, doi: 10.1109/ICCE55644.2022.9852029.

[77] C. T. Nhu, P. N. Dang, L. Do Quang, T. C. Duc, C. P. Jen, and T. B. Thanh, "Development of a microfluidic chip for protein preconcentration using dual gate structure and nanomembrane," *Microsyst. Technol.*, vol. 29, no. 12, pp. 1757–1767, Dec. 2023, doi: 10.1007/S00542-023-05565-Z/METRICS.

[78] C. T. Nhu, L. Q. Quang, C. P. Jen, T. N. Tran, H. N. Cong, T. C. Duc, T. T. Bui, "A Novel Approach to Detect Protein Utilizing the Microfluidic Pre-Concentrator Based on The Impedance Measurement Method," *2023 1st International Conference on Health Science and Technology (ICHST)*, pp. 1-5, 2023, doi: 10.1109/ICHST59286.2023.10565376.

[79] C. T. Nhu et al., "Comparison of Faradaic and Non-Faradaic Impedance Biosensors Using 2-Electrode and 3-Electrode Configurations for the Determination of Bovine Serum Albumin (BSA)," *Anal. Lett.*, 1-13, 2024.

[80] C. T. Nhu, P. N. Dang, M. P. Tien, T. C. Duc, T. B. Thanh, L. D. Quang, "Functionalization of Carbon Electrode Surface Using Polyaniline and Gold Nanoparticles for Protein Immobilization," *Anal. Lett.*, 1-15, 2024. doi: 10.1080/00032719.2024.2349198.

[81] C. T. Nhu, T. B. Thanh, T. C. Duc, P. N. Dang, "Development of a Non-Enzyme Sensor to Detect Glucose Based on the Modification of Copper Electrode" *Arab J Sci Eng*, Vol. 49, pp. 9849–9858, 2024. doi: 10.1007/s13369-023-08594-y.

[82] C. T. Nhu, P. N. Dang, L. H. T. Thuy, L. D. Quang, T. N. Tran, T. L. Thanh, T. L. Ngoc, T. C. Duc, T. B. Thanh, "An evaluation of a gold sur-

face functionalization procedure for antibody binding and protein detection using 11-mercaptoundecanoic acid (11-MUA)" *Biomedical Engineering: Applications, Basis and Communications*, Vol. 36, No.02, pp. 2450002, 2024. doi: 10.4015/S1016237224500029.

[83] C. T. Nhu, D. Q. Loc, N. D. Phu, N. C. Huu, N. T. Thuy, C. D. Trinh, B. T. Tung, "A novel surface functionalization process for carbon electrodes based on the combination of conducting polymer and gold nanoparticles for protein detection" *The 8th International Workshop on Nanotechnology and Application (IWNA 2023)*, pp. 258-261, 2023.

[84] C. T. Nhu, D. Q. Loc, J. C. Ping, C. D. Trinh, B. T. Tung, "Research and Detection of Bovine Serum Albumin using the ScreenPrinted Gold Electrode" *The 4th International Workshop on Advanced Materials and Devices (IWAMD 2023)*, pp. 52-55, 2023.

[85] C. T. Nhu, T. V. Quoc, L. D. Quang, P. N. Dang, S. N. Hong, T. C. Duc, T. B. Thanh, "Novel, compact electrochemical and impedance instrumentation," *Instrumentation Science and Technology*, pp. 1-16, 2024, doi: 10.1080/10739149.2024.2344008.

[86] C. T. Nhu, A. P. Hoang, T. V. Quoc, L. D. Quang, P. N. Dang, T. C. Duc, T. B. Thanh, "Development of a Low-Cost and Compact Medical Image Reconstruction Platform Based on EIT Technique," *IETE Journal of Research*, vol. 70, No. 8, pp. 7044–7057, 2024, doi: 10.1080/03772063.2024.2310137.

[87] C. T. Nhu, N. T. Thuy, N. C. Huu, L. T. Trung, D. Q. Loc, B. T. Tung, "Development of a Compact System Integrating Pre-Concentrator and Electrochemical Measurements for Protein PreConcentration and Detection," *The 10th IEEE International Conference on Communications and Electronics - IEEE ICCE 2024*, pp. 178-183, 2024, doi: 10.1109/ICCE62051.2024.10634676.

[88] C. T. Nhu et al., "Research and Development of A Portable Impedance Measurement System Utilizing AD5941 Analog Integrated Circuit for A549 Lung Cancer

Cell Detection," *2023 1st International Conference on Health Science and Technology (ICHST)*, pp. 1-6, 2024, doi: 10.1109/ICHST59286.2023.10565334.

[89] C. T. Nhu, L. D. Quang, C. -P. Jen, T. C. Duc and T. B. Thanh, "Development of a Protein Enrichment and Detection Microfluidic Platform Based on Ion Concentration Polarization (ICP) and Electrochemical Impedance Spectroscopy (EIS) Techniques" *IEEE Sensors Letters*, vol. 8, no. 9, pp. 1-4, Sept. 2024, doi: 10.1109/LSENS.2024.3450498.

[90] C. T. Nhu, C. P. Jen, L. D. Quang, T. C. Duc and T. B. Thanh, T. V. Ngoc, "NSE protein detection in a microfluidic channel integrated an electrochemical biosensor" *Biomedical Physics and Engineering Express*, Vol 11, No. 1, pp. 1-10 , doi: 10.1088/2057-1976/ad9f69.

[91] Y. Niu, Z. Zhao, and G. Jin, "Detection of Neuron Specific Enolase (NSE) with the Protein Biosensor Based on Imaging Ellipsometry," *J. Anal. Oncol.*, vol. 1, no. 1, pp. 111–116, Jan. 2012, doi: 10.6000/1927-7229.2012.01.01.17.

[92] R. D. Oleschuk, L. L. Shultz-Lockyear, Y. Ning, and D. J. Harrison, "Trapping of Bead-Based Reagents within Microfluidic Systems: On-Chip Solid-Phase Extraction and Electrochromatography," *Anal. Chem.*, vol. 72, no. 3, pp. 585–590, Feb. 1999, doi: 10.1021/AC990751N.

[93] G. A. Parks, "The Isoelectric Points of Solid Oxides, Solid Hydroxides, and Aqueous Hydroxo Complex Systems," *Chem. Rev.*, Vol. 65, no. 2, pp. 177–198, Apr. 1965.

[94] S. Paulie, P. Perlmann, and H. Perlmann, "Enzyme Linked Immunosorbent Assay," *Cell Biol. A Lab. Handb.*, pp. 533–538, Apr. 2023, doi: 10.1016/B978-012164730-8/50065-4.

[95] M. B. Pepys and G. M. Hirschfield, "C-reactive protein: a critical update," *J. Clin. Invest.*, vol. 111, no. 12, pp. 1805–1812, Jun. 2003, doi: 10.1172/JCI18921.

[96] M. R. Pergande and S. M. Cologna, "Isoelectric point separations of peptides and proteins," *Proteomes*, vol. 5, no. 1, Mar. 2017, doi: 10.3390/PROTEOMES5010004.

[97] M. Pirzada and Z. Altintas, "Nanomaterials for healthcare biosensing applications," *Sensors (Switzerland)*, vol. 19, no. 23, 2019, doi: 10.3390/s19235311.

[98] T. Porstmann and S. T. Kiessig, "Enzyme immunoassay techniques. An overview," *J. Immunol. Methods*, vol. 150, no. 1–2, pp. 5–21, Jun. 1992, doi: 10.1016/0022-1759(92)90061-W.

[99] A. D. Powers and S. P. Palecek, "Protein Analytical Assays for Diagnosing, Monitoring, and Choosing Treatment for Cancer Patients," *J. Healthc. Eng.*, vol. 3, no. 4, pp. 503–534, 2012, doi: 10.1260/2040-2295.3.4.503.

[100] E. Primiceri, M. S. Chiriacò, R. Rinaldi, and G. Maruccio, "Cell chips as new tools for cell biology-results, perspectives and opportunities," *Lab Chip*, vol. 13, no. 19, pp. 3789–3802, Oct. 2013, doi: 10.1039/C3LC50550B.

[101] M. I. Prodromidis, A. B. Flown, S. M. Tzouwara-Karayanni, and M. I. Karayannis, "The importance of surface coverage in the electrochemical study of chemically modified electrodes," *Electroanalysis*, vol. 12, no. 18, pp. 1498–1501, 2000, doi: 10.1002/1521-4109(200012)12:18<1498::AID-ELAN1498>3.0.CO;2-Y.

[102] T. V. Quoc, V. N. Ngoc, T. T. Bui, C. P. Jen, and T. C. Duc, "High-Frequency Interdigitated Array Electrode-Based Capacitive Biosensor for Protein Detection," *Biochip J.*, vol. 13, no. 4, pp. 403–415, Dec. 2019, doi: 10.1007/S13206-019-3412-3/METRICS.

[103] A. Raffone et al., "Diagnostic Accuracy of Immunohistochemistry for Mismatch Repair Proteins as Surrogate of Microsatellite Instability Molecular Testing in Endometrial Cancer," *Pathol. Oncol. Res.*, vol. 26, no. 3, pp. 1417–1427, Jul. 2020, doi: 10.1007/S12253-020-00811-5/METRICS.

[104] N. Ramachandran et al., “Next-generation high-density self-assembling functional protein arrays,” *Nat. Methods*, vol. 5, no. 6, pp. 535–538, May 2008, doi: 10.1038/nmeth.1210.

[105] P. A. Raymundo-Pereira, F. M. Shimizu, R. S. Lima, and O. N. Oliveira, "Nanoarchitectonics in Microfluidic Devices for Sensing and Biosensing," *Elsevier Inc.*, 2019. doi: 10.1016/b978-0-12-813341-5.00009-7.

[106] W. Raza et al., “Recent advancements in supercapacitor technology,” *Nano Energy*, vol. 52, pp. 441–473, Oct. 2018, doi: 10.1016/J.NANOEN.2018.08.013.

[107] R. Reeves, “Molecular biology of HMGA proteins: hubs of nuclear function”, *Gene*, vol. 277, no. 1–2, pp. 63–81, Oct. 2001, doi: 10.1016/S0378-1119(01)00689-8.

[108] M. Regiart, A. M. Gimenez, A. T. Lopes, M. N. P. Carreño, and M. Bertotti, “Ultrasensitive microfluidic electrochemical immunosensor based on electrodeposited nanoporous gold for SOX-2 determination,” *Anal. Chim. Acta*, vol. 1127, pp. 122–130, Aug. 2020, doi: 10.1016/J.ACA.2020.06.037.

[109] W. H. Robinson et al., “Autoantigen microarrays for multiplex characterization of autoantibody responses,” *Nat. Med.* , vol. 8, no. 3, pp. 295–301, 2002, doi: 10.1038/nm0302-295.

[110] A. B. Rohom, P. U. Londhe, S. K. Mahapatra, S. K. Kulkarni, and N. B. Chaure, “Electropolymerization of polyaniline thin films,” *High Performance Polymers*, vol. 26, no. 6, pp. 641–646, Sep. 2014, doi: 10.1177/0954008314538081.

[111] J. S. Ross and J. A. Fletcher, “The HER-2/neu Oncogene in Breast Cancer: Prognostic Factor, Predictive Factor, and Target for Therapy,” *Stem Cells*, vol. 16, no. 6, pp. 413–428, Nov. 1998, doi: 10.1002/STEM.160413.

[112] I. Rubinstein and F. Maletzki, “Electroconvection at an electrically inhomogeneous permselective membrane surface,” *J. Chem. Soc. Faraday Trans.*, vol. 87, no. 13, pp. 2079–2087, Jan. 1991, doi: 10.1039/FT9918702079.

[113] J. F. Rusling, C. V. Kumar, J. S. Gutkind, and V. Patel, "Measurement of biomarker proteins for point-of-care early detection and monitoring of cancer," *Analyst*, vol. 135, no. 10, p. 2496, 2010, doi: 10.1039/c0an00204f.

[114] P. Russell, "iGenetics: A Molecular Approach, 3rd edition", *Pearson*, 2009.

[115] J. Šalplachta, M. Horká, and K. Šlais, "Capillary electrophoresis with preparative isoelectric focusing preconcentration for sensitive determination of amphotericin B in human blood serum," *Anal. Chim. Acta*, vol. 1053, pp. 162–168, Apr. 2019, doi: 10.1016/J.ACA.2018.12.010.

[116] T. Sanvictores and F. Farci, "Biochemistry, Primary Protein Structure", *StatPearls*, Oct. 2022.

[117] M. Schmitt, A. S. Sturmheit, A. Welk, C. Schnelldorfer, and N. Harbeck, "Procedures for the Quantitative Protein Determination of Urokinase and Its Inhibitor, PAI-1, in Human Breast Cancer Tissue Extracts by ELISA," *Methods Mol. Med.*, vol. 120, pp. 245–265, 2006, doi: 10.1385/1-59259-969-9:245.

[118] Ü. Şengül, "Comparing determination methods of detection and quantification limits for aflatoxin analysis in hazelnut," *J. Food Drug Anal.*, vol. 24, no. 1, pp. 56–62, 2016, doi: 10.1016/j.jfda.2015.04.009.

[119] K. Shah and P. Maghsoudlou, "Enzyme-linked immunosorbent assay (ELISA): the basics," *British journal of hospital medicine* , vol. 77, no. 7, pp. C98–C101, Jul. 2016, doi: 10.12968/HMED.2016.77.7.C98.

[120] X. Shao, Y. Huang, and G. Wang, "Microfluidic devices for protein analysis using intact and top-down mass spectrometry," *View*, vol. 4, no. 1, p. 20220032, Feb. 2023, doi: 10.1002/VIW.20220032.

[121] S. R. Sompuram, K. Vani, A. K. Schaedle, A. Balasubramanian, and S. A. Bogen, "Quantitative Assessment of Immunohistochemistry Laboratory Performance by Measuring Analytic Response Curves and Limits of Detection," *Arch. Pathol. Lab. Med.*, vol. 142, no. 7, pp. 851–862, Jul. 2018, doi: 10.5858/ARPA.2017-0330-OA.

[122] S. Y. Son, S. Lee, H. Lee, and S. J. Kim, "Engineered nanofluidic preconcentration devices by ion concentration polarization," *Biochip J.*, vol. 10, no. 4, pp. 251–261, Dec. 2016, doi: 10.1007/S13206-016-0401-7/METRICS.

[123] H. Song, Y. Wang, C. Garson, and K. Pant, "Nafion-film-based micro–nanofluidic device for concurrent DNA preconcentration and separation in free solution," *Microfluid. Nanofluidics*, vol. 17, no. 4, pp. 693–699, Oct. 2014, doi: 10.1007/S10404-014-1357-3/METRICS.

[124] T. M. Squires and S. R. Quake, "Microfluidics: Fluid physics at the nanoliter scale," *Rev. Mod. Phys.*, vol. 77, no. 3, pp. 977–1026, Jul. 2005, doi: 10.1103/REVMODPHYS.77.977/FIGURES/47/MEDIUM.

[125] K. Strimbu and J. A. Tavel, "What are biomarkers?," *Curr. Opin. HIV AIDS*, vol. 5, no. 6, pp. 463–466, Nov. 2010, doi: 10.1097/COH.0B013E32833ED177.

[126] L. Sun et al., "Aptamer based surface plasma resonance assay for direct detection of neuron specific enolase and progastrin-releasing peptide (31-98)," *RSC Adv.*, vol. 11, no. 51, p. 32135, Sep. 2021, doi: 10.1039/D1RA05041A.

[127] A. S. Tanak, B. Jagannath, Y. Tamrakar, S. Muthukumar, and S. Prasad, "Non-faradaic electrochemical impedimetric profiling of procalcitonin and C-reactive protein as a dual marker biosensor for early sepsis detection," *Anal. Chim. Acta X*, vol. 3, p. 100029, Nov. 2019, doi: 10.1016/J.ACAX.2019.100029.

[128] C. Tejada Casado, "Avances en el análisis de benzimidazoles en muestras alimentarias, mediambientales y clínicas," Dec. 2018.

[129] S. Trasatti and O. A. Petrii, "Real surface area measurements in electrochemistry," *J. Electroanal. Chem.*, vol. 327, no. 1–2, pp. 353–376, Jun. 1992, doi: 10.1016/0022-0728(92)80162-W.

[130] I. C. Tsai, C. Y. Su, C. C. Hu, and T. C. Chiu, "Simultaneous determination of whitening agents and parabens in cosmetic products by capillary electrophoresis

with on-line sweeping enhancement," *Anal. Methods*, vol. 6, no. 19, pp. 7615–7620, Sep. 2014, doi: 10.1039/C4AY00985A.

[131] L. J. Urio, M. A. Mohamed, J. Mghamba, A. Abade, and S. Aboud, "Evaluation of HIV antigen /antibody combination ELISAs for diagnosis of HIV infection in Dar Es Salaam, Tanzania," *Pan Afr. Med. J.*, vol. 20, pp. 1–7, Mar. 2015, doi: 10.11604/PAMJ.2015.20.196.4934.

[132] S. K. Vashist and J. H. T. Luong, "Immunoassays: An Overview," *Handb. Immunoass. Technol. Approaches, Performances, Appl.*, pp. 1–18, Jan. 2018, doi: 10.1016/B978-0-12-811762-0.00001-3.

[133] K. Veskimäe et al., "Assessment of PARP protein expression in epithelial ovarian cancer by ELISA pharmacodynamic assay and immunohistochemistry," *Tumor Biol.*, vol. 37, no. 9, pp. 11991–11999, Sep. 2016, doi: 10.1007/S13277-016-5062-6/METRICS.

[134] F. Volpetti, J. Garcia-Cordero, and S. J. Maerkl, "A microfluidic platform for high-throughput multiplexed protein quantitation," *PLoS One*, vol. 10, no. 2, pp. 1–15, 2015, doi: 10.1371/journal.pone.0117744.

[135] H. Vu-Dinh, W. Y. Tsao, and C. P. Jen, "Enhanced immunoassay in a nanofluidic preconcentrator utilizing nano-interstices among self-assembled gold nanoparticles," *Biomed. Microdevices*, vol. 24, no. 2, pp. 1–11, Jun. 2022, doi: 10.1007/S10544-022-00619-X/METRICS.

[136] D. Walls, et al. "Protein chromatography" *Springer New York*, 2017, doi: 10.1007/978-1-60761-913-0.

[137] J. Wang, L. lu Han, and Z. Xu, "Nano-electrokinetic ion concentration in the ion enrichment zone," *Microsyst. Technol.*, vol. 25, no. 2, pp. 711–717, Feb. 2019, doi: 10.1007/S00542-018-3999-7/METRICS.

[138] C. Wang, Y. Wang, Y. Zhou, Z. Q. Wu, and X. H. Xia, "High-performance bioanalysis based on ion concentration polarization of micro-/nanofluidic de-

vices," *Anal. Bioanal. Chem.*, vol. 411, no. 18, pp. 4007–4016, Jul. 2019, doi: 10.1007/S00216-019-01756-8/METRICS.

[139] Y. C. Wang, A. L. Stevens, and J. Han, "Million-fold preconcentration of proteins and peptides by nanofluidic filter," *Anal. Chem.*, vol. 77, no. 14, pp. 4293–4299, Jul. 2005.

[140] L. Wu and X. Qu, "Cancer biomarker detection: recent achievements and challenges," *Chem. Soc. Rev.*, vol. 44, no. 10, pp. 2963–2997, May 2015, doi: 10.1039/C4CS00370E.

[141] K. Wu et al., "Recent progress of microfluidic chips in immunoassay," *Front. Bioeng. Biotechnol.*, vol. 10, p. 1112327, Dec. 2022, doi: 10.3389/FBIOE.2022.1112327/BIBTEX.

[142] Y. Xiong, Y. Leng, X. Li, X. Huang, and Y. Xiong, "Emerging strategies to enhance the sensitivity of competitive ELISA for detection of chemical contaminants in food samples," *TrAC Trends Anal. Chem.*, vol. 126, p. 115861, May 2020, doi: 10.1016/J.TRAC.2020.115861.

[143] X. Xu, L. Liu, Z. Jia, and Y. Shu, "Determination of enrofloxacin and ciprofloxacin in foods of animal origin by capillary electrophoresis with field amplified sample stacking–sweeping technique," *Food Chem.*, vol. 176, pp. 219–225, Jun. 2015, doi: 10.1016/J.FOODCHEM.2014.12.054.

[144] H. Yaziji et al., "Consensus recommendations on estrogen receptor testing in breast cancer by immunohistochemistry," *Appl. Immunohistochem. Mol. Morphol.*, vol. 16, no. 6, pp. 513–520, Dec. 2008, doi: 10.1097/PAI.0B013E31818A9D3A.

[145] G. Yossifon, P. Mushenheim, Y. C. Chang, and H. C. Chang, "Nonlinear current-voltage characteristics of nanochannels," *Phys. Rev. E - Stat. Nonlinear, Soft Matter Phys.*, vol. 79, no. 4, p. 046305, Apr. 2009, doi: 10.1103/PHYSREVE.79.046305/FIGURES/6/MEDIUM.

[146] G. Yossifon and H. C. Chang, "Selection of nonequilibrium overlimiting currents: Universal depletion layer formation dynamics and vortex instability," *Phys. Rev. Lett.*, vol. 101, no. 25, p. 254501, Dec. 2008, doi: 10.1103/PHYSREVLETT.101.254501/FIGURES/4/MEDIUM.

[147] M. Yu, Y. Hou, H. Zhou, and S. Yao, "An on-demand nanofluidic concentrator," *Lab Chip*, vol. 15, no. 6, pp. 1524–1532, Mar. 2015, doi: 10.1039/C4LC01480D.

[148] H. Yu, Y. Lu, Y. G. Zhou, F. Bin Wang, F. Y. He, and X. H. Xia, "A simple, disposable microfluidic device for rapid protein concentration and purificationvia direct-printing," *Lab Chip*, vol. 8, no. 9, pp. 1496–1501, Aug. 2008, doi: 10.1039/B802778A.

[149] S. Zhang, A. Garcia-D'Angeli, J. P. Brennan, and Q. Huo, "Predicting detection limits of enzyme-linked immunosorbent assay (ELISA) and bioanalytical techniques in general," *Analyst*, vol. 139, no. 2, pp. 439–445, Dec. 2013, doi: 10.1039/C3AN01835K.

[150] W. Zhang, Z. He, L. Yi, S. Mao, H. Li, and J. M. Lin, "A dual-functional microfluidic chip for on-line detection of interleukin-8 based on rolling circle amplification," *Biosens. Bioelectron.*, vol. 102, no. October 2017, pp. 652–660, 2018, doi: 10.1016/j.bios.2017.12.017.

[151] C. Zhang, D. Shi, X. Li, and J. Yuan, "Microfluidic electrochemical magnetoimmunosensor for ultrasensitive detection of interleukin-6 based on hybrid of AuNPs and graphene," *Talanta*, vol. 240, Apr. 2022, doi: 10.1016/J.TALANTA.2021.123173.

[152] Y. Zheng et al., "HPLC-MS/MS method for the simultaneous quantification of dolutegravir, elvitegravir, rilpivirine, darunavir, ritonavir, raltegravir and raltegravir-β-d-glucuronide in human plasma," *J. Pharm. Biomed. Anal.*, vol. 182, p. 113119, Apr. 2020.

[153] I. Zhivkov, Z. Vasicek, Z. Slavikova, R. Yordanov, and J. Ehlich, "Detection of the Yogurt Incubation Kinetics by Portable Impedance Converter," *2020 29th Int. Sci. Conf. Electron. 2020 - Proc.*, Sep. 2020, doi: 10.1109/ET50336.2020.9238319.

Appendix

Signal processing circuit schematic and Technique drawing

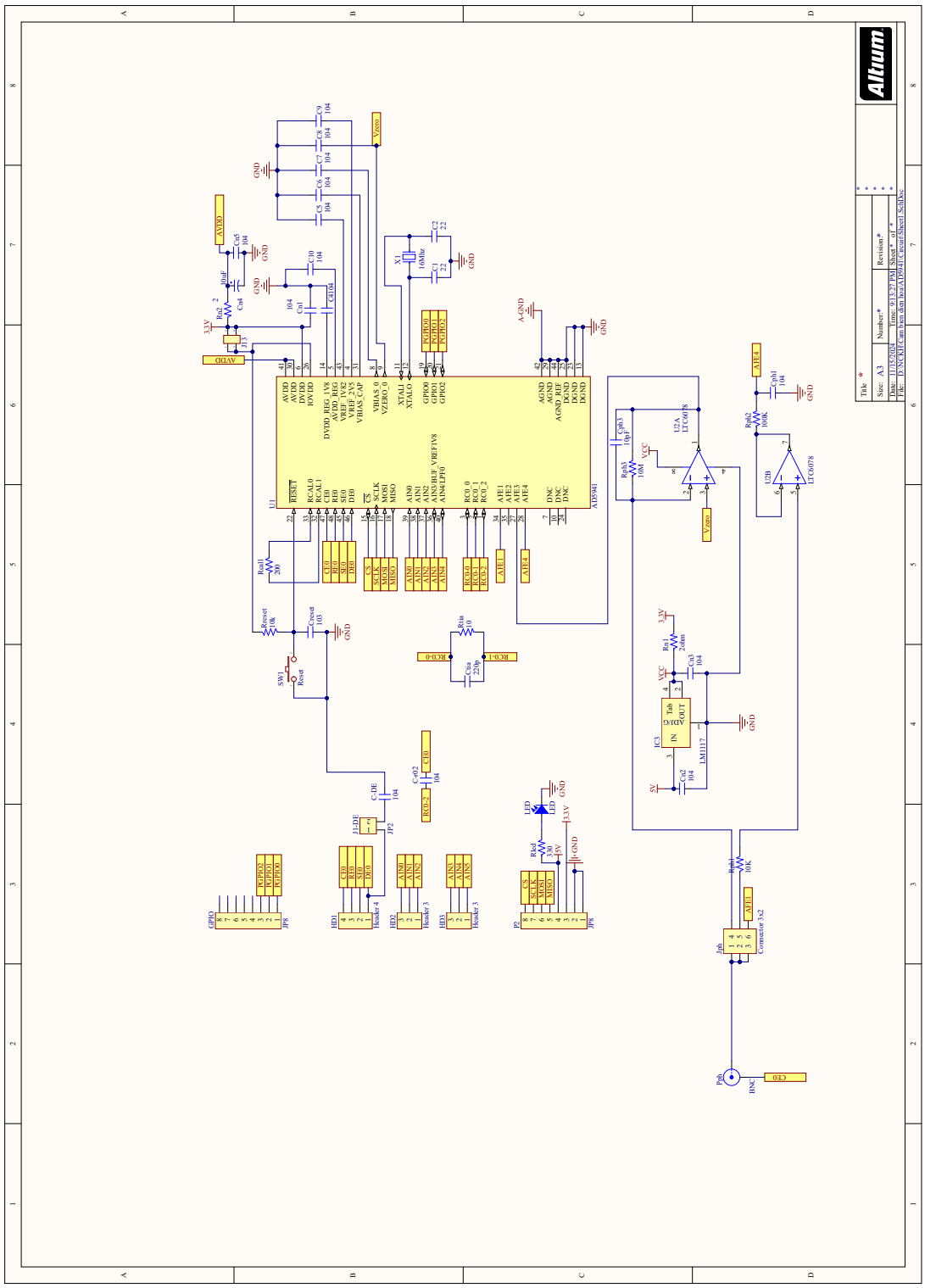

Schematic diagram of electrochemical measuring circuit based on AD5941 analog IC

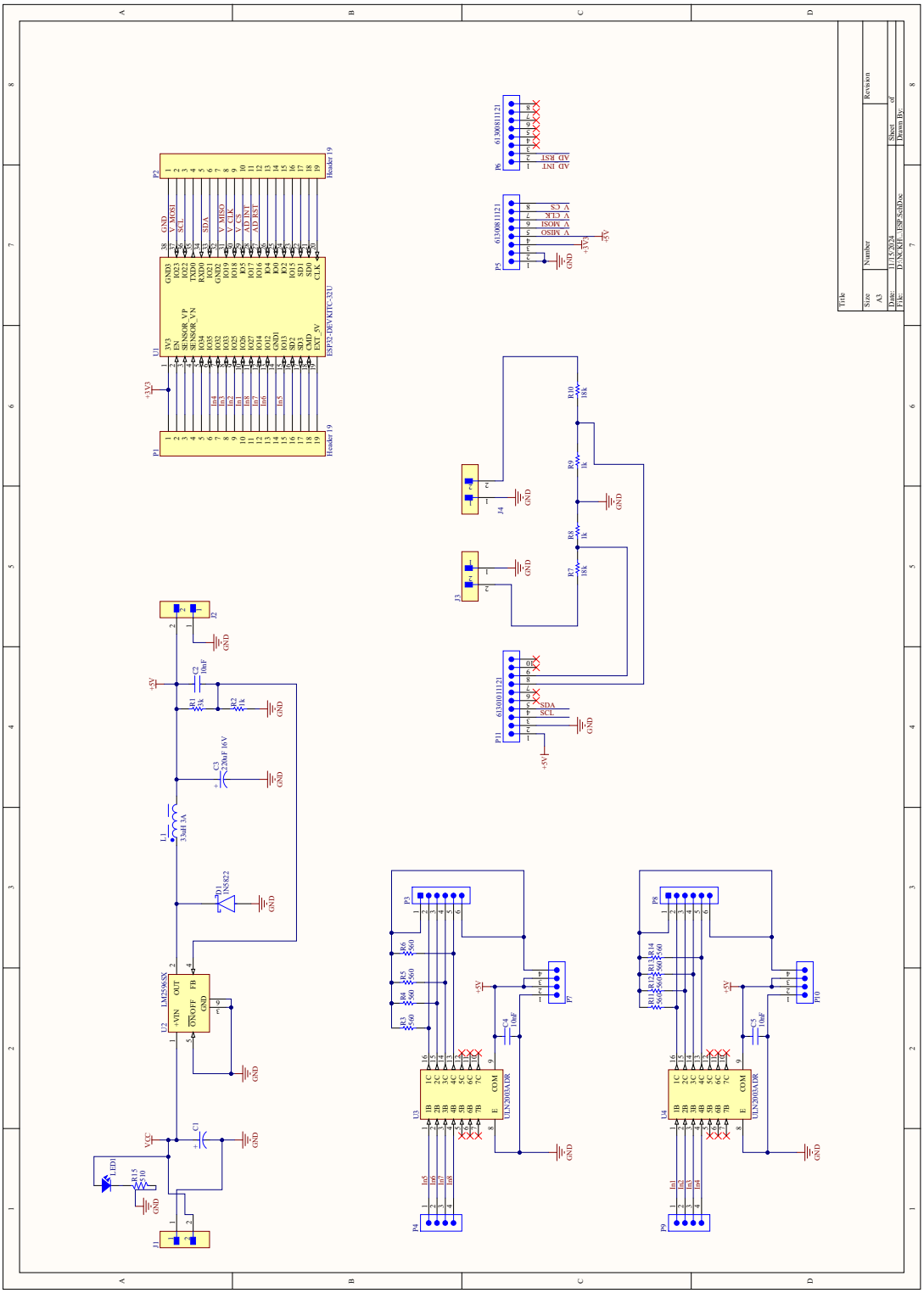

Mother board connecting the measurement board and microcontroller

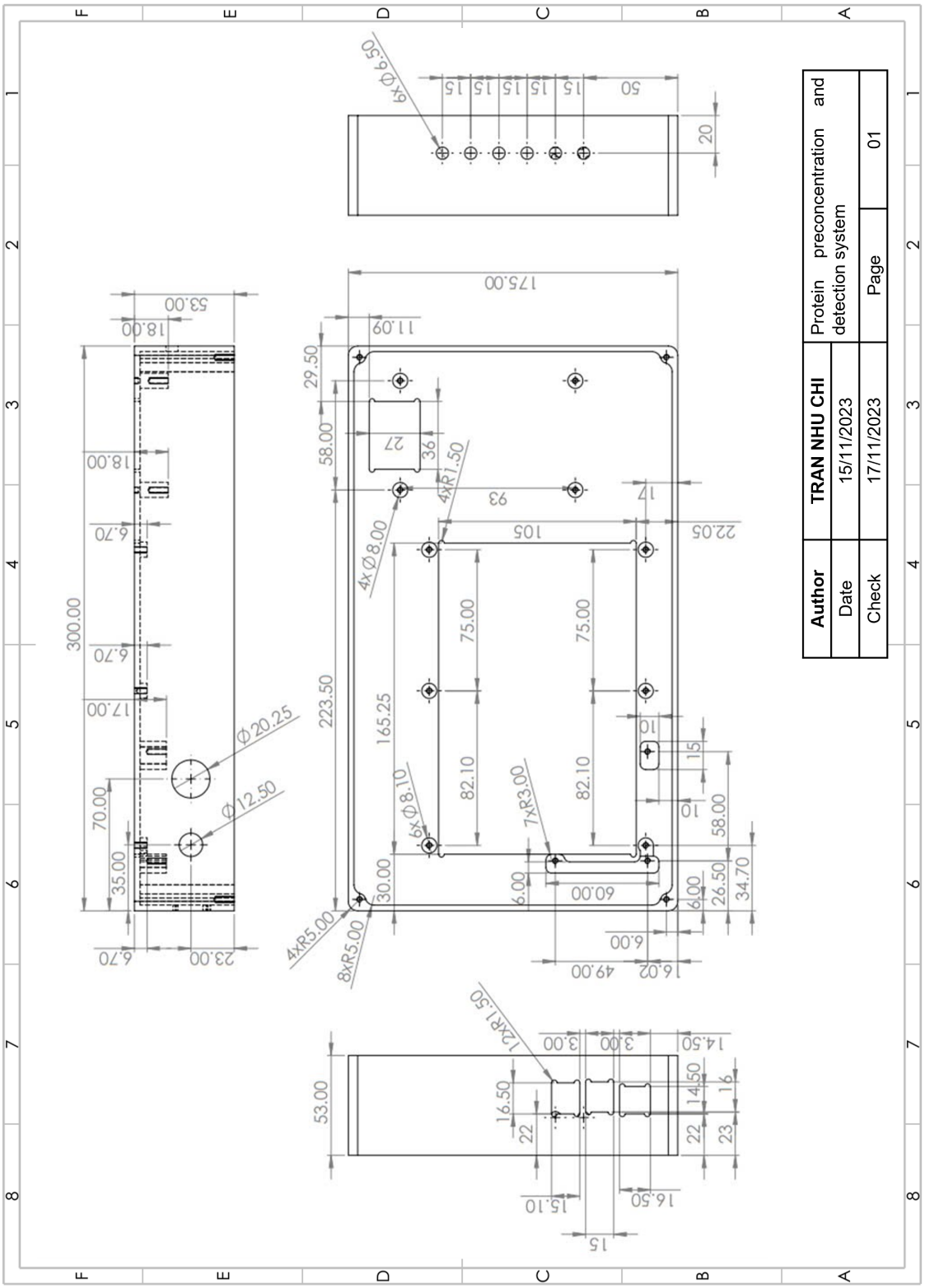

The technique drawing of the proposed system